CLIMATICALLY CONTROLLED SEDIMENTARY PROCESSES ON CONTINENTAL SHELVES

Dissertation

zur Erlangung des Doktorgrades der Naturwissenschaften

am Fachbereich Geowissenschaften

der Universität Bremen

vorgelegt von

Aslı Özmaral

Bremen, April 2017

Gutachter / Reviewer

Prof. Dr. Volkhard Spiess

Prof. Dr. Sebastian Krastel

Date of the colloquium / Datum des Kolloquiums

07.06.2017

TABLE OF CONTENTS

List of Figures

Abbreviations

BIIS   British-Irish Ice Sheet

BKIS   Barents-Kara Ice Sheet

BSW   Brine-enriched shelf water

cal ka BP   calendar thousand years before present (1950)

EPV   Elbe Palaeovalley

GZWs   Grounding zone wedges

IRD   Ice-drafted debris

KMF   Kveithola Trough Mouth Fan

LAT   Lowest Astronomical Tide

LGM   Last Glacial Maximum –nearly all ice sheets at their maximum position (26.5–19 cal ka BP)

MIS   Marine oxygen isotope stage

MSGL   Mega-scale glacial lineation

SIS   Scandinavian Ice Sheet

Summary

Continental shelves with their large-scale depositional and erosional sedimentary structures are governed by the complex interplay between shelf physiography, hydrodynamic regime, sediment flux, and climate-driven eustatic changes. They hold, therefore, detailed archives of past climate and environmental conditions, that in turn are the building stone for understanding the influence of changing climate and sea-level, and for constructing future scenarios or testing palaeo-constructions and -models. The main aim of this thesis is to investigate palaeo-environmental organizations recorded in the elongated depressions and confined depocenters in the southeastern North Sea and northwestern Barents Sea, both of which were affected the Eurasian Ice-Sheet Complex during Late Weichselian.

Along the sub-aerially exposed periglacial environment in the southern North Sea during the late Weichselian, Elbe Palaeovalley (EPV) carried meltwater from southern margin of the Scandinavian ice sheet along with drainage from rivers of North European plain. Although this extremely wide valley was a crucial member in the sensitive North Atlantic climate system by contributing freshwater, but also, in environmental organization of North Sea shelf, there are only a couple of studies having dealt with the EPV up to now. Analysis of sediment echo-sounder and multichannel seismic data along with the sedimentological sampling enabled the identification EPV morphology, up to 5 m deep incisions at its base, and EPV infill in detail for the first time. The base of EPV situates between 40–80 m below the present sea-level, and the braided style palaeodrainage is inferred to have been established during the MIS 2 sea level fall and/or lowstand in a periglacial environment. However, EPV had encountered a sudden gradient change on its downstream part, probably reflecting the southern margin of the confluence of ice sheets in the North Sea during late Weichselian. The moraine ridges flanking the valley probably represent an extension of the Late Weichselian ice sheet from the western Denmark towards Dogger Bank. In fact, around 26-m thick stiff clay succession, likely reflecting glaciogenic origin, is spatially mapped in the southeastern Dogger Bank, and supports the earlier speculations on the existence of an ice-dammed lake south of Dogger Bank. Moreover, this lake provides a further evidence for SIS sourced meltwater found in the Bay of Biscay between 23–19 ka BP. As the ice blockage was supposed to have been collapsed around 18.5 ka BP, the northwestward continuation of EPV, via East Dogger Deep, might have transferred meltwater (possibly from lake discharge) towards Norwegian Channel, and endured its main path towards northerly latitudes. This northerly

segment of the base EPV (between 65–80 mbsl) is characterized by significantly less occurrence of incisions in contrast to its southern segment.

With the subsequent Late Pleistocene–Early Holocene sea level rise, successive depocenters established within the EPV, reflects the evolving hydrodynamic regime in tide- and wave-dominated environment until present. With the first marine influence during the Early Holocene, EPV became an estuary with tributaries, intertidal and subtidal flats. After the drowning of EPV around 10 ka BP, the southern North Sea became a shallow micro-tidal basin that is constricted by Dogger Bank Island. This stage indicates that EPV was the major sedimentary trap of the southern North Sea for easterly sediment transport. With the arrival of Atlantic Water (ca. 8 ka BP) increased strength of currents (tidal and wind-driven) caused disturbance of the main valley infill leading to persistent erosion/non-deposition zone around the western rim of EPV. Coinciding with the deceleration in the sea level rise, the accommodation space of EPV was almost filled by ca. 5.8 ka BP. Briefly, under the control of climate, sea level rise and associated changes in hydrodynamic regime, five stages of the shelf organization are recorded in EPV: (1) bradided river system, (2) estuary (3) shallow basin with restricted connections for Atlantic water (10-8 ka), (4) the southwestern connection establishment with the Dover Strait (8-5.8 ka), and (5) open marine environment (5.8 ka BP) with the drowning of Dogger, respectively.

Moving towards high-latitude continental shelf from North Sea, another key region in the North Atlantic realm is the western Barents Sea close to the center of water mass exchange between North Atlantic and the Arctic Ocean. Here, a high latitude sediment drift (the Kveithola Drift) located confined to a glacially-carved trough in the northwestern Barents Sea. Drift deposits is generally regarded as excellent palaeo-environmental repositories, as they provide high lateral continuity and relatively high accumulation rates together with restricted occurrence of hiatuses. However, there is need to better understand the relationship between bottom current circulation and internal drift geometry, that is linked to paleoclimatic variations. The drift was investigated by densely spaced acoustic data along with lithological and sedimentological investigations in order to examine drift's external and internal geometry for the first time. The complex morphology of the drift is characterized by a main and a minor drift body, two drift lenses in the outer part of the trough, drift patches in the innermost part and small perched sediment patches in a structurally-controlled channel to the north. The drift morphological and internal characteristics, an abrupt northward pinch-out forming a typical drift moat, and gradual tapering to the south, and sedimentary facies with strongly bioturbated sediments, abundant silty/sandy mottles and shell fragments suggest a strong control by a bottom current flowing inside the trough. The formation of Kveithola Drift is inferred to be driven by production of Brine-enriched shelf water (BSW) during the winter season and it flows westward along the moat before

cascading the continental slope. As the onset of the drift deposition started around 13 ka BP, BSW formation must have started around the same time, indicating that the presence of coastal polynyas and increased storminess and/or atmospheric cooling of the surface waters.

Kurzfassung

Kontinentalschelfe und ihre großräumigen Ablagerungs- und Erosionsstrukturen werden von einem komplexen Zusammenspiel der Schelf-Physiographie, des hydrodynamischen Regimes, der Sedimentströme sowie klimaabhängiger eustatischer Veränderungen kontrolliert. Das macht sie zu idealen sedimentären Archiven für vergangene Klima- und Umweltbedingungen und somit zu einem wichtigen Baustein um die Auswirkungen von Klima- und Meeresschwankungen zu entschlüsseln sowie Zukunfts-Prognosen zu erstellen bzw. Paläorekonstruktionen und –modelle zu prüfen. Das Ziel dieser Doktorarbeit ist es, die Veränderungen der Paläoumwelt, dokumentiert in den, durch die Eurasischen Eiskappen zur Zeit der Spätweichsel beeinflussten, länglichen Depressionen und begrenzten Ablagerungszentren in der südöstlichen Nordsee sowie der nordwestlichen Barentsee zu untersuchen.

Während der Spätweichsel wurde Schmelzwasser vom südlichen Rand der skandinavischen Eiskappen (Scandinavian Ice Sheet, SIS) gemeinsam mit den Abfluss der Flüsse der Norddeutschen Tiefebene entlang der subaerischen periglazialen Umgebung der südlichen Nordsee im Paläotal der Elbe (Elbe Palaeovalley, EPV) beförderte. Obwohl dieses sehr breite Tal ein wichtiger Bestandteil für die Süßwasserversorgung im Nord Atlantik war und somit auch einen signifikanten Einfluss auch das empfindliche Klima sowie die Veränderung der Umweltbedingungen des Nordseeschelfs hatte, gibt es bisher nur wenige Studien, die sich mit dem EPV auseinander setzen. Zum ersten Mal hat die detaillierte Analysen von Sedimentecholot und mehrkanalseismischen Daten in Kombination mit sedimentologischen Proben es ermöglicht, die EPV Morphologie mit bis zu 5 m tiefen Einschnitten in den Talboden sowie die EPV Füllung zu identifizieren und kartieren. Der Talboden des EPV liegt zwischen 40 und 80 m unter dem heutigen Meeresspiegel. Außerdem wurde ein Paläodrainagesystem im verflochtenen Stil (braided-style) identifiziert, welches sich vermutlich zur Zeit des MIS 2 Meeresspiegelrückzugs und/oder –tiefstandes in einer periglazialen Umgebung gebildet hat. Des Weiteren zeigt das EPV im Teil flussabwärts eine plötzliche Änderung des Gradientes, welche wahrscheinlich die Vereinigung der Eiskappen in der Nordsee zur Zeit der Spätweichsel widerspiegelt. Die Moränenhügel, welche das Tal flankieren, repräsentieren vermutlich eine Ausdehnung der SIS von West Dänemark bis zur Dogger Bank. Eine Abfolge von ungefähr 26 m mächtigem steifen Ton von wahrscheinlich glazigener Herkunft wurde großflächig entlang der südöstlichen Dogger Bank kartiert und unterstützt vorrangegangene Spekulationen über die Existenz eines Eistausees südlich der Dogger Bank. Außerdem liefert die Existenz dieses Sees weitere Beweise für den Einstrom von SIS Schmelzwasser in den Golf von Biscaya zwischen 23 und 19 ka BP. Da die Eisblockade vermutlich von circa 18.5 ka kollabierte, könnte die nordwestliche Fortsetzung des EPV, entlang des Dogger Tiefs, Schmelzwasser (möglicherweise aus Seen stammend) in Richtung

Norwegischer Kanal abfgeführt haben. Somit wäre der Talverlauf in nördlicheren Breitengraden erhalten geblieben. Dieses nördliche Talbodensegment des EPV (zwischen 65 und 80 m unter dem heutigen Meeresspiegel) weisst im Vergleich zum südlicheren Teil signifikant weniger Einschneidungen auf.

Während des anschließenden Spätpleistozän-Frühholozän Meeresspiegelanstiegs bildeten sich sukzessive Ablagerungszentren im EPV, welche die Entwicklung des hydrodynamischen Regimes in einer gezeiten- und wellendominierten Umgebung bis heute wiederspiegeln. Zum Zeitpunkt des ersten marinen Einflusses während des Frühholozäns hat sich das EPV in ein Ästuar mit Nebenflüssen, sowie Watt- und subtidalen Flächen entwickelt. Nach der Flutung des EPV vor circa 10 ka wurde die südliche Nordsee zu einem flachen Micro-Gezeitenbecken, welches durch die Dogger Bank Insel begrenzt wurde. Diese Phase deutet darauf hin, dass das EPV eine bedeutende Sedimentfalle für den ostwärtigen Sedimenttransport der südlichen Nordsee repräsentierte. Mit der Ankunft des Atlantischen Wassers (vor circa 8 ka) verstärkten sich die gezeiten- und windgetriebenen Ströme und beeinträchtigten dabei die Füllablagerung im Tal und führten zu einer lang anhaltenden Phase der Erosion/Nichtablagerung entlang des westlichen Rands des EPV. Gleichzeitig mit der Verlangsamung des Meeresspiegelanstieges wurde der Ablagerungsraum im EPV nahezu gänzlich gefüllt um circa 5.8 ka BP. Zusammenfassend wurden fünf Stadien der Schelfentwicklung im EPV dokumentiert, die wie folgt zusammengefasst werden können: (1) ein verflochtenes Flusssystem, (2) ein Ästuar, (3) ein flaches Becken mit begrenztem Zugang für das Atlantische Wasser (10 – 8 ka BP), (4) die Etablierung einer Verbindung mit der Straße von Dover (8 – 5.8 ka BP), sowie (5) offene Meeresbedingungen (seit 5.8 Jahren) mit der Flutung der Dogger Insel.

In höheren Breitengrade bildet die Barentsee, nahe des Zentrums des Wassermassenaustauschs zwischen Nord Atlantik und Arktischem Ozean gelegen, eine weitere Schlüsselregion im nordatlantischen Regime. In einem submarinen Gletschertal, welches sich über die nordwestliche Barentsee erstreckt, befindet sich hier ein Sediment Drift (der Kveithola Drift). Durch ihre hohe laterale Kontinuität und Sedimentationsraten sowie durch das eingeschränkte Vorkommen von Hiati, gelten solche Driftablagerungen im Allgemeinen als exzellente Archive für Paläoumweltbedingungen. Ein besseres Verständnis der Zusammenhänge zwischen Bodenströmungen und der internen Driftgeometrie in Verknüpfung mit paläoklimatischer Variationen ist daher nötig. Zum ersten Mal wurde die externe und interne Geometrie des Kveithola Drift anhand von einem engen Netz an akustischen Profilen sowie lithologischer und sedimentologischer Daten untersucht. Die komplexe Morphologie des Kverithola Drifts ist geprägt von einem Haupt- und einem Nebendriftkörper, zwei Driflinsen im äußerem Teil des Tals, unregelmäßigen Drifts entlang des inneren Teils sowie kleinen, unregelmäßigen sedimentären

Bereichen in einem strukturkontrolliertem Kanal im Norden. Die Drift Morphologie und internen Merkmale beinhalten ein abruptes Auskeilen gen Norden, welches den Drift-typischen Graben (den sogennanten Moat) formt, ein graduelles Zuspitzen gen Süden, sowie stark bioturbierte sedimentäre Fazies. Häufig vorkommender Silt/Sand sowie Muschelfragmente deuten auf einen starken Einfluss eines Bodenstroms innerhalb des Tals hin. Die Enstehung des Kveithola Drifts wurde vermutlich durch die Produktion von salzwasserreichem Schelfwasser (Brine-enriched shelf water, BSW) während des Winters angetrieben. Dieses BSW fließt westwärts entlang des Moats bevore es den Kontinetalhang herab stürzt. Da der Beginn der Driftablagerung vorraussichtlich von 13 ka einsetzte, muss die BSW Bildung ungefähr zur gleichen Zeit initiiert wurde sein. Dies deutet auf die Präsenz von küstennahen sogennanten Polynyas sowie erhöhter Sturmaktivität und/oder atmosphärischer Kühlung der Oberflächenwasser hin.

Thesis outline & contribution declaration

The work conducted for this thesis is presented as five chapters. In <u>Chapter 1</u> the motivation and objectives of this study are described, and general introduction regarding Late Quaternary glaciation and deglaciation history of Eurasian ice sheets, glacial structures and current controlled sedimentary processes on the continental shelves, and sea-level rise are introduced. Thereafter, overview of the data acquired during associated cruises and explanations of the methodology used are presented. The next three chapters (Chapter 2, 3, and 4) and Appendix (A and B) comprise manuscripts of the doctoral thesis. Chapter 2 and 3 are pending for submission to the relevant journal; while Chapter 4, Appendix A, and Appendix B are published in peer-reviewed journals.

<u>Chapter 2</u> presents the environmental re-organization that took place in the southeastern North Sea shelf since the Last Glacial Maximum with the main emphasis on the Elbe Palaeovalley and its sedimentary infill. This chapter consists of the manuscript below and it is ready for submission:

> **From an ice-marginal spill-way to a sedimentary trap (Elbe Palaeovalley, SE North Sea)**
>
> Aslı Özmaral, Hanno Keil, Daniel A. Hepp, Tilmann Schwenk, Hendrik Lantzsch, Tobias Mörz, Volkhard Spiess
>
> To be submitted to the *Quaternary Science Reviews*
>
> <u>Author contribution</u>: Acquisition of multi-channel seismic and sediment echo-sounder data, their processing and interpretation have been done by A. Özmaral, as well as writing and preparation of all figures. The MSCL core logging was performed by A. Özmaral and D. Hepp. The samples for the 14C dating was selected and treated by A. Özmaral with the help and utilities provided by H. Lantzsch. Draft versions were reviewed by H. Keil, T. Schwenk, D. Hepp and H. Lantzsch. All co-authors participated in the discussion of results.

<u>Chapter 3</u> unravels for the first time the northward continuation of the Elbe Palaeovalley in the eastern North Sea with regards to late Weichselian ice sheet extension and paleoceanograhic development of the area following the deglaciation. This chapter consists of the manuscript below and it is ready for submission:

The pathway of Elbe Palaeovalley and late Quaternary sedimentary succession in the eastern North Sea

Aslı Özmaral, Hanno Keil, Tilmann Schwenk, Daniel A. Hepp, Volkhard Spiess

To be submitted to the *Marine Geology*

Author contribution: The data acquired by H. Keil and D. Hepp. A. Ouro, T. Ehmen, and A. Özmaral were responsible for seismic data processing. A. Özmaral interpreted the data, prepared figures, wrote and organized the manuscript. T. Schwenk, H. Keil and D. Hepp provided suggestions and feedback.

Chapter 4 deals with the glacially originated Kveithola Trough in the NW Barents Sea and its sedimentary succession after deglaciation with specific focus on the bottom current controlled sedimentation. This chapter consists of the manuscript below:

Evolution of a high-latitude sediment drift inside a glacially-carved trough based on high-resolution seismic stratigraphy (Kveithola, NW Barents Sea)

Michele Rebesco, Aslı Özmaral, Roger Urgeles, Daniela Accettella, Renata G. Lucchi, Denise Rüther, Monica Winsborrow, Jaume Llopart, Andrea Caburlotto, Hendrik Lantzsch, Till J.J. Hanebuth

Published in *Quaternary Science Reviews*

Author contribution: Parasound sediment echosounder data acquisition, handling and stratigraphical interpretation of profiles were done by A. Özmaral, as well as integration of MSCL measurements and sedimentological information into the Parasound profiles during a research stay in Italy under the supervision of M. Rebesco. The version of chapters about methods and results were written by A. Özmaral, who prepared also all figures apart from Fig. 4.2 and 4.9 and gave input to the discussion part. Final version was written by M. Rebesco, and A. Özmaral contributed to the revision after the editor and reviewers' comments.

Finally, Chapter 5 summarizes the main results conclusions derived from three study areas along with the suggestions/recommendations for further research that could be conducted.

Appendix A is a further work in the German North Sea representing the first controlled source electromagnetic survey results and a comparison of resistivity model to reflection seismic data from this area. It is published in the peer-reviewed journal as:

Trans-dimensional Bayesian inversion of controlled-source electromagnetic data in the German North Sea

Romina A. S. Gehrmann, Jan Dettmer, Katrin Schwalenberg, Martin Engels, Stan E. Dosso and Aslı Özmaral

<u>Author contribution</u>: Seismic data acquisition and processing were conducted by A. Özmaral. Interpretation of seismic line was discussed with R. Gehrmann.

Appendix B is a further work regarding Kveithola area that is presented in Chapter 4. This chapter focuses on the submarine glacial landforms that are imprinted on the modern seafloor, and published in the peer-reviewed journal as:

Grounding zone wedges and mega-scale glacial lineations in Kveithola Trough, Barents Sea

M. Rebesco, R. Urgeles, A. Özmaral & CORIBAR scientific party

Published in *Atlas of Submarine Glacial Landforms: Modern, Quaternary and Ancient*

<u>Author contribution</u>: Parasound sediment echosounder data acquisition, handling and figure preparation from the profile were done by A. Özmaral.

1   Introduction

Continental shelves with their large-scale depositional and erosional sedimentary structures are governed by the complex interplay between shelf physiography (e.g. geodynamics), hydrodynamic regime (waves, tides, and currents), sediment flux (e.g. rivers and estuaries), and climate-driven eustatic changes (Fig. 1.1). They hold, therefore, detailed archives of past climate and environmental conditions, that in turn are the building stone for understanding the influence of changing climate and sea-level. This understanding is a key element for modeling. The Quaternary period, with its fluctuating climate and associated global eustatic sea-level changes, is characterized either by roughly similar setting to that of the present day during interglacial periods, or by mostly terrestrial settings when sea levels were more than 100 m below the present level. The latter period caused subaerial exposure of some shelves due to the glacio-eustatic lowering in sea levels, for instance, routes of valleys would have been expanded further beyond the today's shorelines being part of a coastal plain environment, especially on passive margins with their wide continental shelves (Bridgland, 2002).
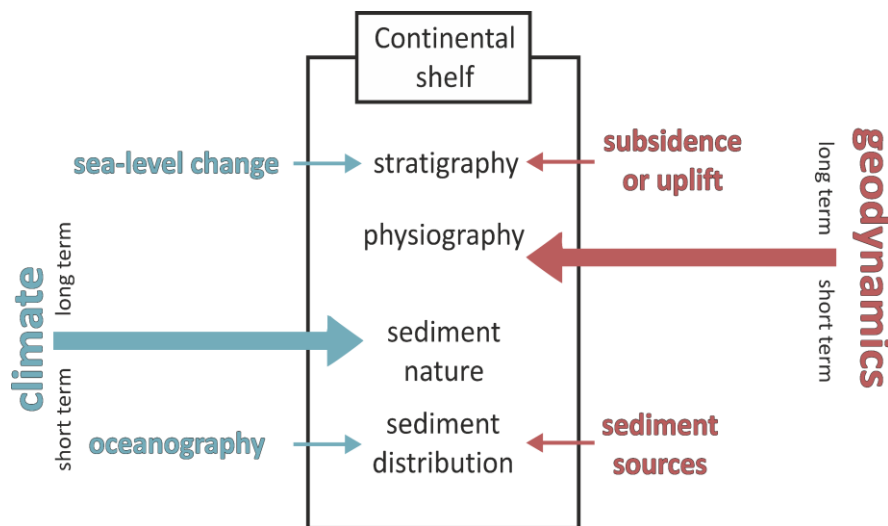
Figure 1.1 Controlling factors on continental shelves in long- and short-term geological timescales after Chiocci and Chivas (2014).

Aside from the wealth of geomorphological and sedimentological information contained within continental shelves and being sediment carriers beyond the shelf edge, these terrestrial landscapes would have been attractive occupation sites for mammalian megafauna along with humans, thereby holding an important potential for the archeological information. Before the

water that is stored by glaciers released by melting of ice sheets, hence rising sea levels and warming climate progressively inundated shelf regions, particularly low-lying areas such that the land area of Europe around the last glacial maximum was around 40 percent greater than today's and the land bridge between continental Europe and Britain existed. In contrast, on high-latitude shelves with their ice-generated depressions at depths of around some hundreds of meters, subaerial exposure was limited only to the innermost parts (Zecchin et al., 2015).

In this thesis, two different areas of European continental shelves (Fig. 1.2) in temperate and high latitude environment were investigated within the framework of MARUM SD2 (*Climatic control on large-scale sedimentary structures*). However, both margins were influenced by the Late Weichselian Eurasian Ice Sheet Complex in terms of glacial processes and sedimentary deposits. Elbe Palaeovalley and Kveithola Trough served as important drainage paths during the last deglaciation of Scandinavian and Barents Sea Ice Sheet, respectively.
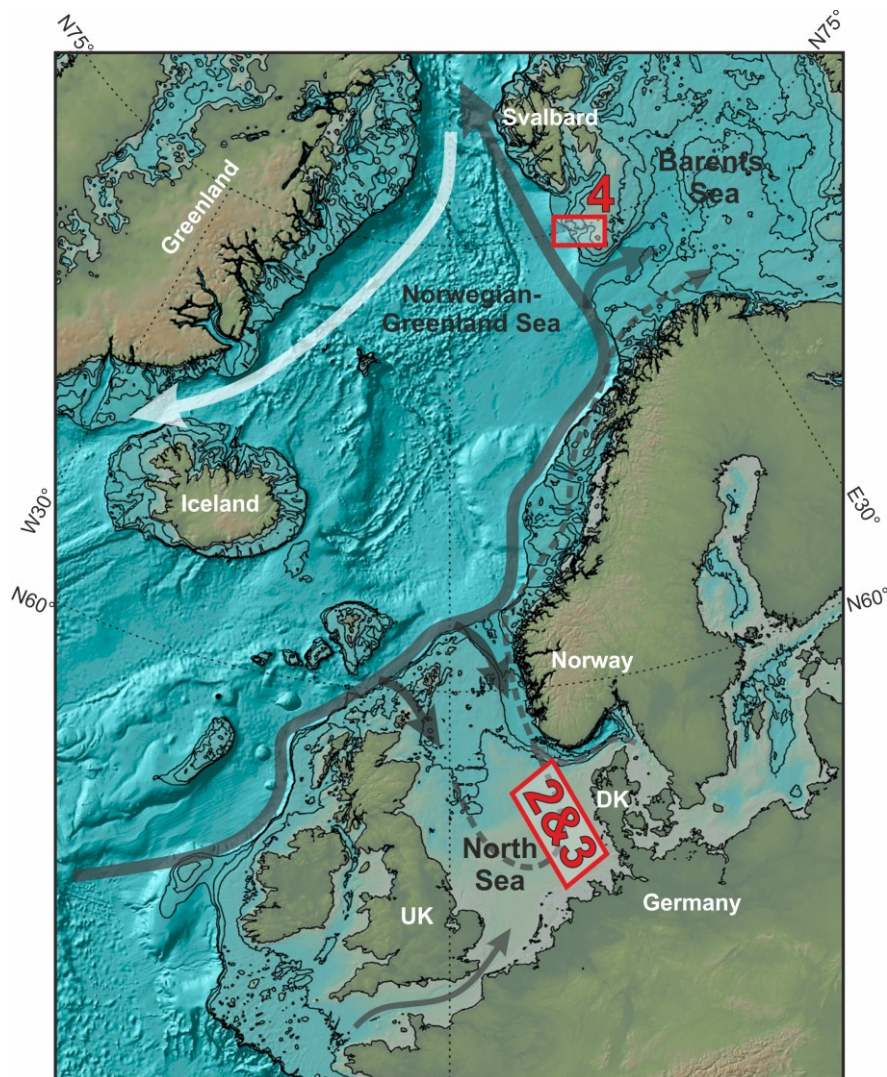
Figure 1.2 Bathymetric overview of study areas in the North and Barents Sea(numbered boxes refer to chapter number). Contours only show 100-400 m depth interval every 100 m. Grey arrows: North Atlantic Current; stippled grey arrows: coastal currents; white arrow: East Greenland Current.

1.1 Study areas and objectives

1.1.1 North Sea

Sea level and climate changes since the last glacial period have led to significant reorganization of the landscape and coastlines in the Northwest Europe (e.g. Shennan et al., 2000). The Elbe Palaeovalley (EPV) has been a large river system whose catchment included continental drainage in the North European plain, particularly the meltwater drainage from the southern margin Scandinavian Ice Sheet (Figge, 1980). During the sea-level rise and flooding of the shelf, such a palaeovalley would be the first to response by reflecting climatic and hydrodynamic variations, together with shallow embayments, estuaries and coastal wetlands (e.g. Hanebuth et al., 2011). Additionally, early–mid Holocene sea level rise is supposed to be the key to estimate the future changes (Siddall et al., 2010). Since the mid-19th century mean sea level has increased by around 1.7 mm yr^{-1} in the North Sea, and also, increased tidal ranges have been measured by tide gauges in the German Bight which are yet to be understood for coastal safety management. Furthermore, possible coastal drowning in Northern Germany could be accelerated by neo-tectonic subsidence as pointed out by (Reicherter et al., 2005).

Regarding the evolution of the North Sea since last glacial period, particularly the Elbe Palaeovalley, a number of issues are to be understood with this study:

- What were the environmental and depositional changes throughout the reorganization of the southern North Sea shelf?
- What are the main controlling factors of the valley infill architecture; which processes govern the sediment transport/deposition?
- What was the fate of the Elbe Palaeovalley outside the German part of the North Sea; was the EPV disrupted by the Late Weichselian (MIS-2) ice sheet in the North Sea on its downstream part? Can we detect imprints of the ice margin and associated sedimentary deposits – as the margin is supposed to be located within the study area?

These scientific questions will be targeted utilizing sediment echosounder and multi-channel seismic data, as well as sediment cores from German, Danish and Norwegian sectors of the North Sea. The data-set allows to carry out the following tasks:

- mapping the morphology of EPV and its speculative pathway in the North Sea,
- describing and interpreting the core lithology, and physical properties perform chronological control for the EPV infill succession and reconstruct and discuss the evolution of the palaeoenvironment in the southeastern North Sea,

3

The results provide the first detailed insights into the EPV, its role in the and late Weichselian deglaciation history (e.g. meltwater contribution to the North Atlantic realm), and Late Weichselian ice sheet presence in the North Sea, therefore contribute to overall evolution of the North Sea throughout the Late Weichselian.

1.1.2 NW Barents Sea

Moving towards high-latitude continental shelf, another key region in the North Atlantic realm is the western Barents Sea close to the center of water mass exchange between North Atlantic and the Arctic Ocean. During late Weichselian, the grounded ice on the Barents Sea is known to have advanced twice to the shelf break in the west (Laberg and Vorren, 1996; Vorren et al., 1998), ice streams occupied cross-shelf troughs, and the deglaciation followed a stepwise pattern (Polyak et al., 1995; Winsborrow et al., 2010; Rüther et al., 2012).

Kveithola Trough within this arctic environment, was a drainage zone for the ice sheet sitting on the Spitsbergenbank (Rüther et al., 2012; Bjarnadóttir et al., 2013). Its confined ice sheet area is supposed to provide intensified response to external forcing parameters linked to the climatic variations in the northern Atlantic realm (Sarnthein et al., 2003a; Rebesco et al., 2011).

Furthermore, in the close vicinity to the polar front, dense winter water formed by seasonal sea-ice production cascades into the Arctic and Nordic Seas, thereby intensifying Atlantic Ocean circulation. As a result, this region is expected to hold the record of variations in sea-ice formation along with the storminess. In this regard, contourites can provide crucial evidence to understand changes in climate and ocean circulation (Rebesco and Camerlenghi, 2008a).

At present, Arctic climate gives signs of rapid change; based on satellite data sea ice cover across the Arctic Ocean has been decreasing by 2–3% per decade, and also, during last two decades surface temperatures has increased around 0.5°C per decade at latitudes above 60°N. (Ślubowska et al., 2005).

Therefore, it is vital to understand past climate changes in this environment that has been significantly affected by present atmospheric warming, and consequently, the following scientific questions will be addressed:

- Which mechanisms have controlled sedimentary successions within the Kveithola Trough, particularly the Kveithola Drift?
- When was the Kveithola drift formed and how was it evolved (e.g. its spatial distribution in the Kveithola Trough)?
- What information can be revealed from the high-resolution sedimentary succession of the Kveithola Drift?

These scientific questions will be targeted utilizing sediment echosounder, multbeam echosounder, and gravity cores from the Kveithola Trough, which allow to

- reveal the palaeoclimatic and palaeoocenographic variability in the western Barents Sea area
- map development stages of the Kveithola drift for the first time
- perform chronological control for the evolution of drift succession
- describe and interpret the core lithology and physical properties
- combine existing bathymetric data and to provide high resolution map

The results will provide a complement to the data and results from the western Barents Sea continental margin, especially to the Kveithola Trough Mouth Fan.

1.2   The Late Weichselian Ice Sheet (Eurasian Ice Sheet Complex) and deglaciation

Northern Hemisphere ice sheets were established 2.6 Ma ago in the early Pleistocene causing variations in the atmospheric and oceanic circulations besides to organization of the physical landscape. Since then for ca. 1.6 Ma, ice sheets were built up and vanished in accordance with the 41 ka cycles related to tilt of the Earth's axis (Imbrie et al., 1992). However, over the last 800 ka the Earth's climate represents a series of glacial-interglacial cycles lasting around 100 ka (eccentricity) and gradual ice sheet growth followed by subsequent abrupt termination establishing a sawtooth curve (Hays et al., 1976; Clark et al., 2009; Berger et al., 2016). Following the last interglacial period (Fig. 1.3) when the climate at least as warm as today or as warm as today, the Earth switched into the glacial mode and the global ice-sheet-reached maxima within the diachronous period between 33 and 19 ka BP that is centered around 26.5 ka BP (Peltier and Fairbanks, 2006; Clark et al., 2009) and the North Atlantic Polar Front moved toward ca. 45°N (Clark et al., 2009). During the late Weichselian maximum, an extensive (the second largest of the Northern Hemisphere) and approximately 2.75–1.75-kilometer-thick ice sheets occupied the northern Europe (from western Ireland offshore to Taimyr Peninsula) (Fig. 1.3; Siegert et al., 2001; Svendsen et al., 2004; Stroeven et al., 2016).

Around half of the massive interlocked ice sheet complex (Eurasian Ice Sheet Complex) on the northwestern Eurasia reached until the continental shelf edge, while its terrestrial margin was lying between North European and Russian plains (Hughes et al., 2016). Each ice sheet within Eurasian Ice Sheet Complex were influenced different external forcing such as sea-level, climate, geothermal heat and Glacial Isostatic Adjustment (GIA), however during the Last Glacial Maximum (LGM) they were evolved as single massive ice complex (Patton et al., 2016). It is composed of initially individual ice sheets: predominantly terrestrial-based Scandinavian Ice Sheet (SIS),

British-Irish Ice Sheet (BIIS), and marine-based Barents-Kara Sea Ice Sheet (Svendsen et al., 2004; Hughes et al., 2016; Patton et al., 2016).
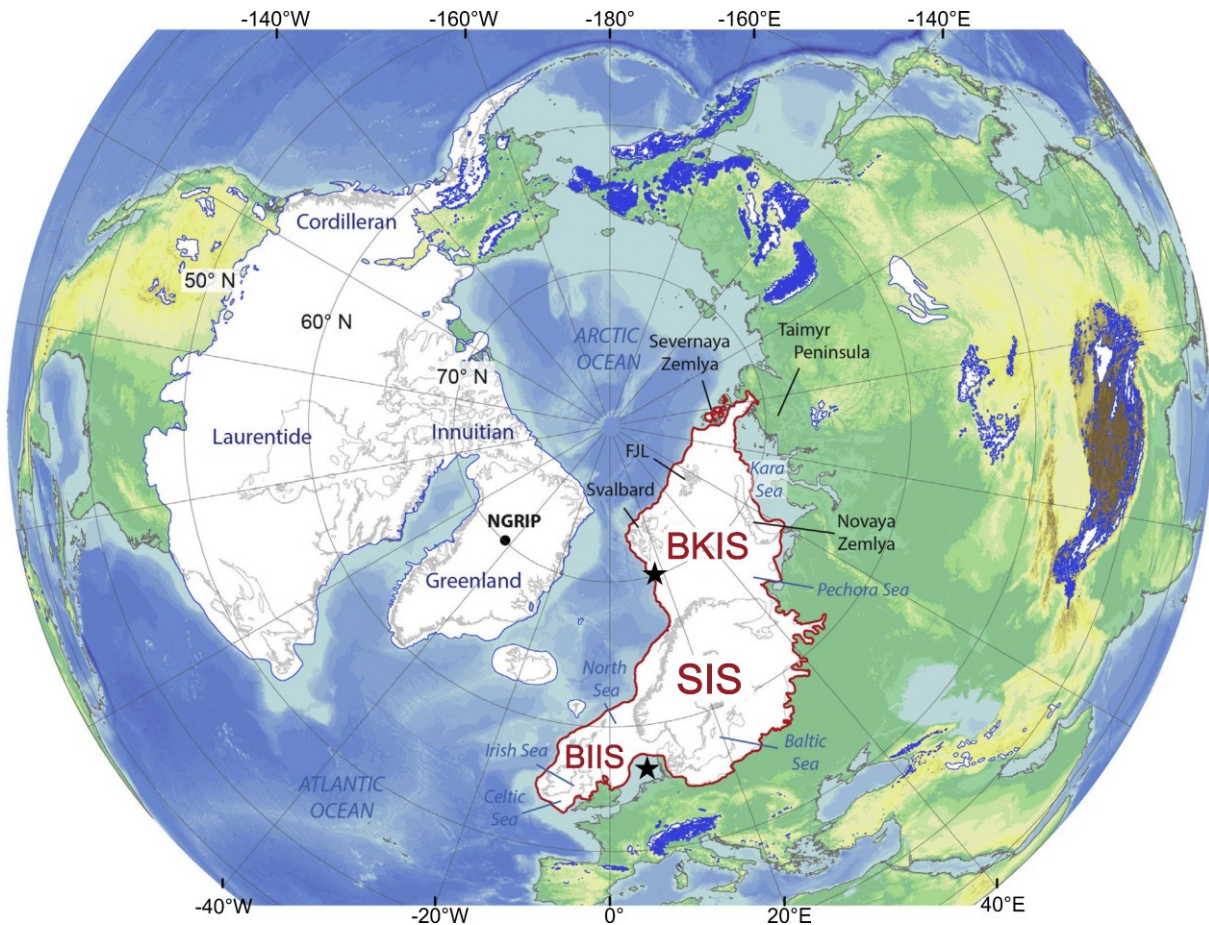
Figure 1.3 The Eurasian Ice Sheet complex (SIS: Scandinavian Ice Sheet; BIIS: British Irish Ice Sheet; BKIS: Barents-Kara Ice Sheet) in the framework of Northern Hemispheric Glaciation during the Late Weichselian (modified from Patton et al., 2016). Red line marks approximate maximal limits of the three Eurasian ice; black stars indicate study areas in the North Sea and Barents Sea.

The western margins of SIS and BIIS advanced across their continental shelves already by 29 ka BP, however it took 6 ka for the ice complex to attain its maximum stand (22.7 ka BP). Owing to the geomorphological imprint, glaciogenic sediment deposition within trough mouth fans, and ice-rafted debris position in cores, the early advance to the shelf recorded for the interval 27–24 cal ka BP for the western margins of Eurasian ice complex (Sejrup et al., 2000; Scourse et al., 2009; Jessen et al., 2010). Based on the glacial landform mapping along with radiometric and cosmogenic nuclide exposure dating, terrestrial limits for the maximum extent on the south and east of the complex were constrained for the interval 25–17 ka BP (Boulton et al., 2001; Kleman et al., 2008; Ehlers et al., 2011a). However, the configuration and chronology for the coalescence of the SIS and BIIS over the North Sea and the eastern extent of the BKIS are still not well-constrained due to the lack of data (Svendsen et al., 2004; Clark et al., 2012b; Hughes et al., 2016; Patton et al., 2016). The North Sea and Atlantic margins were already withdrawing while eastern

margins were advancing until around 20 ka BP, therefore maximum stand of the ice sheet complex was a relatively brief period (Patton et al., 2016; Stroeven et al., 2016). The BIIS was mainly controlled by relatively warm and maritime climate nourished by the weakened North Atlantic current, and it was very sensitive to variations in the sea-level and climate leading to rapid and dynamic advance and retreat (Scourse et al., 2009; Clark et al., 2012a; Patton et al., 2016).

The extensive SIS was mainly controlled by its western topographic relief (Scandinavian Mountains) that triggered the terrestrial eastern margin advance towards east (Boulton et al., 2001; Kleman et al., 2008). On the contrary, BKIS was predominantly marine-based, and grounded at depths down to 550 m, thereby providing an analogue for today's Greenland and Antarctic ice sheets that are grounded below present day sea level (Polyak et al., 1997; Rüther, 2012). The major ice dome developed on the northwestern Barents Sea shelf and it grew towards northern and western margins when the maximum position was established. After the LGM around 18.5 ka BP, the SIS unzipped from the BIIS on the North Sea (Clark et al., 2012a; Sejrup et al., 2016) and the BKIS was separated from the SIS offshore northern Norway (Bjarnadóttir et al., 2014).

Last deglaciation and sea-level rise following the LGM

Due to the built-up and decay of northern hemisphere ice caps, global mean sea levels were varied significantly with amplitudes greater than 100 m (Fig. 1.4; e.g. Lambeck et al., 2002b and Yokoyama and Esat, 2011). The major trigger initiating the Northern Hemisphere deglaciation between 19 and 20 ka was the northern latitude insolation leading to rapid mass loss in ice sheet as demonstrated by Clark et al. (2009) based on their LGM geochronology, and also, the deglaciation, subsequently, amplified by the carbon cycle (increased atmospheric CO_2) and ocean feedbacks (tropical Pacific sea surface temperatures).

Following the last glacial maximum when global mean sea level fell to around 130 m below the present, rapid melting of ice sheets caused high rates of sea level rise (Cronin, 2012); and from LGM until the end of Younger Dryas around 80 m increase in the global mean sea level was caused by the decay of ice sheets (Clark et al., 2012b). The onset of deglaciation in the Northern hemisphere at ca.19.5–19 ka conduce to an abrupt sea-level rise of 5–10 m as a response to northern summer insolation forcing (Clark et al., 2004b). This rise corresponds to 19 ka meltwater pulse (MWP) (Clark et al., 2009). The succeeding sea-level rise was around 15 m between 19–14.7 ka due to the continued retreat of the SIS (Rinterknecht et al., 2006) and Laurentide Ice sheet, this period includes Heinrich event 1 at ca. 17 ka (Hemming, 2004; Clark et al., 2009). Based on fossil coral records, the acceleration in the sea level rise occurred during the time corresponding to the onset of Bølling warm interval around 14.7 ka (concurrent with the MWP-1a) and within 700 years, sea-level rise was 10–20 m, and (Hanebuth, 2000). As any indication for the accelerated retreat for SIS and LIS were not found, the retreat of Antarctic Ice Sheet from its LGM is considered

to be responsible for meltwater contribution that is equivalent to a sea level rise of around 15 m (Weaver et al., 2003; Clark et al., 2009). From 14.0 to 12.9 ka sea-level rise continued until the Younger Dryas cold event (ca. 12.9–11.6 ka; according to Rasmussen et al., 2006) interrupted the postglacial warming during which slowing down in the rate of sea-level rise occurred based on records of low latitude corals (e.g. Bard et al., 2010). The cooling and decrease in the Atlantic Meridional Overturning Circulation (AMOC) during this time attributed to eastern outlet of the Lake Agassiz to the northern Atlantic Ocean (e.g. Broecker et al., 1989) or to the Arctic Ocean (Murton et al., 2010).
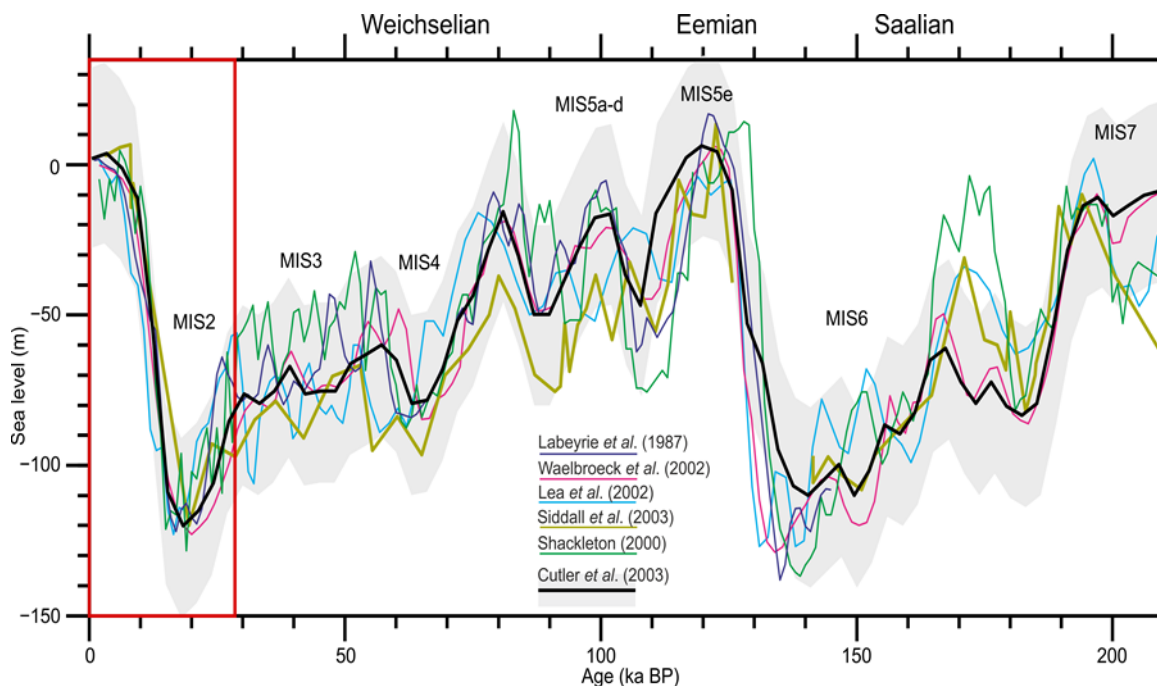
Figure 1.4 Global sea-level curves from the past 200 ka derived from oxygen isotope records (modified after Siddall et al., 2007; full references for the respective data are provided therein). The last glacial cycle is divided into stages MIS 1–5. MIS-4 and -3 stadials resembles the onset of LGM, MIS-2 contains the LGM that is followed by rapid decay of ice and MIS-1 represents the past 11.7 ka (Lambeck et al., 2002a). Red box: interest interval for this thesis. MIS=Marine Isotope Stage.

Climate evolution in Europe during the last deglaciation

Northern Europe during LGM, based on pollen records, was characterized by open, steppe-tundra environments when winter temperatures and precipitations decreased around 5–15 °C and 300–400 mm y^{-1}, respectively (Fletcher et al., 2010; Clark et al., 2012b).

The slight increase in temperature and precipitation marking the conclusion of LGM, pursued by the dry and cold stadial (the Oldest Dryas between 17.5–14.7 ka) when glacial state in vegetation was resumed (Goñi et al., 2000; Clark et al., 2012b). The subsequent rapid temperature increase by 3–5 °C at the onset of Bølling was followed by cool period corresponding to Younger Dryas with a temperature decrease up to 15 °C and resulted in tundra environment again. The abrupt end of

Younger Dryas and rapid temperature increase of around 4 °C – varied latitudinally – occurred at around 11.7 ka (Clark et al., 2012b).

1.2.1 Landforms and formations in glacial and periglacial environments

As several periods in the Quaternary were characterized by several kilometers' thick ice even extending over temperate latitudes of the Northern Hemisphere, (palaeo) landscape was mostly sculpted by combination of glacial erosion and sediments. The land in the vicinity of the glaciers –periglacial landscapes– were under the influence of cold tempreatures leading to permafrost occurrence and tundra-steppe vegetation.

As the distribution of glacial landform assemblages implies a quite range of different appearances in terms of the ice-sheet dynamics and environmental conditions, this section focuses on large-scale landforms observed in the study areas western Barents Sea and North Sea.
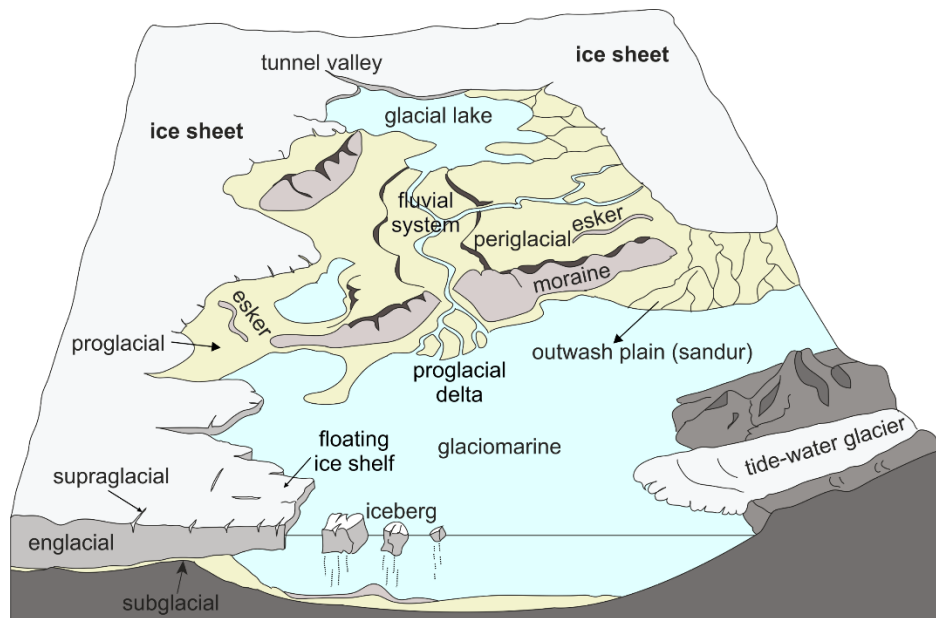
Figure 1.5 Glacial and periglacial environments (modified after Brodzikowski and van Loon, 1991; Janszen, 2012).

Ice-streams drain rapidly interior basins within the ice-sheet and they are the fast-flowing segment of an ice sheet, therefore surrounded by slower flowing ice (e.g. Batchelor and Dowdeswell, 2014). In high latitude climate and oceanography, they play an important role due to their rapid drainage ability during peak glacial conditions thereby huge mass transfer to the ice-sheet drainage basin margin (Andreassen et al., 2004). When the ice was grounded in the Barents Sea, bathymetric cross shelf troughs were occupied by fast flowing (or switching between fast flowing and stagnation) ice streams (Dowdeswell and Elverhøi, 2002). Ice streams in troughs have important protrusions on their mouth at the shelf break called Trough Mouth Fan, are composed mainly of glaciogenic debris flow deposits, and are prominent, among others, on the

Svalbard margin of the Norwegian–Greenland Sea where they have provided evidence for ice-sheet dynamics (e.g. Bear Island (Bjørnøya), Storfjorden, Kveithola Trough Mouth Fan; Vorren et al., 1998; Lucchi et al., 2013; Llopart et al., 2015).

<u>Mega Scale Glacial Lineations</u> (MSGLs) are elongate streamlined curvilinear ridges of sediment that are produced sub-glacially indicating the track of ice-stream. Their lengths are usually around 6–100 km, have width of around 200–1300 m (length to width ratio >10:1), and their spacing ranges between 200 m to 5 km. They were first discovered on the Antarctic continental margin by high-resolution seismic and swath bathymetry investigations (Clark and Stokes, 2003), but later, they also have been discovered in western Eurasia, e.g. inside Kveithola Trough (see Appendix B) and Norwegian Channel (Ottesen et al., 2005; Bjarnadóttir et al., 2013; Ottesen et al., 2016).

<u>Grounding zone wedges</u> (GZWs) are diamictic wedges marking the significant still-stand duration during deglacial ice retreat across the shelf and implying episodic retreat rather than catastrophic (Dowdeswell et al., 2008).

<u>Ice-marginal valleys</u> or spillways are originally referred to German term "Urstromtal". They were aligned parallel to ice front margins in periglacial environments, therefore their courses are related to particular stages of ice sheet limits. These broad valleys (around 25 km wide) collected meltwater from proglacial meltwater channels which were formed across the ice front, as well as river drainage from ice-free areas. They were produced by enormous volumes of water, some of which might be received from catastrophic outbursts related to ice-dammed lakes. Thermal erosion of river banks related to permafrost conditions can be also involved in their formation (Kolstrup, 2005). Ice-marginal valleys recognized not only along the SIS margin, but also along the margin of Laurentide Ice Sheet during the Late Wisconsin and they were associated with catastrophic megaflood events (i.e. outburst floods) (Kehew et al., 2009).

It was in the North Germany where ice marginal valleys were first investigated (Woldstedt, 1950), and in 1909 they were already depicted in the map of the north European Plain by Keilhack (Fig. 1.6; Lüthgens and Böse, 2012). They were situated along North European Plain from Russia to the North Sea where ice-margin transversal meltwater channels cut morphological highs such as till plains (also referred to ground moraine) and end moraine ridges and formed interconnections between ice marginal valleys. The southward proglacial drainage over sandar (i.e. outwash plain) from southern margins of SIS joined east–west flowing rivers towards the North Sea (Figge, 1980; Ehlers and Wingfield, 1991; Ehlers et al., 2004; Böse, 2005). During the Pleistocene glaciations, northward outflow of rivers towards Baltic Sea were blocked by ice sheets; hence their flow was dependent on the position of ice sheet margin such as the Rhine and Meuse in the Netherlands, Elbe, Weser and Ems in Germany. An example of ice-marginal valley (Toruń-Eberswalde) during Weichsel glaciation from German-Polish lowland is shown in Fig. 1.7. This large valley (> 500 km

long, 2–20 km wide) with curved banks is represented by numerous channels (up to 8.5 m deep) of braided system under the periglacial climate (Pisarska-Jamroży, 2015). As being part of the system ice marginal valleys, "Elbe Urstromtal" in the northwest Germany which was the major drainage system of meltwaters that were carried towards present-day's North Sea when the Late Weichselian ice margin (during early MIS 2 or late MIS 3, ca. 34–24 ka BP) was situated around northeast of Elbe Lineament (Ehlers et al., 2011b; Lüthgens and Böse, 2011). In Chapter 2 and 3, further details on its North Sea pathway is presented in detail.
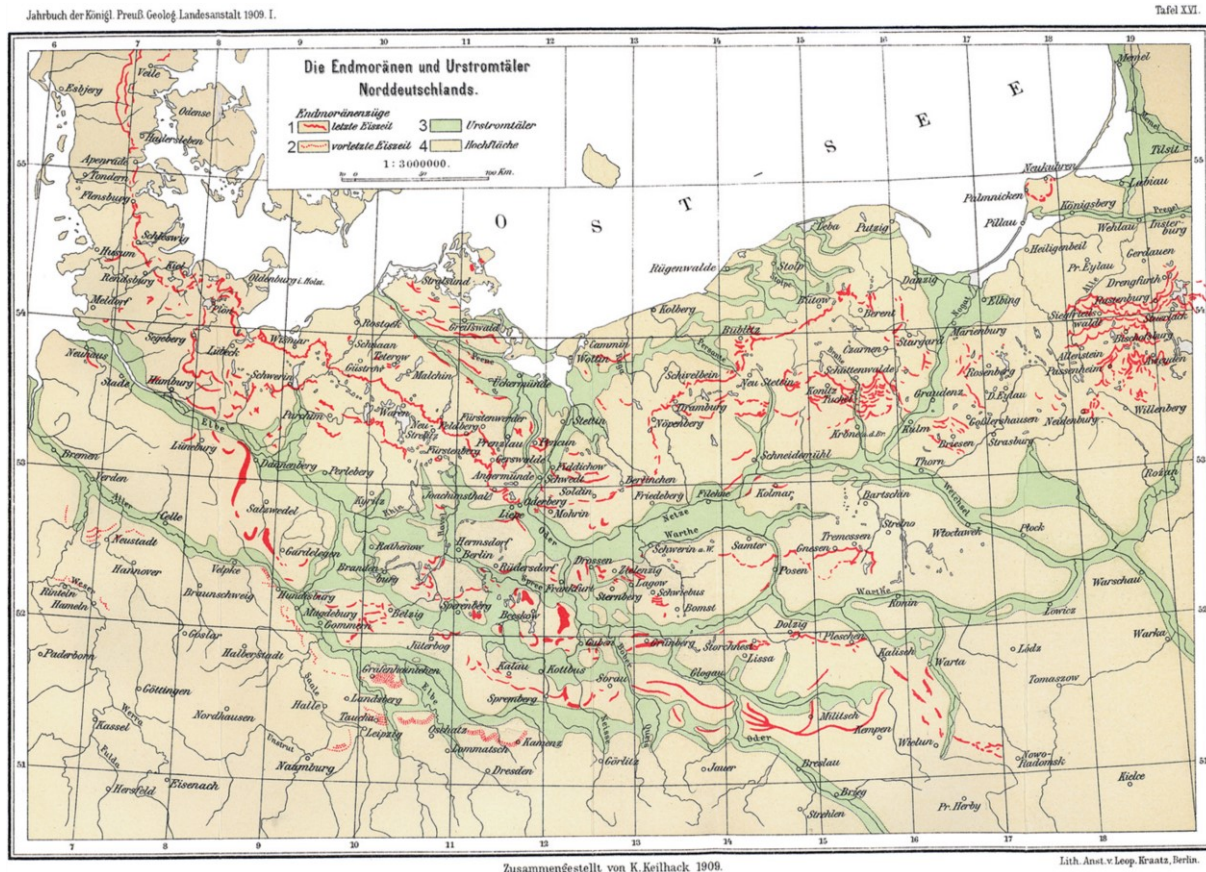
Figure 1.6 Southwestern sector of SIS was drained by a system of ice-marginal valleys the first map by Keilhack (1909). After deglaciation, these valleys were often reshaped by rivers. 1: end moraines of Late Weichsel glaciation; 2: Saale or penultimate glaciation.

Braided river systems are prominent features in ice-marginal valleys as a result of huge amount of glacial debris transport throughout the peak ice melt discharge taking place in summer and spring with limited aggradation. Although not a prerequisite, the braiding pattern is usually established on permafrost that is common for periglacial environment considering that permafrost aids in an effective expansion of channel network (Vandenberghe and Woo, 2002). The response of river systems to changes in climate and environmental conditions during Weichselian were presented and discussed by Vandenberghe and Woo (2002), Huisink (2000), Vandenberghe (1995) and Mol (1997) for some of the European rivers; major changes in vegetation cover, changes in discharge characteristics, the position of the river catchment are

considered to be mainly responsible for the evolution of the fluvial style such as braided, meandering or anastomosing (Fig. 1.8).
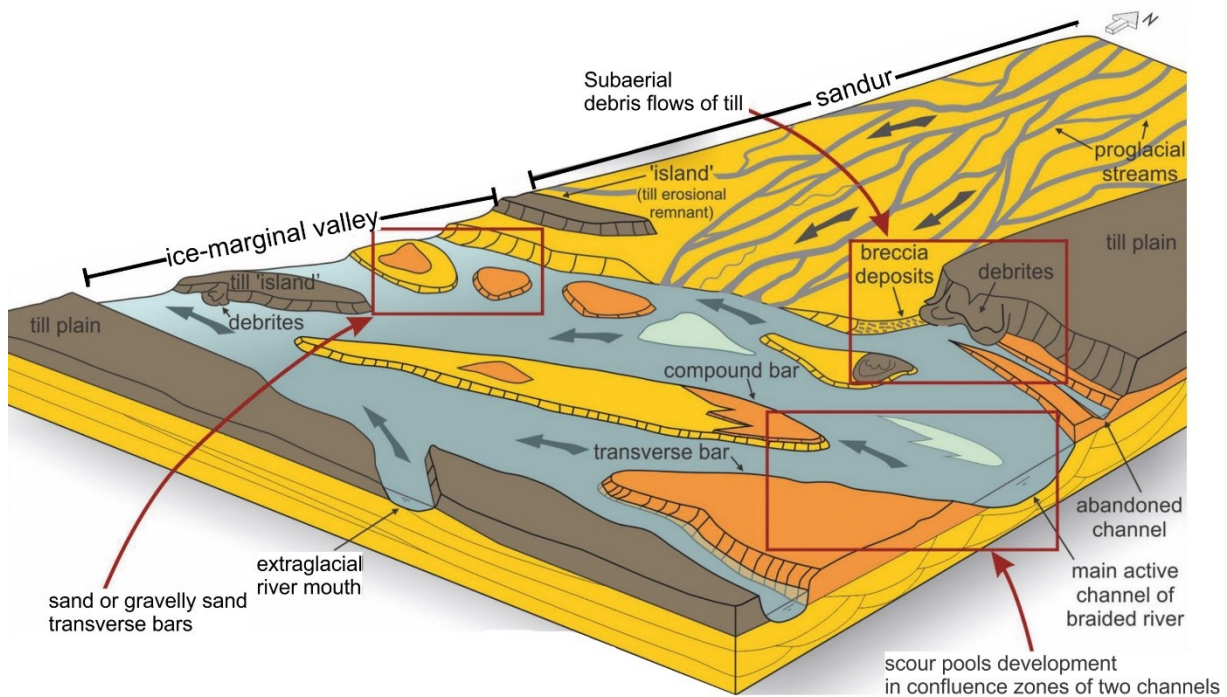
Figure 1.7 Ice-marginal valley during Weichsel glaciation. It drained the water from sandar from north and extraglacial rivers from south (modified after Pisarska-Jamroży, 2015).

<u>Ice-dammed lakes</u> When the meltwater drainage system is impeded by ice margins, water ponding can give rise to formation of an ice-dammed lake that are characterized as being unstable. Breaking down of the dam can be catastrophic if hydrostatic pressure of the lake surpasses the overburden pressure of ice at the lake outlet, or when the lower terrain is exposed by the retreating ice margin, or via overtopping (Stroeven et al., 2016). For instance, north flowing rivers of West Siberia and northern Russian plain (e.g. Yenissei, Ob, and Pechora) were captured by the BKIS and ice-dammed lakes (that were larger than any lake today) were formed during the Quaternary period (Mangerud, 2004). Another example of the biggest lake (349,000 km^2) related to decaying SIS margin was Baltic Ice Lake during Younger Dryas (Jakobsson et al., 2007). In the North Sea, the existence of ice-dammed lake and its overspill (possible catastrophic) during Elsterian, Saalian, and also during Weichselian is inferred and some direct and indirect evidences for glaciolacustrine sediments (i.e. wave-rippled sands, fine grained rainout deposits; Murton and Murton, 2012) are presented by (Smith, 1985; Ménot et al., 2006; Toucanne et al., 2010; Hijma et al., 2012; Cohen et al., 2014).Ice-dammed or proglacial lakes are, among others, important formations for the climate system, since their drainage routes to the ocean can contribute to the sudden climate changes as drainage of the Lake Agassiz contributed to the Younger Dryas (Teller, 1990).

<u>The arcuate shaped</u> sediment accumulations are moraine complexes document either still-stands or ice-front oscillations during glacier retreat (Andreassen et al., 2008; Sejrup et al., 2016) and are represented by poor to well sorted, stratified to weakly stratified sediments and diamictons (Benn and Evans, 2010).
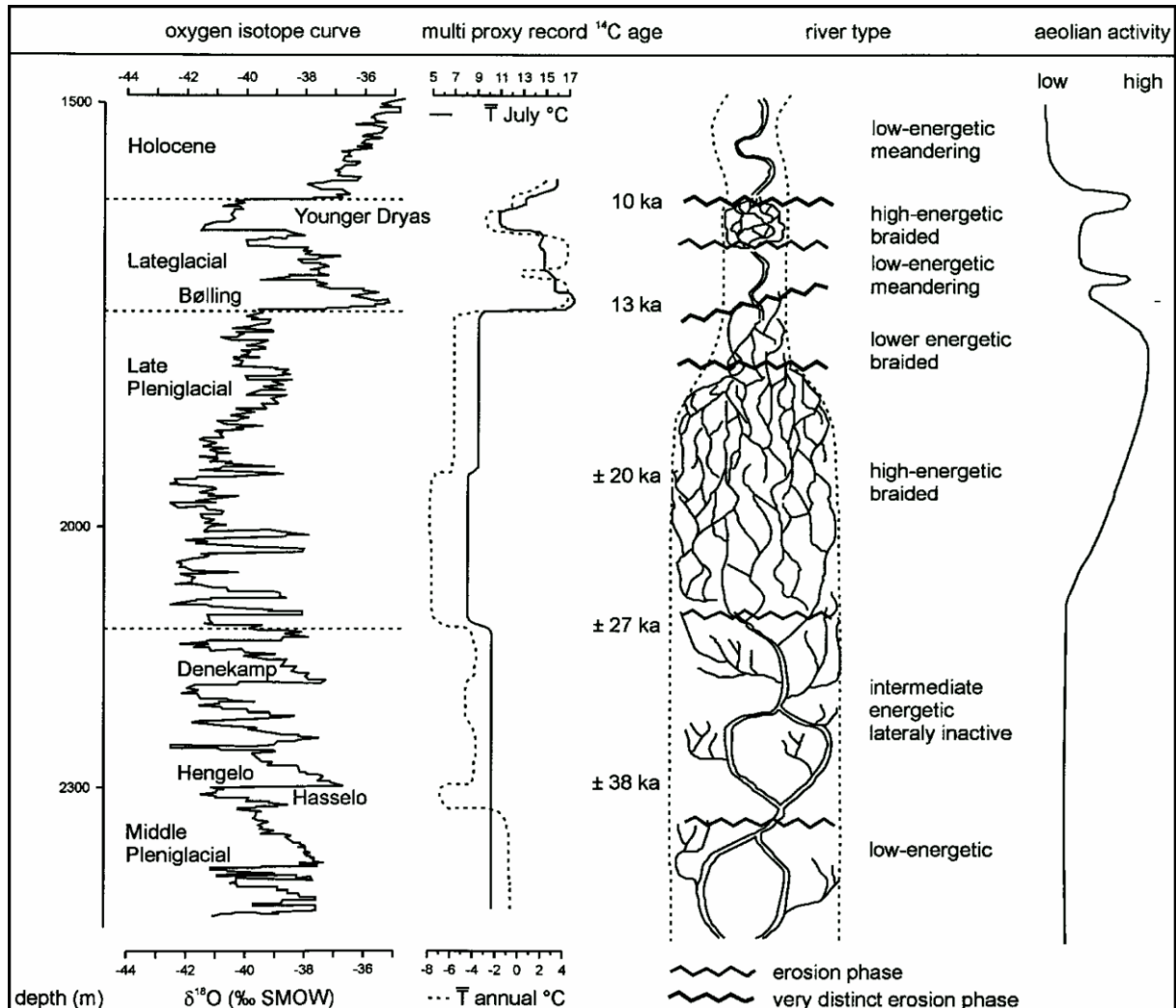
Figure 1.8 Comparison of fluvial behaviour under climatic changes (taken from Vandenberghe and Woo, 2002).

1.2.2 Impact of ice sheets on climate

Several climate modeling studies imply the influence of Northern Hemisphere ice-sheet on climate changes on millennial time scales by the release of fresh water to the North Atlantic, affecting sea surface conditions (salinity and temperature), extent of sea-ice cover, and North Atlantic Deep Water formation (Manabe and Broccoli, 1985; Ganopolski et al., 1998; Clark, 1999). Indeed, northwest European ice sheets together with Icelandic ice sheet is suggested by multi-proxy foraminiferal and geochemical analyses to be the principal driver in millennial-scale AMOC variability during the last glacial period, besides to North American Laurentide ice sheet (e.g. Peck et al., 2006; Bigg et al., 2010; Eynaud et al., 2012) given that both ice sheets were readily available

13

freshwater reservoirs on both sides of the North Atlantic (Toucanne et al., 2015) and large freshwater inputs have been related to iceberg release to ocean or sudden outburst of freshwater from ice-dammed lakes and subglacial meltwater (Lekens et al., 2006). Moreover, significant hydrographic changes along European margin associated with accelerated slowdown of AMOC have been reported by e.g. Hall et al. (2006), Eynaud et al. (2012), Knutz et al. (2007), Lekens et al. (2006), Peck et al. (2007). The sensitivity of the climate system to freshwater was tested on geographic locations such as outlet of meltwater draining river systems and the border of LGM ice sheets by climate modelling which showed that freshwater forcing of Nordic Seas (due to Norwegian Channel Ice Stream) displays direct freshening influence in the vicinity to deep water formation zones in the North Atlantic; while Arctic freshwater forcing has a long-term response associated to sea-ice formation and advection (Roche et al., 2010). What is particularly significant to the SIS and BIIS is that their meltwater injections to the North Atlantic (via The Channel River) and subsequent AMOC destabilization and interhemispheric climate changes have been shown based on Nd isotope record; for between 22.5–21.3 ka BP, 20.3–18.7 ka BP, and 18.2–16.7 ka BP (Toucanne et al., 2015). For instance, the last meltwater event (starting around 18.2 ka BP) was important enough to elicit interhemispheric seesaw event and the Heinrich Stadial-1 (HS1) in the northern Hemisphere. This event lasted for 1500 years to concede the subsequent iceberg release from LIS by mid-depth warming of the North Atlantic, thereby extending the duration of HS1 (Toucanne et al., 2015).

1.3   Relative sea level rise during Holocene

The Northern Hemisphere ice sheets were mostly vanished between 11.6–7.0 ka from early to mid-Holocene due to warming by boreal summer insolation, and also, greenhouse gasses (Marcott et al., 2013; Moossen et al., 2015); and global mean sea-level was about 60 m below the present at the Younger Dryas/Holocene transition (Smith et al., 2011). Relatively high rate (up to 2.5 cm yr^{-1}) of the Early Holocene sea-level rise is estimated by several sea level proxies; however, after 7 ka relative sea level approaches to the global mean sea level when the ice sheet decay was completed (Fleming et al., 1998).

Right after Younger Dryas, ice cores from Greenland indicate rapid rise of ca 15 °C within 1500 years leading to further decay of ice sheets and glaciers (Smith et al., 2011). By the end of deglaciation (ca. 7 ka), rise of around 20–25 m since 9.5–9 ka (Cronin, 2012). The 8.2 ka abrupt cooling event in the Northern Hemisphere is linked to sea-level jumps of approximately 0.4 and 2.1 m in the Mississippi and Rhine-Meuse deltas, respectively (Törnqvist and Hijma, 2012). Moreover, this event has been suggested by Törnqvist and Hijma (2012) to be associated with the freshwater drainage through Hudson Bay from Lake Agassiz leading to perturbations in the North

Atlantic ocean circulation and triggering abrupt cooling events. During the late Holocene (last 2–3 ka) sea level was almost stable until the acceleration dated ca 1900.

1.3.1 Relative sea-level rise in the southern North Sea

Sea-level changes since last glacial maximum was not uniform everywhere as relative sea-level rise is controlled by regional scale factors, that has been recognized after compilation efforts of dated sea-level indicators such as fossil corals, peat deposits, wood from estuarine clays (Woodroffe and Murray-Wallace, 2012). Such regional factors interacting with each other are controlled by different spatial and temporal scales (Kiden et al., 2002), and they mainly are: (i) global/eustatic increase in ocean volume that is climatically controlled; (ii) glacio- and/or hydro-isostatic change due to ice, sediment and water loading; (iii) tectonic subsidence or uplift (Lambeck et al., 1998; Shennan et al., 2000; Vink et al., 2007; Steffen and Wu, 2011). Due to the loss in weight of ice sheets during worldwide deglaciation and the Earth's dynamic response against it, vertical land movements have taken place in previously glaciated or peripheral to these regions, described as glacial isostatic adjustment (GIA). The rebound of former glaciated regions along with the forebulge dynamics, and hydro-isostasy causing a subsidence of the ocean floor and a flexure continental shelves together with ocean siphoning effect contributes to the complex geographical variation in the realtive sea-level rise pattern (Walcott, 1972; Lambeck and Chappell, 2001; Mitrovica and Milne, 2002; Conrad, 2013).

In the northwestern Europe, the post-glacial sea-level history contains these isostatic, eustatic and tectonic contributions (Kiden et al., 2002), making this area difficult to be represented by a common sea-level curve, especially during the Early and Middle Holocene (Vink et al., 2007). The subsiding zone in the North Sea (former glacial forebulge updoming) surrounding the Fennoscandia uplift center is defined by geophysical isostatic models (Lambeck, 1995; Kiden et al., 2002), and it is also recognized by observational data (Mörner, 1979; Kiden et al., 2002). The maximum of this zone is arranged in a relatively narrow band stretching along onshore northwest Russia (Lake Ilmen), central Poland, northern Germany and from there towards southern North Sea (Steffen and Wu, 2011). Relative sea-level data from the northwest Europe (Fig. 1.9) depicts differential crustal movement between the Belgium, the Netherlands, the northwest Germany and the southern North Sea (Vink et al., 2007; Steffen and Wu, 2011). This complex non-linear pattern –aside from the tectonic activity– contains glacio- and/or hydro-isostatic component that increases toward German sector of the North Sea from the Belgian coastal plain (Kiden et al., 2002; Vink et al., 2007). As revealed by Vink et al. (2007), northwest Germany experienced isostatic lowering of around 7.5 m relative to Belgium from 8 cal ka BP until 4.8 cal ka BP. Moreover, over the last 6000 years, isostatic movements have caused subsidence of East Frisian coast with a rate of 0.6 cm/1000 years. (Bungenstock and Schäfer, 2009).
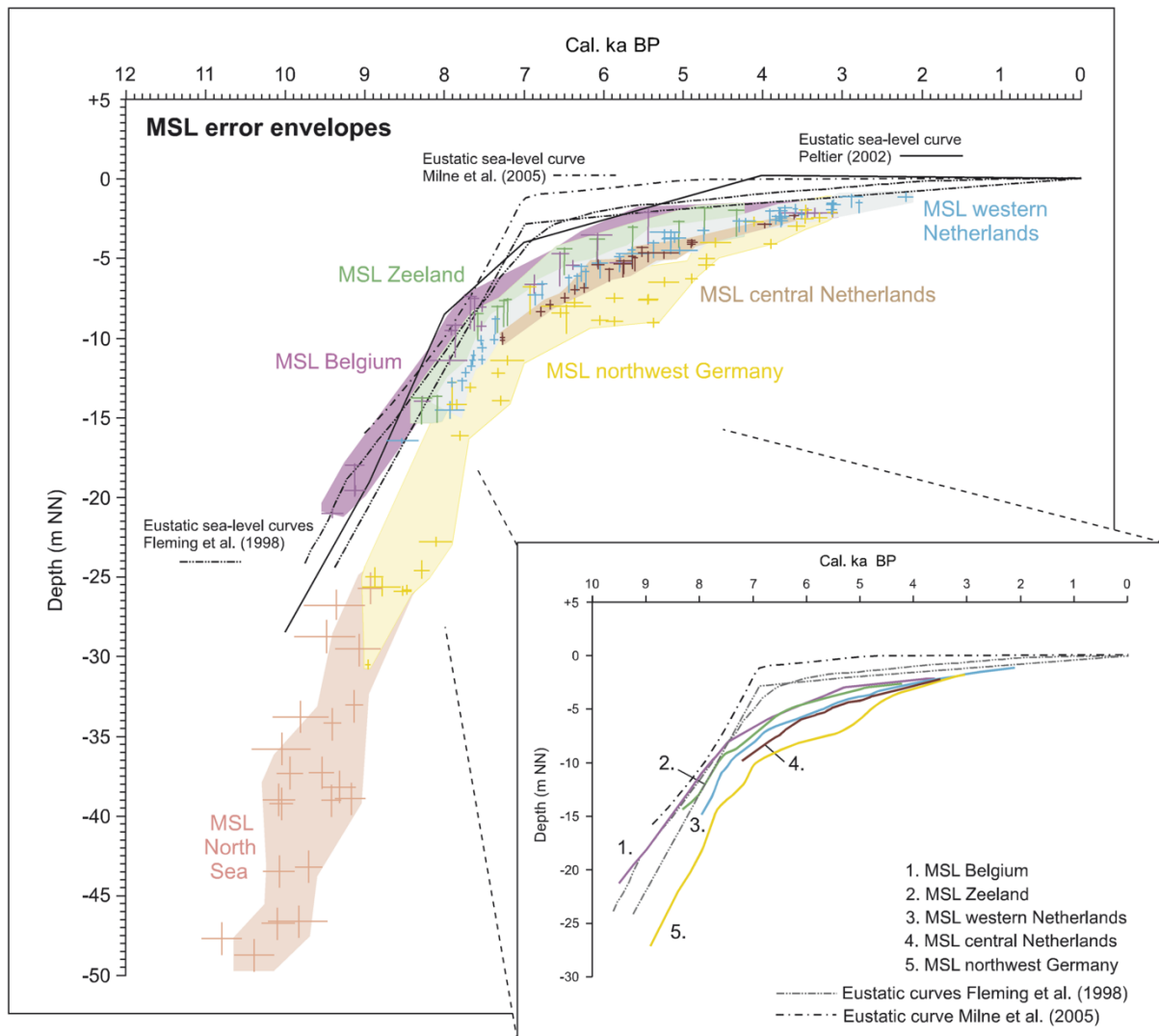
Figure 1.9 Estimated relative mean sea level (MSL) error bands from NW Europe(from Belgium, the Netherlands, Germany and the southern North Sea; mainly derived from basal peats) along with global/eustatic sea-level curves; inset shows the mid-lines of each error band (taken from Vink et al., 2007).

1.3.2 Effects of sea level rise on coastal areas

Continental shelves and coastal lowland regions are the most vulnerable to changes in the sea level caused the morphodynamical changes in the landscape, i.e. by shifting the coastline landward and drowning of incised valleys, thereby formation of estuaries where riverine sediment delivery is not abundant enough to form deltas along the coastal shoreline. In the northwest Europe, swampiness (paludification) of Pleistocene sandy deposits due to the post glacial sea level rise (therefore rise in the groundwater level) led to formation of basal peat as a first development stage in the inundated landscape (Koster, 2005). Intertidal and subtidal conditions subsequently were occurred to be followed by shallow marine environment in the course of the ensuing sea-level rise (Streif, 2004).

Doggerland (Fig. 1.10), for example, characterized the palaeolandscape of the present day North Sea region before the sea-level rise completely inundated the valleys and wetlands (e.g. marshes and swamps) that was attractive to the Mesolithic people (Coles, 2000; Shennan et al., 2000; Gaffney et al., 2007).

The sea level rise affects the coastal system by inundating wetlands, increasing shoreface erosion as well as storm events by increased flooding depths and inundation extents (Passeri et al., 2015). The coastal system tries to adapt to sea level rise by changing its landscape, and marshes, for instance, will try to keep up with the sea-level rise depending on the sediment supplies into the system and the rate of sea level rise. Furthermore, peatland within wetland ecosystems not only present a habitat for variety of plant and animal species, but also, they provide fertile land for agriculture and can be used as fuel. Therefore, sea level rise effects will be on ecological habitats and organisms and will also have socio-economic dimension (Church et al., 2010; Passeri et al., 2015) such that today low-lying coasts, elevations less than 10 m, are populated by more than 10 percent of the world population (Clark et al., 2015).

The most of the coastal morphology, for instance, present-day barrier-inlet systems in the North Sea, was developed when the rapid sea-level rise was slowed or during the stillstands in the sea-level rise. Estuaries, wetlands, tidal inlet/basin systems have rich bio-diversities, but are short-lived/temporary landscapes on geological timescales, and especially tidal flats within this system are the most vulnerable ones for potential relative sea-level rise (van Goor et al., 2003; Dissanayake et al., 2012). The possible impacts of future sea-level rise have been modelled by some studies. The modelling adapted by van Goor et al. (2003) for Wadden Sea inlets showed that inlet/basin systems were able to keep up with more than 10 mm/year relative sea-level rise by accumulating sediment into the system to reach a dynamic morphological equilibrium. Predictions for sea-level rise regarding the period between 1990–2100 ranges between 0.75 and 1.9 m and higher end future prediction of 2 m could drown 1. 5% of the present-day coastal area (Wilmes and Green, 2014).
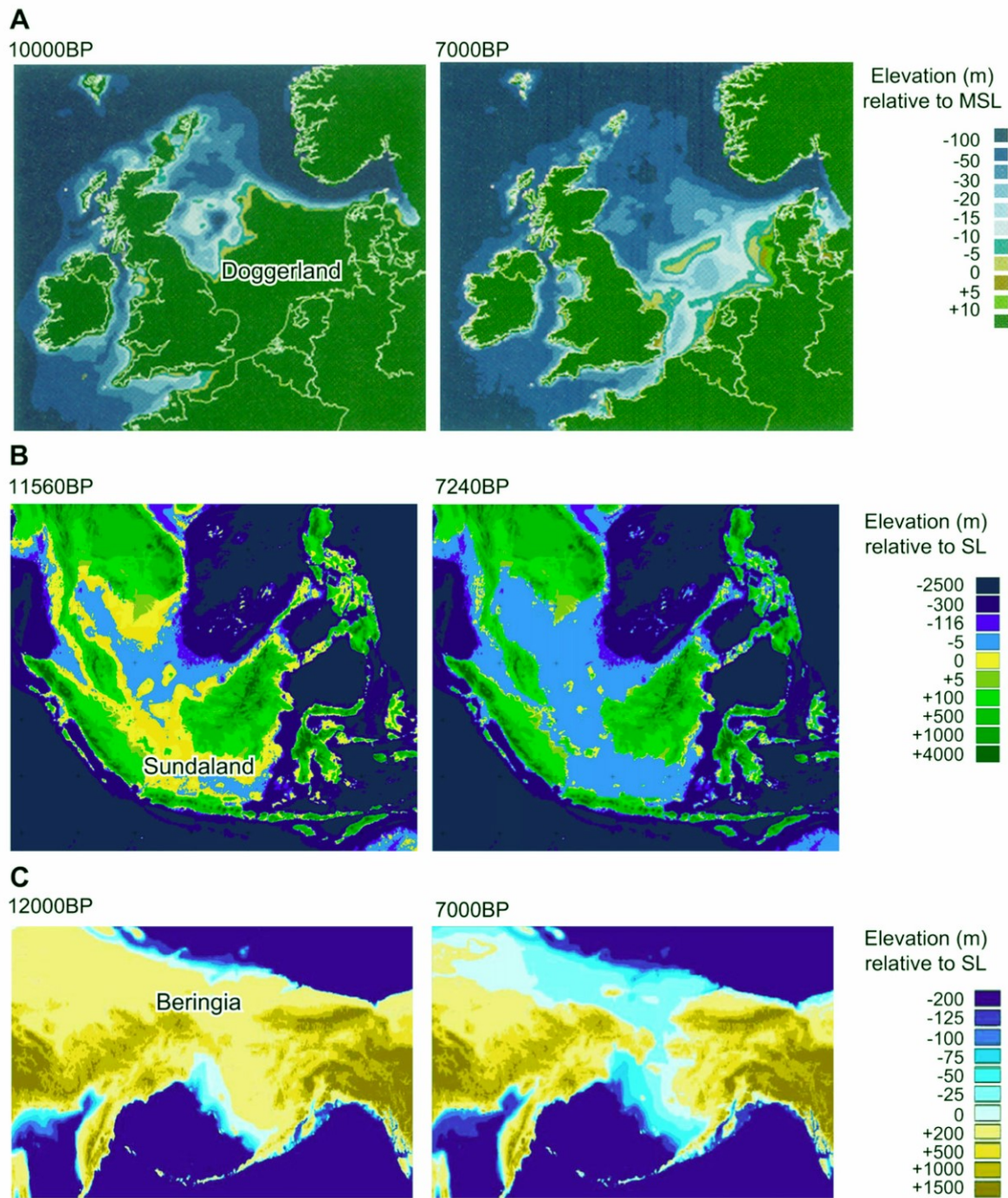
Figure 1.10 The early Holocene flooding of a) Doggerland leading to isolation of Britain from the Europe mainland, b) Sunda shelf area in the southeast Asia, and c) Bering Strait, former land bridge between Asia and North America (taken from Smith et al., 2011).

1.4   Palaeovalleys

Palaeovalleys were created during sea level falls and lowstands, when rivers were adapting to low-stand shorelines, and therefore their erosional bases are considered to be the most remarkable indication for sequence boundaries. Comprehensive research on palaeovalleys (incised valleys) have been conducted since the 1970s, palaeovalleys (van Wagoner et al., 1998);

however, the major advance in studying incised valley systems (and estuaries) initiated during 1990's by reason of their deposits, particularly their sand-prone fills, holding potential as an oil reservoir (Dalrymple et al., 1994; Zaitlin et al., 1994; Gregoire et al., 2017). Aside from hydrocarbon reservoir interest, the lower surface of the incised valleys denotes the expansion of drainage system to the continental shelf, which possibly evacuate sediment/freshwater either to the outer shelf or to the continental slope during the base level fall and lowstand (Blum et al., 2013). Additionally, they comprise one of the most important component of the continental shelves as they have the highest potential to host lowstand and transgressive deposits to document environmental changes, climate events, but also, human activities (Boyd et al., 2006; Chaumillon et al., 2010).

Several studies on palaeovalleys from Precambrian to present day shelf setting implied the influence of changes in the sea-level, climate, tectonics, sediment supply and valley morphology on their infill and stratigraphic architecture (Dabrio et al., 2000; Simms, R, A. et al., 2006; Simms et al., 2010). Late Quaternary and Holocene incised valley systems that became estuaries with the flooding have been studied by e.g. Nordfjord et al. (2006), Rodriguez et al. (2008), Thomas and Anderson (1994).

The typical models of incised valley fill, according to Zaitlin et al. (1994), composed of a landward segment with fluvial deposits, a middle segment where fluvial deposits are covered by central-basin deposits and a seaward segment that contains both fluvial and central-basin and overlain by marine deposits. However, this model was expanded or modified by the subsequent studies (Dalrymple et al., 2006). For example, Garrison and van den Bergh (2006) and Li et al. (2006) presented models that the fill composed of almost only fluvial deposits. Furthermore, Payenberg et al. (2006) showed another example that after complete drowning, the valley was not filled completely, thereby having an accommodation space to be filled later by open-marine sediments like shelf dunes in East coast of Australia. Further example from Hudson Shelf Valley, on the other hand, showed that catastrophic flooding associated with glacial lakes filled the valley by large field of subaqueous bedforms, banks and levees (Thieler et al., 2007). Also, Chaumillon et al. (2010) compared the incised valleys from coasts of France and it turned out that valleys in the same setting (tectonically stable and sediment starved margins) depicted contrasting conditions of hydrodynamics, inherited morphology and sediment supply. They observed that sea-level is the main controlling parameter for the valley formation and its infill as is in the model proposed by Zaitlin et al. (1994). However, for the variations in the infill, the first order controlling parameter was hydrodynamics such as valley location with respect to the littoral drift and tide-, mixed (tide and wave), wave-dominated infill like the categorization made for present-day estuaries or lagoons. The second order controlling factor was attained to inherited morphology of the valley

and the latter in turn controls sediment supply and hydrodynamics (e.g. bedrock related irregularities focus tidal flow).

1.5 Current controlled deposition on shelves

1.5.1 Shallow shelves

As rivers or glaciers sculpt the shelf profile, hydrodynamical processes (i.e. waves and currents) and meteorological conditions since the last deglacial transition take a profound role in inducing the sediment motion and in the re-distribution of sediments (Wright, 1995) by affecting the evolution of coastal and geological basin (Ward et al., 2015). Transport of shelf sea sediment under the control of tides, waves and wind-driven currents is a complex process that relative influence of each can vary on temporal and spatial scales (van der Molen, 2002; Neill et al., 2010; Ward et al., 2016). For instance, long term sediment transport in the present-day's North Sea, particularly the southern North Sea, is mainly dominated by tidal currents although waves and wind-driven currents are also involved in the process (van der Molen and Swart, 2001b; van der Molen, 2002).

Water masses in the ocean basin are forced to rotate around amphidromic points due to the combination of gravitational forces between Moon and Sun, the geometry of the basin, and the Coriolis effect (Schieber, 2016a). On shallow shelf areas (ranging between 10-200 m water depth) in wide passive continental margin setting significant tidal currents usually exist due to the increase in tidal action associated with their greater shelf width. Therefore, on many shelves, these rotating tidal currents are capable of transporting sandy sediment (even medium grained sand) and even mud in bedload (Houbolt, 1968; Stride, 1982; Reynaud and Dalrymple, 2012; Schieber, 2016a).

In epicontinental embayments like "open-mouthed indentations" (e.g. North Sea and Yellow Sea), within continental interiors that have a narrow connection to the open ocean (e.g. Hudson Bay and Baltic Sea), and in straits or seaways (e.g. Dover Strait) that connect larger water bodies, tidal currents interact with waves, wind/storm-induced currents and geostrophic currents (related to global ocean circulation), thereby resulting in variety of sediharrmentary deposits (Reynaud and Dalrymple, 2012) and they can be enhanced by enhanced by local topographic effects such as islands and sand banks. Significant tidal currents are particularly observed in embayments having a tidal resonance or in seaways/straits where the tidal currents are strengthened (Reynaud and Dalrymple, 2012).

Furthermore, regarding the wind-driven circulation in shallow seas, storms occasionally interact with seabed and ease the lateral transport of mud (Swift, 1970; Nittrouer et al., 2007; Schieber, 2016a). For instance, in the Mid Atlantic Bight, the interaction of seasonal winds with the shelf

water instigated bottom currents of around 20 cm/s; wind-circulation, therefore was responsible for moving, reworking surface muds as bedload but also as suspension (Schieber, 2016a). The combination of tidal currents with strong storms that occasionally resuspend seafloor muds could lead to transport of significant amount of sediment (Schieber, 2016b).

The most common, but also the largest bedforms observed in shallow marine settings are current ridges (sand banks) and compound dunes (also called sand waves) which are flow transverse bedforms indicative of strong currents (50–65 cm/sec; Kenyon and Cooper, 2005) and their hydrodynamical agents are mostly tidal currents, e.g. in the southern North Sea (Caston, 1972; Caston, 1981; McCave and Langhorne, 1982; Stride, 1982; Davis and Balson, 1992; Deleu et al., 2004), Celtic Sea (Reynaud et al., 1999), northeastern Australia (Harris, 1989), East China Sea (Liu et al., 2007). Sand ridges are elongated sedimentary bodies, aligned somewhat parallel to the coast and oblique to the peak tidal current direction at angles between 0 and 20° with many kilometers in length, a few kilometers in width and some tens of meters in height (Trentesaux et al., 1999). As a good example of sand ridge from the southern North Sea, Middelkerke Bank, displays four phases of evolution such as palaeovalley infilling, lagoon or subtidal environment, coastal, storm-dominated sand bar, which was the core for overlying offshore sand bank. The composition of this bank varies laterally from prograding oblique to horizontal reflectors and onlap underlying units (Trentesaux et al., 1999). Overall, the deposition of first three units in Middelkerke Bank was suggested to be controlled sea-level rise, while modification of storm dominated sand bar to tidal sand bank might be occurred under the relatively stable sea-level.

1.5.1.1   North Sea

Highly energetic regime in the North Sea is forced by mechanisms such as tides (semi-diurnal), winds and density differences (Backhaus, 1989). The North Sea circulation and main physical mechanisms are summarized in Fig. 1.11. From the north, tidal energy is brought into the North Sea resulting in strong frictional stresses that stir the water column. Aside from tides, winds together with atmospheric pressure changes cause storm surges that may cause several meters increase in the mean sea-level if they overlap with spring tides. Furthermore, density differences are driven by seasonal thermal stratification (e.g. summer thermocline) due to heating and cooling of surface waters, and also, by freshwater inputs (Howarth et al., 1994). The most important rivers with regard to their catchment area are Elbe, Weser, Ems, Rhine, Meuse, Scheldt, Thames and Humber. The suspended particulate matter in the North Sea is sourced from the Atlantic Ocean, from the English Channel, rivers, erosion of the seafloor coastal areas, atmosphere, and primary production and associated sandy or muddy sediments settle in the Wadden Sea, German Bight, and Skagerrak/Norwegian Channel (Ospar Commision, 2000). The remainder of the North Sea floor consists of Pleistocene and Early Holocene relict deposits and of reworked sands and gravels

(Eisma et al., 1987). Sandy beaches, dunes, estuaries (e.g. Elbe, Weser, Rhine and Meuse), tidal inlets and islands in the Wadden Sea exist along the coastal zone from Dover Strait to western Danish coast. Along the east coast of England, estuaries (Humber and Thames), and sand/ mud flats (in the Wash) are also found.
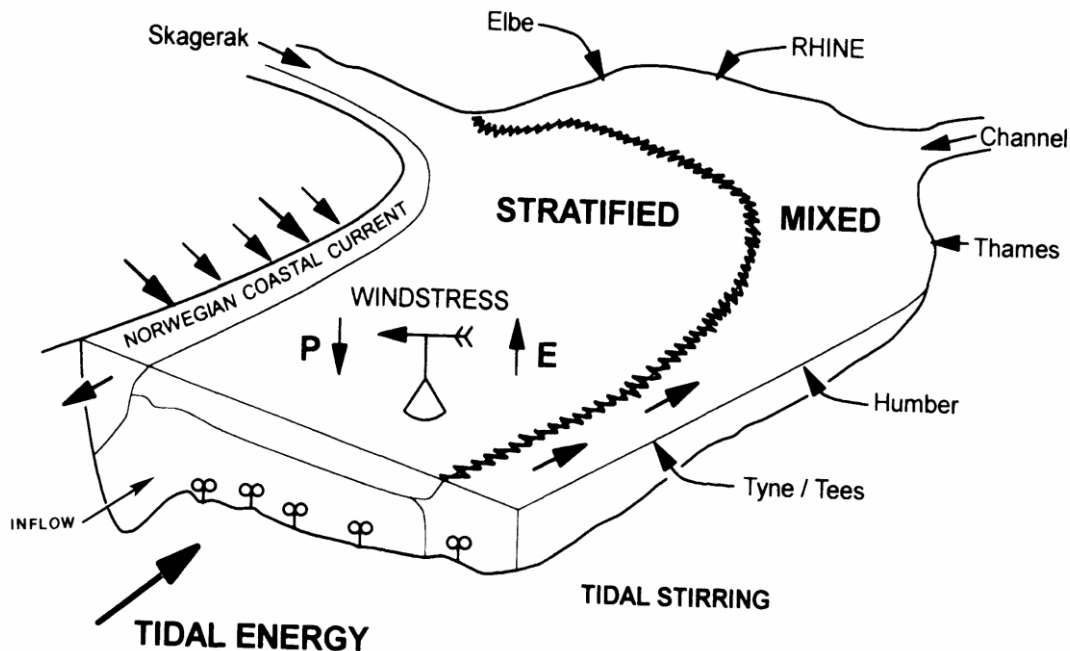
Figure 1.11 Basic physical processes in the North Sea from Charnock et al. (1994). The North Sea as a tide dominated shelf sea depicts strong variations in its currents. Strong tidal currents in the Southern North Sea establishes highly turbulent regime with vertical.

1.5.1.2   Impact of sea level rise on hydrodynamic variations on shelves

Sea-level changes since the LGM have impacted upon the open ocean tidal amplitudes as a result of modifications in the ocean basin geometry, which is indicated by global tidal modelling studies (e.g. Thomas and Sündermann, 1999; Egbert et al., 2004). The impact of sea-level rise on tides also supported by modelling studies from northwest European shelf seas which have indicated considerable changes in tidal dynamics in terms of elevations, currents, and migration of amphidrome positions (Austin, 1991; Shennan et al., 2000; Uehara et al., 2006; Pickering et al., 2012; Ward et al., 2016), including wave climates (Neill et al., 2009) and thereby affecting sediment transport regimes (Gerritsen and Berentsen, 1998; van der Molen and Swart, 2001a; Hall and Davies, 2004; Neill et al., 2010), tidal mixing front locations, and water levels at where tidal-driven mixing takes place (Uehara et al., 2006; Ward et al., 2012) which even influences the primary production and carbon dioxide uptake on the shelf sea (Rippeth et al., 2008).

The change in relative sea-level can cause significant changes in the strength of tidal currents due to the evolved coastal and shelf morphology (Reynaud and Dalrymple, 2012) and such increase in the currents cause bed shear stresses to increase, which therefore increase the kinetic energy for

suspending and transporting the bed material (Pickering et al., 2012), but also lead to increased turbidity of the water column, which in turn, has ecological impact due to reduced light penetration (e.g. Pelling et al., 2013). For instance, according to modelling study by Pickering et al. (2012), a future scenario with 2 m sea-level rise points to large amplitude increases (tens of centimeters higher than present-day levels) in M2 tidal constituent, particularly in present-day shallow areas in the southeastern North Sea and Dutch Wadden Sea. Furthermore, according to UK assessment report on climate change, it seems very likely that already eroding sectors (e.g. widespread in UK and Ireland) of the coast will encounter with higher rates of erosion because of the sea-level rise (Masselink and Russell, 2013).

While wave heights and periods increase with the rising sea level due to increase in fetch length, the effect of wave-induced bed shear stress will decrease considering that it is sensitive to variations in water depths (in contrast to tidal-induced shear stress) as modelled by Neill et al. (2009) and (Neill et al., 2010). Hence, from Late Glacial to present shear stress have varied significantly. The sea-level rise will permit larger waves to arrive to the coast, but their energy loss to the friction with seafloor will be less thereby causing increased coastal erosion and sediment export to the shelf. Therefore, shallow areas like Dogger Bank are prone to be significantly affected by the wave action.

Overall situation over the northwest European shelf with the increasing sea-level during Holocene is that the influence of wave action on sediment transport decreases and tidal currents mainly govern the pathway of sediment transport – as also seen today (Stride, 1982; Neill et al., 2010; Cazenave, 2013).

1.5.2 Glaciated continental shelves

1.5.2.1 Sediment drifts on high latitudes

Sediment (or contourite) drifts are generally elongated parallel to contour-current flow direction and depict themselves as erosion/non-deposition area near the bottom current axis and depositional area that is adjacent to the high velocity zone (contour-current core) with high sedimentation rates (Faugères et al., 1999; Rebesco and Stow, 2001; Faugères and Stow, 2008). They can be found everywhere, from the abyssal floor, via continental margins, to mid- and upper slope, but also, over continental shelves (Faugères and Stow, 2008).

In general, most of them have mounded elongated shape with dimensions ranging from relative small patch drifts (100 km^2) to giant elongated drifts (100,000 km^2). These accumulations can be 10s to 100s km long, with a thickness of 10s to more than 1000 m (Rebesco et al., 2013). Changes in the bottom current strength and location is mainly regulated by climatic conditions. For instance, oscillations in the intensity of Mediterranean Outflow during northern hemisphere

coolings (e.g. Heinrich events and Younger Dryas) lead to contourite formations (van Weering et al., 2008).

High latitudes display variety of current-induced deposits such as contourite drifts and sediment waves along with channel-levee complexes associated with mas-flow processes and turbidity currents that are mainly controlled by climatic conditions. The intercalation between contourite and turbidite deposition is very common and huge amounts of sediments can be released to the shelf edge and upper slope especially on glaciated margins (van Weering et al., 2008). For instance, Metz Drift (East Antarctica), located in an 850 m deep glacial trough on the shelf during late Pleistocene and Holocene, was formed due to the dense saline water flow owing to the seasonal extensive sea-ice coverage due to the presence of coastal polynya (Harris et al., 2001; Presti et al., 2003).

1.5.2.2 Brine-enriched shelf water in polar regions

The occurrence of coastal polynyas (i.e. "persistent and durable ice free areas" surrounded by sea ice and "ice production factories") is the most important hydrographical feature in high-latitude regions. Sea ice, by releasing brine during freezing, supplying fresh water during melting, shielding warm underlying water column against cold Arctic air and reflecting solar radiation, constitutes sensitive part of the high-latitude climate.

The offshore winds, tides and currents, which advect the ice away from the coast are responsible for the formation and maintenance of latent heat polynya. On the other hand, they can also be formed by melting of ice cover due to upwelling of warm water and called sensible heat polynya (Skogseth et al., 2008). In latent heat polynyas, rapid and persistent ice growth is caused by intense heat loss from the open water to the atmosphere (Skogseth et al., 2008). Brine rejection during the sea ice growth results in the formation brine-enriched shelf water (BSW). For instance, in Antarctic coastal polynyas, high ice production resulting in brine rejection leads to dense water formation on shelf, large scale water cascading over shelf edge and formation of world's densest water mass (Antarctic Bottom Water; e.g. Shapiro et al., 2003; Tamura et al., 2008). Along the Arctic coastal margin, many coastal polynyas occur on the shallow shelves, making significant contributions to Arctic Ocean halocline (e.g. Laptev Sea polynya; Thomas and Dieckmann, 2010).

The western Barents Sea shelf, composed of deep troughs surrounded by shallow banks formed during the glacial period, and there the glacially generated Kveithola Trough at 75°N is one of the prominent locations where the densest water masses of the continental shelf are produced (Fohrmann et al., 1998; Rebesco et al., 2016a). These dense waters, BSW, is the result of interplay between topography and accumulation of the dense brine which is formed by salt rejection related to the sea-ice formation in the course of winter times (Fohrmann et al., 1998). The BSW is likewise

observed inside the adjacent Storfjorden Trough during northeasterly winds in winter (Haarpaintner et al., 2001; Skogseth, 2004) in the north of Kveithola Trough. Furthermore, cascading of this water along with winter storminess re-suspends sediment plumes on shelf and sediments are subsequently carried down to the continental slope (Fohrmann et al., 1998; Sarnthein et al., 2003a). Therefore, Kveithola Trough —as one of the cross-shelf bathymetric troughs in the NW Barents Sea neighboring the continental slope— acts as a drainage pathway towards eastern Norwegian Sea for the surrounding Spitsbergen and Bear Island Banks via channels connected to its basin (Fohrmann et al., 1998).

1.6 Data and methods used

This thesis is based on the data collected during the R/V Maria S. Merian cruise MSM 30 (CORIBAR) in 2013, R/V Heincke cruise HE405 in 2013, and cruise HE463 in 2016. During these cruises, seismic and acoustic acquisition were carried out, and sediment gravity cores and vibrocores were collected. Additional sediment echosounder data is provided by HE444 and Sonne SO Cruise 9.

1.6.1 Parametric sub-bottom profiler

High resolution sub-bottom profiles were recorded with a SES-2000 medium from Innomar Technologie GmbH during R/V Heincke cruises HE405, HE463 and HE444 in the North Sea. Parasound system from Teledyne Atlas during R/V Maria S. Merian cruise MSM30 in the Barents Sea and R/V Sonne SO Cruise 9 in the North Sea.

The non-linear hydro-acoustic behavior of water against transmission of two high energy signals with different frequencies results in manipulating the frequency content of sound wave, and thereby harmonics are generated at frequency sum (high frequency parametric signal) and frequency difference (low frequency parametric signal). The latter one with its short pulse length without ringing and large bandwidth affords high vertical resolution of around 20 cm. Moreover, the small footprint owing to narrow beam (4x4.5°) of the transducer makes this source satisfactory for achieving high lateral resolution as well in archaeological, environmental and geotechnical studies (e.g. Wunderlich et al., 2005; Schrottke et al., 2006; Missiaen et al., 2008). The penetration depth, depending on the properties of sediment whether soft or over-consolidated, can be up to 150 m. One disadvantage with high frequency acoustic profiling systems is that not being able to penetrate till because of its consolidated state. Wunderlich et al. (2005) gives comprehensive technical aspects of the system.

1.6.2 Multi-channel seismic

In shallow marine environments (e.g. the North Sea, depths shallower than 50 m), the conventional multi-channel seismic systems achieving deep penetration with their low frequency range (2–100 Hz) are not applicable, as a result of small incident angles (< 30°) of the acoustic wave; hence custom-designed system of Marine Technology / Environmental Research (MTU) working group at the University of Bremen was utilized for data acquisition in the study area. These data were recorded with the MaMuCS-System (MTU).

During cruise HE405, the micro Generator Injector (GI) Gun (provides frequencies up to 600 Hz) data were recorded by 32-channel analogue streamer with 4 m spacing each channel consisting of a single hydrophone. However, with the cruise HE463, the fully digital HTI streamer with 96 single hydrophones at a distance of 1 m were deployed. The depth control of streamers was achieved by birds. When the sound source is a small airgun (micro-GI) there is a good compromise between penetration and vertical resolution ($\sim$ 1m) provides. The small chamber volume of 2x0.1 L allows fire rates of 1.5 s, thereby enhancing the signal to noise ratio.

Data-set were processed with the software package VISTA Seismic Processing 2D/3D by following standard processing scheme. The calculations of exact positions of source and receiver, and their geometry relative to the GPS antenna were performed with software Wingeoapp 0.9.8 (Hanno Keil). In order to obtain gathers that are reflected from common subsurface midpoint, CMP-binning performed along the line. The setup of CMP bin size for GeoB13 data was 2 m, while for GeoB16 it was 1 m. After CMP binning, dead and noisy channels were extracted, and gun delay is corrected by applying bulk shift in time which is vital for accurate two-way travel time of reflections. On selected CMP gathers, the root mean square (RMS) velocities are interactively identified. The velocity model is subsequently used for the Normal Move-Out (NMO) correction. Vertical time shifts within CMP gathers due to movement of the ship and the sea surface, were attempted to correct by residual statics correction module of Vista. After stacking all CMPs, migration is performed as a final step. The Finite Difference (FD) migration method was chosen for both data-set, as this method tolerates the possible errors in the velocity model. Migration is the imaging process by which diffraction hyperbolas are collapsed, dipping events are moved to their true spatial positions, thereby spatial resolution is increased. Additional steps such as F-K filter (for e.g. eliminating the ghost), 4D-DEC (for post-stack random noise removal) and SRME (for multiple suppression) were performed for some lines. Extended explanations for seismic data processing methods are given in great detail by Yilmaz (2001).

1.6.3 Sediment core data

Vibrocorers and gravity corers were used to retrieve sediments in the North and Barents Sea, respectively. A gravity corer with lengths of up to 12 m and top weight of 1.5 tons was used in muddy environments in the Kveithola Trough. A Geo-Corer 6000 Vibrocoring system (VC) with a barrel length of 5.80 m was used for fine, middle and coarse sands that characterize the seabed of the North Sea. Sediment cores were cut into 1-m segments and split into two halves, and core imaging and visual descriptions were made. Sample preparation for ^{14}C dating measurements comprised of wet sieving into coarse and fine fractions, oven-drying, sonic sifting and sample (e.g. plant remains and foraminifers) extraction under a binocular microscope.

Physical poperties were measured on half-sections. Changes in grain-size distribution or in the ratio of terrigenous and biogenic component in sediments are mainly reflected by their physical and acoustic properties, which are of interest in palaeo-environmental and palaeo-climatic studies (Weber et al., 1997). A standard GEOTEK multi sensor core logger (MSCL) was used on half-core sections of gravity and vibro-cores in order to measure physical properties such as compressional P-wave velocities, the amount of magnetically susceptible material, and attenuation of gamma rays at 1 cm and 2 cm intervals. Cores were allowed to equilibrate to ambient room temperature before the start of measurements, which is important especially for the accuracy of velocity measurements. P-wave velocity varies with porosity, lithology and the bulk density of the material, and in marine sediments, for example, lithification and consolidation, occurrence of free gas and fracturing also controls the velocity (Blum, 1997). Magnetic susceptibility is the magnetic behaviour of material as a response to an exerted magnetic field. It is useful for core-to-core correlation and provides reliable proxies for stratigraphic changes, characterization of lithological units, changes in sedimentary provenance (terrigenous or iron mineral content) and diagenetic environment (Blum, 1997). Gamma density measurements can reveal changes in the lithology and porosity, coring disturbance, but also, can be used together with p-wave measurements to construct synthetic seismograms by allowing the calculation of acoustic impedance.

2 The Elbe Palaeovalley: evolution from ice-marginal valley to sedimentary trap (SE North Sea)

Aslı Özmaral[a,b], Hanno Keil[b], Daniel A. Hepp[a], Tilmann Schwenk[b], Hendrik Lantzsch[b], Tobias Mörz[a,b], Volkhard Spiess[b]

[a]*MARUM—Center for Marine Environmental Sciences, University of Bremen, D-28359 Bremen, Germany*

[b]*Faculty of Geosciences, University of Bremen, D-28359 Bremen, Germany*

Abstract

The present day North Sea has been organized and sculpted as a result of the climate, hydrodynamics and eustatic fluctuations. Along the sub-aerially exposed periglacial environment in the southeastern North Sea during the late Weichselian, at least 210 km long–40 km wide SE–NW trending Elbe Palaeovalley (EPV) carried meltwater from southern margin of the Scandinavian ice sheet along with drainage from rivers of North European plain. Although this extremely wide valley was a crucial member in the sensitive North Atlantic climate system by contributing freshwater to Bay of Biscay and/or Nordic Seas, but also in understanding of the environmental organization took place in the Northwest European shelves under the sea level control, there are only a couple of studies having dealt with the EPV up to now. That resulted in the untested palaeo-reconstructions and -modelling studies such as drainage pathway, sea-level, tidal and the sediment transport modelling. Analysis of sediment echo-sounder data along with the sedimentological sampling and mapping enabled the identification EPV morphology, up to 5 m deep incisions at its base and EPV infill in detail for the first time. The base of valley situates 65 m below the present sea-level, and the palaeodrainage aligned in SE-NW with its braided system during the MIS 2 sea level fall and lowstand in a periglacial environment. With the post-glacial sea-level rise, EPV became an estuary with tributaries, intertidal and subtidal flats with a limited sediment supply. After Early Holocene, sea-level rise drowned the Elbe Palaeovalley system around 10 cal ka BP, it subsequently became the major sedimentary trap of the southern North Sea. Under the control of sea level rise and associated changes in hydrodynamic regime, three stages of the shelf organization are recorded in valley infill succession after drowning; shallow basin with restricted connections for Atlantic water, the southwestern connection establishment with the Dover Strait, and open marine environment (5.8 cal ka) with the drowning of Dogger, respectively.

2.1   Introduction

Continental shelves, that were sub-aerially exposed during lowstands of sea-level, incised by river valleys, and inundated during high-stands of sea-level, represent important archives for the history of reorganization between marine and terrestrial environment and for the dispersion of sediment either on the shelf or out of the shelf towards deep ocean (e.g. Blum and Törnqvist, 2000; Meijer, 2002; Bourillet et al., 2003; Blum et al., 2013). Palaeovalleys (incised valleys) that were created as a response to base level fall encompass non-marine, estuarine and open-marine infill facies (Dalrymple et al., 1992; Dalrymple et al., 1994; Zaitlin et al., 1994; Greene et al., 2007) all of which are controlled by variations in sea-level, climate, gradient of the shelf and hydrodynamics on the region (Wellner and Bartek, 2003; Payenberg et al., 2006; Reijenstein et al., 2011).
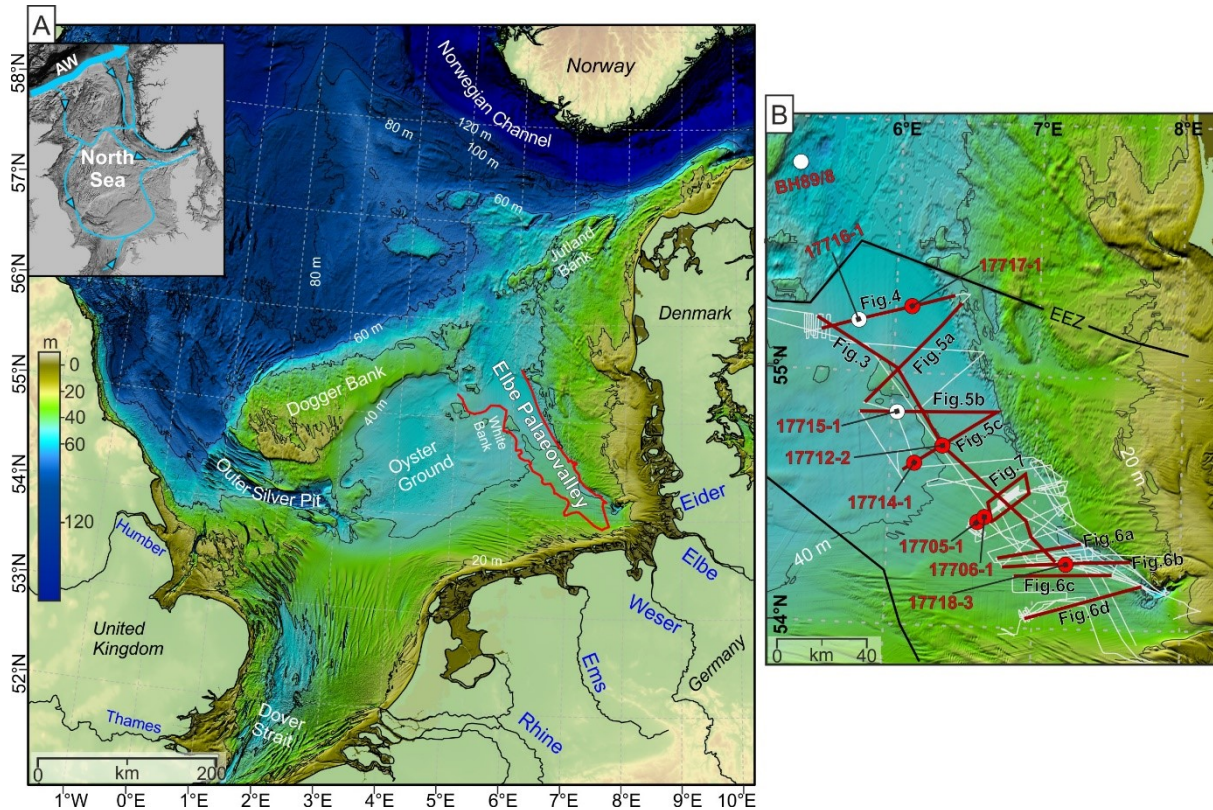
Figure 2.1 Bathymetry of the Central and Southern North Sea **(A)**, from the European Marine Observation and Data Network (EMODnet) hydrography portal), Elbe Palaeovalley (EPV) in the southeastern North Sea (200 km long and 25–50 km wide; red outline). Drainage from rivers Ems, Weser, Elbe and Eider discharged across the present North Sea through EPV. Inset map shows present-day Atlantic water (AW) inflow to the North Sea, about 50% of AW is mixed with fresh water from rivers before it leaves the North Sea via the Norwegian Channel (Winther and Johannessen, 2006; Talley et al., 2011). **B)** Echo-sounder tracklines (white) and vibro-coring sites in the study area.

The Elbe Palaeovalley (EPV) or "Elbe-Urstromtal" (ice-marginal valley) as a drowned river valley is located in the southeastern North Sea between 53°–56°N latitude, and 3°–9°E longitude and at water depths between 35 and 50 m (Fig. 1). With its width of around 40 km and length of around 210 km, it played a major role in the Late Weichselian and Early Holocene palaeo-drainage network of the Northwest Europe. The meltwater and sediment flux from the southern sector of Scandinavian Ice Sheet (SIS) along with extra-glacial rivers were collected by the Elbe Palaeovalley system as an ice-marginal valley until the ice margin retreated to the modern Baltic coastline around northeast Poland (river Vistula) where the flow diversion created the Baltic Ice Lake (Ehlers et al., 2004; Pisarska-Jamroży, 2015). The analogy to the EPV which carried meltwater flux to the Nordic Seas and/or towards Bay of Biscay (Ménot et al., 2006; Toucanne et al., 2010; Toucanne et al., 2015) was the northwestern deglacial drainage outlet of Late Wisconsin Laurentide Ice Sheet via Mackenzie River system in Beaufort Shelf as thousands of cubic kilometers of freshwater from were discharged towards Arctic Ocean (Fisher and Smith, 1994; Murton et al., 2010; Westaway and Bridgland, 2010), thereby contributing significantly to weakening of the Atlantic Meridional Overturning Circulation (AMOC) and triggering the abrupt

cooling event (Condron and Winsor, 2012). The critical position of the North Sea, as a possible meltwater contributor from SIS and BIIS to the North Atlantic climate system (Clark et al., 2004a; Lekens et al., 2005; Lekens et al., 2006; Gupta et al., 2007; Toucanne et al., 2010; Clark et al., 2012a; Toucanne et al., 2015; Sejrup et al., 2016) causing a positive feedback mechanism that led to the further weakening of Atlantic Meridional Oceanic Circulation and accelerated the decay of Northern Hemispehere ice sheets has recently been recognized (Plaza-Morlote et al., 2017).

However, relatively little attention has been given to the role of EPV as a drainage pathway and sediment depocenter of the shelf sedimentary system. Although several paleogeographical reconstructions included EPV as a main proglacial drainage collector in the southern North Sea along with the Late Weichselian ice-sheet extents (e.g. Coles, 2000; Houmark-Nielsen and Kjaer, 2003; Houmark-Nielsen et al., 2012; Toucanne et al., 2015), none of these studies have been conducted for the EPV itself. The compilation of a palaeo-landscape/environmental model for the North Sea, therefore, is still to a certain extent hypothetical suffering from a lack high-resolution seismic stratigraphy and sedimentological data. Besides to Northern Hemisphere ice sheet aspect, the subsequent development of EPV under the sea-level rise as a marine embayment (as an estuary or a tidal basin with its channels and flats) together with Dogger Bank as a topographic barrier-like feature against incoming Atlantic Water around the pre-Holocene coastline (Fig. 1) make EPV a unique element in the North Sea system as the valley is expected to aid in understanding of post-glacial sea-level rise, sediment supply, and hydrodynamic regime evolution in the Southern North Sea.

The extension of this ice-marginal valley in the North Sea was first mapped by Figge (1980) between SW Helgoland and White Bank using analogue acoustic boomer profiling. More detailed evaluation of seismic sections following Figge (1980) was conducted by Schwarz (1996) in order to investigate possible control by the salt structures and buried tunnel valleys lying stratigraphically beneath the EPV; however, in a few cases direct correlation was observed regarding their distribution along the German sector of the North Sea. Later, coinciding with the northern extension of the EPV, in a 51 m long borehole located in the Danish sector of the North Sea, biostratigraphy and Holocene environmental evolution under the rising sea level were investigated based on the foraminiferal assemblages by Konradi (2000). Since then, there is a gap in the literature regarding the spatial framework of postglacial sedimentary processes in the southeastern North Sea, particularly in the EPV, as integrated chronological and sedimentological studies have been carried out only for the coastal regions (e.g. Zeiler et al., 2000; Gerdes et al., 2003; Streif, 2004; Behre, 2007; Bungenstock and Schäfer, 2009; Wolters et al., 2010).

The aim of this study was to (i) understand the re-organization palaeo-landscape/environment of the southeastern North Sea shelf since the Late Weichselian and the evolution of the EPV, and to

(ii) elucidate EPV's sedimentary infill pattern and its main controlling factors under the variations of the sea-level and climate. Owing to the very high vertical and horizontal resolution achieved by parametric echo-sounder data and vibro-cores that penetrated into the sandy North Sea sediments, EPV`s geometry and sedimentary infill architecture could be investigated in a great detail for the first time. Focusing on the evolution of around 8000 km² area wide palaeovalley whose accommodation space has allowed for about 17 m thick infill during late Weichselian–Holocene, this study hopefully clinches an argument for the speculated palaeo-drainage and -coastline in the southern North Sea from the last glaciation up to modern conditions today.

2.2   Regional Setting

North Sea as a shallow marginal sea situating in the Northwest European continental shelf is open to the Atlantic Ocean via the Dover Strait to the southwest and to the north, and to the east it is connected to the Baltic Sea (Fig. 1). Epicontinental North Sea basin, underlied by Mesozoic rifts, was surrounded by British Isle, Fennoscandian Shield and central and western Europe with a narrow connection (around present day's Norwegian Channel) to the North Atlantic Ocean during the Cenozoic (Ziegler, 1992). During Late Miocene, Pliocene and Early Pleistocene Southern North Sea served as a major depocenter for deltaic sediments associated with the former Baltic River System and north German rivers under the control of both the Mesozoic Central Graben and climate (Cameron et al., 1993; Rasmussen, 2004). Subsequently, several ice waning and waxing since the Middle Pleistocene (780 ka BP) controlled the later sedimentation in the area. Each glaciation ended with tidal marine environments that is more or less similar to the present-day condition. Therefore, regarding the shelf architecture of the study area, several landscape adaptations (ranging from glacial, fluvial, aeolian and marine) have taken place as a result of Pleistocene glacial and interglacial periods coupled with sea-level changes. During the oldest Elsterian stage (MIS 12 or 10; according to Toucanne et al. (2009b) and Litt et al. (2007), respectively) and Saalian Complex stage (MIS 8–6), the study area was completely covered by glaciers and it was characterized by subglacial tunnel valleys with incisions of around 500 m deep (Huuse and Lykke-Andersen, 2000; Streif, 2004; Lutz et al., 2009). Subsequent Eemian interglacial lasted between 126–115 ka BP correlating to MIS 5e. Later, several alternating stadials and interstadial characterize the Weichselian Stage from 115–11.6 ka BP (from MIS 5c to the beginning of MIS 1). Weichsel glaciation caused the area being dominated by periglacial processes (Fig. 2). The palaeo-drainage system of the rivers Elbe, Weser, Eider (Figge, 1980; Köhn, 1991) and Ems (Hepp et al., 2017) discharged across the present-day southeastern North Sea through a 30-40 km wide EPV to the Central North Sea. In the wake of post-glacial transgression, EPV, Pleistocene glacial leftovers like end-moraines Borkum Riffgrund and Sylt from Saale glaciation (Pratje, 1951) and Dogger Bank (assumed from Weichsel glaciation) have configured the

landscape of the southeastern North Sea (Veenstra, 1965; Carr, 2004; Carr et al., 2006; van Heteren et al., 2014).
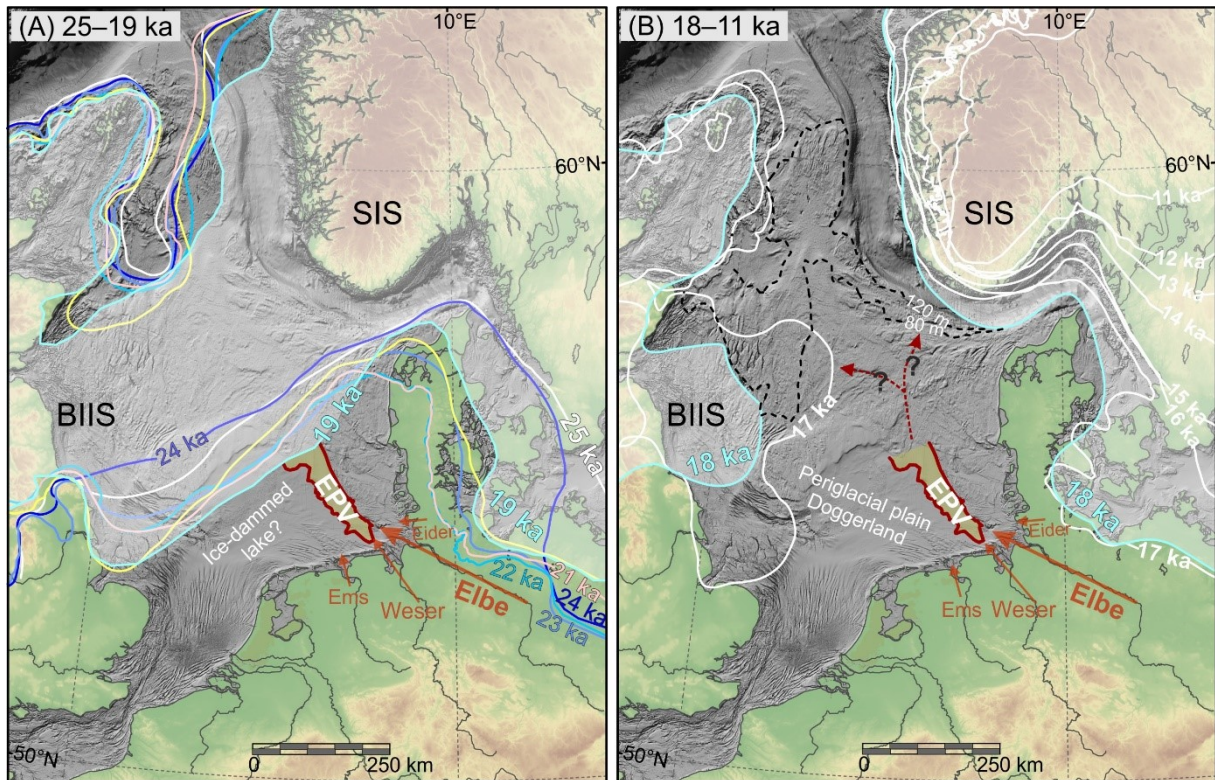
Figure 2.2 Elbe Palaeovalley and Late Weichselian ice sheet extents extents (according to Hughes et al., 2016) between **A)** 25–19 ka BP, possible blockage of EPV due to ice-sheet confluence around Dogger Bank and **B)** 18–11 ka BP, ice-free for the possible EPV drainage outlet(s). Most of the present southern North Sea basin was dry land (Doggerland), dominated by periglacial conditions, and the rest was partly surrounded by Weichselian ice sheet correlating with the MIS 2. Weichselian ice advances were not simultaneous, therefore the "LGM" term was region dependent. During the late Weichselian, meltwater carried by EPV that extended northwest towards the modern North Sea along with confluence of rivers Weser, Ems and Eider (Figge, 1980; Gibbard et al., 1988). Note that present-day topography and bathymetry (with 80 and 120 m contours as black dashed line) is used; for the Late Weichselian–Holocene coastline modelling of the NW European shelf, the reader is referred to Ward et al. (2016) and Lambeck (1995).

2.2.1 Sea-level and climate since late Weichselian in the southern North Sea

During the Last Glacial Maximum, 24–19 ka BP (Fig. 2), the sea-level was approximately 134 m below the present level (Lambeck et al. (2014); corrected for isostatic effects) and today's North Sea was exposed as a periglacial landscape. The coastline was located approximately 600 km farther north today (or 350 km north of Dogger Bank; Streif, 2004) at the western rim of Norwegian Channel and Devil's Hole. This caused the development of a drainage system toward the continental shelves (Gibbard et al., 1988), discharging meltwater from the SIS along with drainage from northern Europe carried by EPV to the North Sea (Ehlers and Gibbard, 2004).

Since decades there is an ongoing debate on whether the maximum extents of BIIS and the SIS led to ice sheet coalescence during the MIS 2 (Sejrup et al., 2000; Boulton et al., 2001; Graham et al.,

2007; Sejrup et al., 2016) or these ice sheets were independent from each other (e.g. Jansen, 1976; Long et al., 1988; Ehlers and Wingfield, 1991) with Dogger Bank located in between as a thrust block moraine (Carr et al., 2006). The speculated ice connection might have resulted in the formation of an ice-dammed lake at the southern margin ice sheet (Fig. 2a; Valentin, 1957a) in a topographic depression possibly around Oyster Ground, as it was evidenced for the previous glaciations (Mangerud, 2004; Toucanne et al., 2009a; Cohen et al., 2014; Sejrup et al., 2016). If such meeting of ice sheets was the case during MIS 2, the northward drainage of the EPV must have been prevented and drained into this large lake. In fact, Toucanne et al. (2009a), Toucanne et al. (2015) and Ménot et al. (2006) stated that between 30–18 ka BP SIS drainage via north German rivers (Elbe, Weser) was directed to the Bay of Biscay via possible ice-dammed lake. On the contrary, studies from Denmark (Houmark-Nielsen and Kjaer, 2003; Lambeck et al., 2010; Houmark-Nielsen et al., 2012) and the Norwegian Sea (Lekens et al., 2006) suggested that southern SIS margin meltwater drainage was towards north (i.e. Arctic Seas) between 30–20 ka although there might have been short epochs of ice sheet coalescence between SIS and BIIS. Due to the existence of several reconstructions and assumptions on North Sea ice sheet extent, recently reconstructed ice sheet extensions with 1 ka interval based on an extensive compilation conducted by Hughes et al. (2016) are presented in Fig. 2. A possible drainage pathway of EPV towards north(west) was ice-free when ice sheets were unzipped and started to collapse ca. 18.5 ka (Sejrup et al., 2016).

The onset of the marine transgression following the LGM caused a stepwise submergence of the periglacial landscape (Fig. 2b) and accompanied by a coastline shift of about 600 km towards south (Streif, 2004). Based on the rate of the sea level rise three major stages are defined by Streif (2004). During the first stage between 18.0 to 10.3 ka BP, the sea-level rose from a low stand of about 130 m to about 72 m below present-day sea-level (Streif, 2004) when the environment was similar to tundra in northern Siberia and Canada today (Dittmers et al., 2008; Flemming and Çağatay, 2014). Regarding the period between 14.5 and 13.0 ka BP, Rise et al. (2008) constructed models of depositional environments at the Norwegian Channel, and he attained this interval to the riverine input by northward drainage of palaeo-rivers off Germany. Progressive inundation of brackish water via Outer Silver Pit took place during this first stage (Wolters et al., 2010).

During second stage, the rate of RSL was much more rapid; from 10.3 until 7.1 ka BP, the sea-level rose from about 72 to 25 m below the present sea-level (Streif, 2004). Moreover, the compilation of both existing and new sea-level indicators (mostly basal peats), revision of previous Holocene relative sea level (RSL) curves of southern North Sea, and geodynamic Earth and ice modelling revealed a differential crustal movement between Belgian, the Netherlands, northwest Germany and the southern North Sea associated with tectonic and post glacial glacio (and hydro) isostatic

subsidence. The differential isostatic subsidence, for instance, in Northwest Germany in comparison to Belgium was around 7.5 m ka between 8 and 4.8 cal ka BP (Vink et al., 2007), which represented by relative elevations between sea-level data from these regions.

At the beginning of the second stage, the North Sea coastline was located around 300 km farther north than today. According to Jelgersma (1979), Köhn (1991) palaeocoastline coincided with today's 60 m-depth contour line (between north of the Dogger Bank and northern tip of Denmark) when a watershed (Doggerland – a vast tundra) existed between the Dogger Bank and the isle of Texel (Coles, 2000). The Elbe River's drainage system was located east of this watershed. Holocene marine transgression in the EPV from the north between Denmark and Dogger Bank led to estuarine from the east of Dogger Bank, and then open-marine conditions introduced by the Outer Silver Pit (Konradi, 2000). Between 9 and 8 ka BP, Streif (2004) reported a broad development of tidal flat sediments in the southern North Sea. At around 8.3 ka BP, the opening of the English Channel via the Dover Strait inundated "Doggerland" (Coles, 2000) and left Dogger Bank as an island in the southern North Sea so that strong tidal currents were brought in. Prior to the last stage of Streif (2004), Dogger Bank was submerged around 7.5 ka BP (Fitch et al., 2005), which might have also caused a significant change in the hydrographical circulation (Konradi, 2000). This last stage with relatively low rate of SLR continued until the present sea-level was established and it is characterized by a 25 m rise by developing today's coastal zones with sandy barrier islands, coastal marshlands, tidal flats, tidal channels and estuary mouths along the coast of German Bight (Streif, 2004; Bungenstock and Schäfer, 2009).

2.2.2 Hydrographic setting and sediment dispersal

The interaction between seabed morphology, tidal residual currents and wind effects results in a complex and dynamic hydrography controlling the morpho-dynamics of the southeastern North Sea seafloor (Becker et al., 1992; Dippner, 1993). The modern mean residual currents (total current minus the oscillatory tidal current) have an anti-clockwise direction parallel to the coast (Mittelstaedt and Soetje, 1982). Calm wind situations advocate the development of the large cyclonic circulation on the area over the EPV (Dippner, 1993).

Generally, two main water masses exist in the study area (Becker et al., 1983). These water masses influenced by (i) the Central Southern North Sea Water (NSW) originating from North Atlantic and (ii) the Continental Coastal Water (CCW), a mixture of Atlantic surface water from the English Channel and river discharge directly from Ems, Weser and Elbe and indirectly from Rhine and Meuse (Becker et al., 1992). NSW's bottom layer component (NSBW) shows a strong coupling to seafloor morphology and is found above the EPV. Given that this area still forms a morphological depression with depths greater than 40 m, EPV is a possible core path for bottom waters (Otto et

al., 1990). Besides, deeper channel-like features like the Outer Silver Pit in the western North Sea and the Dover Strait in the Southern Bight also allow bottom water to flow (Otto et al., 1990).

Owing to its tides and winds, the southeastern North Sea waters are well mixed vertically, although stratification can temporarily develop depending on the freshwater discharge and/or warm and calm weather conditions. Seasonal thermal stratification occurs at 40 m depth contour, except over Dogger Bank (Huthnance, 1991).

The surface sediments of southeastern North Sea sediments are mobile due to wave and current action; strong shear currents or wave action re-suspends sediment prior to support transportation by tidal or residual currents (Becker et al., 1992). With a velocity range between 45–54 cm/s (Mittelstaedt and Soetje, 1982), tidal currents are able to transport sand in the German North Sea (van der Molen, 2002). Regarding entire southern North Sea, the bottom material can be mobilized by wind waves. Even water depths up to 45 m, (van der Molen, 2002) observed erosional bottom stratigraphy, washout of bottom features, high concentrations of suspended sediment and large wave-induced orbital current velocities. Therefore, the capacity of the ambient currents (forced by tides, wind and local density differences) is enhanced by wind waves, which results in the ease of sand transport (van der Molen, 2002). In summary, wind waves and wind-driven currents, possibly aided by tidal currents, determine the sediment transport on and around the Dogger Bank, in the Oyster Grounds and in the German Bight. These transport processes feature a predominant southeast transport direction of sandy sediments on the Dogger; while the silty and organic rich surface sediments in the Oyster Grounds are tranthe 40sported northeast. In the German Bight, littoral transport converges in the southeastern corner, and the transport during storms is away from the coast to a deeper water (van der Molen, 2002).

2.3   Data and Methods

2.3.1 Sediment echosounder data

The study is built on the sediment echosounder data were collected during the HE405 cruise on board R/V Heincke in 2013 along a network of EPV transects covering an area of 70 x 200 km (Fig. 2.1). Grids of closely spaced profiling were also surveyed at some areas of interest inside and at the rims of EPV. As a complementary data, additional sediment echosounder profiles were analyzed from the R/V Sonne SO Cruise 9 (in 2014) and R/V Heincke cruise HE444 (in 2015). Track lines belonging to these three cruises are shown in Fig. 2.1.

The sediment echosounder data were acquired using the hull-mounted SES-2000 medium system (INNOMAR Technology) and Parasound (Teledyne Atlas Hydrographic), the both of which utilizes the parametric effect to gain acoustic data with high vertical and horizontal resolution. In

principle, two primary sound waves of slightly differing frequencies are transmitted. Due to the non-linear interaction of these sound waves, a secondary sound wave is transmitted with the difference frequency of the primaries. The secondary low frequency was set to 4 kHz for both systems providing a vertical resolution of up to 20 cm. The horizontal resolution depends on the beam width, which is 2° for the SES medium and 4.5° for the Parasound system, resulting in footprints of <2 m and <4 m, respectively. The sub-bottom penetration of the acoustic signal was up to 18 m for the EPV infill, while it was less outside of EPV where relatively thin (up to 3 m) mobile sands directly drape the consolidated Pleistocene sediments.

The SES and Parasound raw data were converted to seg-y data format using custom developed software (H. Keil, University of Bremen) and loaded into Kingdom software (IHS) project for interpretation by applying the seismic stratigraphy principles as introduced by Mitchum et al. (1977). Using the Kingdom software capabilities, unconformities were mapped, and thicknesses as well as volumes of the derived acoustic units were calculated. The two-way travel time to depth conversion was done by using an acoustic velocity of 1500 m/s. The data was corrected according to the Lowest Astronomical Tide (LAT) by using the bathymetry provided by the Federal Maritime and Hydrographic Agency of Germany (Bundesamt für Seeschifffahrt und Hydrographie).

In the case that acoustic blanking impeded the interpretation, multi-channel seismic data gathered during R/V Heincke cruise HE405. These data were gathered with a Mini GI Gun as source and, as receiver, with 32-channel streamer composing of single hydrophones. A standard seismic processing was carried out including binning with a distance of 2 m, NMO-correction, static correction, stacking and FD migration.

2.3.2 Sediment core data

The sediment cores were collected during HE-405 cruise at 16 sites in the center and on the flanks of the EPV using a vibrocorer. A Geo-Corer 6000 vibrocoring system, provided by the company Geo-Engineering.org (Bremen, Germany) with a barrel length of 5.80 m, yielded sediment cores with fine, middle and coarse sands from the late Pleistocene-Holocene North Sea sediments. Visual core description and imaging were performed partially on board and onshore. The visual core description included information about color, lithology, sedimentary structures and visual determined grain size. Physical properties such as gamma ray attenuation (dependent on porosity and density of sediments), compressional wave velocity, and magnetic susceptibility (with a Bartington point sensor MS2E) were measured on half sections of ten cores (GeoB177-05, -06, -08, -09, -10, -11, -12, -15, -17, -20) with a resolution of 2 cm using a GEOTEK Multi-Sensor Core Logger (MSCL) at the MARUM (University of Bremen, Germany). Raw data were corrected from

artefacts (e.g. voids and core section breaks) prior to the correlation with the seismic stratigraphy and lithological information. Apart from cores obtained during HE-405 cruise.

Radiocarbon ages were determined at five samples from cores GeoB17714-1 (4.77–4.79 mbsf), GeoB17715 (3.45–3.46 mbsf), GeoB17717-1 (1.10–1.11 mbsf), Geob17718-3 (5.31-5.32 mbsf), and GeoB17721 (4.76-4.77 mbsf; Table 1). We selected plant fragments, benthic foraminifers and ostracods for dating; the peat was dated as bulk sample. Samples were submitted to the Poznań Radiocarbon Laboratory in Poland. Additionally, we used published radiocarbon ages by Konradi (2000), Vink et al. (2007), and Alappat et al. (2010) which were re-calibrated for a better reproducibility (Table 1). The dates were calibrated with the CALIB v. 7.1.0 software (Stuiver and Reimer, 1993) using the IntCal13 data set for plant fragments and bulk peat samples; while we used the Marine13 calibration data set for foraminifer and ostracod and mollusc samples (Reimer et al., 2013). The reservoir correction value (ΔR= –3 ± 27 yr) for the North Sea in the Marine13 calibration curves is determined from Cage et al. (2006) who reported regional ΔR values for the Northeast Atlantic Shelf sea region. The mean values from the calibrated age range of ±1σ are normalized to calendar year and indicated as cal ka BP (Table 1). In addition, the Median Probability (MP) of the probability distribution determined by the software since it provides more reliable estimation of the sample calendar age (Telford et al., 2004).

2.4   Results

2.4.1 Overview of Elbe Palaeovalley morphology based on the echosounder profiles

The EPV stretches from the SW of Helgoland in a northwestern direction through the whole German sector of the North Sea and still expresses a shallow and narrower depression in the modern seafloor (Fig. 2.2). The palaeo margins of EPV has a length of about 210 km, and widens from roughly 25 km in the south to more than 50 km in the north (Fig. 2.1). The base of the EPV deepens from south toward north from 39 m to until 63 m mbsl, with a gradient of approximately 0.13 m/km (Fig. 2.3).

The margin of the EPV shows several spatial bends (Fig. 2.1); occurring mostly at the western flank (south of the White Bank) and one at the eastern flank near the Amrum Bank. The three spatial bends in the southernmost part (Fig. 2.7a), close to the mouths of the Elbe, Weser and Ems Rivers, are more hypothetical due to a less number of seismic profiles. The eastern margin of the valley runs parallel to the recent coastline

Table 2.1 Radiocarbon dates and calibrated ages (WD: water depth in LAT; SD: sample depth).

Core ID	Lab ID	Coordinates	WD (m)	SD (mbsf)	Sample type	[14]C age (a BP)	1σ range (cal a BP)	2σ range (cal a BP)	Median Probability (cal a BP)	Location (relative to EPV)
GeoB17718-3	Poz-83150	54°15.50'N 07°13.20'E	38.5	5.31–5.32	Plant fragments	9510±50	11017–11067	10921–11085	10,822	S-channel infill (FU) (Fig. 6b)
GeoB17714-1	Poz-83147	54°38.50'N 06°10.00'E	41	4.77–4.79	Plant fragments	9280±50	10405–10565	10278–10585	10,463	N-infill (OU)
GeoB17717-1	Poz-83188	55°15.78'N 06°06.91'E	48.6	1.10–1.11	Benthic foraminifers and ostracods[d]	5420±35	5741–5861	5680–5900	5798	N-infill (SU)
GeoB17715-1	Poz-83149	54°50.58'N 06°02.14'E	41	3.45–3.46	Peat	8870±50	9905–10153	9766–10179	10,003	N-W rim
GeoB17721-1	Poz-83151	54°03.03'N 06°58.58'E	33	4.76—4.77	Peat	9970±50	11270–11599	11248–11693	11,411	S-Tributary (Ems)
BH89/8[a]	AAR-4460	55°49.00'N 05°17.00'E	55	17–17.10	Mollusc fragments[d]	10250±90	11126–11393	11053–11690	11,274	N-infill (?)
FR07(35VC)[b]	Hv-25767	54°59.96'N 05°35.19'N	40	4.50	Basal peat	9970±140	11243–11704	11170–12024	11,512	N-Outside W rim
FR07(35VC)[b]	Hv-25768	54°59.96'N 05°35.19'E	40	5.50	Wood	13010±250	15203–15945	14671–16321	15,555	N-Outside W rim
Gauss 1987/5	—	55°04.63'N 05°49.69'E	43	5.74	Fen peat base	9165±230	9941–10692	9675–11085	10,353	N-Outside W rim (Fig.3)
245[c]	—	54°41.80'N 06°11.50'E	41	4.75	Fen peat top	9000±200	9778–10377	9550–10576	10,091	N-Western flank
BSK VC-15[c]	—	54°54.18'N 06°52.61'E	34	0.46	Fen peat base	8250±100	9092–9401	9012–9462	9231	N-Outside E rim
H15/2V[c]	—	54°10.17'N 06°57.07'E	35	4.35	Fen peat top	8975±90	9931–10232	9744–10271	10,067	S-Outside W rim (Fig. 6c)
H18/3V[c]	—	54°06.60'N 06°55.20'E	34	3.40	Fen peat middle	8535±150	9308–9728	9126–10004	9535	S-Outside W rim
280[c]	—	54°07.09'N 07°12.79'E	36	2.95	Fen peat middle	9000±200	9778–10377	9550–10576	10,091	S-Western flank (Fig.6d)
FR07(49VC)[b]	Hv-25778	53°51.69'N 07°31.31'E	20	4.75	Peat	8490±130	9301–9593	9123–9885	9478	Shore region Frisian Islands

The cross-valley shape is generally asymmetric provided by a smooth/gentle western flank and a steeper eastern flank (Figs. 2.4, 2.5). Mean values regarding flank slopes range between approximately 0.04 and 0.06° for the western flank and 0.07 and 0.11° for the eastern flank, except in the southernmost part of the valley close to Helgoland where the eastern flank is not well developed (Fig. 2.6).

Furthermore, incisions, bars, ridges, and terraces are noticeable in the cross-section profiles. Several incisions were observed in all profiles across the valley base (see Figs. 2.3–7, and Fig. S1). Bars, which can reach heights of up to 3 m (Fig. 6a), occur between the incisions of the valley base. Ridges occur along some parts of the western flank of the EPV (Fig. 2.5). The morphological terraces at the eastern flank were observed in two cross profiles (Fig. 2.5a and Fig. S1) and situated around 9 m above the adjacent thalweg and with a width of around 2 km.
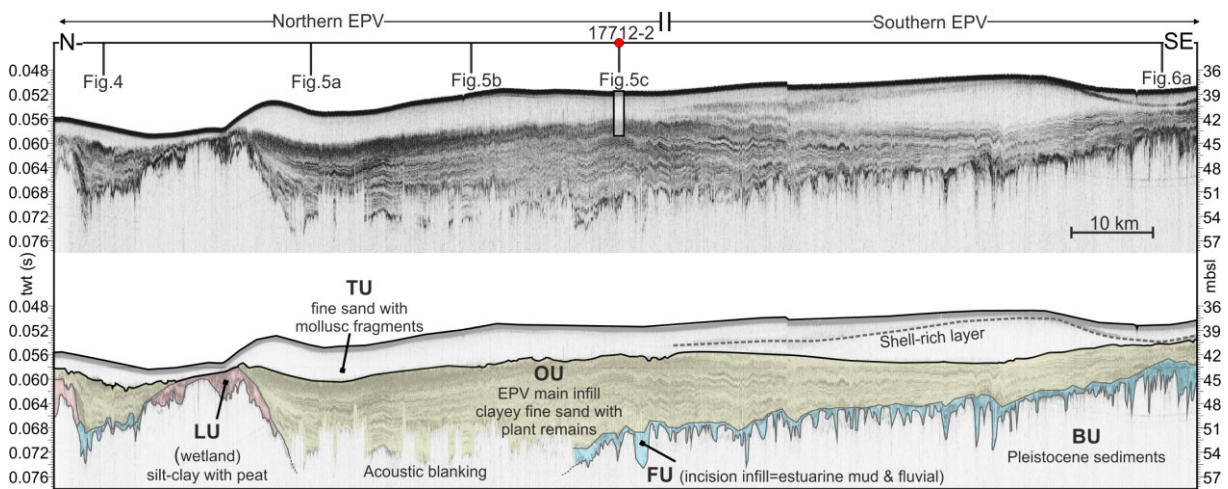
Figure 2.3 NW-SE echo-sounder profile along the valley, for location see Fig. 2.1. Northern–southern discrimination of EPV is based on local features of infill pattern. BU, FU (blue), LU (pink), OU (yellow) and TU represent acoustic units defined. Dashed line indicates shell rich-layer, which fades out in TU towards east and north of the valley. The depth axis here and the rest of profiles was determined using a velocity of 1500 m/s. Depth values were corrected to LAT.

2.4.2 Seismoacoustic stratigraphy of the Elbe Palaeovalley

The strong subsurface reflector of the EPV's base and its subsequent infill of up to a thickness of 17 m were identified from sub-bottom profiles. The infill of the EPV was divided into 5 major units based on their acoustic facies: (i) a complex infill of the incisions (FU), (ii) units of acoustically transparent lenses (LU), (iii) acoustic units OU and SU with internal inclined sub-parallel, well-defined reflectors, and finally, (iv) acoustically transparent unit (TU) that fills the shallowest part of the valley. These facies, including their spatial and vertical distributions as well as variations, will be described in detail in the following (Fig. 2.7).

2.4.2.1 The acoustic base of Elbe Palaeovalley (S1)

The acoustic base of EPV (S1) is represented in all seismic cross profiles by a prominent acoustic reflector, which separates the valley infill from the basement beneath, hereafter named BU could be only identified by accompanying high resolution multi-channel seismic lines (Fig. 2.6a). The valley base is characterized by numerous up to 5 m deep and about 200–500 m wide V- and U-shaped depressions (Figs. 2.3, 2.4, 2.5, 2.6, 2.7). Local acoustic blanking zones with an upper enhanced reflection hamper acoustic
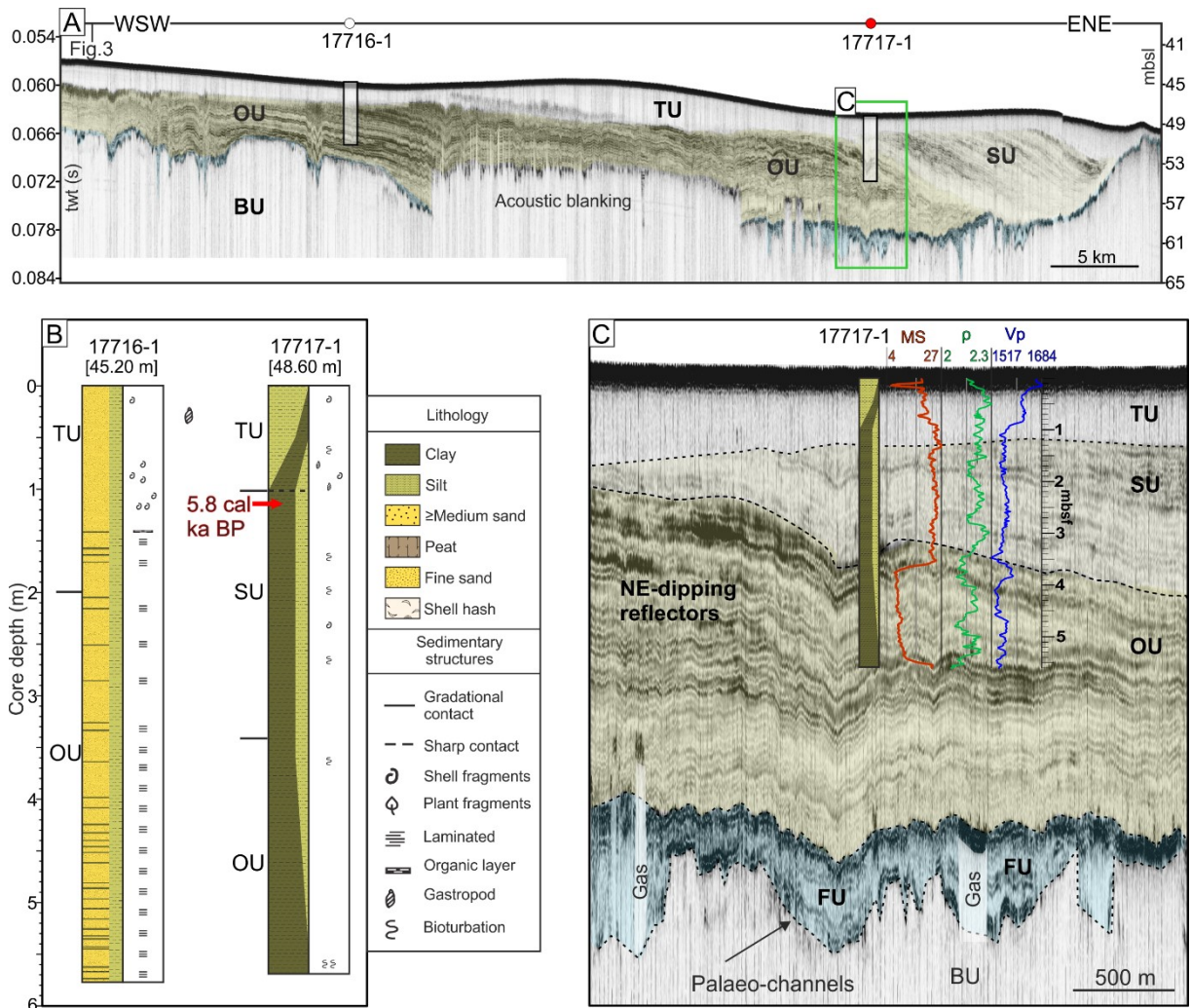
Figure 2.4 The valley transverse profile from the northernmost part of the study area **(A)**. Lithology and sedimentary structures of cores GeoB17716-1 and 17717-1, red arrow in 17717-1 indicates radiocarbon dated sample position **(B)**. Correlation of MSCL results of 17717-1 with the acoustic units **(C)**. MS, magnetic susceptibility (10^{-6} SI); ρ, wet bulk density (g/cm^3); Vp, p-wave velocity (m/s).
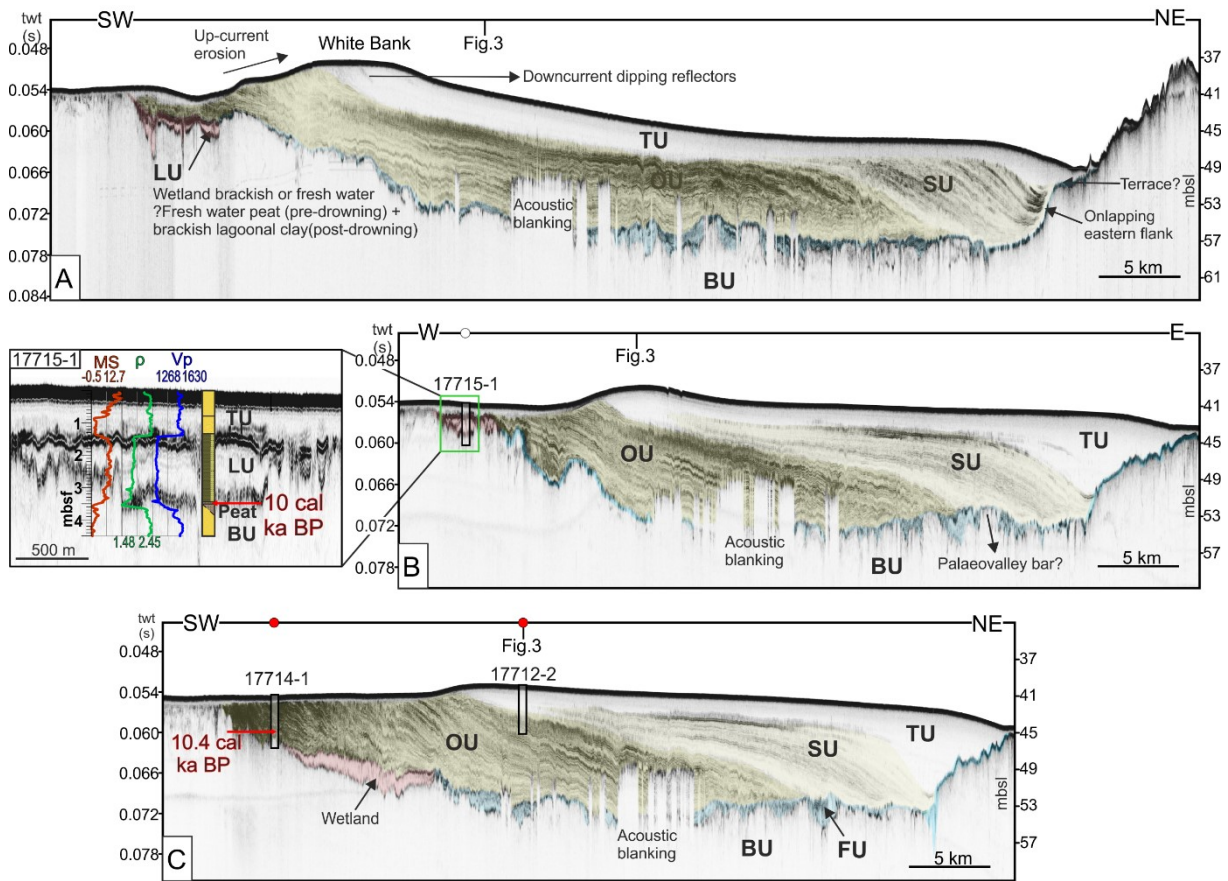
Figure 2.5 Valley transverse profiles from northern part of the EPV **(A–C)** where most of the acoustic blanking and inclined erosional truncation of OU's top are observed. Note the relationship between lateral extent of truncation, sedimentary bulge or ridge on the seafloor height, but also the moat-like representation SU. A close-up from **B** shows MSCL log of core GeoB17715-1 and peat was sampled for radiocarbon dating. Sedimentary structures of cores GeoB17714 and 17712 in **(C)** are given in Fig. 2.9. See Fig. 2.1 for profile locations and Fig. 2.4 for core description legend.

signal penetration down to the S1. They mostly accumulated on the northern EPV at depths greater than 9 meter below seafloor (Figs. 2.3 and 2.8a) and relatively numerous narrower zones which can be directly related to the thalweg of incisions (Fig. 2.7). The occupation by these acoustic blanking zones extends seaward and reaches a width of around 12 km (Fig. 2.3, 4 and 2.8a).

Detailed mapping of the EPV's base was possible in a small (49 km²) pseudo-3D survey with profiles spaced 50 m apart (see Fig. 2.1 for location of the survey), sheds a light on the character of the incisions (Fig. 2.7). Based on the pseudo-3D map, five, up to 5 m deep, southeast–northwest orientated channels can be traced through this small study area; one channel reveals a nearly straight course, whereas the other channels show slight bending or bifurcation.

2.4.2.2 Incised channel fills (FU) and transparent lenses (LU) at the base

The valley base is partly overlain by small acoustic units FU and LU: FU represents the infill of incisions at the valley base, whereas LU represents acoustically transparent lenses. Nearly all

43

incisions are filled by FU except some relatively deeper incisions close to the foot of the eastern flank (Fig. 2.6e).

FU is characterized by continuous high amplitude reflections and configured in an inconsistent manner as complex (Fig. 2.6b, c), onlap (Fig. 2.6e), divergent (Fig. 2.6d), and prograded reflection pattern.

LU was observed occasionally on the western flank of the EPV only and is absent in the eastern flank. It represents acoustically transparent facies. The outer shape appears as lenses with a maximum width of 6 km and thickness of 2 m (Fig. 2.5).

The upper boundary of units FU and LU is represented by, moderate to high amplitude reflector S2 that becomes less pronounced at the foot of eastern flank.

2.4.2.3 The main Infill of the Elbe Palaeovalley (OU, SU, and TU)

The main EPV infill is characterized by three acoustic units, referred in the following as Oblique Unit (OU), Sigmoid Unit (SU), and Transparent Unit (TU).

<u>Oblique Unit (OU)</u> This unit represents almost 43 % of the total EPV infill (Table 2.2) with a maximum thickness of 13 m in the central part of the study area. It is attached only to the western part of the EPV and, following the widening of the EPV, its width increases from 12 km to 36 km seaward, (Figs. 8b, d). OU thins out towards the northeast but also along-valley to the southeast, where it terminates (Figs. 2.6d, 8b). OU is only absent at the very southeastern part of the valley where water depths are less than 35 m (Fig. 6d). Dipping internal reflectors of OU are densely spaced, show high to moderate, amplitudes, and maintain a progradational oblique pattern by downlapping onto the lower bounding surface S2 around the valley axis. OU often terminates against the above-mentioned bars at the valley floor, (bars in Fig. 2.5b and 2.6a). The continuity of reflectors within acoustic unit OU is disturbed by acoustic blanking zones.

The upper boundary of OU changes laterally in the cross section of the valley: above the western flank, the reflectors are generally truncated, whereas around the central valley, the upper boundary is concordant interrupted by only a few erosive small incisions.

<u>Sigmoid Unit (SU)-Northern</u> EPV SU is only identified along the eastern side of EPV. This unit fills mainly the space left by OU in the eastern part of the valley and comprises 8% of the total valley infill (Table 2.2). It has a width of around 13 km, and depending on the valley occupation of OU, gets narrower seaward where it reaches a maximum thickness of around 6 m (Fig. 2.7e). This unit consists of progradational sigmoid reflectors showing mainly weak to moderate amplitudes, which partly increases to the east (Fig. 2.5). These reflectors onlap onto OU in the western part of

the valley, but downlap onto the valley base reaches a infill and it merges with S1 in the central part, and again onlap onto the eastern flank.
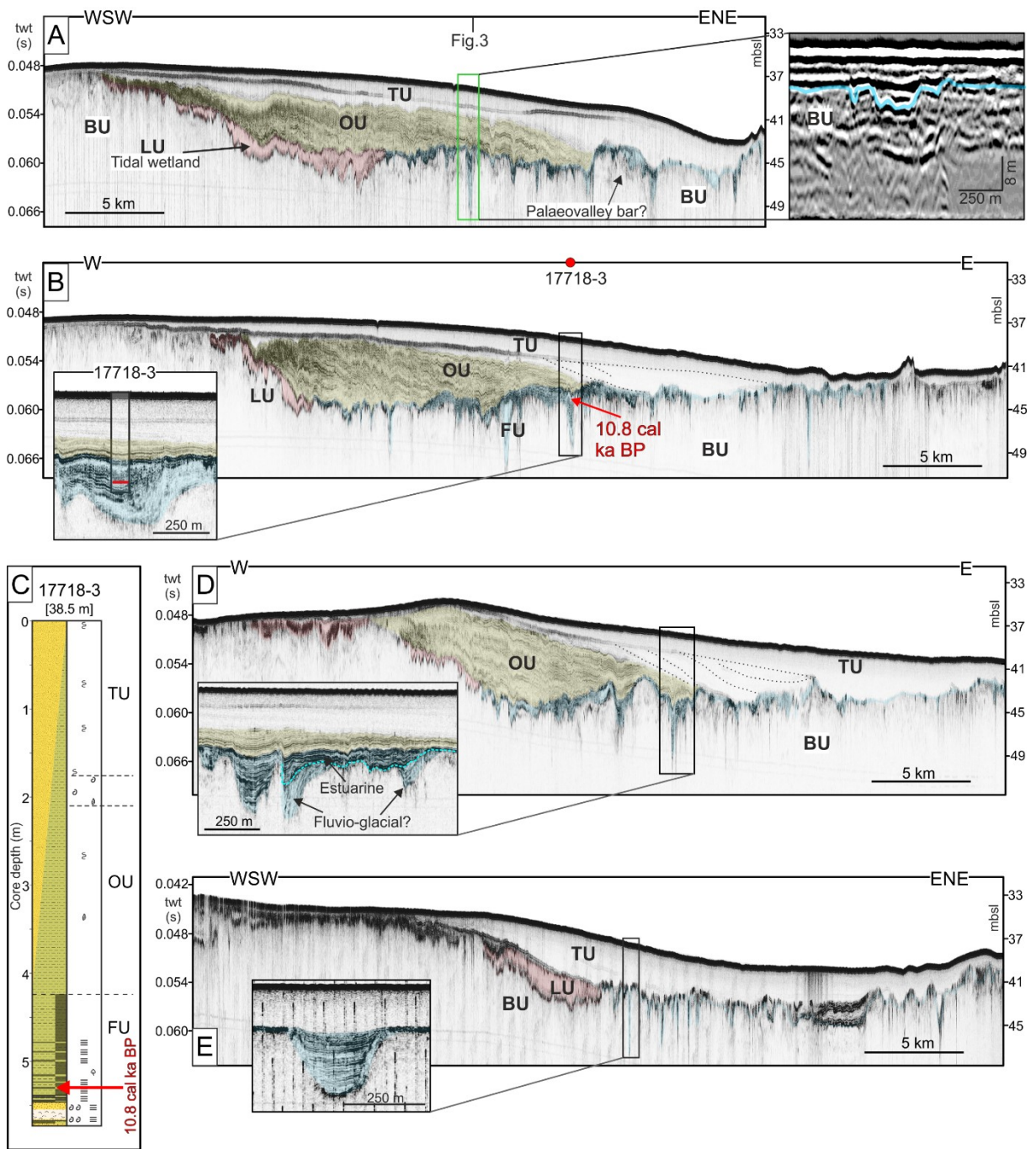
Figure 2.6 Valley transverse profiles from southern part of the EPV, where eastern flank is not well expressed, in contrast to the northern EPV. Close-ups (indicated by green rectangle) show the incision ns at the base and their infill pattern (blue shaded). **A)** Echosounder profile and close-up from its accompanying multi-channel seismic profile GeoB13-168. **B–C)** The core GeoB17718-3 penetrates until the upper part of incision infill (see related close-up), red marks indicate the dated sample and dashed lines indicate the interpretation of very dimly represented internal reflections. **D)** Ridge on the seafloor (as in Fig. 5) appears again on the seafloor. **E)** The southernmost valley cross section where OU is absent from the EPV infill.

Table 2.2 Calculations of area and volumes of different acoustic units calculated with the Kingdom software.

Acoustic unit	Area (x 10^6 m^2)	Gross volume (x 10^6 m^3)
FU (3d pseudo)	49	18
FU+LU	7739	4924
OU	4704	28812
SU	1585	5154
TU	7764	26725
EPV total	7739	65615

Table 2.3 Summary of the seismoacoustic units and associated sedimentary facies (further correlation shown in Fig. 9 including MSCL).

Seismo-acoustic unit	Seismostratigraphic description *Lower boundary: 1* *Upper boundary: 2* *Reflection pattern: 3* *Amplitude: 4*	Core description *Top contact: 1* *Lithology and sedimentary structures: 2*	Environment of deposition & inferred age
BU	1: – 2: Truncation 3: Chaotic–hummocky 4: –	1: Sharp 2: Fine sand with black coal particles	Fluvioglacial, glacial, dry land > LGM
FU	1: Onlap 2: Concordance–truncation 3: Complex, prograded, onlap, transparent infill 4: High to low	1: Gradual 2: Medium sand with agglomeration of shell fragments overlain by clayey fine sand to clayey silt	Periglacial –Fluvioglacial, fluvial, estuarine LGM–11.2 cal ka
LU	1: – 2: – 3: Transparent 4: Low	1: Gradual 2: Silty clay (+peat)	Estuary & wetland 11.2–10 cal ka
OU	1: Downlap 2: Erosional truncation 3: Oblique progradational 4: High to medium	1: Sharp–gradual 2: Fine sand with alternating layers of clay–laminated at western side, bioturbation increases towards east and up, coarsening up	Very shallow marine (tidal basin south of Dogger Bank Island) 10–8 cal ka
SU	1: Downlap–onlap 2: Truncation–toplap 3: Sigmoid progradational 4: Medium to low	1: Gradual 2: Silty clay bioturbated	Shallow marine (full connection to the English Channel) 8–5.8 cal ka
TU	1: – 2: Seafloor 3: – 4: Low	1: Seabed 2: Fine sand–medium sand with shell fragments, coarsening up	Open marine (after submergence of Dogger Bank Island) <5.8 cal ka
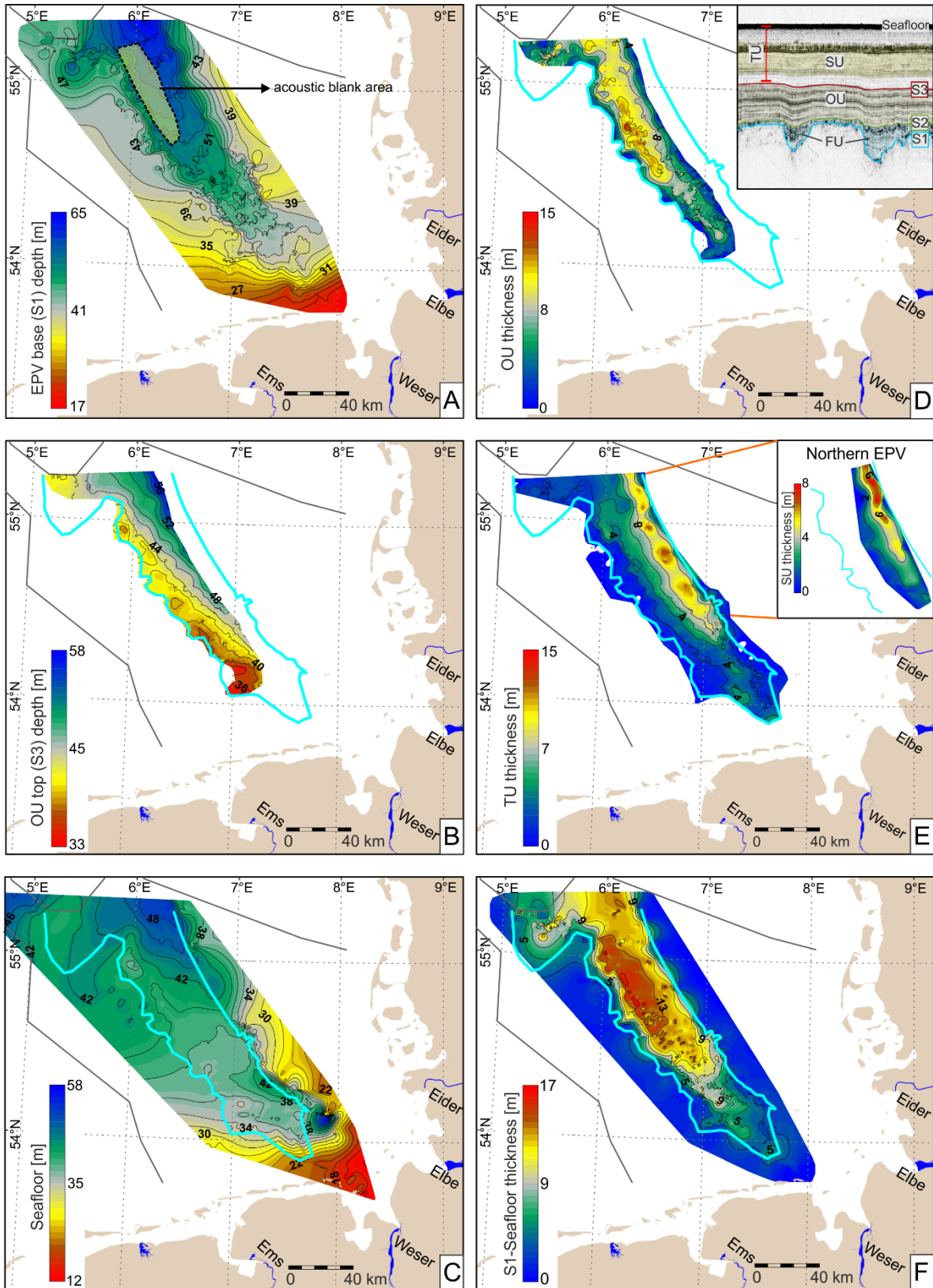
Figure 2.7 Maps of reflectors and units **A)** Base of the EPV (S1). Overlayed grey shaded area marks the extent of the acoustic blanking zone (Fig.5). **B)** Top of the acoustic unit OU, whose depocenter established in the south of White Bank (see Fig. 2.1). **C)** Seafloor. **D)** Thickness of unit OU **E)** thickness between OU top and seafloor **F)** Thickness of the total EPV infill. Blue line indicates valley rim. On the top-right corner, an example section for mapping description.

Transparent Unit (TU) Characterized by its transparent acoustic facies, TU is the uppermost unit filling the valley (almost 40 %), as well as areas outside of the valley (Fig. 2.7e). The upper boundary of TU represents the seafloor nearly in the whole profiles along the survey area except of small areas in the western part of the valley where OU outcrops at the seafloor (Fig. 2.6a, b and 2.5c).

At this western side of EPV (close to the western margin), the seafloor shows in the northern part of the study area an up to 2 m high positive relief ("ridge feature"). The crest heights of these ridges are inversely dependent on the width of the area characterized by erosional truncation into OU. The location of these ridges corresponds to the White Bank area (55°N, 6°E) in the North Sea (Figs. 1 and 3). Besides, seafloor exhibits an undulating topography near the eastern rim of EPV. Depending on the steepness of eastern flank, seafloor has a channel-like appearance at this part.

In the southern part of the EPV, a prolonged reflector has been identified within the TU. This reflector vanishes towards east and north of the EPV, but also sometimes merges with the seafloor (Fig. 2.3). Its amplitude decreases towards northwest and fades out.

2.4.3 Correlation between acoustic data and sediment cores

The cores are mainly composed of greenish gray or dark grayish brown fine to medium sands, clayey fine to medium sands and silty clays. In two cores (GeoB17715-1 and 17721-1), peat layers were identified between 350 and 400 cm. These two cores show alternating layers of clay, silt and fine sand above peat layer, that is overlied by medium and/or sand. All cores contain mollusks and plant fragments and bioturbation. Prominent layers of mollusks agglomerates were observed at cores GeoB17714, GeoB17718-3 and GeoB17720-2. Generally, OU has a uniformly low magnetic susceptibility and density values with respect to overlying and underlying units (Fig. 2.9).

The qualitative comparison of acoustic units and sedimentary facies as well as MCSL measurements (Fig. 2.9) reveals the following correlation:

Acoustic unit BU: Based on cores GeoB17705-1, GeoB17706-1 and GeoB17714-1 the composition of BU consists of greenish gray fine sand (125–250 μm) with tiny grains of black minerals, which significantly differs from the composition of the EPV infill (see below).

Reflector S1: The base of the valley was penetrated only at the westernmost rim of the EPV by cores GeoB17714-1, GeoB17715-1, and GeoB17719-1. At site GeoB17714-1, an about 10 cm thick agglomerate of fragmented mollusks at 0.25–0.35 mbsf corresponds to the strong reflector S1. At the western rim of the EPV (Fig. 2.5b, GeoB17715-1) Reflector S1 coincides with a 50 cm thick layer of heavily decomposed peat at depths of 3.37–3.87 mbsf.
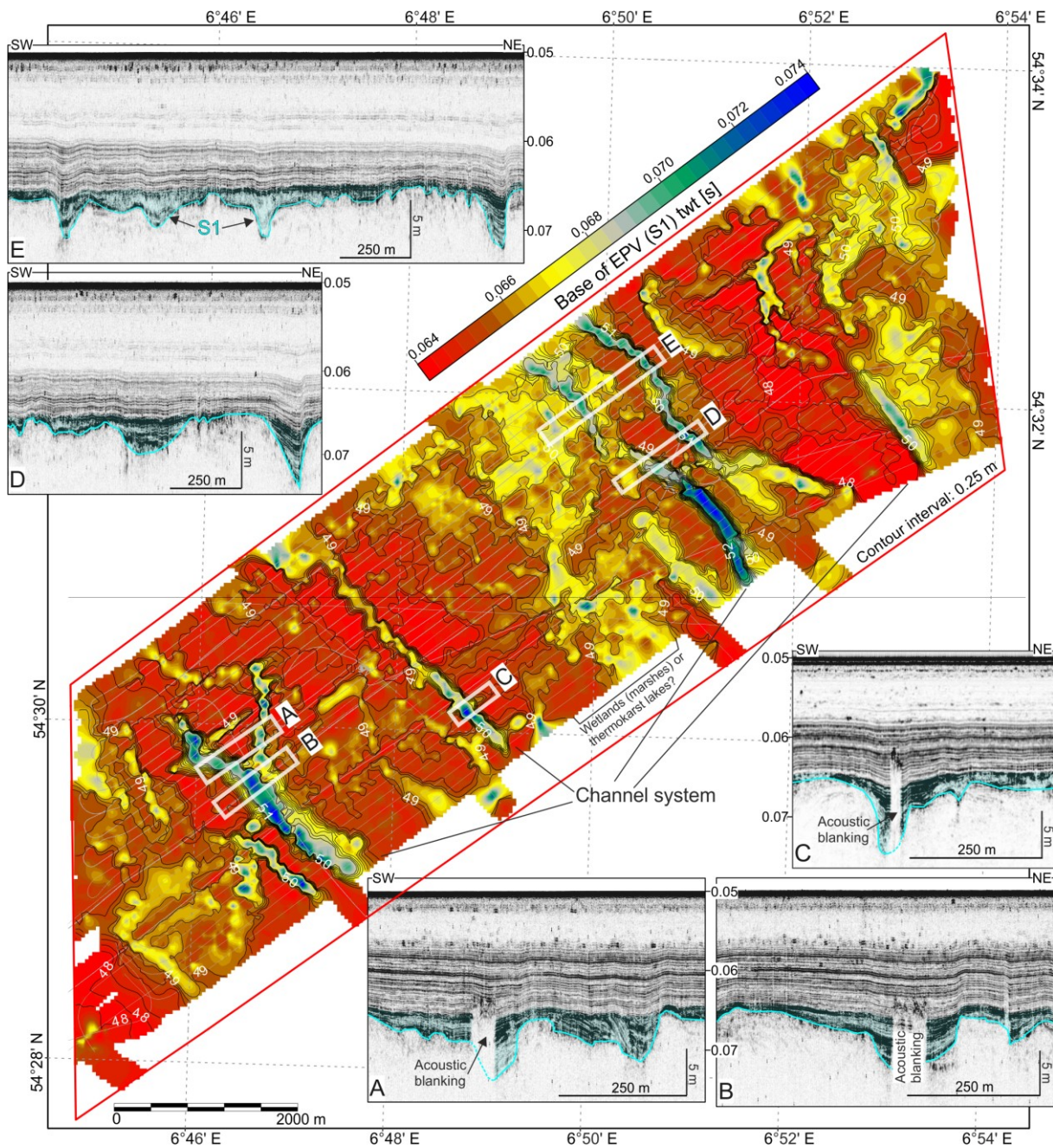
Figure 2.8 Drainage network of the Palaeovalley, revealed by mapping of the S1 reflector in the pseudo 3D study area (location is shown in Fig. 2.1). **A–E)** Echosounder sections of 3–5 m deep incisions and their infill pattern. Only incision infill is indicated (blue shading). Note the relation between the incisions and acoustic blanking in A, B and C.

Acoustic unit FU: Sediment core GeoB17718-3 (Fig. 6b) was the only core which reached down to the upper part of FU. The FU is composed of alternating layers of dark greyish brown medium sand intercalated agglomerations of well preserved and a few fragmented marine shells (Cardiidae) overlaid by very dark greenish gray clayey silt coarsening upward to clayey fine sands with common shell fragments as well as plant and wood fragments. Radiocarbon dating of plant fragments, from core depths between 5.31–5.325 mbsf, gives an age of 10.8 cal ka BP (Table 2.1 and Fig. 6b).

<u>Acoustic unit LU:</u> The heavily decomposed peat layer observed at the western rim of the EPV (GeoB17715-1) coincides with the base of LU (Fig. 2.5b). LU itself is composed of stratified silty clays. MSCL results show a rapid downcore decrease in gamma density (e.g. from 2.4 to 1.4 g cm-3) and p-wave (e.g. from around 1700 to 1200 m/s) at the base of LU, while magnetic susceptibility showing an increasing trend. Radiocarbon dating of peat from GeoB17715-1, from core depths between 3.45–3.46 mbsf, gives an age of 10 cal ka BP (Table 2.1 and Fig. 2.5b).

Reflector S2: S2, which represents the boundary between FU and LU to the overlying OU coincides with a gradual change in grain size observed in core GeoB17718-3, but also with an erosive (sharp) contact in Core GeoB17715-1.

<u>Acoustic unit OU:</u> It is mainly composed of fine sand with clay layers. At the western flank, we observed 1–25 mm thick alternation of clay and fine sand layers with organic matter (GeoB17714-1), whereas sediments at the valley center becomes highly bioturbated (e.g. GeoB17712-2). Radiocarbon dating of plant fragments from GeoB17714-1, from core depths between 4.77–4.79 mbsf, gives an age of 10.4 cal ka BP (Table 2.1 and Fig. 2.5c).

<u>Acoustic unit SU:</u> Based on Core GeoB17717-1, SU is mainly composed of silty clay (Fig. 2.4c). However, there is an upward trend to coarser sands with increasing contents of fragmented mollusks (coarsening upward) and less bioturbation accompanied by a slight change in color from greenish gray to dark grayish brown. Also, magnetic susceptibility shows a sharp transition from lower mean values in OU (3 x 10-6 SI) to higher mean values in SU (20 x 10-6 SI) between 3.0 and 3.3 mbsf. Radiocarbon dating of benthic foraminifers and ostracods from GeoB17717-1, from core depths between 1.10–1.11 mbsf, gives an age of 10.4 cal ka BP (Table 2.1 and Fig. 2.5c).

<u>Acoustic unit TU:</u> This uppermost unit was identified in all cores, and TU is composed of dark greyish brown fine sands or fine to medium sands with fragmented and a few well-preserved mollusks and gastropods. Mean magnetic susceptibility is about (12 x 10-6 SI).

2.5 Discussion

The observations of the sedimentary infill structures of the southern EPV favor an interpretation of several stages of Holocene sedimentation history incorporating different sedimentation processes. During this transgressive phase the valley morphology, but also a larger scaled hydrodynamic situation in the study area seemed to have affected the depositional environment. In the following, a stratigraphic and procedural model for the Late Weichselian/Holocene development of the EPV is suggested and discussed in respect to the environmental changes related to the last deglaciation phase and the relative sea-level rise (Fig. 2.10).

2.5.1 Valley base morphology and drainage direction

The base of the EPV (S1) (Fig. 5) represents an erosional morphology cutting the subsurface (BU) and it most likely representing shelf exposure surface during Weichselian glacial maximum. Based on the existing coring information the exact formation history of the valley morphology cannot be unraveled in this study. Deeper penetrating MCS profiles show that the high amplitude base reflector S1 incises into the underlying unit BU (Fig. 6b), which is expected to be Pleistocene tills, fluvial, and glacio-fluvial sediments composed of fine to medium sands with intercalations of wood fragments or Tertiary coal particles (Ludwig et al., 1981; Alappat et al., 2010). However, the floor of the valley becomes occasionally amalgamated with the S2 on the western valley flank where peat mainly accumulated (see section 5.2). Therefore, overall morphology of the valley may have a diachronous nature, in fact such diachrony was shown by an experimental study (Strong and Paola, 2008) that the different time markers are preserved at the outer edges (preservation of the younger event) and near the valley axis (the oldest event).

However, considering the overall width of the associated palaeochannel network (around 40 km), the low gradient of the S1, and the width/depth ratio of around 100 for individual palaeochannels (considering the classification of rivers Rosgen (1994) based on morphological characteristics), EPV supports an interpretation as a braided style activity. Moreover, inconsistent incision configuration (e.g. Fig. 8) probably evidence the laterally migrating development (Gibbard and Lewin, 2002; Vandenberghe, 2008) as it would be expected within the braided system with its episodic discharge of snow melt (Mol, 1997; Kaiser et al., 2012). At the beginning of last glacial period (warm-cold transition), not deep but wide lateral extent braided rivers in lowland settings had strong influence on valley morphology (Vandenberghe, 2008). In fact, excessively wide (mean 25 km) ice-marginal valleys dominated in the North European plain particularly during the coldest phases of Weichselian (e.g. Mol et al., 2000; Pisarska-Jamroży, 2015). The interaction between river style evolution of Elbe system with climatic shifts (i.e. cold-warm transitions vs. incision) has not been investigated yet, in contrast to other large rivers of European drainage system (Turner et al., 2013). Nevertheless, considering the broad dimension of the valley we tentatively attain the timing of the main valley formation to the coldest period of the Late Weichselian.

The remarkable valley asymmetry with a rather steep eastern and a very gentle, laterally undulating western slope and latitudinal differences in valley cross-sections (Fig. S1) are probably related to the combination of parameters such as tributaries, different microclimatic (palaeoenvironment) conditions, lithological differences at opposite flanks, and possibly, neo-tectonic and isostatic activity have been taking place in the southern North Sea (Marotta et al., 2000; Kiden et al., 2002; Reicherter et al., 2005). Although such parameters are difficult to

interpret as the onset phase is still unknown without reliable age and sedimentological information from the affected BU sediments, several processes may have influenced the shape is described shortly in the following:

The steep eastern flank in the northern EPV is most likely to be related with remnants of compressed and thrusted Pleistocene (Saalian or earlier) terminal-moraines at the eastern boundary of the EPV (Figge, 1983; Gehrmann et al., 2015), and this might have prevented valley widening. Indeed, boulder field, (Sylt Outer Reef) in the close vicinity to northern EPV associated with former moraines, is identified on the seafloor (Diesing and Schwarzer, 2006).

Regarding gentler western flank, tributary junctions at the western valley flank influence western valley flank and rim (Hepp et al., 2017) already identified one major tributary (associated to Ems river, Fig. 1a), which is located at 54° N in the southwestern part of the valley. In contrast to northern EPV, eastern flank on the most southern EPV, is not well-expressed and even situates in a level significantly lower than accompanying western flank there.

Besides, frost creep occurring due to frozen groundwater in the pore spaces of soil and sediments in permafrost areas might be responsible for erosion of the western flank (Fig. 6b) and creating solifluction terraces during late Pleistocene periglacial climatic conditions (Long and Stoker, 1986; Dixon, 2013).

Valley asymmetry presumably could be the result of differential crustal movements associated with composite tectonic and glacio (post-glacial) isostatic processes in the southern North Sea (Mörner, 1979; Kiden et al., 2002), as it is most likely that EPV coincide with the zone post glacial forebulge subsidence (Vink et al., 2007).

Drainage direction

Elbe River's course on the EPV appeared to have been determined by subsidence in the North Sea Basin, in fact in Northern Germany terminal moraines and ice-marginal valleys are in accord with NW–SE directed basement fault and morphological lineaments (Gibbard et al., 1988; Reicherter et al., 2005). Coinciding with that the mapped EPV base incisions (Fig.5) and the shape and inclination of the valley –at least until the eastern Dogger Bank (Figs. 4 and 8) –indicate a drainage direction towards NW. At the Dogger Bank region, two draining directions are possible: a westward drainage south of Dogger Bank or a northward drainage towards the Norwegian Channel. Assuming an ice barrier between the SIS and the BIIS to the north before 18 ka and considering SIS sourced signals in north-eastern Bay of Biscay sediments (Toucanne et al., 2015), the westward option would require either meltwater overflow over the western flank of the valley or a dedicated westward drainage pathway of the EPV south of Dogger Bank (Fig.3 and Fig.4 western extension). Based on the presented data no indications for a westward depressed

pathway could be found, in contrary the base of the western valley extension is dipping towards EPV (Fig. 7a) and is more likely related to a tributary system originating from Dogger Bank (Coles, 2000). Nevertheless, meltwater overflow events in presence of a northern ice barrier seem reasonable. However, further investigations, especially to the East and North-East of Dogger Bank are necessary to address the questions on the northern pathway of the EPV.

2.5.2 Valley infill

2.5.2.1 Incision infill – FU (Fluvioglacial, fluvial and estuarine)

As shown in chapter 4.2.2 unit FU, filling the EPV base incisions, has different internal structural configurations, partially in vertical direction, but also, changing between individual incisions. Although no samples are available from these deeper parts of FU, it is likely that these structures represent fluvioglacial or fluvial sediments with their prevailed prograded onlap fill pattern, based on sandy fluvial sediments revealed from a 51 m drill hole BH 89/8 located further north in the Danish sector (Konradi, 2000).

Acoustic blanking of the high frequency sediment echosounder data caused by high gas contents in the sediments masks deeper lying sediments at several areas in the innermost zones of northern EPV (Figs. 3, 5) making it especially difficult to investigate the properties of the incisions and FU there. Multichannel seismic data exhibit polarity reversals at these zones concentrated on the incision locations. Depending on the nature of the gas this might indicate a higher content of organic matter in unit FU considering that bacterial degradation of the organic matter is preserved on the base of valleys or buried depressions. Further studies and gas analyses are necessary, however, to address this shallow gas.

The upper part of the FU infill may represent the onset of marine transgression with a broadened cross section of the fluvial (or meltwater) channel, characterized by either acoustically transparent, chaotic facies or horizontal configuration in relatively low energy environment (Fig. 6b) according to the core GeoB17718-3. In this core, FU indicates medium sand with shell fragments bounded with a sharp contact above by clayey silt. This plant fragments of upper FU (at 43.8 mbsl) is dated to 10.8 cal ka, and based on the sea-level curve from Vink et al. (2007) sea-level was around 47 m lower than the present, both indicate that the EPV was an estuary at that time (Fig. 7). The first marine influence in hole BH 89/8, 200 km farther north of GeoB17718-3, at 17 mbsf (72 mbsl) was dated to 11.2 cal ka BP (Table 1 and Fig. 1).
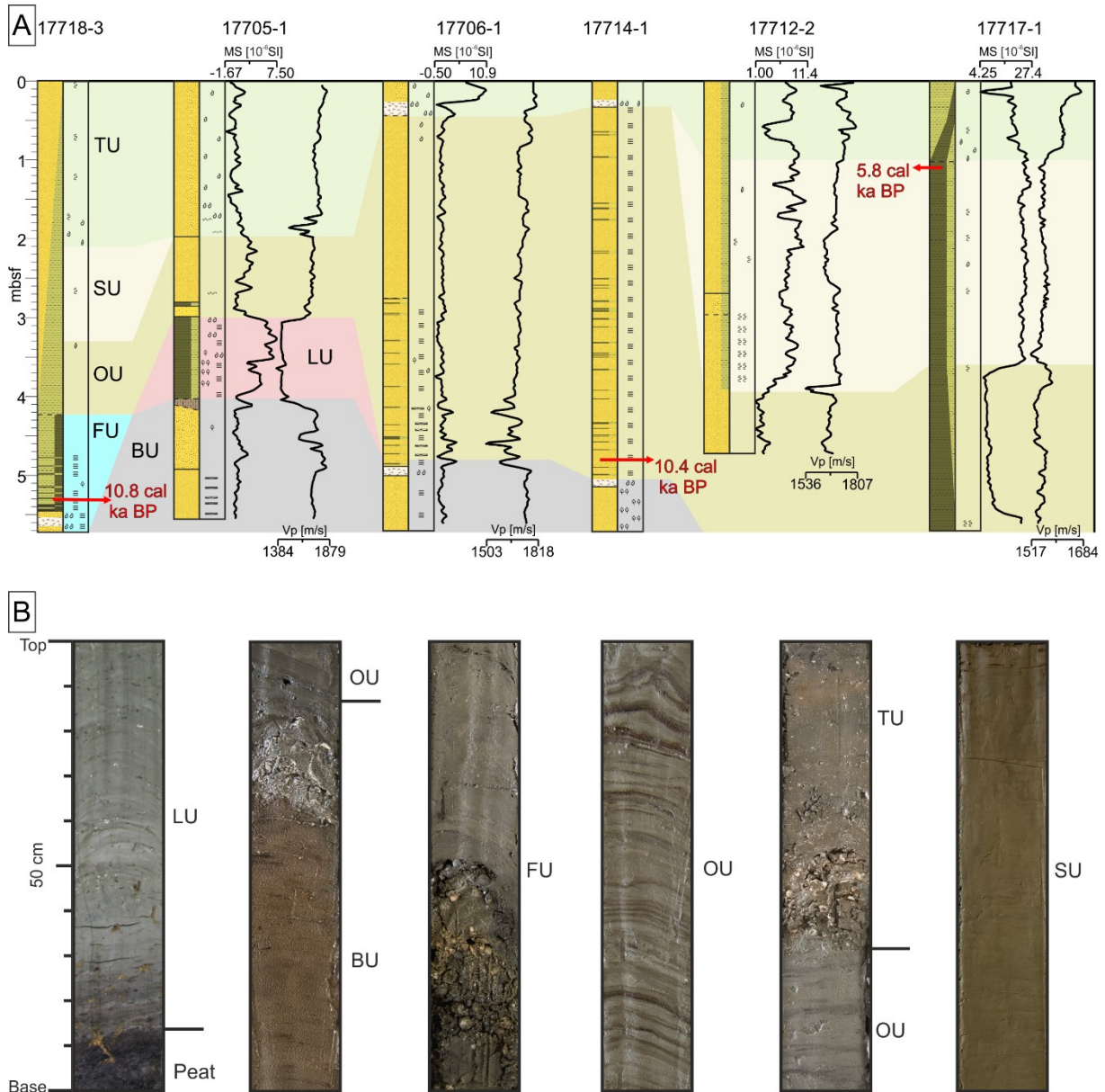
Figure 2.9 Acoustic unit correlation with MSCL logs, core description and the obtained ages **(A)**. The selected core locations are shown in Fig. 2.1 indicated as red-filled circles. For core legend see Fig. 2.4b. **B)** Core photographs from the main stratigraphic units: BU=Fine sand; lower FU=medium sand with agglomeration of shell fragments; upper FU=Clayey fine sand to clayey silt; LU=laminated silty clay with fragments of shell and gastropods; OU=Fine sand with alternating layers of clay; SU=Silty clay; TU=Fine sand with shell fragments.

2.5.2.2   Transparent lense-shaped unit – LU (Wetlands)

Peat is the major contributor for the understanding of Holocene coastal chronology of the southern North Sea under the decelerated rate the sea level rise, and basal peat has commonly used as a marker for the organization of terrestrial environment along with marine inundation in the northwest Europe (Shennan et al., 2000; Streif, 2004; Behre, 2007; Vink et al., 2007; Alappat et al., 2010). Organic rich peat is usually developed in wetlands, and typical wetland sediment sequences, that were formed along with the first marine influence, usually consist of peat, layers

of silt clay with sporadic lenses of sandy silt and mollusk and/or plant fragments, which overlies the sandy terrestrial surface (Alappat et al., 2010). Based on core FR07(35VC) in the western surroundings of EPV (Alappat et al., 2010), the lowermost part of the peat layers (below S1) are made up of Pleistocene fluvioglacial sands.

In the EPV, acoustic unit LU situating on the western rim and attached to the flank represents significant lower gamma density and p-wave values than surrounding sediments, suggesting the high organic content or presence of peat within this unit, as the presence of them can decrease the acoustic velocity ingestion of water (Missiaen et al., 2002; Silva and Brandes, 1998). Therefore, this acoustic signature of LU could indicate the preferable core sites for peat sampling regarding further studies, as there is a lack in sea level index data in the northern part of the study area (see Vink et al., 2007). As unit LU is characterized as a combination of peat, and silty clay, interpreted as freshwater marshes or brackish/lagoonal environment when EPV was an estuary. Based on the stratigraphic levels of LU and mapping (Fig. 7a), the sea level must have been around 41 m lower than the present level, when wetland systems prevailed in the palaeo-estuary.

In summary, based on the dating results and existing sea-level curve, including the section 5.2.1, the general environmental interpretation would therefore be: uppermost upper unit of FU represents subtidal zone; while LU along the western flanks represents intertidal zone that is exposed during low-tide and LU situated on the western rim (above flanks) represents supratidal zone (Fig. 10).

2.5.2.3 EPV's main infill: OU, SU, and TU (current controlled sedimentation)

The geometry of internal reflectors of the acoustic unit OU indicate that sediments for this unit transported towards the valley from its western side by two main mechanisms: either this unit is deposited via the tributaries of EPV or it represents a current controlled deposition after marine inundation of the western flank. The first scenario is based on the recent study by Hepp et al. (2017) who identified two tributaries (500–1500 m wide) of the EPV around the southeast of Dogger Bank and around the northwest of Ems river mouth, which are connected to the western margin of EPV. Although the similarity between clinoform geometry of OU and seismic expression of deltaic sedimentation and existence of occasional muddy interbed within overall sandy composition of OU, none of the cores correlating with OU appears to be of pure fluvial origin. In fact, considering possible drainage catchment area for each tributary (i.e. Ems and SE Dogger), it is unlikely that these two tributaries held a potential for the transport of approximately 28812×10^6 m^3 riverine sediment that would be deposited over a minimum 120 km long western flank and built up an extensive deltaic clinoform. This would bring another question about the existence of undiscovered tributaries at the western flank, preferably closer to the main depocenter of OU (Fig. 7) around Oyster Ground. However, internal reflectors of OU are

isochronous along the valley axis (Fig. 3) and any evidence for deltaic fans do not exist in our extensive data set. But also, peats (basal) are found on the western rim of the valley (Table 1) within unit LU that underlies unit OU, meaning that western part of the valley (i.e. including Oyster Ground) must have been already flooded during the early Holocene.

Considering the reasons above, tributary feeder system is rejected for being responsible of bulk of the EPV infill, and it is most likely that unit OU deposited after the drowning of previous estuarine environment. Regarding this second scenario, eroded sediments of postglacial fluvial channels around Dogger Bank area (Fitch et al., 2005; Alappat et al., 2010) or speculated freshwater lake around Oyster Ground during Younger Dryas (Ludwig et al., 1981; Köhn, 1991) might have been the sediment supplier for the EPV, which are transported towards the valley under the current control.

The dating of plant fragments from the base of unit OU reveals an age of 10.4 cal ka BP, however this age seems to be older than expected as the age of peat sample (Fig. 9) from LU is 10 cal ka, which is in agreement with other ages revealed from peat samples in Table 1. and the age revealed from upper part of FU onto which unit LU downlaps is 10.8 cal ka. Therefore, dated plant fragments must have been the reworked sample, possibly from wetlands on the western rim. Considering this, we propose that deposition of OU initiated not before 10 cal ka BP when the sea level was up to 41 m lower than present. In order to establish enough accommodation space to deposit unit OU, a rise of 7 m in the sea level would have been necessary, taking into account that southernmost cross section valley infill is absent from the unit OU. In this southernmost part sea level was probably not able to rise above the flank that was at ~ 34 mbsl (between 9.5–8.8 cal ka BP; Vink et al., 2007). Therefore, the environment in the southern North Sea must have been very shallow marine during deposition of OU (Fig. 10) with connection to the northern North Sea via Outer Silver Pit and EPV while Dogger Bank was an island. Thus, initiation of OU deposition must have been dependent on the marine flooding of Oyster Ground region, meaning also that Dogger Bank must have already been isolated.

Palaeotidal modelling study indicate the micro-tidal conditions prevailed during this interval as there was a propagation of progressive and damped wave from Outer Silver Pit towards east (van der Molen and Swart, 2001a). An eastward transport and decreasing trend is perfectly reflected in the geometry of unit OU. However, the significant amount of sediment deposited in the valley is likely suggest the contribution of waves (by stirring up the sand) and wind-driven currents (by advection) in this shallow environment during Early Holocene, which is most probably depicted in cores by clay interbeds (e.g. GeoB17714-1).
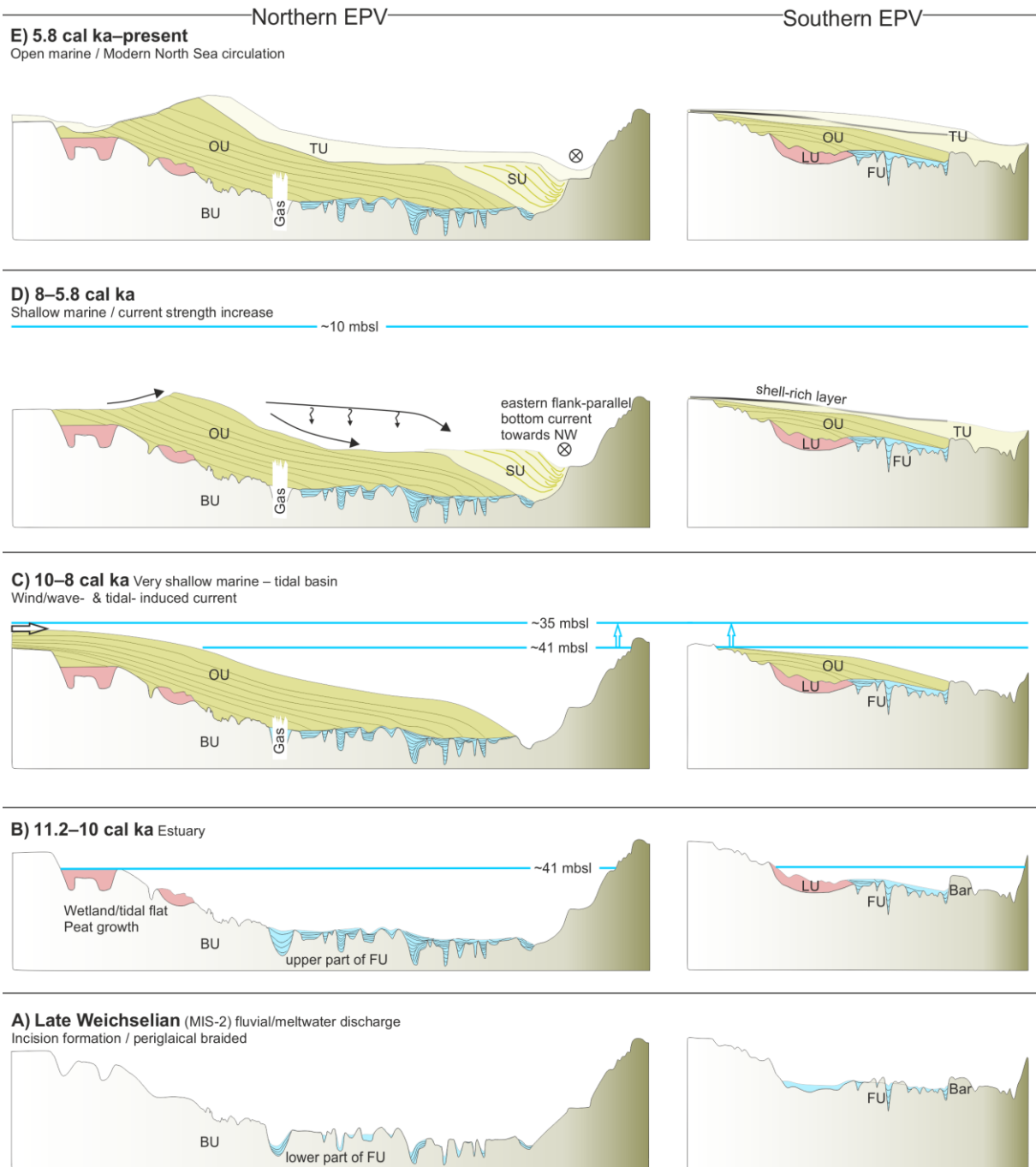
Figure 2.10 Conceptual evolutionary model of EPV from subaerial shelf exposure and incision formation during Late Weichselian glacial **(A)**, the first marine influence in the valley and sea-level controlled peat growth **(B)**, submergence of valley flanks during the Early Holocene sea-level rise main valley infill OU tidal transport aided by wave suspension **(C)**, truncation of OU and deposition of SU beneath the wave-base level **(D)**, decelerated sea-level rise during mid-Holocene and deposition of modern North Sea sands **(E)**.

After a sea-level of ~–34 m reached, tidal energy might have been brought in this shallow environment by Atlantic Water inflow from the Dover Strait leading to an increase in the tidal current strength, thereby tide-induced shear strength was increased. According to Lambeck (1995) the connection of the Dover Strait to the present North Sea was established between 9–7.7 cal ka BP.

In the northern EPV, this new hydrodynamic system probably resulted in the erosion/non-deposition of unit OU, thereby not allowing more sediment to avalanche above OU around the western flank. Accordingly, sediment supply for unit SU was probably mainly sourced from truncation of OU, as the truncated zone of unit OU coincides with the unit SU deposition in the northern EPV (Fig. 7e, S1). This truncation zone indicates the presence of persistent current even in modern conditions, which results in very thin accumulation or absence of uppermost unit.

The units above OU is characterized by a relative increase in magnetic susceptibility. Such increase is likely point to the increased terrigenous material contribution (e.g. rivers of Southern North Sea and/or East Anglian Plume and increased coastal erosion).

The last prominent change in the southern North Sea after Dover Strait connection is represented in unit TU which indicates an increase in grain size, the amount of shell fragments, shell-hash layer, and also, based on foraminiferal assemblages, represent fully marine conditions (Konradi, 2000). According to the age obtained from the top of unit SU, this change must have been younger than 5.8 cal ka BP, when sea level was up to 10 m lower than present and the rate in sea level rise was already decelerated (Vink et al., 2007) may have been related to offset in the influence of complete drowning of Dogger Bank – as final drowning of Dogger Bank island was proposed to be around 8.2 cal ka BP (Weninger et al., 2008; Ward et al., 2006).

2.6   Conclusion

The sediment echosounder and high-resolution seismic data along with groundtruthing by sediment cores brought new insights into the palaeo-landscape/environment of southeastern North Sea and its drainage network via Elbe Palaeovalley (EPV) in terms of drainage pathway, valley infill geometries and controlling parameters. The base of EPV was traced in detail and infill pattern of late Weichselian/Holocene sediments accumulated in the southeastern North Sea identified by means of seismic stratigraphy with the correlation of sedimentary facies for the first time with this study since the Elbe Palaeovalley in the North Sea was introduced by Figge (1980).

• 	The EPV represents a braided system with several palaeochannels/incisions are likely represent erosional landscape associated with the MIS 2 sea-level fall and lowstand when the southern North Sea was a subaerial exposed shelf. According to valley morphology and traced incisions at valley base in pseudo-3D area, palaeo-drainage trends towards northwest. Moreover, valley has an asymmetrical cross-section with its seep eastern and gentle western flank in the northern part; while eastern flank is not well-expressed in the southern part. Possible factors such as tributary junctions, different microclimatic (palaeoenvironment) conditions, lithological differences at opposite flanks, former moraines and possibly, neo-tectonic and isostatic activity in the southern North Sea could be behind for its morphology.

- Valley was invaded by the sea earlier than the surrounding shelf of the southern North Sea, and when valley became an estuary, a tidal wetland environment, especially along the western flank, prevailed. In the estuarine setting, salty water incursion probably created the tidal scour adjacent to eastern valley flank.

- The lowermost part of incision infill, interpreted as river/meltwater carried sediments, while the uppermost incision infill represents estuarine sediments dated to 10.8 cal ka BP.

- After drowning of the estuary in the early Holocene, EPV was the main sedimentary trap in the North Sea (excluding Norwegian Channel). Three stages are defined for the development of infill under the control of sea level rise and accordingly changing hydrodynamic regime. First stage was characterized by a shallow basin constricted by Dogger Bank island until the sea level reached a level of 34 m below the present. The bulk of the EPV infill was already established during this stage by the eastward advection of sediment. Tidal currents aided by wind waves during early Holocene were responsible for the resuspension of the sediments, possibly around Oyster Ground, which later filled bulk of the valley as it acted as a current shed zone.

- During the second stage, the increase in tidal current, possibly after 8 cal ka BP with full connection to the English Channel, indicated by erosion/non-deposition zone at the most western side of the valley but filling of the remaining accommodation space of the valley under the bottom current control until 5.8 cal ka.

- Around 5.8 cal ka current strength was increased coinciding with decelerated rate of sea-level rise, and fully marine conditions established.

- The EPV still partly controls the sediment transport in the southeastern North Sea.

This work is a further contribution to the development for future long-term shoreline change studies since a future scenario for the coastal drowning of the German coast is hypothesized to be taken place around the coastal continuation of Elbe River, but also for testing of modelling studies (e.g. palaeo-shoreline, -sea level, -tidal conditions in the NW European shelf). On the other hand, the results would be of interest to archaeologists and geomorphologists, particularly working in the prehistoric drowned landscapes. Nevertheless, the exact timing of Late Weichselian incision and sedimentary structures underlying the valley base are still remained to be resolved due to the limited penetration depth (maximum 6 m in this study) of coring methods. But also, further multidisciplinary chronological studies (e.g. 14C-dating and/or OSL-dating), biostratigraphy analysis (e.g. pollen and ostracods), sediment provenance analysis are necessary on the way to establish the robust chronological framework for which this study could be used as a groundwork. Finally, in order to fully understand the evolution of EPV, particularly its northern extension, and its interaction with the North Sea ice-sheet (e.g. if it affects the North Sea ice-sheet stability or

even development) further studies in the Oyster Ground and in the eastern/northeastern Dogger Bank are recommended.

Acknowledgements

3 The pathway of Elbe Palaeovalley and late Quaternary sedimentary succession in the eastern North Sea

Aslı Özmaral[a,b], Hanno Keil[b], Tilmann Schwenk[b], Daniel A. Hepp[a], Volkhard Spiess[b]

[a]MARUM—Center for Marine Environmental Sciences, University of Bremen, D-28359 Bremen, Germany

[b]Faculty of Geosciences, University of Bremen, D-28359 Bremen, Germany

Abstract

During the last glacial period, Elbe Palaeovalley was the major drainage path in the southeastern North Sea regulating the meltwater and river drainage from the North European Plain to the outer North Sea. Although valley's northwestward path defined in the German sector of the North Sea from previous studies, the northern continuation is still a question mark. The uncertain position of the southern margin of the British-Irish and Scandinavian Ice Sheet (SIS) in the North Sea during the late Weichselian adds further uncertainties regarding its northward path such as blockage by the coalesced ice sheets along Dogger Bank.

According to first results based on the sediment echosounder and multichannel seismic data, Elbe Palaeovalley had encountered a sudden gradient change near the eastern Dogger Bank, which is interpreted to be reflecting the southern margin of the North Sea ice sheets during late Weichselian together with moraine ridges flanking the valley. These moraine ridges probably represent an extension of the SIS from the western Denmark towards Dogger Bank. Furthermore, around 26 m thick stiff clay succession found in the southeastern Dogger Bank, most likely indicates glaciogenic sediments of the previously speculated ice-dammed lake related to the fluctuating ice margin along Dogger Bank. Hence, this lake provides a further evidence for SIS sourced meltwater found in the Bay of Biscay between 23–19 ka BP. As the northern ice blockage of the Elbe Palaeovalley near the eastern Dogger Bank was destroyed around 18.5 ka BP, East Dogger Deep as a northwestward continuation of Elbe Palaeovalley, transferred meltwater towards Norwegian Channel. After the abrupt change of East Dogger Bank, Elbe Palaeovalley endured its main path towards northerly latitudes with less incisions developed at its base compared to its upstream part in the German Bight.

With the subsequent Late Pleistocene–Early Holocene sea level rise, successive depocenters established within the Elbe Palaeovalley, reflects the evolving hydrodynamic regime in tide- and wave-dominated environment until present under the control of valley morphology. The succession in the first phase is composed of the estuarine sediments including fluvial input, particularly from eastern Dogger Bank. The second phase represents shallow marine environment controlled by tidal currents when the Atlantic Water entrance through Outer Silver Pit left the Dogger Bank as an island. The third phase (ca 8.5 cal ka) starts with the arrival of Atlantic Water via English Channel. After this phase, increased strength of currents (tidal and wind-driven) distributed deposition mainly on the eastern valley and towards the southeastern Dogger Bank over which winds from west overwhelms the sediment transport and deposition takes place close to the present day tidal amphidromic point.

3.1   Introduction

Continental shelves, particularly those of shallow ones, are subject to interplay between glacial, marine and terrestrial environments, thereby yielding archives of palaeoenvironmental change (Fitch et al., 2005; Hijma et al., 2012; Müther et al., 2012; Mellett et al., 2013). The eastern North Sea shelf is a key region, especially for the interval between Late Weichselian–Holocene, in understanding of the drainage systems, and their relation with ice sheets and relative sea level. In this climatically controlled setting, the prominent feature Dogger Bank situates, two ice sheets had met and Elbe Palaeovalley found its route from the present day German coast. In the North German lowland, the valley of the lower Elbe was assumed to be originated when urstromtal (glacial spillway) was formed during Weichsel glaciation. The urstromtal drained meltwater from the Weichselian ice margins in the north together with other eastern urstromtals towards North Sea (Hagedorn, 1989). Including the subglacial drainage of southern part of SIS, the urstromtal network had a huge catchment area (ca. 1 5x10^{5}km^2) that is expected to have contributed to the offshore sedimentation in the North Sea (Westaway and Bridgland, 2010).

The drainage of river systems in the North German Lowland to the North Sea is determined by northwesterly alignment of these Pleistocene urstromtals (Hagedorn, 1989). Previous study by Özmaral et al (in prep) Weichselian Elbe Palaeovalley and related incisions at the base and its post glacial infill were mapped in the southeastern North Sea, however, the continuation of the valley towards central North Sea remained unclear.

The most recent agreed set-up of the Late Weichselian ice sheets in the North Sea is the confluence of British-Irish Ice Sheet (BIIS) and Scandinavian Ice Sheet (SIS) that had been possibly terminated around the Dogger Bank (Sejrup et al., 2000; Svendsen et al., 2004; Clark et al., 2012a; Hughes et al., 2016; Sejrup et al., 2016). Dogger Bank as prominent feature in the North Sea, represents a large moraine belt stretching W–E along with the Main Stationary Line in Denmark (Cameron et al., 1993; Carr et al., 2006). Therefore, its depositional environment proposed to be an ice marginal surrounded by BIIS and SIS (Carr et al., 2006). Regarding these two ice sheets, especially the advance and retreat of their southern margins, there are probably way more speculations on their chronology, interaction and dynamics than the data available. Several reconstructions (around fifteen scenarios) concerning their maximum extent in the North Sea was compiled by (Laban, 1995).

Quaternary studies in the eastern central North Sea have mainly focused on either coastal zone of the Danish North Sea or offshore local tunnel valley formations of Pleistocene epoch owing to the data collected mostly for oil and gas reserve investigations such as boreholes, 2D and 3D seismic, which is also a case for the southeastern North Sea. As there is the lack in very high resolution seismic and sediment echosounder profiles, core material, and inconsistency between available

dating samples, Late Weichselian ice sheet history in the central (and partly southern) North Sea largely remains uncertain and seems to be challenging to solve (e.g. Patton et al., 2016).

Just recently, Sejrup et al. (2016) classified and mapped glacial landforms belonging to last glacial period that were unknown up to know in the central and northern North Sea by combining high-resolution bathymetry, sub-bottom profiles, previous information on the chronology from cores (both onshore and offshore) and embedding prominent earlier reconstructions into their results. Although these datasets were mostly accumulated on the northern North Sea and Norwegian Channel, the outcome of their study points to the previously underestimated occupation of Late Weichselian ice sheets and their highly complex interaction in the North Sea (Sejrup et al., 2016).

The coalesced SIS and BIIS must have blocked northwestward drainage course of Elbe system and redirected its drainage towards southwest as proposed by Toucanne et al. (2010). The blocked drainage of the Elbe over the central North Sea together with drainage from other northwest European rivers (i.e. Rhine, Thames, Maas, Seine and Solent) led to enormous sediment laden meltwater discharge to the Bay of Biscay via overspill of potential ice-dammed like in the southern margin of the ice sheet between 21–18 ka (Ménot et al., 2006; Gupta et al., 2007; Toucanne et al., 2009a; Toucanne et al., 2010; Plaza-Morlote et al., 2017). Following the unzipping and collapse of BIIS and SIS, proposed ice-dammed lake discharged along a northwesterly line towards Norwegian Channel which assumed to be coincide with freshwater input obtained at the mouth of the Norwegian Channel dating to 18.6 ka (Lekens et al., 2005; Sejrup et al., 2016). These discharge events must have been contributed to the destabilization of oceanic circulation (e.g. Clark et al., 2004a; Roche et al., 2010; Toucanne et al., 2010) as Atlantic Meridional Oceanic Circulation was susceptible to freshwater perturbations originating from western European margin (i.e. Fennoscandian Ice Sheet Margin and Channel River Outlet). Therefore, European Ice Sheet margin played a crucial role affecting the global climate system (Toucanne et al., 2015). Thus, the transport of freshwater–possibly in a catastrophic manner– related to ice-dammed lakes (besides to ice streams) may provide insight on the abrupt historical changes in thermohaline circulation (Sejrup et al., 1998).

Following the deglaciation, southern North Sea and shallower parts of the central North Sea were exposed to subaerial conditions together with rivers, lagoons, salt marshes (e.g. Elbe Palaeovalley, Doggerland); while the deeper parts (i.e. northern North Sea and Norwegian Channel) were mainly controlled by glaciomarine mud deposition in subglacial palaeovalleys (e.g. Cameron et al., 1993; Coles, 2000; Gaffney et al., 2007; Stoker et al., 2011). With the onset of the Holocene sea level rise, this periglacial landscape was re-organized under the evolving hydrodynamic regime (Özmaral et al., in prep). Herein we present sediment echosounder and very high resolution multi-channel seismic data together with some vibrocores depicting the landscape in the eastern central

North Sea (German, Danish and southernmost Norwegian sector) as a follow-up for the outcomes of Özmaral et al (in prep.). The objectives, therefore, are (1) to follow pathway of Elbe Palaeovalley and investigate the continuation (or absence) of incisions (2) to contribute to the recent knowledge on ice sheet positions by integrating Elbe Palaeovalley into recent findings (3) elucidate the Late Weichselian glacial and post glacial sedimentary environments, especially the link between current-induced bedforms and palaeoceanographic conditions and landforms. This study, therefore, provides a first overview using the high-resolution imaging of the sediments in the eastern North Sea.
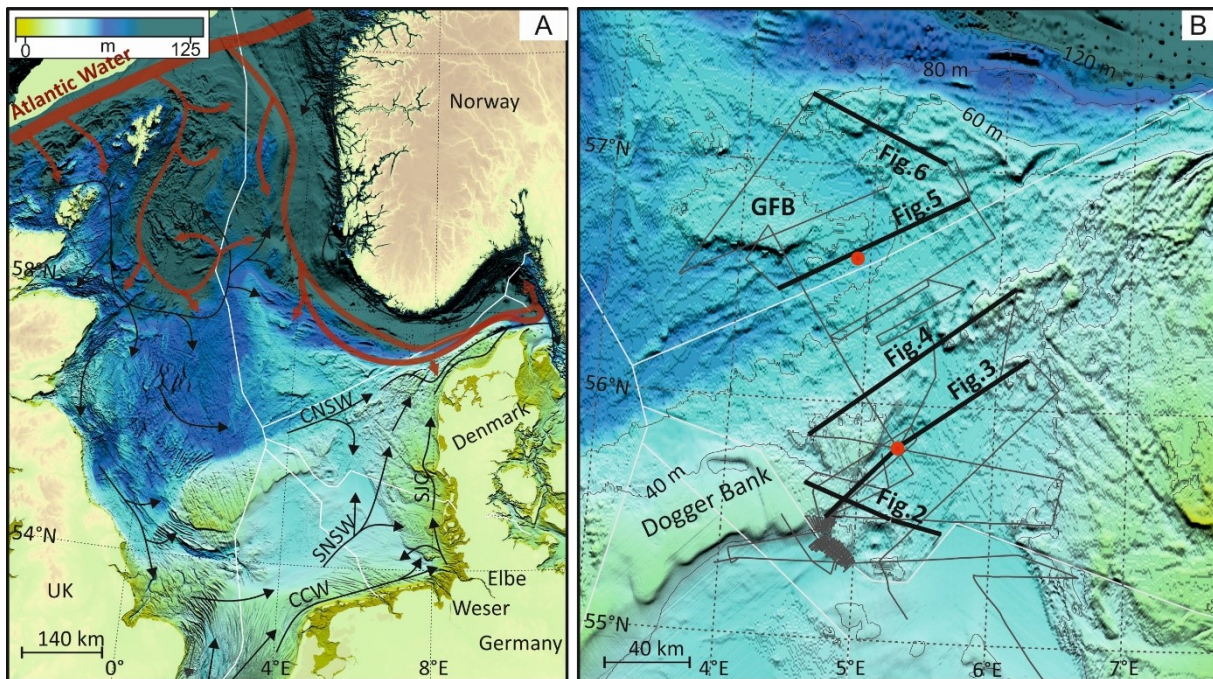
Figure 3.1 Bathymetry from EMODnet and general North Sea circulation (arrows) of the North Sea from Longva and Thorsnes (1997) and Gyllencreutz and Kissel (2006) b) Data collected during cruise HE463 (grey lines). Contour interval is every 20 m. Red circles indicate the chronological constrains by previous studies referred in the text. GFB: Great Fisher Bank, SNSW: Southern North Sea Water, CNSW: Central North Sea Water, SJC: South Jutland Current, CCW: Continental Coastal Water.

3.2   Regional setting

Study area extends between 55°00′–57°30′N latitude and 3°–7°E longitude in water depths ranging between 30 and 70 m in the eastern North Sea (Fig. 3.1). The connection to the Atlantic Ocean occurs via English Channel in the south, while in the north there is an open connection to the Norwegian Sea with a shelf break around 200 m water depth. The Dogger Bank with minimum water depth of around 20 m somewhat separates southern North Sea (water depths of around 40–50 m) from the Central North Sea. Besides to Dogger Bank, another prominent morphologic feature in the North Sea is the Norwegian Channel stretching parallel to the Norwegian coast with depths of more than 400 m and even more in Skagerrak region with depths around 750 m (Eisma and Kalf, 1987; Otto et al., 1990).

65

The general circulation in the North Sea is a basin-wide anticlockwise circulation driven by in and outflows and interaction with the bottom topography. The prevalent propagation of Atlantic Water into the North Sea occurs at the north and it exhibits seasonal variation (i.e. maximum inflow occurs during winter months) (Nauw et al., 2015). Around 58°N, the south flowing Fair Isle Current splits into two branches; one flows eastwards following the 100 m bathymetric contour and the other branch continues propagating southwards following the east coast of Great Britain serving for the Central North Sea Water (CNSW) and Southern North Sea Water (SNSW). CNSW is mixed with Scottish coastal water which transported eastwards along the north of Dogger Bank due its positive relief (Danielssen et al., 1997). In the southern North Sea, the Atlantic Water inflows via the English Channel. The Channel Water is responsible for Continental Coastal Water (CCW) and SNSW, and their mixing together with main riverine runoff from the southern coast (i.e. Elbe, Rhine, Weser and Ems) produce the Jutland Coastal Water (JCW) flowing northwards along the western Denmark parallel with the SNSW, thereby gradually increases its salinity by horizontal mixing. The JCW mixes then with the inflow of Atlantic Water and Baltic Water in the Skagerrak where the main northerly outflow occurs along the western Norwegian coast (Danielssen et al., 1997). Overall, tidal motion along with the westerly winds and baroclinic effects cause the overall anticlockwise circulation pattern, and horizontal and vertical mixing of water masses. However, during summer the waters are stratified except for the mixed shallower parts (for a detailed physical oceanography review see Otto et al., 1990).

North Sea, has been existent since late Cretaceous as a result of series of rifting episodes. As an epicontinental basin during Cenozoic, it was restricted by land-masses of Scandinavia, the British Isles and Central Europe linked to the Norwegian-Greeland Sea via narrow seaway (Ziegler, 1988). Cenozoic succession is underlain by Mesozoic Central Graben and Paleozoic Ringkøbing-Fyn High –as an intra-basinal barrier controlling the depositional pattern– in the central and eastern North Sea and was affected by salt diapirs beneath (Sørensen and Michelsen, 1995; Clausen et al., 1999; Huuse et al., 2001). Progressive pro-deltaic and deltaic sediments of Baltic River system filled the basin from Oligocene to mid-Pleistocene (Huuse et al., 2001). The general Pleistocene stratigraphic succession can be subdivided as deltaic and marine dominated environment during the early Pleistocene, and glaciogenic configuration from Mid-Pleistocene to Holocene. The separation between them is a glacial unconformity associated with widespread network of subglacial tunnel valleys (Stewart and Lonergan, 2011; Stoker et al., 2011; see Huuse and Lykke-Andersen, 2000; Graham et al., 2011 for a tunnel valley review in the North Sea) whose advance and retreat dynamics resulted in several generations of subglacial tunnel valleys (Kristensen et al., 2007; Andersen et al., 2012).

Terrestrial evidence from the northern central Europe revealed three major glaciations; Elsterian, Saalian and Weichselian (e.g. Ehlers and Wingfield, 1991; Ehlers, 2011; Houmark-Nielsen et al., 2012). Most of the northern Europe and the North Sea was occupied by Elster and Saale glaciations (Long et al., 1988; Ehlers, 2011). While Elsterian and Saalian ice sheets period covered the study area, Weichselian maximum limit is undetermined due to the lack of evidence –such as ages of glaciogenic deposits as well as difficulties in combining dates from North Sea, UK and Denmark (Sejrup et al., 2016). Weichselian maximum regarding the southern extent in the North Sea is simply assumed as a line that links the Skipsea Till in eastern England to the main stationary line of Denmark, which coincides with the south of Dogger Bank meaning that most part of our study area might have been covered by ice until the final disintegration of BIIS and SIS around ca. 18.5 ka (Houmark-Nielsen and Kjaer, 2003; Clark et al., 2012a; Sejrup et al., 2016). SIS and BIIS connection during Weichselian was proposed earlier by Valentin (1957b), Sejrup et al. (1998) based on inferred Weichselian age for the subglacial valleys.

3.3   Methods

Parametric sediment echosounder (SES-2000), high-frequency multi-channel seismic data and sediment cores were acquired during HE463 expedition of RV Heincke on Danish, Dutch and Norwegian sectors of the central North Sea in 2016 as a follow-up cruise of HE405 that took place in 2013. The survey occupies an area of around 58000 km² around the east side of the Dogger Bank with profile spacing around not more than 35 km. The sub-bottom profiler, hull-mounted on RV Heincke, provided satisfactory and detailed structural illustrations for relatively softer Late Weichselian/Holocene sediments (e.g. muddy sands) in the central North Sea, however penetration is usually constrained in the case of compact sediments (e.g. glacial diamictons–till), therefore for deeper information multi-channel data were used for the interpretation.

As conventional multichannel seismic systems (MCS) mainly aim at deep penetration with low frequencies (2–100 Hz), custom developed Bremen multi-channel seismic system, which is suitable for shallow marine environments, was utilized during the cruise. The system consists of digital streamer with 96 channels, each of which contains only one hydrophone along with mini generator-injector (GI) air gun. Seismic processing was performed with software VISTA. After binning with 1 m and trace editing, a band pass filter was applied. Velocity analysis was performed, and subsequently, normal-move-out (NMO) and spherical divergence correction were carried out. Finally, the finite difference time migration was executed on the stacked sections.

The interpretation of acoustic units was mainly based on echosunder profiles depending on their variations in the reflectivity, internal reflection and external geometries. In case of the penetration limitation or signal hampering, the interpretation benefited from the multichannel seismic data

although data coverage was less than sub-bottom profiling (e.g. around 50 km distance between two adjacent tracks) due to time constraints. The depth conversion is performed with the p-wave velocity of 1500 ms^{-1}. The mapping of basal surfaces and thickness calculations were conducted with Kingdom Suite (IHS) software.

As a supplemental for uppermost sedimentary layers, vibrocores were acquired. Vibrocoring is approved to be the most appropriate sampling device for over-consolidated and surficial North Sea sands compared to gravity coring. The core penetration was limited to 6 m with the vibrocorer, therefore, coring sites were chosen carefully under the control of echosounder profiling.

Bathymetric data were obtained from the European Marine Observation and Data Network portal for bathymetry (EMODnet) which is compiled from best available data sources together with GEBCO 2014 data in the case of data gaps. Danish sector coincides with the area where GEBCO data is used (Fig. 3.1).

3.4   Results

The base of the Elbe Palaeovalley was mapped based on both sediment echosunder and MCS. Four main acoustic units based on sediment echosounder data were identified depending on their reflection strength, geometry, lateral continuity and reflector terminations. Example sections inholding the complete unit succession are presented in Figs. 3.2 and 3.3. We first describe the morphology of the valley then the depositional units in the following sub-sections.

3.4.1 Elbe Palaeovalley

The base of the Elbe Palaeovalley defined by the previous study (Özmaral et al., in prep) in the German sector, and herein, the base is followed along Danish and Norwegian sectors of the North Sea. In general, the prominent differences regarding valley transversal sections compared to German sector were scarcity of both incisions at the base and well-pronounced valley flanks.

Elbe Palaeovalley morphology in Danish and Norwegian sectors can be split up as three zones taking the Dogger Bank as a reference. Around southeastern part of the Dogger Bank (until latitude ca. 55°40′N), the valley reaches a width of around 50 km. The base is partly obscured by acoustic blanking zone as this was already observed in the north of latitude 55°N in the German sector; however, according to seismic sections, base of valley is situated around 0.085 s (ca. 64 meter below sea level–mbsl).
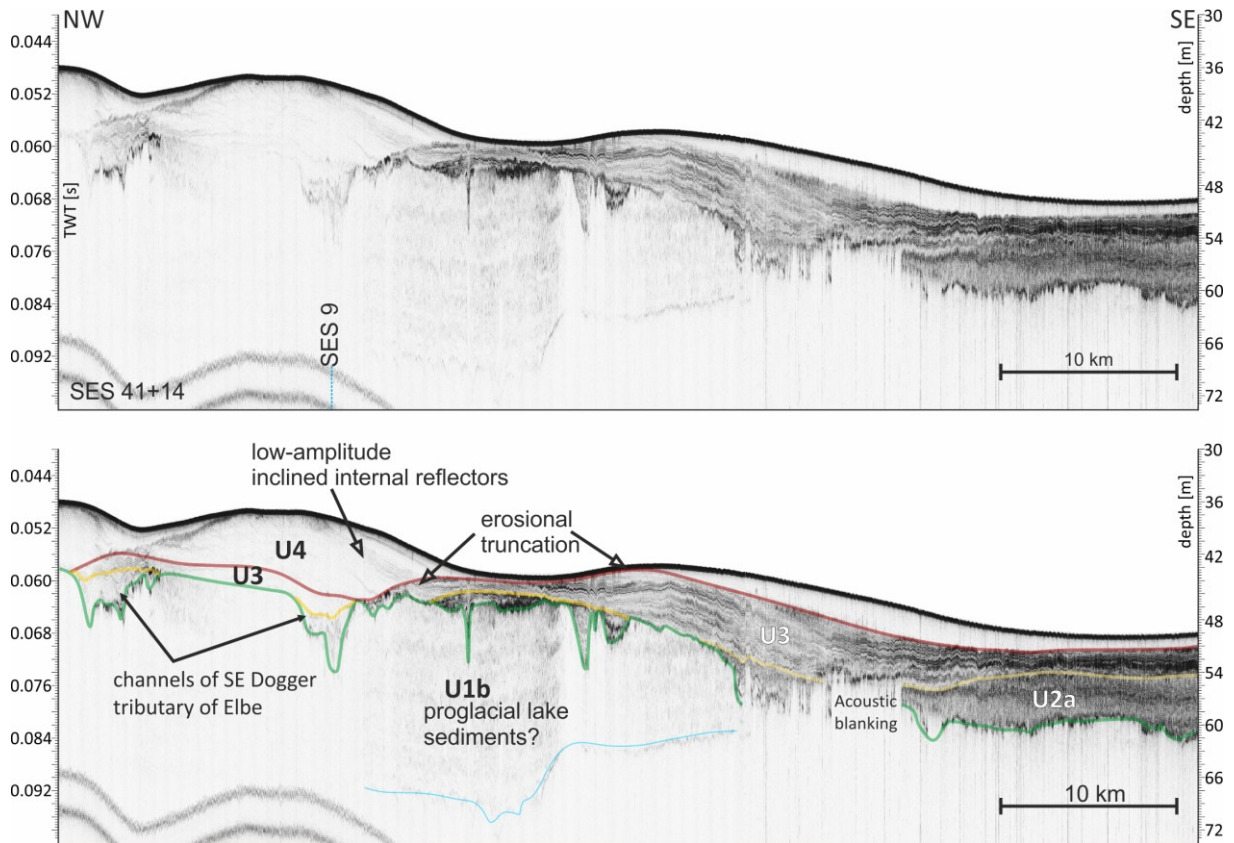
Figure 3.2 NW–SE Echosounder profile (SES41+14) showing acoustic units defined. Profile locations are shown in Fig. 2.1.

Around eastern Dogger Bank (until latitude ca. 56°30′N), the most prominent changes were observed (Figs. 3.3 and 3.4). Here, the valley deviates from more or less uniform shape and it is characterized by the diversity in relief. The smaller and V-shaped incisions –as in the German sector– are not observed in this sector; instead positive relief of around 5 km wide and around 12 m high comprises valley base (Fig. 3.3). The depth of base of the valley ranges between 0.092 s (ca. 70 mbsl) and 0.112 s (ca. 84 mbsl). On its western shoulder around 40 km wide area shows several incisions up to 9 m deep and 2 km wide. Towards western Danish coast valley base gets shallower (0.076 s) and eastern flank is not well-developed here. Right near the eastern end of the Dogger Bank the valley becomes narrower down to 20 km, but also prominent and abrupt change in its depth (0.112 s) was observed (Fig. 3.4). Both valley flanks herein are characterized by relatively higher gradient of around 15 m/km (compared to southern adjacent transverse section whose western flank is around 1.5 m/km). Further away from north of Dogger Bank, the valley seems to be split into branches; 20 km wide depressions with two or three incisions reaching 0.096 s (ca. 72 mbsl). Either these branches merge in the northward direction or one branch follows a westerly direction through a 5 km wide channel following the south of Great Fisher Bank. Here, unfortunately our survey outline (between 0°E –2°E) precludes further certainty. However, after that point (north of 56°N), in the adjacent northwards transverse lines in the Norwegian

sector, a 40-km wide depression with occasional incisions again down to 0.096 s was recognized (Fig. 3.5). The most northern profiles are located around eastern Great Fisher Bank and close to the southern side of the Norwegian Channel. The valley continues in the 30 km wide depression near the eastern side of the Great Fisher Bank with the base reaching 0.090 s. On the line, parallel to the southern flank of the Norwegian Channel, we observed two valleys at depths 0.088 s (ca. 65 m) and 0.092 s (ca. 70 m) with a width of around 5 km (Fig. 3.6).
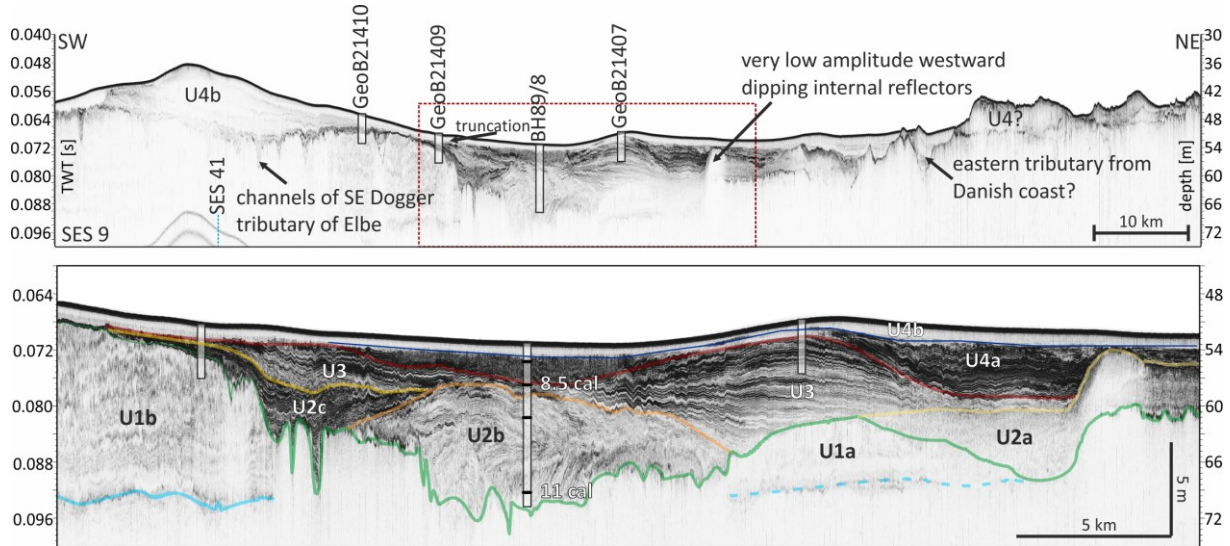
Figure 3.3 SW–NE echosounder profile (SES 9) transverse to the Elbe Palaeovalleytogether with the vibrocores collected during HE463 and the well BH89/8 with datings from Konradi (2000).

3.4.2 Depositional units

Acoustic units are described from bottom to top with an increasing order of numbers. The acoustic unit descriptions are summarized in Table 3.1. Mapping of units are presented in Figs. 3.7c, 3.8a, 3.8b, and 3.8c.

3.4.2.1 Unit 1

Unit 1a has transparent acoustic facies and represents steeply dipping positive relief either at the base of the valley thereby being buried by overlying valley infill or flanking the valley by outcropping on the seafloor, on the eastern side of the Elbe Palaeovalley (Fig. 3.4). In cross section the width changes between 2 and 10 km. Their height reaches up to 18 m above the adjacent seafloor and 36 m above the adjacent base of Elbe Palaeovalley. The crests are located at present day seafloor between 39 and 42 m.

Unit 1b consists of very gently undulating subparallel internal reflector configuration with low amplitude. Its continuity is restricted to signal penetration related to the overlying units. The base of this unit is an undulating surface. Its top truncated by incisions that are situated on the western side of Elbe Palaeovalley, around southeast Dogger Bank (Figs. 3.2 and 3.3). The thickness reaches

up to 26 m. It is only found north of 55°N and its western extent is limited to our survey outline. The eastern extent seems to be constricted by Elbe Palaeovalley as it was not possible further mapping of this unit towards western Danish coast (Fig. 3.7c). A correlation with vibrocores shows stiff clay.
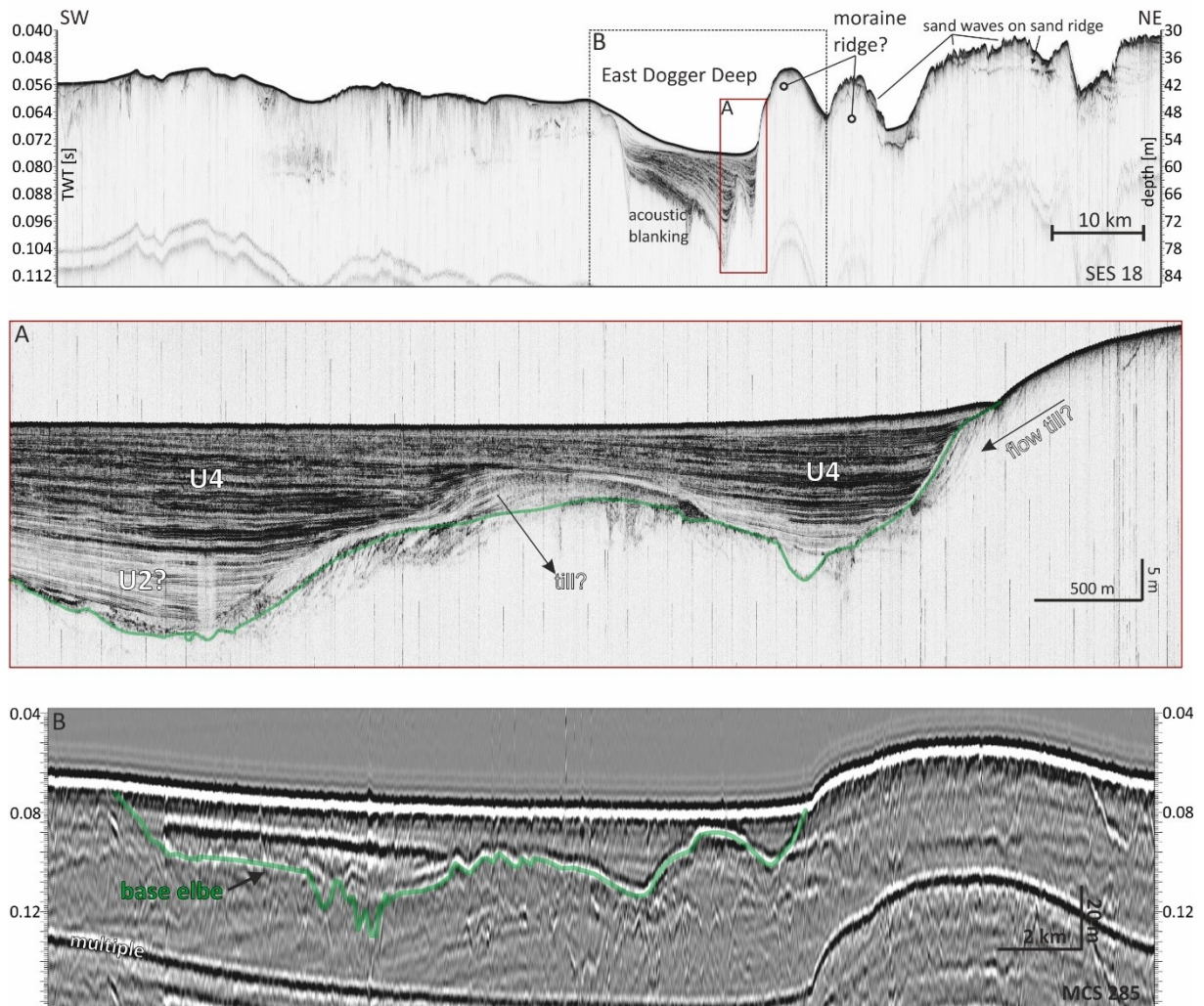
Figure 3.4 SW–NE Echosounder profile (SES 18) from the East Dogger Deep. A) Close-up of SES profile. B) Close-up from accompanying MCS line showing the base of the valley that is hampered by acoustic blanking in the SES line.

3.4.2.2 Depositional units within the Elbe Palaeovalley

Unit 2

Unit 2 (U2) characterizes the lowest infill of Elbe Palaeovalley found at water depths not shallower than 0.070 s twt (ca. 52 m). It is both confined to the valley borders, and incision infills on the western Elbe Palaeovalley. Several subunits are observed within Unit 2 (Figs. 3.3 and 3.8a). The subunit lettering here may not represent chronological order (i.e. U2b and U2a might have been deposited isochronously).

71

Unit 2a (U2a) represents chaotic reflections with low to high amplitude. An exception is the lateral gradual change to very low amplitude inclined reflectors (Fig. 3.3). Acoustic blanking zones are usually observed within this unit; therefore, the base is not detectable in sediment echosounder. Nevertheless, MCS profiles show that its lower boundary correlates with the base of Elbe Palaeovalley. It is overlied by U3. The external geometry is mounded. The thickness is around 9 m. The core from the part with very low amplitude inclined internal reflectors shows fine sand.

Unit 2b (U2b) represents hummocky clinoform pattern with low amplitude. It is overlied by U3. The external geometry is mounded. Unit 2b is only found above the deepest meandering part of the valley. The thickness is around 11 m. The correlation with vibrocores shows silty fine sand.

Unit 2c (U2c) is composed of sigmoid with high amplitude reflectors. It is attached to the western flank and external form is wedge-shaped. It onlaps onto U2b. This unit also includes the incisions on the western flank as an onlap, a divergent and prograded fill pattern. It is overlied by U3. Thickness is around 5 m. This unit is represented by fine sand with silty clay layers.

Unit 3

Unit 3 (U3) is the most prominent sedimentary body of the Elbe Palaeovalley. It was previously defined in shallower sector of the Elbe Palaeovalley (Özmaral et al., in prep), which was described as oblique progradational reflectors downlapping onto the top of incision infills. It overlies Unit 2. Oblique pattern towards northwest along the valley (closer to the Dogger Bank) becomes sigmoid progradational (Fig. 3.3). Its top is truncated on the western side of the Elbe Palaeovalley. This unit's spatial distribution seems to be dispersed near the eastern Dogger Bank (Fig. 3.8b) although more or less uniform shape was observed in the German Bight. The correlation with vibrocores shows fine sand with clay layers.

Unit 4

Unit 4a (U4a) is represented as both a divergent fill or prograded fill with high amplitude reflectors. It is observed around eastern and southeastern Dogger Bank (e.g. Fig. 3.3). The correlation with vibrocores shows silty clay with fine sand layers and clayey silt with sand layers.

Unit 4b (U4b) is the uppermost unit and consists of eastward/south eastward dipping reflectors. Low amplitude prograding reflectors taper towards the Elbe Palaeovalley where acoustic facies switches to a transparent character, and then, it fills the eastern side of the Elbe attaining a sigmoid progradational reflector configuration. The correlation between vibrocores and U4b shows a gradual lateral change in grain sizes from west to east; medium sand, fine sand and clayey silt, respectively.

It is important to note here we defined the uppermost deposition within the East Dogger Deep as belonging to U4. Although the sill does not allow for a direct relation, a similarity in the reflector

configuration and spatial distribution, as revealed by mapping (Fig. 3.8c), led us to define the uppermost deposition as U4.

Table 3.1. Summary of acoustic units.

Acoustic Unit	Reflection configuration	Amplitude	Reflection termination Bottom (B) Top (T)	Position relative to Elbe Palaeovalley and Dogger Bank
U1a	Acoustically transparent	–	T: seafloor –	Flanking the valley from eastern side
U1b	Parallel (wavy)	Low	– T: Truncation	W of valley (its base amalgamates with Elbe base?)
U2a	Chaotic	Low–high	B: Elbe base? T: Concordant	In the valley basin (continues north of East Dogger Deep?)
U2b	Hummocky clinoform	Low–moderate	B: Elbe base? T: if not truncated, concordant	Adjacent to the western flank of the valley (only SE Dogger Bank)
U2c	Sigmoid	High	B: Onlap T: Concordant	Adjacent to the western flank of the valley (only SE Dogger Bank)
U3	Oblique–sigmoidal	Moderate–high	B: Downlap T: Truncation (locally)	Attached to W flank (including German Bight) + expands beyond the western flank in S Dogger Bank
U4a		High	B: Concordant and onlap T: Truncation (locally)	E + SE Dogger Bank
U4b	Acoustically transparent, locally sigmoidal prograding clinoforms	Low	B: Onlap T: Truncation	Eastern infill of the valley + S & SE Dogger (+ continues north via East Dogger Deep?)

3.5 Discussion

3.5.1 Ice-dammed lake during Late Weichsel glaciation in the North Sea (25–19 ka BP)

Generally Quaternary incised valleys are associated with the fourth-order sea level cycles, and they can be simple-fill or compound-fill which are governed by number of observed incision and infill (Zaitlin et al., 1994). Compound-fill types are the most common examples on passive continental margins (Maselli and Trincardi, 2013). However, incised valleys generated by single incision event are less common, and they are linked to the base level fall associated to last glacial-interglacial cycle (e.g. Maselli and Trincardi, 2013) or significantly increased drainage period associated to ice melting as in, palaeovalley systems in the English Channel (Smith, 1985; Lericolais et al., 2003; Gupta et al., 2007) and Hudson Shelf Valley (Thieler et al., 2007). The Elbe Palaeovalley represents a single stage incision with possible modification of fluvial drainage by meltwater drainage, however its distinction to other systems is the possible ice sheet blockage of

northwards drainage route during the last glacial period. Moreover, in contrast to Elbe Palaeovalley, the valleys that carried meltwater are today empty of deposits such as Hudson Shelf Valley and Northern Valley in the English Channel and their scales are much lower (e.g. valley cross sectional area).
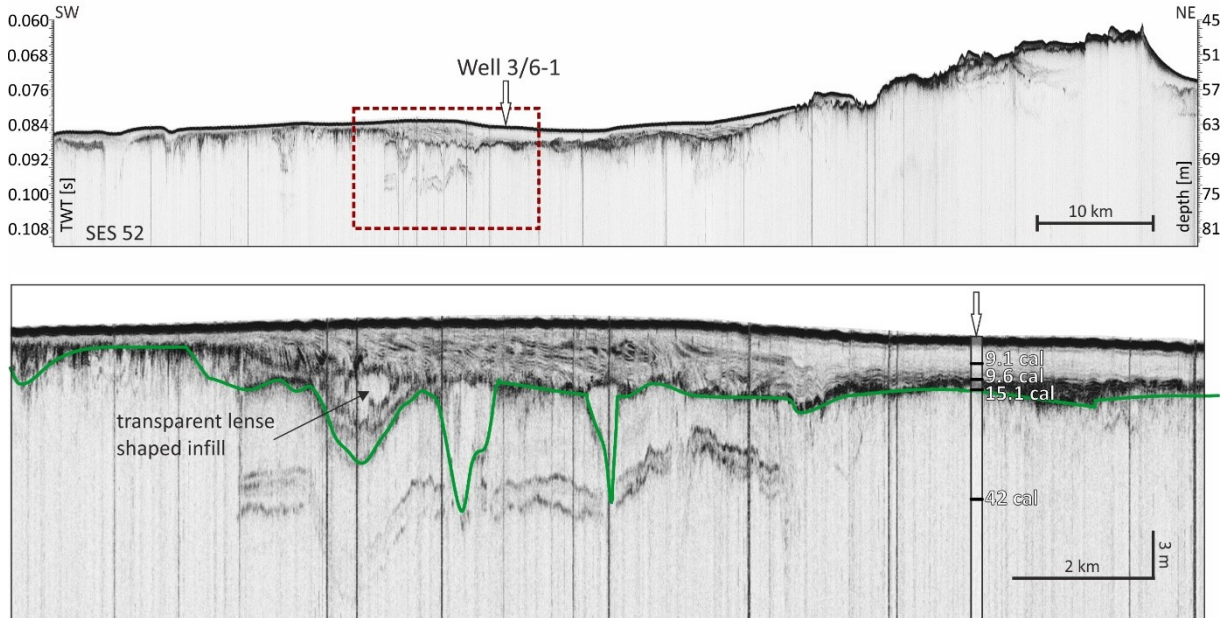

Figure 3.5 SW–NE Echosounder profile (SES 52) showing the Elbe Palaeovalley continuation further north in the Danish North Sea, the eastern border of the valley coincides with ice front position of Sejrup et al. (2016) and most likely representing ice marginal landforms on which Holocene sand waves (?) had been developed. The close-up (red dashed rectangle) shows projected well from Hammer et al 2016 which indicates that the valley must be older than 15.1 cal ka BP.

The most prominent difference of the Elbe Palaeovalley in the study area compared to shallower shelf (German sector, Özmaral et al., in prep) was the scarcity of incisions on the valley base. This could be counted as one of the evidence for the ice sheet(s) occupation between Dogger Bank and western Denmark. Very recent studies have started to stress the previously underestimated extent of the Weichselian ice sheet in the North Sea (Toucanne et al., 2010; Toucanne et al., 2015; Hughes et al., 2016; Sejrup et al., 2016) and it seems that relatively older theories of Valentin (1955) and Tesch (1942) has turned out to be accepted now. The maximum extent of SIS trends south-north through Schleswig-Holstein and Jutland, and from northern Jutland turns towards E–W direction and passes into the North Sea (around Dogger Bank), then connect with BIIS (Valentin, 1957b; Sejrup et al., 1998; 2000; 2005; 2009; 2016). We observed ridges around 8 km wide and reaching 20 m above the seafloor (40 m high above the base Elbe) bordering Elbe Palaeovalley from the east (Fig. 3.4), which is in accord with the proposed southern margin of SIS between 25–19 ka BP (Sejrup et al., 2000; Larsen et al., 2009; Hughes et al., 2016). Given E-W trending belt of moraines are defined in the close vicinity (east of 6°E) (Jensen et al., 2010), these ridges herein (Fig. 3.4) most likely represent moraines belong to the Weichselian ice lobe

advancing towards southern North Sea leading to indication for the blockage of Elbe Palaeovalley route towards northwest. On the other hand, Sejrup et al. (2016) defined the same location as sand waves. We indeed observed sand waves (2–3 m in height and 100 m in width) in this area, however it seems likely that they are formed on top of and/or nearby already existing ridges.

Furthermore, Unit 1b represents 24 m thick layered reflectors and correlates to dark olive brown laminated (darker and lighter layers) stiff clay sediments with high calcium carbonate content thereby indicating likely a glaciogenic environment, possibly an ice-dammed lake. In fact, the extent of the Unit 1b interestingly coincides with the ice sheet extents between 25–19 ka BP according to the compiled reconstructions by Hughes et al. (2016) (Fig. 3.7). This unit was not encountered south of 55°30′N in the German sector, however eastern and western extension of Unit 1b needs further investigation as mapping does not represent the whole extension of any possible lake or ice-marginal depositional environment further west in the Dutch sector. The western continuation of the ice-dammed lake probably maintained through the Oyster Ground as it was already proposed by Clark et al. (2012a) and Clark et al. (2012a). Towards east, this unit is terminated by channel belong to Elbe Palaeovalley, however we propose that the base of Unit 1b amalgamates with the base of the Elbe Palaeovalley in the direction towards the western Danish coast (Fig. 3.3). In fact, Houmark-Nielsen and Kjaer (2003) and Larsen et al. (2009) in their palaeogeographical reconstructions indicate drainage of proglacial rivers from western Denmark between ca. 23–21 ka BP into the Elbe Palaeovalley, that also continued until around 17 ka BP besides to main meltwater drainage through Elbe Palaeovalley established from the southern margin of SIS in the North German Plain. Briefly, the ice-dammed lake and related sediment laden meltwater that is mainly from North European lowlands and southern margin of the SIS even recorded in the Bay of Biscay that had affected destabilization of the thermohaline circulation (Toucanne et al., 2010).

To sum up, we propose that its northwestward drainage of Elbe Palaeovalley was blocked adjacent to southeastern/eastern Dogger Bank. This led to a change in the northwesterly drainage of Elbe Palaeovalley to a southwesterly drainage. A coincidence between existence of Unit 1b and the absence of small scale V-shaped incision (mapped by Özmaral et al., in prep) probably gives hint that the southern Elbe Palaeovalley (i.e. in the German sector) was connected to the proposed ice-dammed lake.

3.5.2 Discharge towards Norwegian Channel (18.5–15 ka BP)

A prominent deep zone (thereafter we call it East Dogger Deep) reaching to almost 81 m probably points to the drainage outlet of ice-dammed lake (Fig. 3.4). This drainage was thought to took place after 18.5 cal ka BP and provided prominent meltwater towards Norwegian Channel at the

same time aided in the disintegration of BIIS and SIS (Lekens et al., 2005; 2006; Sejrup et al., 2016) . Further north of the Dogger Bank, Elbe Palaeovalley here with a width of around 30–40 km and 3–6m deep occasional incisions at the base followed mainly the northwestward path (Fig. 3.7a). Ling Bank Drainage Channel as called by Sejrup et al. (2016), obviously represents our Elbe Palaeovalley continuation in the Danish and Norwegian sectors. Although any sub-bottom profile belong to the channel was not presented in their study, our mapping result belongs to the base coincides with their ice extent reconstruction spanning over 18.5–17 cal ka BP related to the ice-dammed lake drainage via this channel entering the Norwegian Channel around 59°N, around where ca. 35 m thick depocenter within Norwegian Channel related to drainage channel was observed. Hence, it is likely that Elbe Palaeovalley in this sector must have been formed during this time interval that might indicate southern part (south of Dogger Bank) was formed much earlier. Moreover, the well 3/6 of Hammer et al. (2016) from Elbe Palaeovalley give evidence that it was formed before 15.1 cal ka BP (projected location of this well is shown in Fig. 3.5).

Furthermore, Elbe Palaeovalley in the northern part of our study area seems to be surrounded in the east by ice marginal landforms such as arcuate terminal moraine ridges with wedge-shaped cross sections (Figs. 3.5 and 3.6) after following to ice marginal landform description made by Sejrup et al. (2016) in the close vicinity.

Mapping of the base Elbe (Fig. 3.7a) also revealed relatively narrow channel formation with a width of around 2 km following southern Great Fisher Bank. The MCS data from this area shows tunnel valley formation right beneath these channels. Therefore, either this channel indicates that it was preferable for Elbe to use the upper part of tunnel valley as one of the pathway –besides to main northwestward path– or it was not a branch of the Elbe Palaeovalley, but was related to front of BIIS lobe facing southeast and associated retreat had been supposed to occur towards NW (Sejrup et al., 2016) in line with the channel (i.e. tunnel valley) orientation.

Overall, the impact of this drainage after separation of ice sheets along the Elbe Palaeovalley towards Norwegian Channel was again the freshwater input (around 18.5 ka BP) but this time to the North Atlantic (Lekens et al., 2005; Sejrup et al., 2016).

3.5.3 Elbe Estuary between 15–10.8 ka BP (Unit 2)

After the full deglaciation of Norwegian Channel around 15 ka BP and when the sea level reached −70 m, we suggest that the channel indicated at 0.092 s (ca. 70 m) in the most northeastern section (Fig. 3.6) was the more southerly outlet of Elbe Palaeovalley towards the Norwegian Channel. As location of these channels coincide with the depocenter in the Norwegian Channel that was thought to be associated with riverine input from southern North Sea, and probably by Elbe River (Rise et al., 2008) between ca. 14.5–13 ka BP (after full deglaciation of Norwegian Channel).

The northwestern sections in the Norwegian sector, the infill of Elbe Palaeovalley (between 0.088–0.084 s) is not included in the thickness map of Unit 2, on account of that acoustic facies of the infill indicates different characteristics such as chaotic facies with low amplitude (Fig. 3.8) compared to the southern adjacent valley transverse section. Furthermore, in the well 3/6-1 (Hammer et al., 2016), Unit 2 situates in between dated intervals of 15.7 cal ka BP and 9.6 cal ka BP (the well location corresponds to tapered part of Unit 2 and within 5 km projection distance, Fig. 3.5). Here, Unit 2 deposition might be associated with entrance of the Central North Sea Water from west interacting with the Great Fisher Bank instead of Elbe estuary mouth processes. For future studies, core information to be retrieved from Unit 2 could provide insight into the infill here, as the thickness of around 3 m convenient even for a vibrocore.
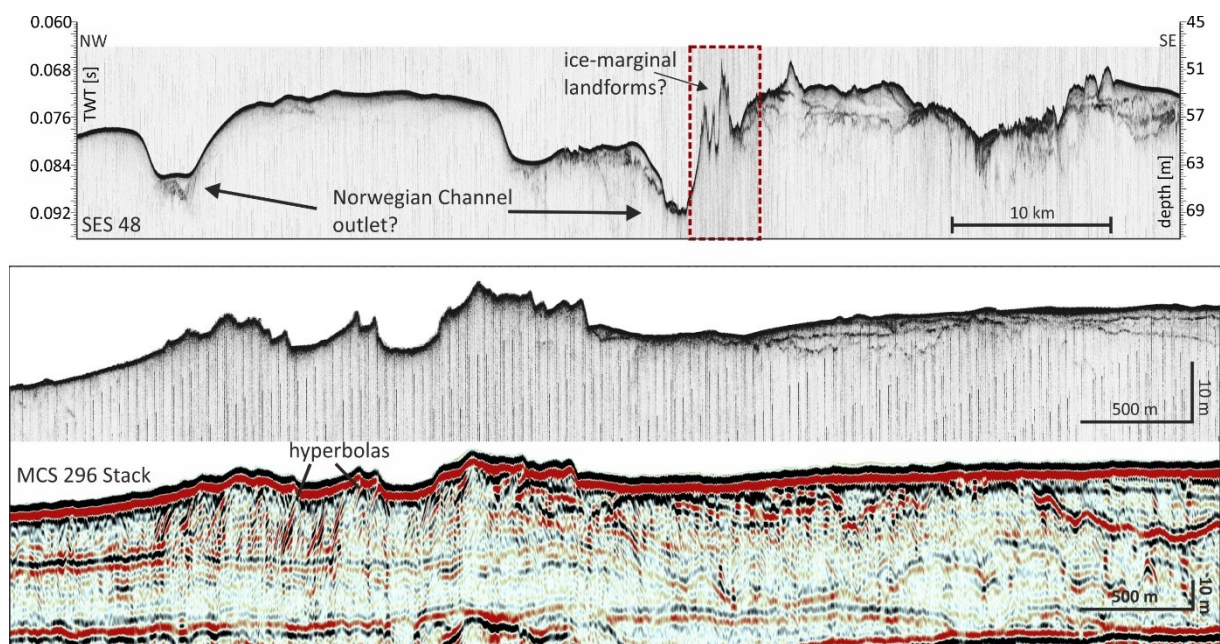
Figure 3.6 NW-SE Echosounder profile (SES 48) showing the possible Elbe Palaeovalley connection to the Norwegian Channel through 2 km wide channels reaching maximum 0.096 s twt. The close-up (together with accompanying MCS stacked section) shows the ice front positons associated with arcuate terminal moraine ridges (Sejrup et al., 2016).

Through the eustatic sea-level rise, incised valleys were likely transformed into estuaries (Nordfjord et al., 2005). Therefore, morphology of incised valleys decides the estuarine topography (Mattheus and Rodriguez, 2011) and if accommodation space is endured, usually major component of the incised valleys are the estuarine deposits (Lericolais et al., 2001; Nordfjord et al., 2005) which influence spatial distribution of subsequent full marine depositional environment. For example, Elbe estuary today in the German coast is covered by large compound tidal bedforms in 10–30 m water depths within the turbidity maximum zone, which are in the meso/macro tidal setting (Kwoll et al., 2014). The distance from fresh-salt water transition is around 40 km today (Kappenberg and Grabemann, 2001). Although Elbe Estuary today is artificially affected, and palaeo-river discharge and catchment properties might have been

changed, we observed complex depositional succession of Unit 2 at the mouth and upstream from the palaeo estuary mouth (Fig. 3.4) also within approx. 40 km zone (Fig. 3.8). Further upstream in the palaeoestuary (i.e. German sector) this complex succession was not evident (Özmaral et al., in prep). Unit 2 must have been deposited in the estuary setting before the complete drowning of the Elbe Palaeovalley – before the full connection to the Oyster Ground had been established by the early Holocene sea-level rise. Accordingly, we propose that Unit 2 was deposited during slowly rising sea level or even during the sea-level still-stand likely between ca. 13. 8 cal ka BP judging from the sea-level curve represented by Hammer et al.(2016, and references therein) and ca. 10.8 cal ka BP (Özmaral et al., in prep). Although East Dogger Deep is significantly deep to allow marine influence easily, morphological high (or sill) at the valley base around –53 mbsl (Fig. 3.7a) seems to be provided somewhat sheltered environment for the southern part given that the top Unit 2 deposition is limited to depths around 57–55 mbsl. Hence, Unit 2 was probably dominated by riverine input which might also lead to an ebb tidal delta in front of the estuary mouth (Fig. 3.8a). During this period, channels observed on the western flank must have been still active and feeding the Elbe Palaeovalley (or Elbe palaeo-estuary). These channels represent the tributary system connected to the Elbe Palaeovalley from southeast of Dogger Bank (Fig. 3.7) which was previously discovered by Hepp et al. (2017). According to foraminifer assemblages belong to the well BH 89/8 studied by Konradi (2000) in which our Unit 2 correlates with the zones associated with subtidal or tidal flat environmental setting under freshwater influence.

Also during this time, probably wetlands were developing in the southern part such as unit LU together with peat defined there by Özmaral et al (2017). Due to the above mentioned fluvial activity in the southeastern Dogger Bank, LU and also the peat formation here were probably not favored or destroyed later compared to the southern part.

3.5.4 The start of drowning of the Elbe Palaeovalley since 10.8 cal ka (Unit 3 + Unit 4)

Unit 3 is equivalent to the Oblique Unit (OU) of Özmaral et al (2017) based on the continued mapping of this unit towards Danish sector, but also, on the analogous sedimentological succession. The start of OU deposition in the German Bight was previously dated as being younger than 10.4 cal ka BP when the Elbe Palaeovalley estuary transformed into a shallow sea that was receiving the Central North Sea water mass from Outer Silver Pit and East Dogger Deep (i.e. when Dogger Bank became emergent as an island).
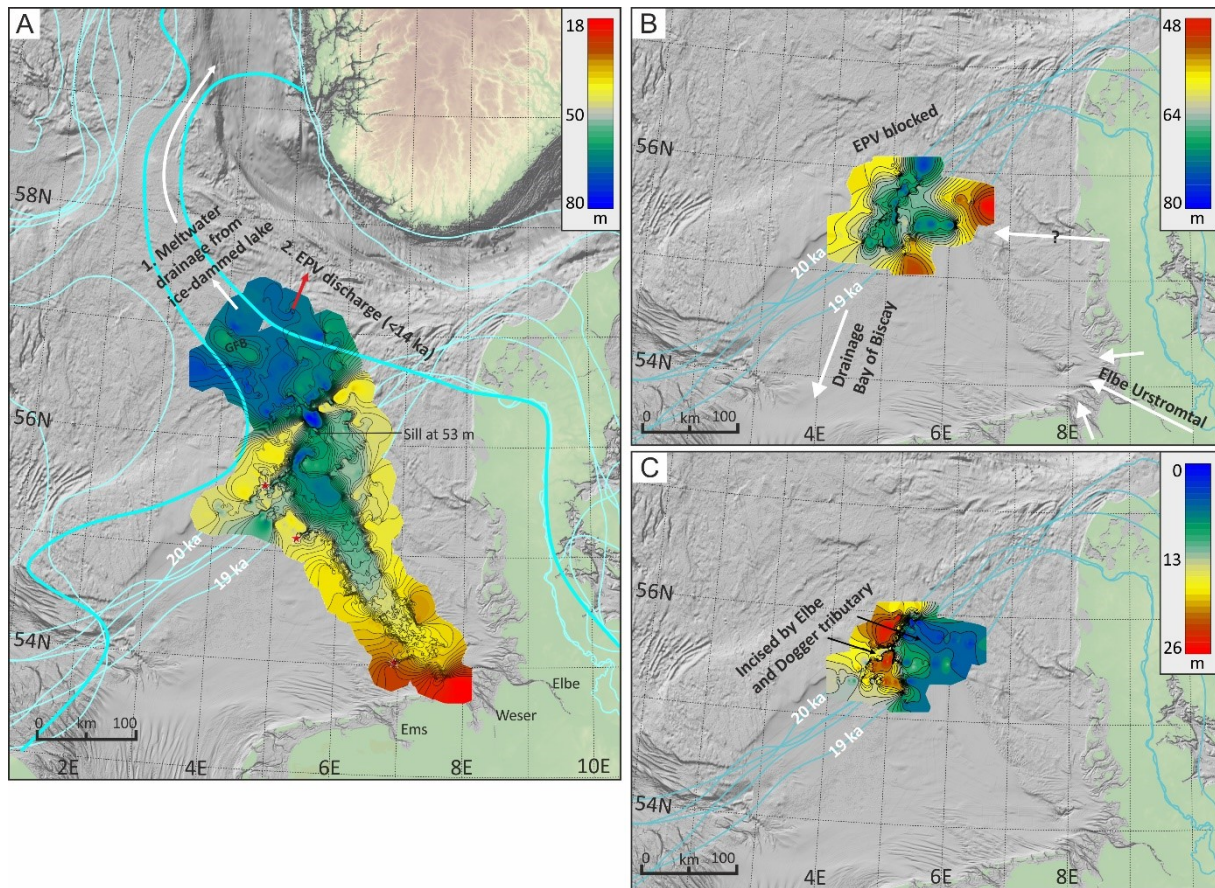
Figure 3.7 Mapping results a) The base of the Elbe Palaeovalley compiled with the dataset from several cruises (contour interval is 1 m). The North of East Dogger Deep was free of ice sheet occupation leading to meltwater drainage to the Norwegian Sea between 18.5–17 ka BP (after Sejrup et al 2016). Star shape indicates tributaries of Elbe from Dogger Bank. b) The base of Unit 1b. We propose here that the Elbe Palaeovalley had been probably connected to the lake from the south, therefore southern Elbe was probably already established during this time. c) Thickness map of Unit 1b.

In the German Bight, Unit 3 (OU) represented relatively coherent outer geometry along the valley and its depocenter is mainly attached to the western flank and constricted by the western valley rim. As revealed by mapping of Unit 3 (Fig. 3.8), this pattern changes in the vicinity of southeastern Dogger Bank where depocenter is spread in the vicinity of the gate (around 50 mbsl) connecting Elbe to the Oyster Ground (Fig. 3.7), attaining a shape like a tidal sand bank. This likely indicates the first phase of deposition affected by the Central North Sea entering from the west in addition to in-out tidal energy coming from East Dogger Bank, when the amphidromic system was not established in the southern North Sea yet (van der Molen and Swart, 2001a). In fact, the transitional environment is reflected in the corresponding sedimentological expression of Unit 3 such as fine sand with clay layers including plant fragments and organic matter nodules in the lower part and slight increase in shell fragments towards the upper part (e.g. GeoB21407; Fig. 3.3). Within a short time, when the sea level was around 36 m (before ca 9 cal ka BP), Unit 3 already occupied most of the valley as being responsible most of the infill. The most of the Oyster Ground must have been drowned thereby shifting the depocenter of Unit 3 to more southerly

position (Fig. 3.8b) In conclusion, Unit 3 represents a transitional environment from estuarine conditions to a shallow marine environment.
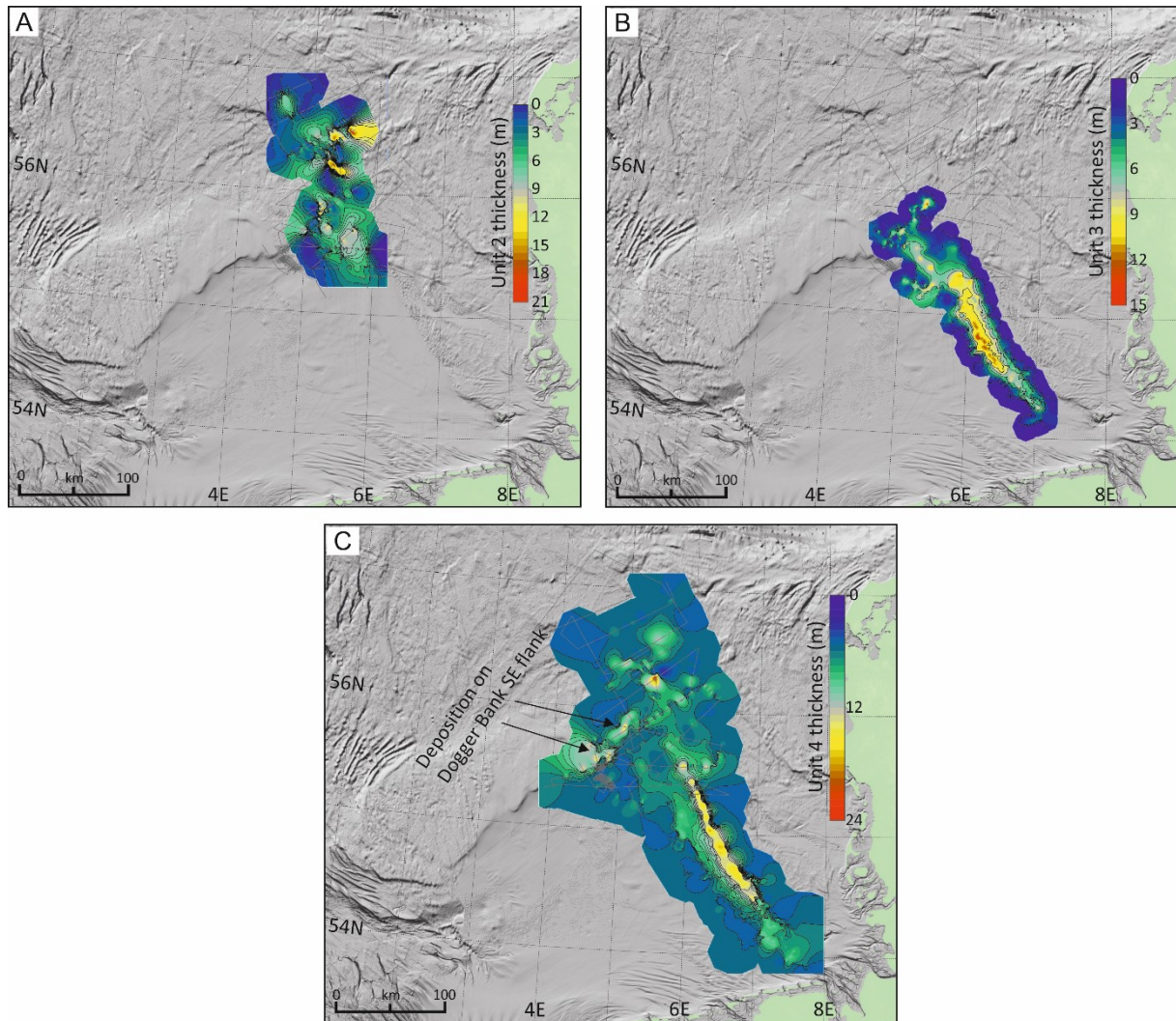
Figure 3.8 Thickness maps a) Unit 2 is probably controlled by fluvial input, note the possible tidal delta in front of the East Dogger Deep and acoustic blanking was not observed above Unit 2 b) Unit 3 tidal and wind driven easterly transport from Oyster Ground c) Unit 4 indicates northwesterly transport towards East Dogger Deep from southern valley. The anticlockwise circulation established around Dogger Bank probably affects Unit 4's depositional pattern, but also depositional pattern coincides with the thermocline calculated by Hill et al (2008). Since Early Holocene, deposition in the northern Danish and Norwegian sectors of the study area were not prominent.

In addition, here we collected echosounder profile crossing the location of 51 m deep well BH89/8 in which foraminiferal assemblages were studied by Konradi (2000). Given the uppermost surface of associated unit is dated to 8.5 cal ka BP (Fig. 3.2) by Konradi (2000), we interpret that erosion of Unit 3 is related to new hydrographic regime introduced in the southern North Sea. It is most likely associated with entrance of Atlantic water through English Channel which was also occurred around 8.5 cal ka BP (Jelgersma, 1979; Lambeck, 1995; Gyllencreutz, 2005).

Unit 4 is equivalent to the Transparent Unit (TU) that also includes Sigmoid Unit (SU) of Özmaral et al (2017). Its deposition observed as an overgrowing body on the truncated zones of Unit 3 (Fig. 3.2). It is therefore most likely that deposition of Unit 4 needed sediments belongs to Unit 3 and Dogger Bank as a core. Besides, Unit 4 fills the empty space left along the eastern side of the valley. Based on the reflection configuration, we also included upper infill of East Dogger Deep (Fig. 3.4) within Unit 4, although we note here the relatively large distance between tracklines.

Unit 4 deposition might have been related to new hydrographic regime introduced in the area due to the entrance of Atlantic water mass through English Channel Also, it is thus likely that thermohaline circulation of the North sea has started to develop soon after the sea level was high enough to let dense water trapped beneath seasonal thermocline that recognized present day by Hill et al. (2008) and Brown et al. (1999). Indeed, mapping of Unit 4 showed that its pattern somehow coincides with bottom horizontal temperature gradients calculated by Hill et al. (2008). In their study, they found cold and dense winter water trapped beneath thermocline that is established during summer related to tidal mixing fronts. Along these bottom fronts jet flows are created parallel to the surface temperature fronts. Deriving from the results of Hill et al. (2008), bottom flow on the eastern side of the Elbe Palaeovalley flowing SE-NW may have been related to frontal-jets associated to summer stratification. However, the valley succession since early Holocene with closely spaced cores and dating could provide much more detail into the discussed environments and in near future.

3.6   Conclusion and future work

The first high resolution seismic and echosunder profiles representing the Elbe Palaeovalley in the Danish–Norwegian sectors of the North Sea and the Late Weichselian glacial and post-glacial depositional history collected from eastern North Sea. Unit 1a is interpreted to be glaciogenic landforms that is most likely a part of Late Weichselian moraine ridge belt that trends in E-W direction and merging with the Jutland Bank. Around 26 m thick succession of Unit 1b is interpreted as proglacial sediments deposited when the coalescing Scandinavian Ice Sheet and British-Irish Ice Sheet fluctuated across the Dogger Bank. Recently, coalesce of these ice sheets during last glacial period have started to receive acceptance in contrast to some past speculations or underestimations on the absence of ice sheet meeting in the Central North Sea. These previous speculations were lacking in high resolution seismic images. The data interpreted here supports the existence of an ice-dammed lake between around 23–19 ka BP in the southern North Sea. According to recent studies, ice sheets were independent following deglaciation around 18.5 ka BP, we therefore attain this period in the formation Elbe Palaeovalley that is most likely younger than its southern part (in the southern Dogger Bank). Elbe Palaeovalley found its path in between ice fronts or ice lobes further northwestward after the East Dogger Deep.

The post-glacial depositional history within the Elbe Palaeovalley has been controlled mainly by its own morphology, relative sea level rise, and associated changes in the tidal and wave/wind energy probably since ca. 11.7 cal ka BP. Estuarine sediments (Unit 2) were only able to fill eastern/southeastern surrounding of Dogger Bank before the complete drowning of the Elbe when the sea level was slowly rising from –70 to –50 m. Unit 3, subsequently, deposited in low energy marine conditions with the start of accelerated sea level rise and its deposition ceased around 8.5 cal ka BP when the sea level reached -30 m. With the accelerated early Holocene sea level rise, residual tidal currents associated with southern and central North Sea Water masses were responsible for the huge sand ridge-like formation in and above the western flank of Elbe Palaeovalley, as Elbe Palaeovalley is oriented transverse to the prevailing wind and tide driven currents. This period even resulted in overgrowth above the western flank. Lastly, Unit 4 deposition took place in an open marine environment when the present day hydrodynamic regime started to be formed and the subsequent processes much more controlled by currents than the sea level rise.

A coherent and detailed picture and chronological framework of the late Weichselian ice-sheet positions and post glacial sedimentary processes will certainly be improved by ensuing sedimentological, geochemical studies, as well as dating of cores that have been already collected from the region, especially around Dogger Bank. We believe that the most crucial material for dating belongs to the sediments representing acoustic Unit 1b as it has the potential to explain age relation between the proposed proglacial lake and the Elbe Palaeovalley. Moreover, the compilation of extant high resolution studies from adjacent areas (i.e. on sediment echosounder and core material) and potential long sediment cores together with the already conducted mapping efforts will finally provide a North Sea-wide picture of the palaeoenvironment since the last glacial period. In future studies, high quality core material is necessary in order to interpret sediment genesis and palaeoenvironments, thereby enabling to develop precise chronologies. The recent studies have already started to investigate Late Pleistocene and Holocene succession of the North Sea owing to the development in the sediment echosounders which will help to take steps further than the speculations about drainage pathways, ice margin positions and palaeo-hydrodynamic regime, all of which is supposed to affect North Atlantic climate system, regarding especially the fluxes of sediment and freshwater on the terrestrial to ocean route. Besides, high resolution data presented here, Elbe Palaeovalley infill pattern and huge depocenter related to East Dogger Deep will be essential in the development and improvement of palaeo-tidal and sediment transport models, but also in the archaeological studies of Northwest Europe. However, in future studies, a target-oriented multibeam bathymetric data could provide a high level of detail on sandwaves and ridges observed here to decipher the sediment transport pattern in the Danish and German North Sea. For all mentioned suggestions above, this study could be taken as a basis.

4 Evolution of a high-latitude sediment drift inside a glacially-carved trough based on high-resolution seismic stratigraphy (Kveithola, NW Barents Sea)

Michele Rebesco [a], Asli Özmaral [b], Roger Urgeles [c], Daniela Accettella [a],

Renata G. Lucchi [a], Denise Rüther [d, e], Monica Winsborrow [d], Jaume Llopart [c],

Andrea Caburlotto [a], Hendrik Lantzsch [b], Till J.J. Hanebuth [b, f]

[a] OGS, Sgonico, TS, Italy

[b] MARUM—Center for Marine Environmental Sciences, Bremen, Germany

[c] Institut de Ciències del Mar, CSIC, Barcelona, Spain

[d] CAGE – Centre for Arctic Gas Hydrate, Environment and Climate, Department of Geology, UiT The Arctic University of Norway, Tromsø, Norway

[e] Faculty of Engineering and Science, Sogn og Fjordane University College, Sogndal, Norway

[f] School of Coastal and Marine Systems Science, Coastal Carolina University, Conway/SC, USA
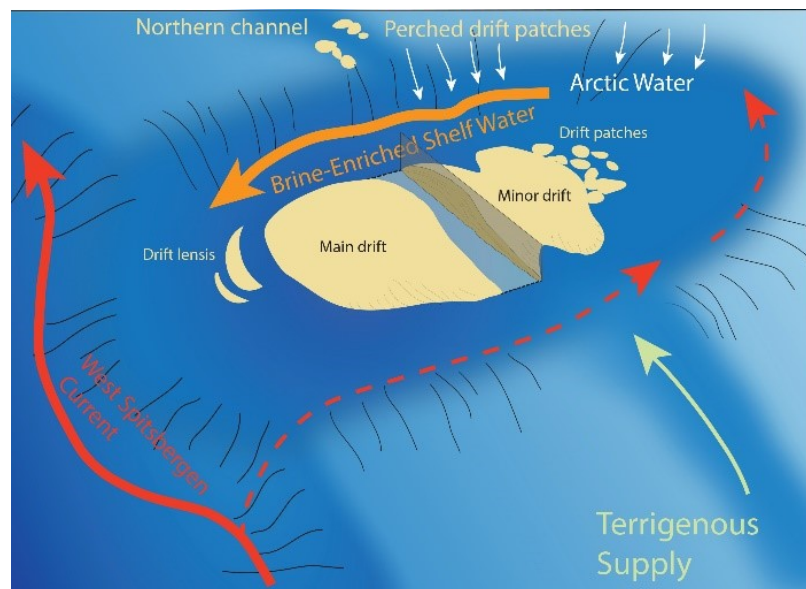
Abstract

Kveithola is a glacially-carved, E-W trending trough located in the NW Barents Sea, an epicontinental shelf sea of the Arctic Ocean located off northern Norway and Russia. A set of confined sediment drifts (the "Kveithola Drift") is located in the inner part of the trough. In general, drift deposits are commonly characterized by high lateral continuity, restricted occurrence of hiatuses and relatively high accumulation rates, and thus represent excellent repositories of palaeo-environmental information. We provide for the first time a detailed morphological and seismostratigraphic insight into this sediment drift, which is further supported by some preliminary lithological and sedimentological analyses. The complex morphology of the drift, imaged by combining all available multibeam data, includes a main and a minor drift body, two drift lenses in the outer part of the trough, more or less connected drift patches in the innermost part and small perched sediment patches in a structurally-controlled channel to the north. The seismic (Parasound) data show that the main and minor drift bodies are mainly well-stratified, characterized by sub-parallel reflections of moderate to high amplitude and good lateral continuity. The reflectors show an abrupt pinch-out on the northern edge where a distinct moat is present, and a gradual tapering to the south. Internally we identify the base of the drift and four internal horizons, which we correlate throughout the drift. Two units display high amplitude reflectors, marked lensoidal character and restricted lateral extent, suggesting the occurrence of more energetic sedimentary conditions. Facies typical for contourite deposition are found in the sediment cores, with strongly bioturbated sediments and abundant silty/sandy mottles that contain shell fragments. These characteristics, along with the morphological and seismic information, suggest a strong control by a bottom current flowing along the moat on the northern edge of the drift. Though both Atlantic and Arctic waters are known to enter the trough, from the west and the north respectively, brine-enriched shelf water (BSW) produced during winter and flowing westward in the moat, is suggested to be responsible for the genesis of the Kveithola Drift. The formation of BSW is inferred to have started around 13 cal ka BP, the onset of drift deposition, suggesting that conditions leading to atmospheric cooling of the surface waters and/or the presence of coastal polynyas and wind or floating ice shelves have persisted on the western Barents Shelf since that time. The units inferred to have been deposited under more energetic sedimentary conditions (tentatively dated to the Younger Dryas and to 8.9–8.2 cal ka BP) are suggestive of stronger BSW formation. In general, we infer that variations in the bottom current regime were mainly related to BSW formation due to atmospheric changes. They could also have been a response to successive episodes of grounded and sea ice retreat that allowed for a first limited, later open shelf current, which progressively established on the western Barents Sea shelf.

4.1 Introduction

Sediment (or contourite) drifts are sedimentary bodies in the open ocean produced by the accumulation of sediment under the control of bottom currents (Faugères et al., 1999; Rebesco and Stow, 2001; Stow et al., 2002; Rebesco, 2005; Rebesco and Camerlenghi, 2008b; Rebesco et al., 2014a). Bottom currents are influenced by a number of factors: foremost, on the large scale, by the global thermohaline circulation, but also by geostrophic currents, the tidal system, internal density-driven pulses and local topography (e.g. Hanebuth et al., 2015). Variations in strength and location of bottom currents are in phase with climate changes (e.g. Voelker et al., 2006).The drift deposits are generally characterized by high lateral continuity (allowing for a robust correlation of seismic profiles and cores), restricted development of hiatuses (generally of limited temporal extent), and accumulation rates higher than in the adjacent hemipelagic deposits (Rebesco et al., 2014a). These characteristics make sediment drifts an excellent repository of palaeoceanographic information.

This fact is particularly true for high latitude contourites where both bottom current strength and sediment flux are primarily controlled by extreme climatic conditions (van Weering et al., 2008; Rebesco et al., 2013). In fact, it is at high latitudes that cold, dense waters are produced, driving the global thermohaline circulation. It is also at high latitudes that sediment supply to the open ocean is dramatically enhanced at times when ice streams are grounded at or near the continental shelf edge (Laberg et al., 2012). Glacial troughs on high-latitude continental margins also contain a record of the effects of dense brine waters, produced by the formation of sea ice in polynya areas, together with supercooled water masses formed below ice shelves (Borchers et al., 2016).

Despite significant recent advances in contourite studies, a sound connection between contourite deposits, basin evolution and oceanographic processes still remains to be established (Rebesco et al., 2014a; Müller-Michaelis and Uenzelmann-Neben, 2015). In particular, there is the need to better understand the relationship between internal drift geometry and bottom current circulation, and to link the recorded sedimentary changes to variations in the palaeoclimatic system.

The primary aim of this paper is to study the external and internal seismostratigraphic geometries of a high latitude sediment drift located in a glacially-carved trough in the northwestern Barents Sea, an epicontinental shelf sea of the Arctic Ocean located off the northern coasts of Norway and Russia. The drift was already briefly described by Rüther et al. (2012) and Bjarnadóttir et al. (2013) as they mainly focused their work on the glacial and deglacial history of the Kveithola Trough. On the contrary, this contribution provides unprecedentedly detailed seismic and morphological information about this sedimentary deposit, supported by some preliminary lithological and sedimentological investigation. The higher resolution of the acquired acoustic

data allows for a more detailed interpretation, about the nature and characteristics of the bottom currents from which the drift was formed, providing a detailed discussion of the processes involved in the formation of the drift as well as external forcings that influenced the drift deposition and evolution. In this study, we define and correlate the main stratigraphic units that constitute the drift. On this basis, we investigate drift's evolution, i.e., the framing palaeo-environmental conditions which led to the formation of these units and the sedimentary deposit as a whole. This includes a discussion of the possible bottom current flow conditions that may have controlled its growth dynamics.

4.2 Background

Kveithola is a glacially-carved trough located in the NW Barents Sea (Fig. 4.1). This trough was occupied by a fast-flowing ice stream that drained ice from Spitsbergenbanken in the north and from Bear Island in the south during the last glaciation (Andreassen et al., 2008; Rebesco et al., 2011; Rüther et al., 2012; Bjarnadóttir et al., 2013; Rebesco et al., 2014b; Llopart et al., 2015). The trough extends in E-W direction over 90 km with a width of less than 15 km and an average water depth of 300–350 m along its axis. The transverse profile of the trough is U-shaped with relatively steep flanks (dipping about 4° and locally 6° or more) and a very flat thalweg, which lies more than 150 m below the average depth of the surrounding shallow continental shelf in which it is incised. The axial profile along the thalweg is markedly staircase-like, composed of five transverse ridges about 15 km apart from each other. These ridges are composed of grounding-zone wedges (GZWs) and grounding-line fans both inferred to have formed by deposition of subglacial till and a dominance of subglacial meltwater plumes during the episodic phases of last deglacial ice stream retreat (Rebesco et al., 2011; Bjarnadóttir et al., 2013; Rebesco et al., 2016b). The position of GZWs was likely controlled by small pre-existing morphological steps generated by NNW-SSE faults and/or wave-cut terraces (Lebesbye and Vorren, 1996). These normal faults (the easternmost and major one being the Knølegga Fault at the eastern termination of the Kveithola Trough) belong to a faulted basin geometry that for most parts reflects phases of extension associated with the opening of the Norwegian-Greenland Sea since the Cretaceous (Gabrielsen et al., 1990; Bergh and Grogan, 2003). We infer that these faults also generated the structural depressions ("channels"), which we observe to the north and south of the inner part of the Kveithola Trough (Fig. 4.1). Apart from the structural control, the present-day seafloor morphology is largely inherited from the palaeo-seafloor topography which formed at the time of GZW formation. Following deglaciation, this morphology was draped by a relatively uniform glaciomarine blanket more than 15 m thick. This glaciomarine blanket covers the whole trough and is inferred to be characterized by plumites and ice-rafted debris (Rebesco et al., 2011; Bjarnadóttir et al., 2013; Lucchi et al., 2013; Hanebuth et al., 2014; Llopart et al., 2015). Finally, a

sediment drift (the "Kveithola Drift") is present in the inner part of the trough associated to a field of pockmarks (Bjarnadóttir et al., 2013). This drift is inferred to have been formed by sediments supplied by dense bottom currents, mainly infiltrating via a large channel that is connected to the innermost Kveithola Trough from the north (Thomsen et al., 2001; Bjarnadóttir et al., 2013). While Bjarnadóttir et al. (2013) gave a general account of glacial, deglacial to Holocene acoustic units of the Kveithola Trough, this manuscript focus on the Holocene Kveithola drift units described in far greater detail. The Parasound, operated at 4 kHz, provides a much higher resolution than the Chirp data presented in Bjarnadóttir et al. (2013) and Rüther et al. (2012). The drift deposit that was initially subdivided in two subunits (CU1 and CU2) by the latter authors, is now sub- divided in five units thanks to the detailed Parasound record. The Drift chronology previously suggested by Rüther et al. (2012) is strengthened by the new dates presented in this paper.
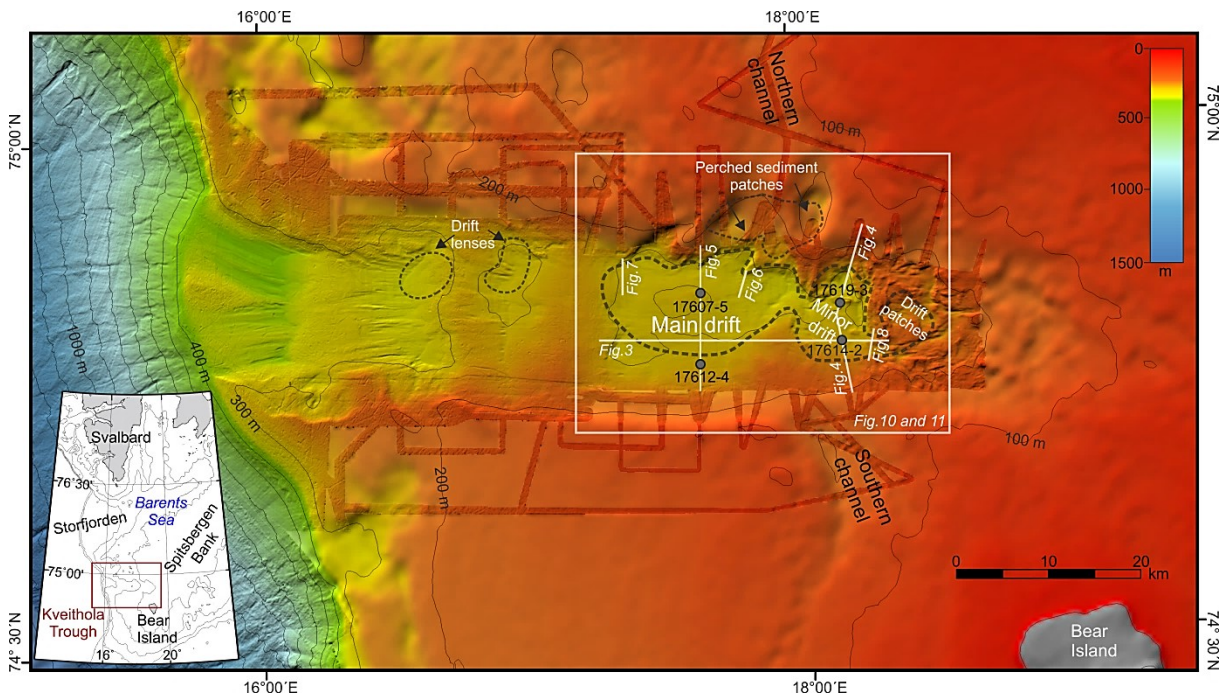
Figure 4.1 Bathymetric map of the Kveithola Trough produced using all available multibeam datasets (see text for details) superimposed onto IBCAO data (Jakobsson et al., 2012). Grid size: 20 m for depth less than −700 m depth and 40 m for deeper data; vertical exaggeration: 2.7; Light Direction Attitude 35°; Azimuth −30°. The locations of the Parasound sediment echosounder profiles and of sediment coring sites presented in this paper are indicated, and the box shows the location of Fig. 4.10 and 4.11. A dashed black line indicates the outline of the Kveithola drift bodies. Location map of the study area is shown in the bottom-left corner.

The Kveithola drift complex developed after the Last Glacial Maximum (LGM) that took place at about 21.5 cal ka BP (calibrated thousands-years before present) when the ice reached the shelf break at the western Barents Sea margin (Vorren and Laberg, 1996). According to Bjarnadóttir et al. (2013), the onset of deglaciation in the Kveithola Trough may have coincided with that of the larger Storfjorden palaeo-ice stream trough located south of Svalbard (Pedrosa et al., 2011) at about 20–19 cal ka ago (Rasmussen et al., 2007; Jessen et al., 2010; Lucchi et al., 2013; 2015).

However, it took several thousands of years before the Kveithola Trough was completely free of ice. In fact, the upper part of the glaciomarine blanket was deposited during the Late Bølling/Allerød interval (about 14.2–13.9 cal ka BP according to Rüther et al. (2012), and the lower part of the blanket is inferred to have started to deposit at the beginning of the Bølling interstadial (Rüther et al., 2012; Bjarnadóttir et al., 2013) which coincides with the start of the global Meltwater Pulse 1a (14.65 cal ka BP, Deschamps et al., 2012). According to Rüther et al. (2012), the Kveithola sediment drift was deposited after 13.1 cal ka BP. For the upper part of the drift, an age of about 11.2–10.3 cal ka BP is inferred by Rüther et al. (2012), who also identified a sand unit deposited after about 8.2 cal ka BP, coinciding with the 8.2 ka climate event (Alley et al., 1997) and the associated meltwater pulse event MWP-1c (Blanchon et al., 2002; Bird et al., 2010). The drift thins out at the coring sites studied by Rüther et al. (2012) who sampled the drift only in its peripheral area, where the thickness is one tenth of that recorded in the depocenter. Therefore, only the lower part of the drift (Drift 2 of Bjarnadóttir et al., 2013) was sampled and studied by Rüther et al. (2012). As the previously studied cores are not from the thick part of Drift 2, it is uncertain whether they can contain the youngest part of Drift 2 sediments. It is equally dubious if any of the sediments forming the upper part of the drift (Drift 1 of Bjarnadóttir et al., 2013) was present in the cores studied by Rüther et al. (2012). It was, however, believed by these authors that at least a thin interval of Drift 1 sedimentary sequence was present in their cores, inferred to be of early Holocene age.

Palaeoecological and palaeoceanographic changes in the nearby brine-enriched environment of the Storfjorden Trough occurred in relation to past climate changes since LGM have been recently constrained through the distribution of benthic calcareous and agglutinated foraminiferal species (Rasmussen and Thomsen, 2014; 2015). The outer shelf of Storfjorden Trough experienced open marine conditions during the deglaciation from about 15 to 11.7 ka BP, whereas the inner part was still occupied by grounded ice. The study by Rasmussen and Thomsen (2014; 2015) revealed that enhanced sea ice and stronger brine formation occurred during the cold periods including the Older Dryas, the Intra-Allerød Cold Period and the Younger Dryas. In general, the colder periods show a stronger influence of Arctic water, with higher brine production and more corrosive bottom water, whereas warmer periods show a stronger influence of Atlantic Water and decreased influence of brine production.

4.3   Hydrographic setting

The western margin of the Barents Sea is influenced by the West Spitsbergen Current (Fig. 4.2), a warm and saline Atlantic-derived water that flows northwards along the eastern side of the Fram Strait (e.g. Aagaard et al., 1973; 1987). Some branches of this current enter the Barents Sea (e.g. Poulain et al., 1996). Recent studies have documented the ability of this current to transport sand-

sized sediments and to generate sand waves in the outer Bear Island Trough (King et al., 2014; Bøe et al., 2015). The bottom circulation pattern is strongly influenced by the topography so branches from the main current penetrates into the glacial troughs on the continental shelf (e.g. Storfjorden, Bjørnøyrenna, and possibly Kveithola Trough), following the contours. When the bottom current encounters a topographic barrier, it turns laterally and backwards toward the continental slope (e.g. Midttun, 1990; Fohrmann et al., 2001; Stiansen and Filin, 2008) after being efficiently mixed and cooled down on the shelf. In fact, the Atlantic Water in the Barents Sea is cooled by the atmosphere and mixing occurs through wind, wave, and ice motion, leading to the formation of the Arctic Surface Water (Boyd and D'Asaro, 1994). In the northern part of the Barents Sea fresh and cold Arctic Surface Water flows from northeast to southwest (Fig. 4.2) reaching Spitsbergenbanken and the Kveithola Trough (Midttun, 1990; Stiansen and Filin, 2008). Dense bottom-water masses are produced on the Barents shelf during winter (Aagaard et al., 1985; Thomsen et al., 2001) as a consequence of atmospheric cooling, as well as sea-ice freezing and brine rejection (Rudels and Quadfasel, 1991). Summer remnants of brine-enriched shelf water (BSW) in morphological shelf depressions have been observed in several areas of the Barents Sea (Quadfasel et al., 1988; Blindheim, 1989). The BSW collected in such depressions flows to the shelf edge in the form of gravity plumes and cascades down the continental slope (Aagaard et al., 1985; Quadfasel et al., 1988; Jungclaus et al., 1995; Schauer, 1995). Kveithola in particular, connected to a system of structurally-controlled channels that drain parts of the Spitsbergen and Bear Island Banks, operates as a drainage system for BSW (Fohrmann et al., 1998 and references therein; Thomsen et al., 2001). The source water of the observed outflow is provided by the East Spitsbergen Current, advecting Arctic Water during summer and early winter, and a mixture of Arctic and Atlantic Waters during late winter (Schauer, 1995). On its way, the BSW flow is assumed to erode the seafloor and transport sediment into the deep sea, resulting in cascading of high-density turbidity plumes that may contribute to maintain the gullies free of sediment still today (Fohrmann et al., 1998; Llopart et al., 2015). Such turbidity plumes, mainly active during deglaciation, result in a high-accumulation area on the Storfjorden Trough-Mouth Fan (Fohrmann et al., 2001). In fact, several intrusions of turbid water up to 200 m thick were observed at and simulated for the upper continental slope (Fohrmann et al., 1998), strongly correlating with temperature and salinity inversions, which indicate advection of shelf bottom water from the Kveithola Trough (Thomsen et al., 2001).
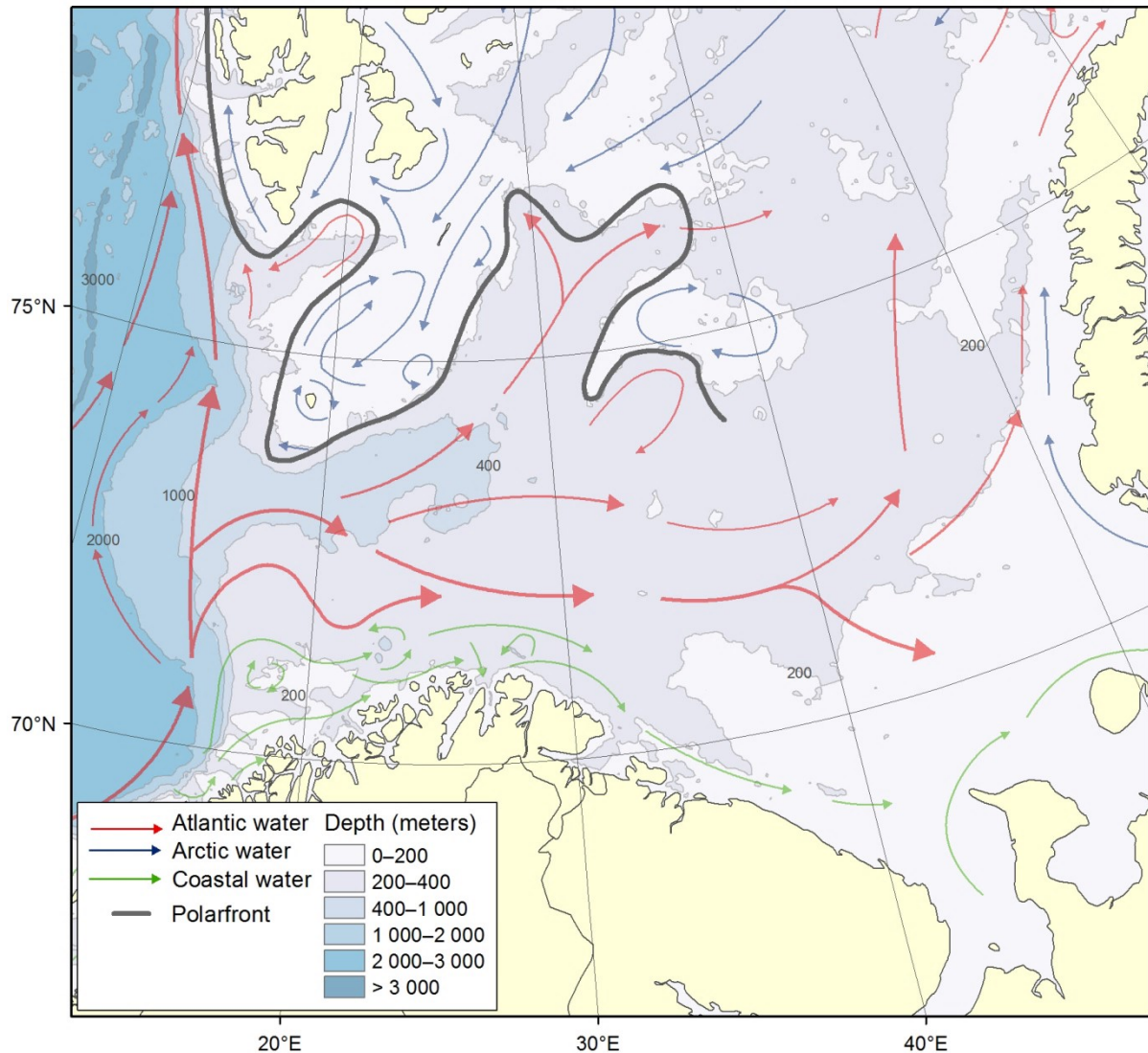
Figure 4.2 The main features of the circulation and bathymetry of the Barents Sea. Modified after Stiansen and Filin, 2008. Courtesy of Karen Gjertsen, Norwegian Institute of Marine Research. To be noticed the branches of the West Spitsbergen Current penetrating into the glacial troughs on the continental shelf (e.g. Storfjorden, Bjørnøyrenna, and possibly Kveithola Trough), following the contours and eventually turning and exiting again toward the continental slope.

4.4   Materials & methods

Multibeam bathymetric data were acquired during four different cruises with different vessels: SVAIS (Camerlenghi et al., 2007), EGLACOM (Zgur et al., 2008), GlaciBar (Andreassen et al., 2009), and CORIBAR (Hanebuth et al., 2013). The four datasets have been jointly reprocessed at OGS by importing all data in Caris Hips&Sips. Refraction problems were likely generated by closely spaced velocity changes in the water column, not always adequately sampled by the acquired SVP probes. We corrected for refraction problems during post processing with the refraction tool at our disposal in Caris. We applied Admiralty Tables Tide on all datasets. To reject spurious data, we used a surface filter based on 2D editing in Subset Editor. Caris Fieldsheets were exported in xyz

and imported in Global Mapper UTM 33 WGS84 (20 m grid size for depth less than −700 m and 40 m for deeper data). To maximize seafloor morphology we used a vertical exaggeration of 2.7 and Light Direction Attitude 35°, Azimuth −30°. We imported IBCAO 73°–78°N (UTM33), created an opportune common colorscale, and a contour layer based on all used dataset layers.

Parametric sediment echosounder data used in this study were acquired using the shipboard hull-mounted Parasound system (Atlas Hydrographic) on board of the German R/V Maria S. Merian during the MSM30 (CORIBAR) cruise in 2013 (Hanebuth et al., 2013). The Kveithola Trough and its drift deposits (including the perched sediment patches infilling a 50-km long, structurally controlled shallow-shelf channel connected to the inner trough from north) were covered with a dense grid of Parasound profiles. The chosen frequency of 4 kHz provides a vertical resolution of up to 20 cm, whereas the horizontal resolution is approximately 7% of the water depth. The maximum penetration of the acoustic signal was close to 40 m (estimated using a sound velocity of 1500 m/s for depth conversion). The Parasound data were processed and converted to seg-y data format using in-house developed software (H. Keil, University of Bremen), and successively displayed with the Kingdom Suite software (Seismic Micro-Technology).

A Gravity Corer with the variable lengths of 3, 6, or 12 m and a top weight of 1.5 tons was deployed within the Kveithola Trough during the CORIBAR cruise at 11 stations, and selected examples from these sediment cores are presented in this paper (see Table 4.1). Two cores (GeoB17607-5 and GeoB17612-4) were collected on the main drift body and two (GeoB17619-3 and GeoB17614-2) on the minor drift body. Of these, two (GeoB17607-5 and GeoB17619-3) are located on the center of the drift that is thick and well stratified, and two (GeoB17612-4 and GeoB17614-2) are located on southern flank of the drift where the Parasound data show a condensed succession. Before the cores were split for visual description and sampling, they were scanned with the Multi-Sensor Core Logger (MSCL) at MARUM (University of Bremen, Germany) using a step size of 1 cm for gamma-ray density and magnetic susceptibility measurements.

Five dating points (Table 4.2) were opportunely taken from the end of the core sections, before splitting (Grave, 2014). Those samples were collected in order to have preliminary reference information about the ages of the drift. Suitable samples of in-situ preserved bivalve shells, and scaphopods, were carefully selected for radiocarbon dating and measured at the accelerator mass spectrometer (AMS)-[14]C Radiocarbon Laboratory Poznan, Poland. The results were calibrated with CALIB v. 7.1.0 (Stuiver and Reimer, 1993) using the Marine13 calibration data set (Reimer et al., 2013) with an average marine reservoir effect dR = 67 ± 34 for the area south of Spitsbergen (Mangerud and Gulliksen, 1975). The mean values from the calibrated age range of ±1sigma are normalized to calendar year and indicated as cal a BP (or cal ka BP). In addition, the Median

Probability (MP) of the probability distribution that is determined by the software, is reported as more reliable estimation of the sample calendar age (Telford et al., 2004; online Calib Manual).

Table 4.1 Sediment cores.

Core ID	Core location	Coordinates	Water depth (m)	Sediment recovery (cm)
GeoB17607-5	Centre of the main drift	74°50.71' N 17°38.28' E	298	920
GeoB17612-4	Southern flank of the main drift	74°46.46' N 17°37.75' E	287	270
GeoB17614-2	Southern flank of the minor drift	74°47.64' N 18°08.76' E	287	796
GeoB17619-3	Centre of the minor drift	74°49.64' N 18°09.28' E	298	682

Table 4.2 Radiocarbon dating.

Core ID	Lab ID	Depth bsf (cm)	Sample type	^{14}C age (cal a BP)	1σ range (cal a BP)	2σ range (cal a BP)	Median Probability (cal a BP)
GeoB 17607-5	Poz-63467	920	Scaphopods	9250 ± 50	9891–10107	9754–10160	9980
GeoB 17612-4	Poz-64368	185	Bivalve shell	10230 ± 50	11106–11222	11010–11290	11160
GeoB 17612-4	Poz-64369	270	Planktonic foraminifera	11200 ± 50	12591–12693	12547–12757	12650
GeoB 17614-2	Poz-64371	Core catcher	Bivalve shell fragments	11600 ± 50	12929–13101	12820–13172	13010
GeoB 17619-3	Poz-64372	498	Scaphopods	8330 ± 40	8713–8919	8624–8970	8800

4.5   Results

4.5.1 External geometry of the drift

The Kveithola sediment drift has a complex morphology, comprising a main, outer drift body, about 200 km² in extent, and a minor, inner one about 100 km². In addition there are several small depocenters associated to these two deposits: two drift lenses as already highlighted by Bjarnadóttir et al. (2013) in the outer part of the Kveithola Trough (about 20 km²), more or less connected patches of local drift deposits in the innermost part of the Kveithola Trough, and other small perched sediment patches in local depressions in the channel north of the trough (Fig. 4.1).

The existence of further patch drifts in local depressions outside Kveithola Trough, beyond the coverage of our sub-bottom data, cannot be excluded.

The drift, comprised of lensoidal units, shows a thickness of up to over 30 ms in its center and thins towards the margins (Fig. 4.3). These units rest on top of a sub-parallel, more laterally continuous blanket. Overall, the drift has a broadly mounded shape. However, the geometry of the drift is largely controlled by the morphology of the underlying stratigraphic units. In fact, the highs within the drift correspond to elevated areas of the underlying glacial units. The disconnection of the main (outer) and minor (inner) drift body is similarly related to the underlying morphology: a buried GZW, transverse to the axis of the Kveithola Trough, is located between the main and minor drift bodies, and only covered by a greatly reduced drift thickness (less than 5 ms). Due to this topographic control by the underlying strata, the morphology of the drift is complex, showing several local highs, and the areas of maximum thickness (highest sedimentation rate) do not necessarily correspond to bathymetric highs or basement lows (see Fig. 4.3).

The thinning by lateral termination of the internal seismic reflectors occurs in an asymmetric way with an abrupt pinch-out on the northern edge and gradual tapering on the southern edge (Figs. 4.4 and 4.5). To the south the drift has a sedimentary tail that progressively thins southward due to reduced sedimentation rate during deposition as shown by the seismic profiles (see the following chapter). This tail onlaps the southern flank of the Kveithola Trough and its tip is located at about 250 m water depth, thus about 50 m shallower than the central, mounded part of the drift found at about 300 m water depth.

4.5.2 Internal geometry of the drift

The seismic expression of the Kveithola Drift is mainly well-stratified, characterized by sub-parallel reflections of moderate to high amplitude and good lateral continuity, without any major unconformity. The subdivision of the sedimentary fill into seismic units was done by means of an analysis of reflection terminations and internal reflector patterns (Fig. 4.6). In the following, we describe reflection horizons and intervening seismic units stratigraphically from bottom to top:

Horizon 1 (cyan): Bottom of the glaciomarine unit and top of the underlying glacial till. The horizon is identifiable throughout the whole trough, marking the change from transparent (below) to layered (above) strata and is concordant with the overlying Horizon 2.

Unit 1.a: Reflections with the highest amplitudes are observed within this unit. However, they become faint and semi-transparent towards the bottom and top of this unit. Reflector configuration within the unit is parallel. The thickness of this blanket unit (about 15 ms) is laterally remarkably uniform. Although reflections are continuous and parallel inside the trough, this continuity is often lost at the flanks.

Horizon 2 (red): Main internal acoustic boundary of the glaciomarine blanket. This distinct regional reflector corresponds to reflector D1 of Rebesco et al. (2011).

Unit 1.b: This unit is made of moderate amplitude, high-frequency, parallel internal reflections. The lower part of this unit is the upper section of the glaciogenic blanket.

Horizon 3 (green): Base of the drift, which overlies concordantly Unit 1.b. This horizon marks a sharp change in acoustic facies from the well-layered, moderate-amplitude reflections of the unit 1.b to lower amplitudes above. It corresponds to the base of drift 2 of Bjarnadóttir et al., 2013 (see Table 4.3).

Unit 2.a: This unit has low amplitude reflectors. The basal reflections terminate in an onlap onto Unit 1.b at the periphery of the drift. In some cases, a sedimentary mound with downlap in both directions is observed (Fig. 4.7).

Horizon 4 (dark blue): Strong internal reflector within the lower part of the drift. It marks the change from low amplitude reflectors (below) to moderate amplitude reflectors (above).

Unit 2.b: The amplitude of reflectors in this unit is generally higher than in the underlying one and increases upward in many cases (Fig. 4.6). Local downlap onto the underlying Horizon 4 is often noticeable (Fig. 4.7).

Horizon 5 (light blue): Top of the lower part of the drift (top of drift 2 of Bjarnadóttir et al., 2013). Locally, the continuity of this boundary is interrupted by small depressions (interpreted as palaeo-pockmarks).

Unit 3.a: Semi-transparent unit at the base of the upper part of the drift (the drift 1 of Bjarnadóttir et al., 2013).

Horizon 6 (dark pink): Local, small-scale depressions or palaeo-pockmarks are present along this boundary (Fig. 4.6). It marks the change from low amplitude reflectors (below) to moderate amplitude reflectors (above).

Unit 3.b: This unit has relatively high amplitude reflectors, which is generally increasing towards the top (Fig. 4.6). Local downlap onto the underlying Horizon 6 is often noticeable.

Horizon 7 (pink): This reflector marks the transition from relatively high amplitude reflectors (below) to very low amplitudes (above).

Unit 4: This unit has very low amplitude reflectors and it appears, in pseudo-relief plots, to be almost acoustically transparent.

Seafloor (yellow): The seafloor is always a very high amplitude reflector, locally showing small depressions interpreted as pockmarks (e.g. Figs. 4.5b and 4.6).

Table 4.3 Comparison, using two crossing sub-bottom profiles, between the seismostratigraphic interpretation of this study (profile 20130724-014159) and that of Bjarnadóttir et al., 2013 (profile 09KA_JM081). In the two outermost columns, the available datings (in cal. ka BP) are indicated.
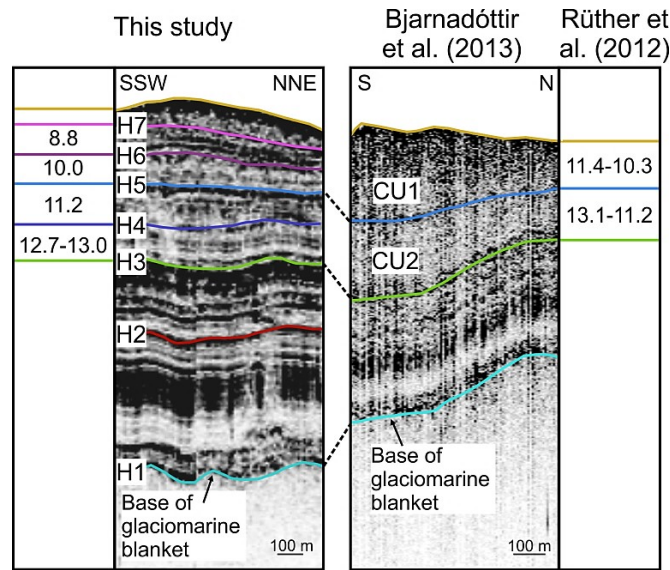
The depocenter onlaps onto the underlying well-stratified units at its periphery and onto the underlying highs (GZW). The reflection amplitudes tend to vary vertically in a recurrent pattern (Figs. 4.4–4.6). In particular, two units display high amplitude reflectors (Units 2.b, 3.b). These units show a lensoidal character (mainly towards the periphery of the drift) and are of restricted lateral extension. In fact, their margins terminate in advance with respect to the underlying and overlying more transparent units (Fig. 4.6).

Nonetheless, the most distinctive feature of the drift is the termination of reflectors towards the moat, i.e., the channel-like morphological depression along its northern edge (Figs. 4.4-4.5). This termination, locally very abrupt with a reduction of more than 20 m in thickness over a distance of only a few hundreds of meters, seems to be produced initially by erosion and later by persistent non-deposition (Figs. 4.4 and 4.5). In fact, the moat is mainly produced by downlap and pinching out of drift strata against the top of the underlying glaciomarine blanket that drape the entire Kveithola Trough. Close to the termination, the lower reflectors of the drift dip towards the center of the Kveithola Trough like those of the glaciomarine blanket, but the upper reflectors of the drift dip into opposite direction due to the progressive thickening at the center of the drift, which continued to the present (see the close-up A in Fig. 4.4). In general, the lower drift units (Units 2.a and 2.b) close to the moat are more affected by erosion, whereas the upper drift units (Units 3.a and 3.b) are more affected by downlap termination. Downlap is also visible at the base of the drift (onto the green Horizon 3) within local sediment mounds (Fig. 4.7). The internal character of the drift body located at the innermost part of the Kveithola Trough is condensed and it is not possible to distinguish different internal units (Fig. 4.8). In that area, the drift is constituted of transparent facies and seems to present several adjacent depocenters or connected patch-drifts.
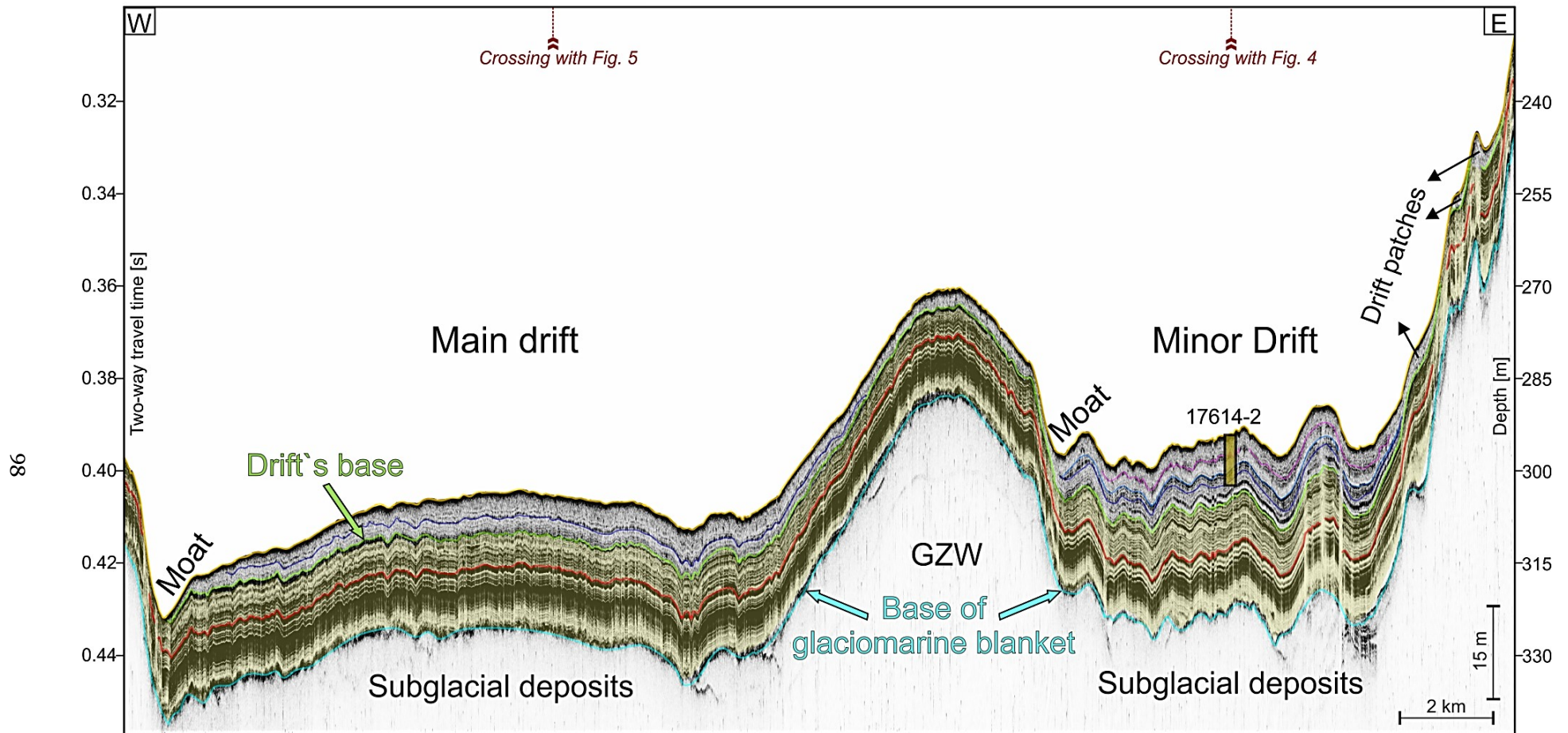
Figure 4.3 Longitudinal E–W trending Parasound profile across the main and minor Kveithola Drift body. The morphology of the drift is strongly controlled by the morphology of the underlying stratigraphic units. The drift thins across a pre-existing bathymetric high (a GZW), whereas the underlying glaciomarine blanket (highlighted in yellow in all seismic profiles) is less affected (almost constant thickness). See location in Fig. 4.1. (For interpretation of the references to colour in this figure legend, the reader is referred to the web version of this article).
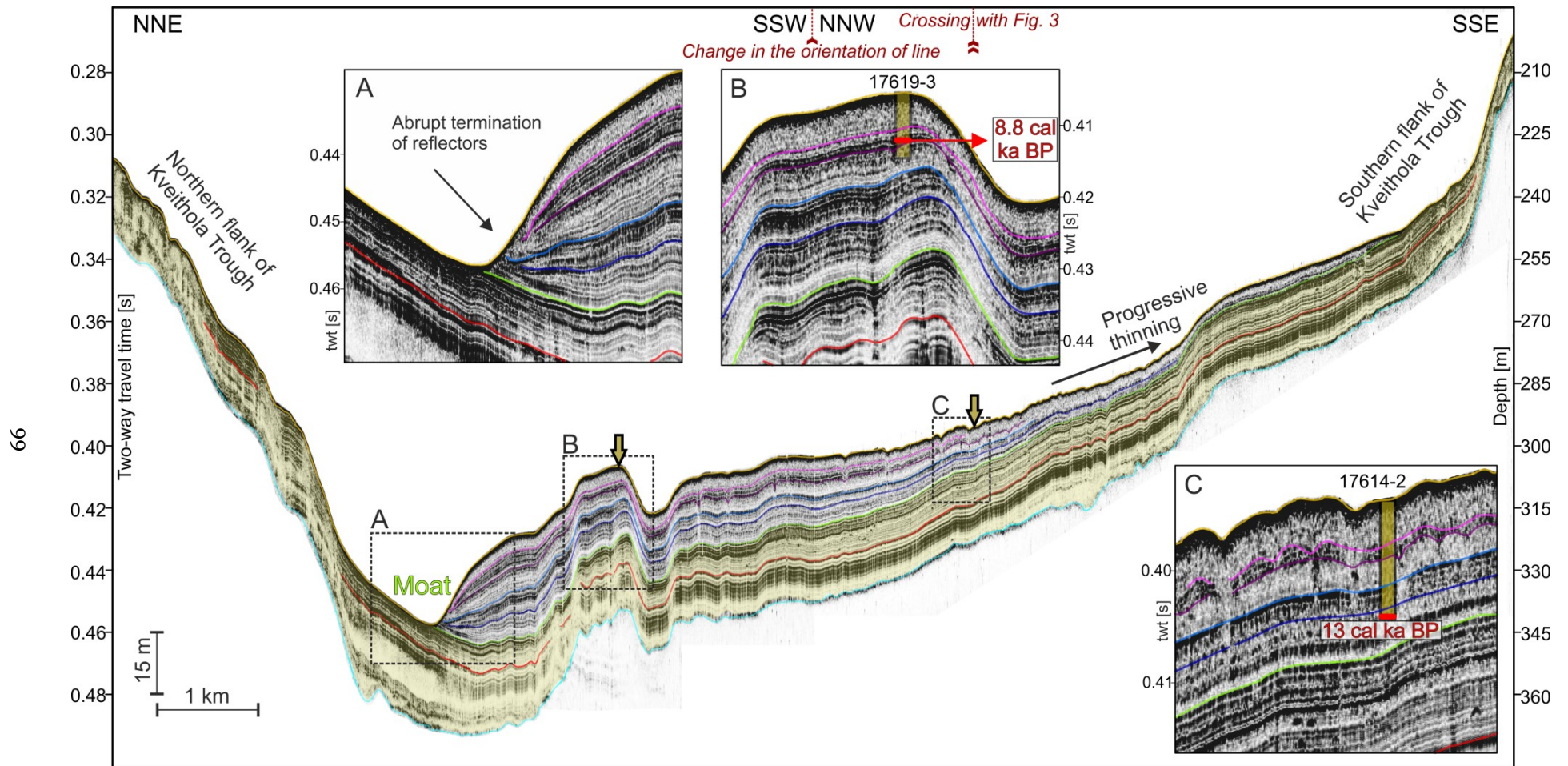
Figure 4.4 Transversal NNE–SSW Parasound profile across the main Kveithola Drift body. The drift shows an abrupt pinch out towards the moat on the northern edge and a progressively thinning tail on the southern edge. Locations of core GeoB17607-5 from the central (expanded) part of the drift and of core GeoB17614-2 from the marginal (condensed) part of the drift are also shown. See location in Fig. 4.1.

Figure 4.5 Transversal N–S Parasound profile across the main Kveithola Drift body. Locations of core GeoB17619-3 from the central (expanded) part of the drift and of core GeoB17612-4 from the marginal (condensed) part of the drift are also shown. See location in Fig. 4.1.
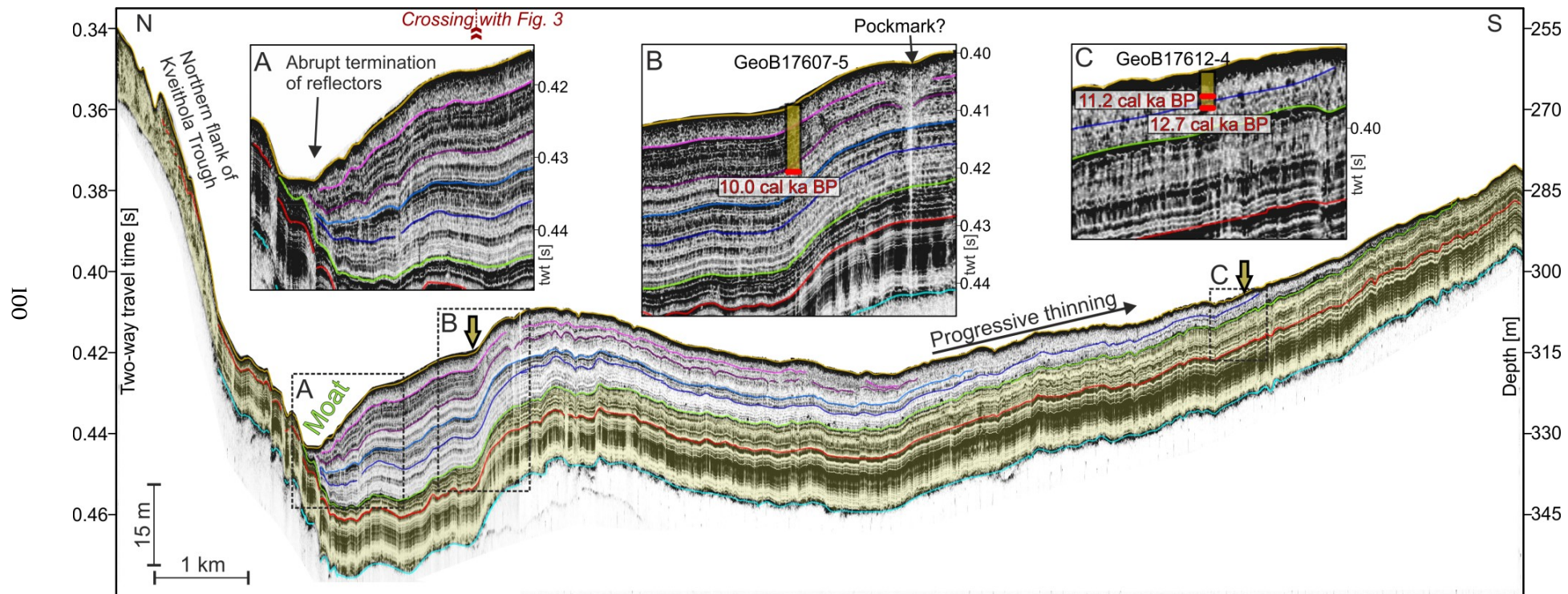
4.5.1   Lithological characteristics and sedimentary sequence

The sedimentary sequence recovered in the area of the Kveithola drifts contains two main stratigraphic intervals. The younger one is formed by heavily bioturbated sediments with abundant silty/sandy mottles, and sparse shell fragments (light and dark cyan backgrounds in Fig. 4.9). The older stratigraphic interval is characterized by higher values of magnetic susceptibility and lower values of wet bulk density (light and dark pink backgrounds in Fig. 4.9). Articulated bivalve shells and scaphopod tubes, both in life position, occur scattered throughout the sediment and were the most suitable targets for dating (Fig. 4.9). The sediments are bioturbated and locally finely laminated (e.g. core 17612-4, 2.55–2.70 m; 17614-2, 4.20–6.60 m). Sparse IRD occur at the base of core 17614-2. The transition between the two main stratigraphic intervals corresponds to an irregular, possibly erosive surface, which is overlain by normally graded sediments located at the base of the younger interval as detected during the visual description of the cores. In core 17612-4, the graded sands at the base of the younger interval, contain mud chips (Fig. 4.9), whereas in core 17607-5 such transition appear more gradual. According to our radiocarbon dating the transition between the two stratigraphic intervals occurs at 8.8 cal ka BP (based on core 17619-3, Table 4.2).

Core correlation based on the lithological succession, magnetic susceptibility and the five radiocarbon dates (Table 4.2), reveals that core 17607-5, located in the center of the well-stratified main, outer drift body, contains the most expanded (high-resolution) sequence, recording the last 10 ka; core 17619-3, located in the center of the minor, inner drift body (eastern part, Fig. 4.1), contains a more condensed succession; and cores 17614-2 and 17612-4 located along the southern flank of the minor and main drift bodies, respectively, recovered the most condensed part of the drift depocentre spanning the last 13 ka.

4.6   Interpretation

We consider the abrupt termination to the north of the internal reflectors of seismic Units 2a to 4 and the broadly mounded geometry of the Kveithola Drift as principal diagnostic features allowing it to be interpreted as a bottom current-controlled sediment drift. This interpretation is consistent with the sediment characteristics observed in the core dataset (see Stow and Faugères, 2008 and references therein for contourite facies) and with the interpretation of Bjarnadóttir et al. (2013), who first recognized the presence of a drift within the Kveithola Trough. Furthermore, we interpret that the moat, with reflector termination along the northern edge of the drift, to have been formed by focused bottom currents (Faugères et al., 1999; Rebesco and Stow, 2001; Stow et al., 2002; Rebesco, 2005; Rebesco and Camerlenghi, 2008b; Rebesco et al., 2014a). This moat extends as a laterally continuous feature along the entire northern edge of the drift, with local

bends and a more pronounced character in correspondence of local morphologic promontories. The moat therefore provides a means to reconstruct the path of the inferred bottom current flow that controlled the development of the sediment drift and its geometry (Fig. 4.10).
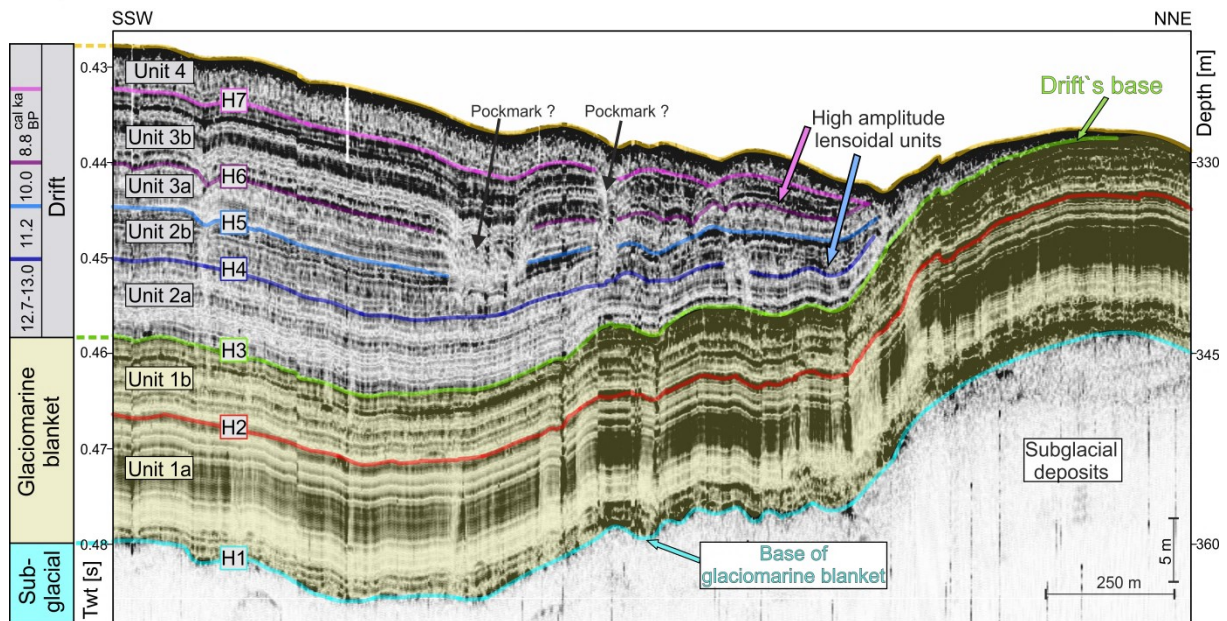

Figure 4.6 Close up of NNE–SSW Parasound profile across the northern edge of the Kveithola Drift. Identified seismic horizons and intervening units are indicated. The available datings are indicated in the column to the left. The relatively minor extent and higher amplitude of Units 2.b and 3.b are apparent. See location in Fig. 4.1.

Conversely, no moat is visible on the southern edge of the drift. In some places a polished floor with relatively coarser sediments (swept by bottom currents) borders the southern margin of the drift where the slope locally steepens. Nonetheless, the drift sediments are thinning very gradually to the south, and eventually terminating at a seafloor depth much shallower than that of the moat on the northern edge (Figs. 4.4 and 4.5). The drift is hence confined to the deeper part of the Kveithola Trough, but it does not display the typical geometry of confined drifts. Such drifts are typically mounded, elongated along the main axis of the trough and show a moat on both flanks of the trough (Faugères et al., 1999; Stow et al., 2002; Rebesco et al., 2014a). In the typical confined drift case, the bottom current flows in opposite directions on the two opposing flanks of the drift. The hypothesis of a confined drift is, however, not completely discarded for the Kveithola Drift, but the typical confined drift case described in the literature does not seem to apply here. This may be due to the fact that the bottom current flows on one flank of the drift differs significantly from that on the opposite side (see the following discussion in the chapter "Water masses responsible for drift genesis").

It is often a challenge to differentiate whether a stratified, slope-related depocenter is mainly built up by current-controlled (contouritic) or by gravity-driven (turbiditic) sedimentation processes

(Rebesco et al., 2014a). Thus, the diagnostic information obtained needs to be interpreted carefully. A turbiditic system would result in a uniform or fan-like infill of pre-existing depressions with ponding of reflectors in the deepest parts and onlap at the depression margins. The geometry of the Kveithola drift (Figs. 4.4 and 4.5) show downlaps and a moat, suggesting that some contribution of sediments from turbidity currents to the formation of the sedimentary body occurred (e.g. irregular surfaces overlay by normally graded sands with mud chips of core 17612-4, Fig. 4.9) but it was completely subordinate, at a large scale, to bottom water reworking of sediments.
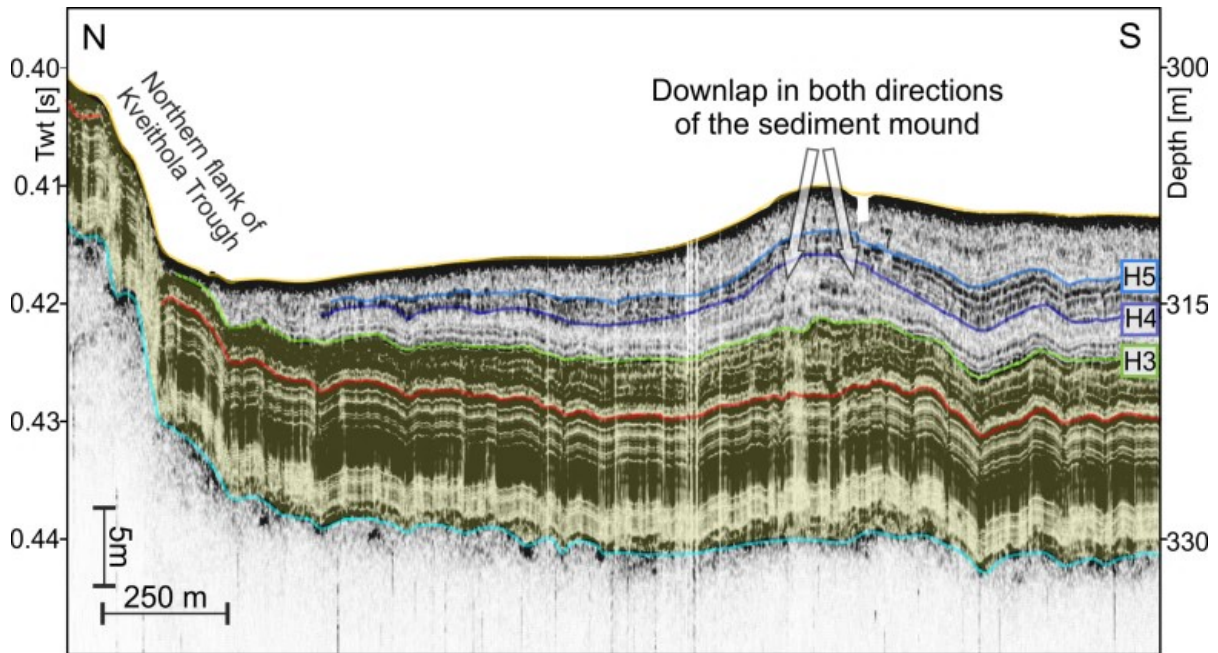
Figure 4.7 Close up of N–S Parasound profile across a mounded feature on the western edge of the Kveithola Drift. A marked downlap in both directions can be observed within this small sedimentary mound. See location in Fig. 4.1.
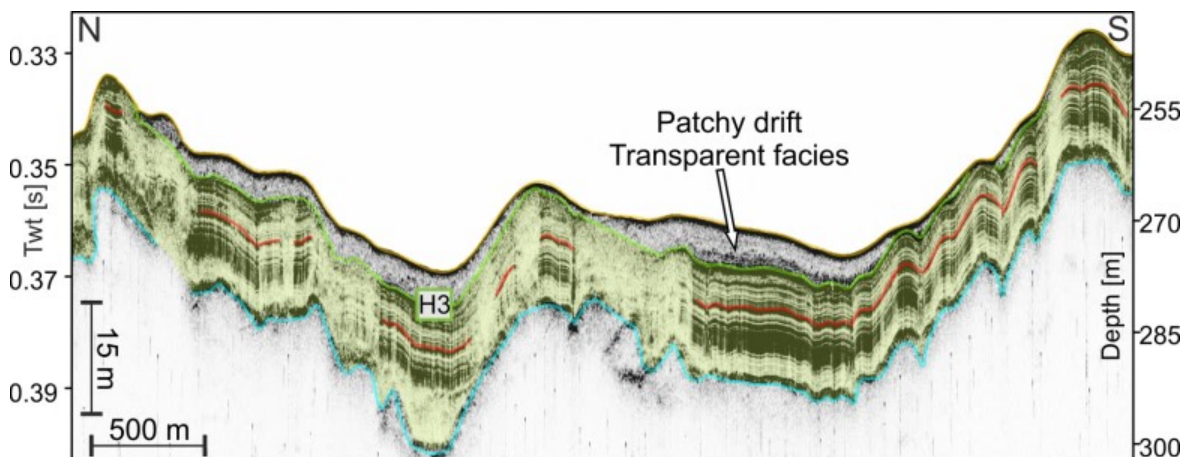
Figure 4.8 Transversal N–S Parasound profile across the eastern edge of the innermost part of the Kveithola Drift. In this area, the drift shows condensed, transparent facies and includes several depocenters or connected patch-drifts. See location in Fig. 4.1.

We note that the seismic facies of Units 2.b and 3.b shows a higher amplitude, a more pronounced lensoidal geometrical character and a restricted lateral extent (more prone to terminate against the highs) with respect to the other drift units (Fig. 4.6). We infer that this acoustic character suggests the occurrence of more energetic sedimentary conditions. The higher amplitude may correspond to a higher density contrast between sedimentary beds of variable mean grain size. This interpretation is also supported by the presence of normally-graded internal laying above irregular/erosive bases (e.g. cores 17612-4, 104 cm; 17614-2, 420 cm; 17619-3, 498 cm, Fig. 4.9). In core 17612-4 the coarser part of this graded interval contains also mud chips, supporting the hypothesis of quite energetic flows. Enhanced sediment transport could either take place in the form of downslope flow, like turbidity currents, or in the form of a more persistent sandy grain flow having a pulsing-mode supply type such as storm wave activity on the surrounding shelf banks. Such a supply could also occur in the form of suspension clouds originating on the shallow shelf and raining down over the depression as known from slope canyon systems and from shelf edges (Bender et al., submitted; Voigt et al., 2013). Alternatively, the higher density contrast between coarser and finer sediments may reflect a variation in strength of the bottom current (coarser grained sediments resulting in stronger reflections during periods of intensified velocity).

We also note that the depocenters of the main, minor and patchy, innermost drift bodies are not in a central position with respect to their lateral extents but are displaced towards the moat (Figs. 4.10 and 4.11). This is exactly what is expected in case of sediment delivery by a bottom current running inside the moat. In fact, where the bottom current is the main factor controlling sediment deposition, it is common to find the depocenter in relatively slack water next to the current axis where the sediment transport occurs (Rebesco et al., 2014a). The patchy drift in the innermost part of Kveithola Trough shows a completely transparent, condensed and mounded (not ponding, nor draping) seismic facies. These characteristics also hint to a bottom current control rather than to turbidity current or hemipelagic draping processes (Fig. 4.8).

We noticed that the older drift units (Units 2.a and 2.b) appear to be more affected by erosion (Fig. 4.6) than the overlying drift units (Units 3.a and 3.b). The lower drift units also show local sediment mounding with downlap on both opposing sides (Fig. 4.7). This configuration may suggest variability on the current strength and path. In particular, this configuration may indicate that the drift was more actively shaped in its earlier phase, a time with a powerful bottom current flow regime, while deposition was maintained and enhanced with continuous growing in its upper part. We hence assume that the lower part of the drift can be ascribed to the overall shaping phase and the upper drift part to the later growth phase.

The thickness of the underlying glaciomarine blanket is remarkably constant (across the whole trough) and is scarcely affected by the preconditioned morphology of the subglacial sediment underneath. This observation confirms the interpretation that these glaciomarine deposits are mainly affected by vertical settling, i.e., hemipelagic draping during open water conditions, plumite fall-out and ice-rafted debris as suggested by previous authors (Rebesco et al., 2011; Rüther et al., 2012; Bjarnadóttir et al., 2013; Lucchi et al., 2013; Hanebuth et al., 2014; Lucchi et al., 2015).
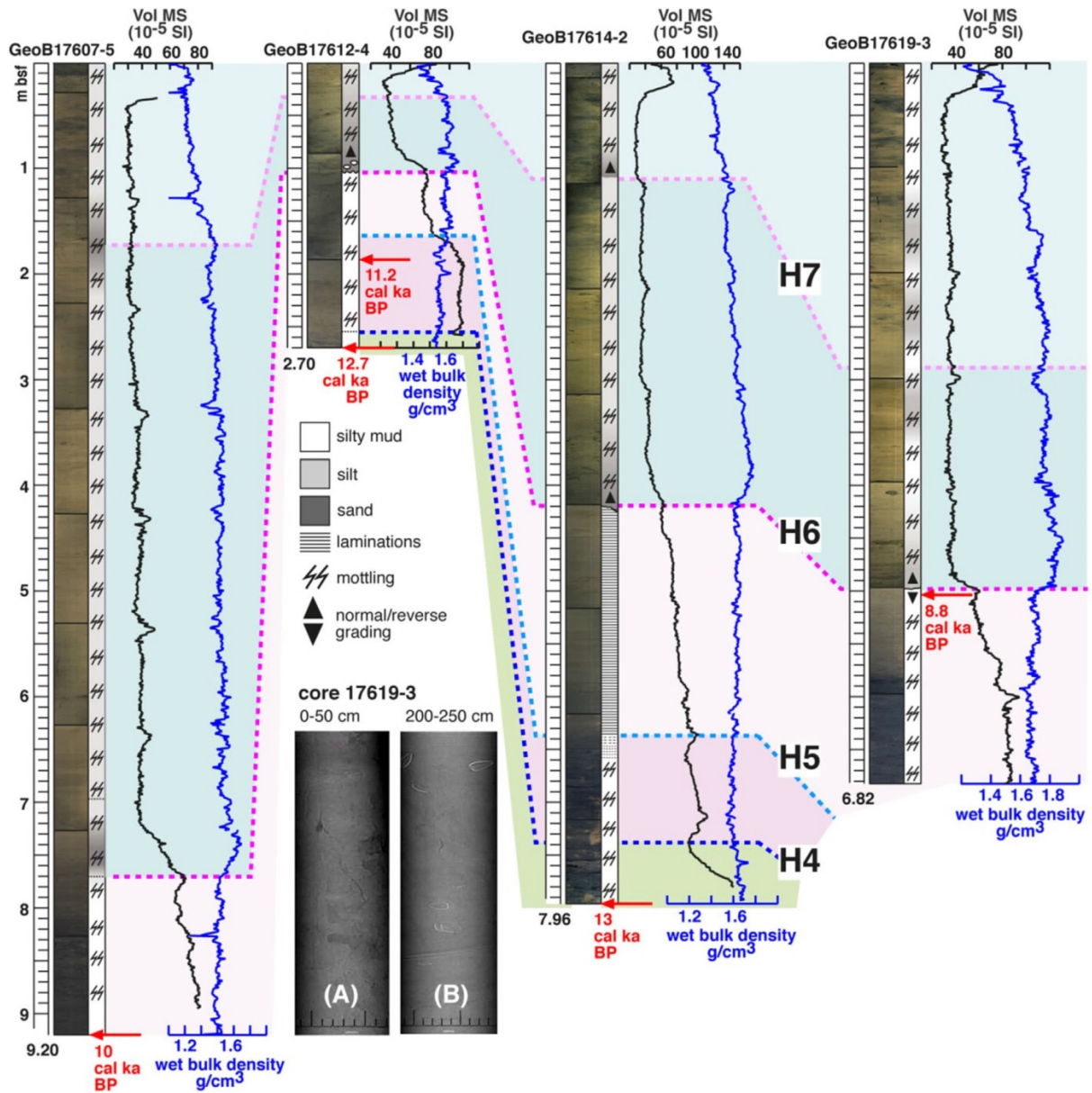
Figure 4.9 Down core logs of four selected cores from the main and minor Kveithola Drift bodies showing sediment photographs, lithology (log), magnetic susceptibility (black curve) and bulk density (blue curve). Core correlation is based on sediment facies, magnetic susceptibility and wet bulk density trends, and 5 calibrated ¹⁴C dates (red arrows). Two x-ray facies are also included to show two typical sedimentary structures: bioturbated mud (A) and articulated bivalve shells (B). Core location in Fig. 4.1.
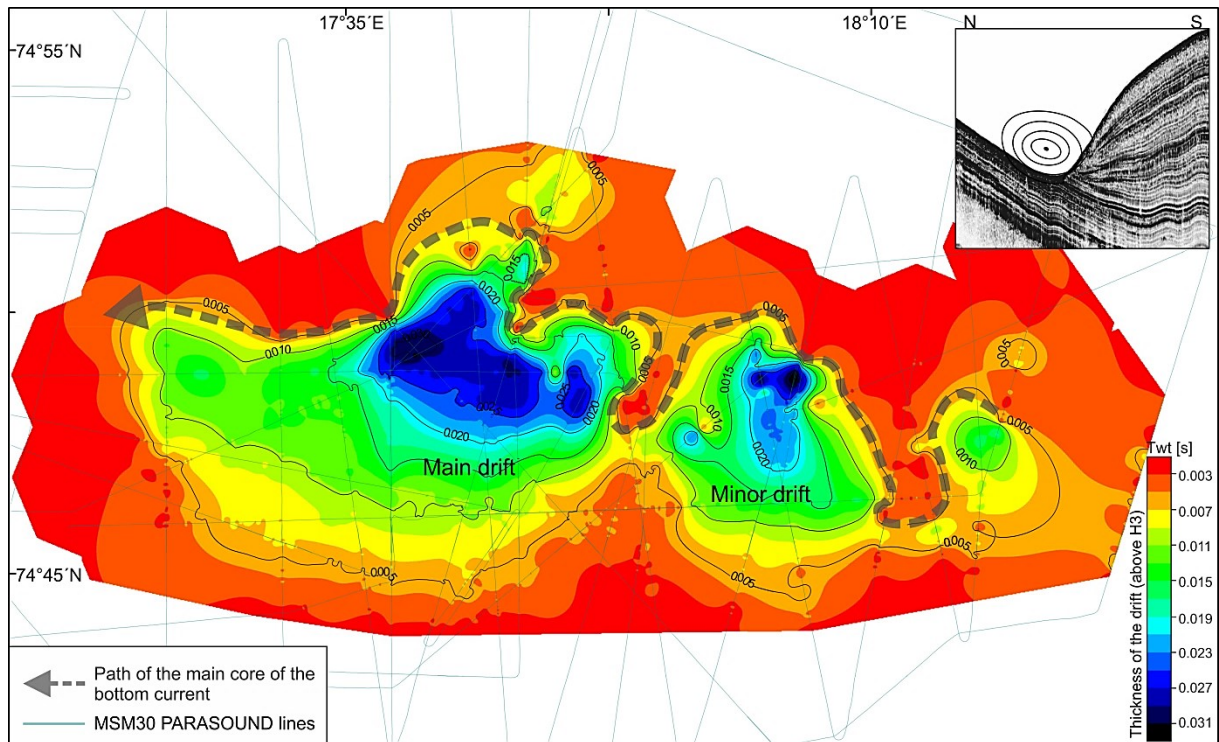
Figure 4.10 Isochore time map showing the sediment thickness (in seconds) of the Kveithola Drift. Location of all Parasound profiles acquired in the drift area during cruise MSM 30 is also shown. The detailed path of the main core of the bottom current (dashed line) is interpreted by connecting the position of the moat in the various Parasound profiles. The inset shows an example of the moat visible in seismic section with drawing of the inferred core of the bottom current.

4.7 Discussion

4.7.1 Water masses responsible for drift genesis

The geometry of the drift suggests a powerful bottom current on the northern side of the Kveithola Trough. Such a current may have three possible origins:

1)   Atlantic Water;

2)   Arctic water;

3)   Brine-enriched shelf water (BSW).

1) In the first case, a branch of the West Spitsbergen Current could enter the trough from the west (Fig. 4.12). This scenario would be favoured by the Coriolis force pushing the current towards the right and the Atlantic water would follow the bathymetry and turn against the northern trough slope at the eastern termination of the trough. A similar process is already documented to happen in Storfjorden (e.g. Midttun, 1990; Fohrmann et al., 2001; Stiansen and Filin, 2008). In this case two opposing currents would develop on the two sides of the Kveithola Drift, as it is described for confined drifts (Faugères et al., 1999). However, on the southern edge of Kveithola Trough no moat is visible and there the sedimentary tail of Kveithola drift is relatively shallow (up to 250 m

depth). This observation is not consistent with this scenario since it is difficult to envision a bottom water that does not leave any significant erosive imprint on the southern edge of the drift whereas at a few km distances it is able to generate a moat at nearly 350 m water depth on the northern edge.

2) In the second case, cold Arctic water enters the region from the northeast and reaches the eastern end of the Kveithola Trough (as documented by Stiansen and Filin, 2008). The cold Arctic water may enter the trough and follow the bathymetry. However, this water is characterized by low salinity and it is a relatively superficial water mass that by itself is not likely to sink from Spitsbergenbanken to the bottom of the Kveithola Trough and prevent deposition of sediments on the seafloor.

3) BSW is produced during winter and forms a shelf water (Aagaard et al., 1985) which accumulates in morphological depressions of the continental shelf. In due course, this dense water spills over the depressions and cascades into the regional troughs and then down the continental slope. Dense shelf water is known to have the capacity to locally erode the seafloor, to transport significant amounts of sediment into the deep sea, and to lead to the formation of local depocenters (Fohrmann et al., 1998). We therefore consider it most probable that such dense water mass flow is responsible for the genesis of the Kveithola Drift and for the moat at its northern edge.

4.7.2 History of BSW production

The moat in the Kveithola Trough has been active since the time of Horizon 3, which defines the base of the drift. This situation suggests that the formation of BSW started around 13 cal ka BP, as determined by the oldest date from the lowest part of the drift. The same age was obtained by Rüther et al. (2012) for the onset of drift deposition. It is hence inferred that the onset of BSW production was a response to climatic forcings as the atmospheric cooling of the surface waters on the western Barents Shelf or the presence of coastal polynyas and wind influence (e.g. Skogseth et al., 2008; Wobus et al., 2013). We infer that such conditions persisted since the onset of drift deposition. BSW production could also have been somehow related to the re-establishment of the inflow of Atlantic water following the last glacial maximum. However, the shift to interglacial conditions is inferred to have occurred at 11.2 cal ka BP (Jessen et al., 2010) and brine formation is inferred to have further increased from about 8200 years BP reaching periodic maxima during the last 4000 years BP (Rasmussen and Thomsen, 2014; 2015).

Conversely, other processes seem to have prevailed prior to drift deposition when the glaciomarine drape formed (Units 1.a and 1.b). The underlying glaciogenic blanket, inferred to have been deposited during the Bølling/Allerød interval (14.6–13.9 cal ka BP; Rüther et al., 2012;

Bjarnadóttir et al., 2013), is assumed to be characterized by the presence of plumites and ice-rafted debris. Therefore, melt water production seems to have persisted in Kveithola pointing to ice cover on the shallow Spitsbergenbanken during that time interval.

Unit 2.b developed between 12.7 cal ka BP (the age point just below Horizon 4, Figs. 4.5c and 4.9) and 11.2 cal. ka BP (the date from the condensed succession above Horizon 4, Figs. 4.5c and 4.9). This latter age is consistent with a date of 11.2 cal ka BP obtained by Rüther et al. (2012) for the end of Drift 2 deposition, which corresponds to the overlying Horizon 5 in this study. The lower part of Unit 2.b may hence have deposited during the Younger Dryas (12.8–11.7 cal ka BP, Broecker et al., 2010), when there was an intensifying of ice conditions as documented by low primary productivity (Aagaard-Sørensen et al., 2010) and enhanced IRD supply (Ślubowska-Woldengen et al., 2007). Though thermohaline circulation may have been hampered during this period by an increase in freshwater supply (Hald and Hagen, 1998; Ebbesen and Hald, 2004; Ślubowska-Woldengen et al., 2007), a stronger brine formation occurred (Rasmussen and Thomsen, 2014; 2015).

We infer that more energetic sedimentary conditions were present during the development of the higher amplitude, less extensive Unit 2.b (and 3.b) with respect to the lower amplitude, more extensive Unit 2.a (and 3.a). This situation is in apparent contrast with a general reduction in bottom current activity during the Younger Dryas period (Hald and Hagen, 1998; Ebbesen and Hald, 2004; Ślubowska-Woldengen et al., 2007), but is in agreement with the evidence for stronger BSW formation in the nearby Storfjorden (Rasmussen and Thomsen, 2014; 2015). The following stage of the drift (upper drift interval, Drift 2 of Bjarnadóttir et al., 2013) developed during the Pre-boreal time interval, which was characterized by a sudden rise in sea surface temperatures of the Arctic Water (Hald et al., 2007), with high primary productivity and absence of IRD (Aagaard-Sørensen et al., 2010). In Unit 3.b, similarly to Unit 2.b, we infer more energetic sedimentary conditions (erosive/irregular surface overlain by normally graded sediments, Fig. 4.9). The erosive surfaces of this lithological boundary are particularly evident in the most-southerly cores (17612-4 and 17614-2). Such depositional conditions may reflect a new period of climatic deterioration. The only age we have for this unit (younger than 8.8 cal ka BP.) indicates that at least parts of the unit were deposited during the short atmospheric cooling interval of 8.8–8.2 cal ka BP, reported by Sarnthein et al. (2003b). The younger Unit 4 would therefore have developed during the Holocene thermal optimum, which occurred at about 8 cal ka BP according to Hald et al. (2007).
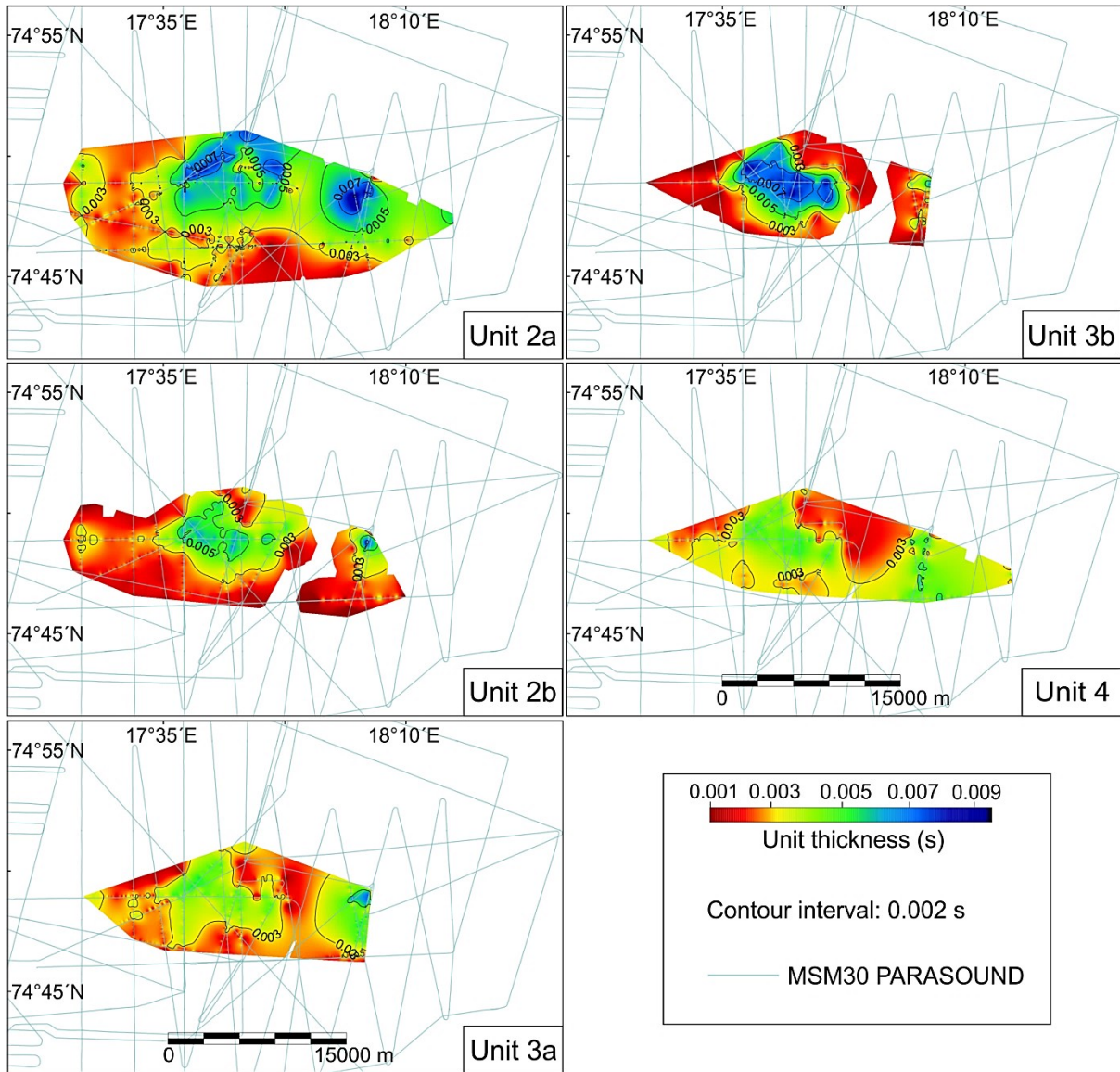
Figure 4.11 Separate isochore time maps showing the sediment thickness (in seconds) of the various units of the Kveithola Drift. Location of all Parasound profiles acquired in the drift area during cruise MSM 30 is also shown.

We therefore infer that the broad variations in current regime were mainly related to fluctuations in BSW formation intensity that we assume was connected to the variations in the regional atmospheric temperature and/or presence of coastal polynyas and wind influence. However, it is also likely that changes in the intensity of BSW formation are a response to successively retreating grounded ice as well as development from perennial to seasonal sea ice conditions that allowed the stepwise establishment of initially limited, and later open, shelf current system on the western Barents shelf.

The mean winter limit of sea ice extension is controlled by the flow of Atlantic water and broadly corresponds to the position of the Polar Front. Its position in the western Barents Sea is fairly stable at present days. The fluctuations through time during the Holocene, determined by

investigating past ice extents and oceanographic conditions in sedimentary records, allowed an evaluation of variations in Atlantic water inputs to the Arctic (Voronina et al., 2001). During the 11.0–10.5 ka BP time interval the Polar Front was located close to the Barents Sea margin and then moved eastward till 7.5 ka BP when the present-day oceanographic pattern was established (Risebrobakken et al., 2010). The mid Holocene (8–5 cal ka BP) was in general characterized by relatively warm and stable conditions. In contrast, highly variable conditions were recorded since about 5 cal ka BP, with cooler temperatures and extended sea ice cover with southward migration of the Polar Front (Voronina et al., 2001).
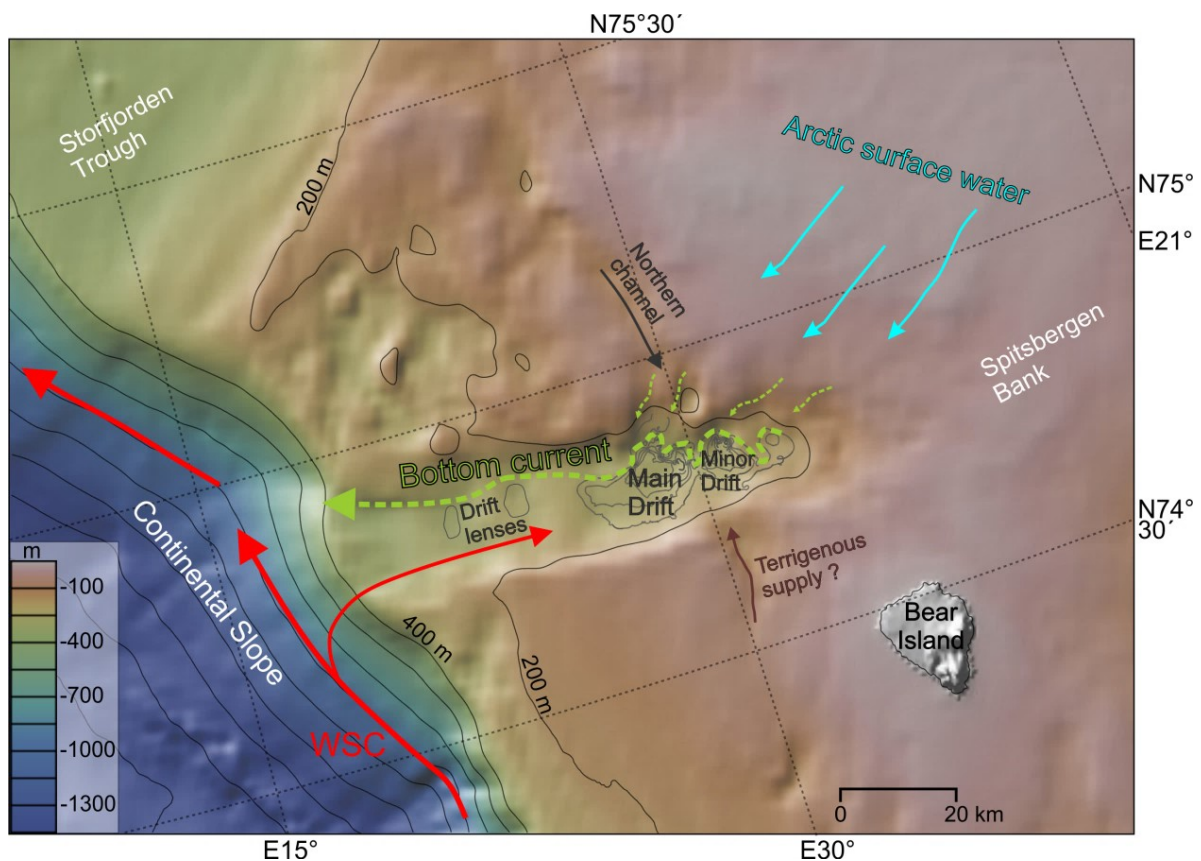
Figure 4.12 Schematic diagram of the inferred currents in the Kveithola Trough area superimposed onto IBCAO bathymetry (Jakobsson et al., 2012) plotted using GeoMapApp (http:// www.geomapapp.org). The contours of iso-thickness of the Kveithola Drift (every 5 ms) are also shown. A branch of the West Spitsbergen Current (WSC) (red arrow), may enter the trough, follow the bathymetry and turn west on the northern side. In light blue is the cold Arctic surface water coming from the north. Bottom current flow (green dashed arrows) within the moat to the north of the Kveithola Drift is inferred to be comprised of brine-enriched shelf water spilling from morphological shelf depressions to the north of the Kveithola Trough. A possible preferential terrigenous supply (mainly through a structurally controlled southern channel) is also shown (brown arrow). (For interpretation of the references to colour in this figure legend, the reader is referred to the web version of this article).

4.8 Conclusions

- We provide detailed morphological, seismostratigraphic, lithological and sedimentological insights into the construction of the Kveithola trough-confined drift.

- This drift is characterized by a complex structure comprising a main and a minor drift bodies, two drift lenses in the outer part of the trough, a series of more or less connected drift patches in the innermost part, and small perched sediment patches in a channel to the north.

- The drift mainly shows sub-parallel reflections of good lateral continuity, an abrupt northward pinch-out forming a typical drift moat, and gradual tapering to the south.

- We identified the base of the drift and four internal horizons, defining 5 sedimentary units, which we correlated throughout the drift.

- Two units display high amplitude reflectors, a marked lensoidal character and restricted lateral extension, suggesting more energetic sedimentary conditions.

- Sedimentary cores show a facies typical for contourites with strongly bioturbated sediments, abundant silty/sandy mottles and shell fragments.

- The drift morphological and internal characteristics suggest a strong control by a bottom current flowing inside the trough, mainly along the moat at the northern edge of the drift.

- Brine-enriched shelf water (BSW) produced during the winter season is inferred to be the driver responsible for the genesis of the Kveithola Drift. The BSW flows westward along the moat before cascading the continental slope.

- The formation of BSW is inferred to have started around 13 cal ka BP, the onset of drift deposition, suggesting that atmospheric cooling of the surface waters and/or the presence of coastal polynyas and wind influence on the western Barents Shelf dominated from this time. In alternative, supercooled water masses formed below a floating ice shelf may have influenced BSW formation (Borchers et al., 2015).

- We suggest that the two units with marked lensoidal character show more energetic sedimentary conditions. Though we do not have yet conclusive dating for these units, sediment and seismic correlation suggest they date Younger Dryas and 8.8–8.2 cal ka BP respectively. This situation during cold periods is in apparent contrast with a general reduction in bottom current activity indicated by Hald and Hagen (1998), Ebbesen and Hald (2004), Slubowska-Woldengen et al. (2007), but in agreement with the evidence for stronger BSW formation in the nearby Storfjorden (Rasmussen and Thomsen, 2014, 2015).

- More detailed insight into these processes may be gained through sedimentological analysis of the available sediment cores, for which this seismostratigraphic study provides a solid framework.

Acknowledgements

5   Conclusions and future perspectives

5.1   North Sea

The main aim of this thesis was to reveal palaeo-environmental information contained within the large-scale elongated depressions of continental shelves and their confined sedimentary depocenters by means of sea-level, climate and hydrodynamic variations. In this regard, two study areas from temperate and arctic continental shelf in North Atlantic realm were investigated in great detail for the first time. Both study areas served as important drainage paths during the last deglaciation of Eurasian Ice Sheet Complex, but also as a sediment trap on the continental shelf recording the clues for the past.

The first two parts of the study was dealt with Elbe Palaeovalley in the North Sea and its evolution since Late Weichselian glacial period. Owing to the very high vertical and horizontal resolution achieved by parametric echo-sounder data and multi-channel data along with sedimentological information, Elbe Palaeovalley's morphology, sedimentary infill architecture and its main controlling factors could be investigated by unprecedented data-set. The base of Elbe Palaeovalley situates between 40–80 m below the present sea-level, and the associated braided style drainage system is inferred to have been established during the late Weichselian glacial period in a periglacial environment when sea levels were 130 m below the present. The incisions (2–3 m in height and 100 m in width) mapped in southern segment of the valley base revealed a northwestward alignment. However, in the northern segment, scarcity of incisions, abrupt gradient change in the valley base, significant changes in the valley cross-sections and the presence of possible glaciogenic deposits preserved within the valley were inferred to be the result of downstream blockage by the Late Weichselian ice sheet in the North Sea. Furthermore, the first evidence for the postulated ice marginal lake related to the coalescence of ice sheets around Dogger Bank during the last glacial period was revealed in this study. As there are probably way more speculations on the extension or presence of Late Weichselian ice sheet in the North Sea than the data available, the results herein from northern segment of the valley is expected to clinch an argument for the conceptual palaeoenvironmental reconstructions in the North Sea such as previously underestimated extension of the Late Weichselian ice sheet.

With the subsequent Late Pleistocene–Early Holocene sea level rise, successive depocenters established within the Elbe Palaeovalley, reflects the evolving hydrodynamic regime in tide- and

wave-dominated environment of the southern North Sea until present under the control of valley morphology. Overall, the Elbe Palaeovalley represents a rare example and significantly deviates from the of Quaternary palaeovalley (incised valley) models as bulk of the infill is related to establishment of the hydrodynamic regime since early Holocene sea-level rise without significant fluvial or estuarine sediment. The results presented here on Elbe Palaeovalle provides a firmer basis on which to test or refine palaeoenvironmental constructions as well as future or existing models such as sediment transport, ice-sheet and shoreline change.

Some chronological and sedimentological questions still exist, which will be only possible with employing cores penetrating down to the deeper structures (at least 10 m). Therefore, the integrated work with a wide range of sedimentological studies on already existing sediment cores (up to 6 m) at the University of Bremen is strongly recommended for future work, and the data collaboration between research groups (from i.e. U.K., Denmark, The Netherlands, Norway), but also, industries such as marine renewable energy and offshore hydrocarbon should be further established, thereby very high vertical resolution (~20 cm) achieved by the sediment echosounder could be much more remunerated. The most interesting future work would be on nicely laminated unit (Chapter 3, Unit 1a) that interpreted as lake sediments by groundtruthing. According to our mapping this unit (Unit 1a) expands towards Oyster Ground, it is necessary to conduct further studies there in order to fully understand ice-dammed lake - Dogger Bank - Elbe Palaeovalley relation.

The future detailed analysis on the sediments that interpreted here as valley infilling sediments, wetland environments would be vital for assessing the archaeological potential of drowned landscapes of the North Sea. Submerged archaeological landscapes on continental shelves have been receiving increased appreciation (Ward and Larcombe, 2013; Roebroeks, 2014) by recent researches as more high resolution geophysical data and innovative GIS analysis of 3-D seismic have become available (e.g. Gaffney et al., 2007), the results presented in this study has the potential to be integrated into multidisciplinary studies or enable targeted marine geo-archaeological studies, and can therefore, be evaluated as a guide in order to identify marine prehistoric environment on the Northwest European Shelf (e.g. occupation of NW European landscapes by Late Palaeolithic and Early Mesolithic hunter-gatherers following the retreat of ice sheets and also their response/adaptation to the rising sea levels and changes in the climate van der Plicht et al. (2016)).

5.2   Barents Sea

Densely spaced, high resolution acoustic data acoustic data together with age control allowed for a detailed interpretation and discussion regarding the nature and characteristics of the bottom

currents which have led to drift formation and as well as external forcings that influenced the drift deposition and evolution in the northwestern Barents Sea. Detailed morphological, seismo-stratigraphic, lithological and sedimentological insight into the construction of a trough-confined contouritic drift by correlating the base of the drift and four internal horizons, defining five successive sedimentary units revealed with this study. The drift has a complex morphology, strongly controlled by underlying bathymetry. The existence of steady and persistent bottom currents is implied by moat observed along northern flank of the trough. The genesis of the Kveithola Drift is related to Brine-enriched shelf water produced during the winter season seems to be the driver responsible. Accordingly, the formation of this water is inferred to have started around 13 cal. ka BP, the onset of drift deposition. This suggest the atmospheric cooling of surface waters along with coastal polynyas and influence of katabatic winds on the western Barents Shelf established at this time. Furthermore, it is inferred that that more energetic sedimentary conditions prevailed during abrupt cooling events; during Younger Dryas and short atmospheric cooling event 8.9–8.2 cal ka BP.

Furthermore, cascading of this water along with winter storminess re-suspends sediment plumes on shelf and sediments are subsequently carried down to the continental slope (Fohrmann et al., 1998; Sarnthein et al., 2003a). Therefore, Kveithola Trough —as one of the cross-shelf bathymetric troughs in the NW Barents Sea neighboring the continental slope— acts as a drainage pathway towards eastern Norwegian Sea for the surrounding Spitsbergen and Bear Island Banks via channels connected to its basin (Fohrmann et al., 1998).

High-resolution age model of the drift and more detailed insight into the processes that was discussed in Chapter 4 could be gained through sedimentological and biostratigraphical analysis of the available sediment cores from CORIBAR cruise, for which this study will provide a solid framework. Further studies, especially on benthic foraminifera is expected to strengthen/improve the construction of palaeo-environmental (i.e. brine-influenced environment by sea-ice formation and polynyas) and -oceanographic changes in the Kveithola Trough as they have been used as indicators (directly or indirectly) of bottom currents, salinity, sea-ice occurrence, oxygen level, temperature of the water etc. On the other hand, possible future study that combines seismic and CTD measurements could reveal watermass distribution in the Kveithola in great detail.

Acknowledgements

References

Aagaard, K., Darnall, C., Greisman, P., 1973. Year-long current measurements in the Greenland-Spitsbergen passage. Deep Sea Research and Oceanographic Abstracts 20(8), 743–746.

Aagaard, K., Foldvik, A., Hillman, S.R., 1987. The West Spitsbergen Current: Disposition and water mass transformation. Journal of Geophysical Research 92(C4), 3778–3784.

Aagaard, K., Swift, J.H., Carmack, E.C., 1985. Thermohaline circulation in the Arctic Mediterranean Seas. Journal of Geophysical Research 90(C3), 4833–4846.

Aagaard-Sørensen, S., Husum, K., Hald, M., Knies, J., 2010. Paleoceanographic development in the SW Barents Sea during the Late Weichselian–Early Holocene transition. Quaternary Science Reviews 29(25-26), 3442–3456.

Alappat, L., Vink, A., Tsukamoto, S., Frechen, M., 2010. Establishing the Late Pleistocene–Holocene sedimentation boundary in the southern North Sea using OSL dating of shallow continental shelf sediments. Proceedings of the Geologists' Association 121(1), 43–54.

Allen_1999_Geological impacts on coastal wetland.

Alley, R.B., Mayewski, P.A., Sowers, T., Stuiver, M., Taylor, K.C., Clark, P.U., 1997. Holocene climatic instability: A prominent, widespread event 8200 yr ago. Geology 25(6), 483–486.

Andersen, T.R., Huuse, M., Jørgensen, F., Christensen, S., 2012. Seismic investigations of buried tunnel valleys on- and offshore Denmark. Geological Society, London, Special Publications 368(1), 129–144.

Andreassen, K., Laberg, J.S., Vorren, T.O., 2008. Seafloor geomorphology of the SW Barents Sea and its glaci-dynamic implications. Geomorphology 97(1-2), 157–177.

Andreassen, K., Nilssen, L.C., Rafaelsen, B., Kuilman, L., 2004. Three-dimensional seismic data from the Barents Sea margin reveal evidence of past ice streams and their dynamics. Geology 32(8), 729.

Andreassen, K., Winsborrow, M., Bjarnadóttir, L., Rüther, D., Borque, J., Lucchi, R., Caburlotto, A., 2009. Barents Sea and the West Spitsbergen Margin, UiT 2009. Marine Geophysical/Geological Cruise to Outer Bear Island trough, Kveithola trough and the West Spitsbergen Margin, p. 33. Cruise Report. RV/Jan Mayen 2.-19.07.2009, University of Tromsø.

Austin, R.M., 1991. Modelling Holocene tides on the NW European continental shelf. Terra Nova 3(3), 276–288.

Backhaus, J.O., 1989. The North Sea and the climate. Dana 8, 69–82.

Bard, E., Hamelin, B., Delanghe-Sabatier, D., 2010. Deglacial meltwater pulse 1B and Younger Dryas sea levels revisited with boreholes at Tahiti. Science (New York, N.Y.) 327(5970), 1235–1237.

Batchelor, C.L., Dowdeswell, J.A., 2014. The physiography of High Arctic cross-shelf troughs. Quaternary Science Reviews 92, 68–96.

Becker, G.A., Dick, S., Dippner, J.W., 1992. Hydrography of the German Bight. Marine Ecology Progress Series 91, 9–18.

Behre, K.-E., 2007. A new Holocene sea-level curve for the southern North Sea. Boreas 36(1), 82–102.

Bender, V., Hanebuth, T., Nagai, R., submitted. Sediment export dynamics from a high-energy continental shelf as recorded on an uppermost-slope terrace (off Uruguay). Sedimentology.

Benn, D.I., Evans, D.J.A., 2010. Glaciers & glaciation, 2nd ed. ed. Hodder Education, London.

Berger, A., Crucifix, M., Hodell, D.A., Mangili, C., McManus, J.F., Otto-Blisner, B., POl, K., Raynaud, D., Skinner, L.C., Tzedakis, P.C., Landais, A., Margari, V., Martrat, B., Masson-Delmotte, V., Mokeddem, Z., Parrenin, F., Prokopenko, A.A., Rashid, H., Schulz, M., Riveiros, N.V., 2016. Interglacials of the last 800,000 years. Reviews of Geophysics 54(1), 162–219.

Bergh, S.G., Grogan, P., 2003. Tertiary structure of the Sørkapp-Hornsund Region, South Spitsbergen, and implications for the offshore southern extension of the fold-thrust Belt. Norsk Geologisk Tidsskrift 83(1), 43–60.

Bigg, G.R., Levine, R.C., Clark, C.D., Greenwood, S.L., HAFLIDASON, H., Hughes, A.L.C., Nygård, A., Sejrup, H.P., 2010. Last glacial ice-rafted debris off southwestern Europe: The role of the British-Irish Ice Sheet. Journal of Quaternary Science 25(5), 689–699.

Bird, M.I., Austin, W.E., Wurster, C.M., Fifield, L.K., Mojtahid, M., Sargeant, C., 2010. Punctuated eustatic sea-level rise in the early mid-Holocene. Geology 38(9), 803–806.

Bjarnadóttir, L.R., Rüther, D.C., Winsborrow, M.C.M., Andreassen, K., 2013. Grounding-line dynamics during the last deglaciation of Kveithola, W Barents Sea, as revealed by seabed geomorphology and shallow seismic stratigraphy. Boreas 42(1), 84–107.

Bjarnadóttir, L.R., Winsborrow, M.C., Andreassen, K., 2014. Deglaciation of the central Barents Sea. Quaternary Science Reviews 92, 208–226.

Blanchon, P., Jones, B., Ford, D.C., 2002. Discovery of a submerged relic reef and shoreline off Grand Cayman: Further support for an early Holocene jump in sea level. Sedimentary Geology 147(3-4), 253–270.

Blindheim, J., 1989. Cascading of Barents Sea bottom water into the Norwegian Sea. Rapp. P. V. Réun. Cons. Int. Explor. Mer 188, 49–58.

Blum, M., Martin, J., Milliken, K., Garvin, M., 2013. Paleovalley systems: Insights from Quaternary analogs and experiments. Earth-Science Reviews 116, 128–169.

Blum, M.D., Törnqvist, T.E., 2000. Fluvial responses to climate and sea-level change: A review and look forward. Sedimentology 47(745), 2–48.

Blum, P., 1997. Physical properties handbook: a guide to the shipboard measurement of physical properties of deep-sea cores. ODP Tech. Note 26.

Bøe, R., Skardhamar, J., Rise, L., Dolan, M.F., Bellec, V.K., Winsborrow, M., Skagseth, Ø., Knies, J., King, E.L., Walderhaug, O., Chand, S., Buenz, S., Mienert, J., 2015. Sandwaves and sand transport on the Barents Sea continental slope offshore northern Norway. Marine and Petroleum Geology 60, 34–53.

Borchers, A., Dietze, E., Kuhn, G., Esper, O., Voigt, I., Hartmann, K., Diekmann, B., 2016. Holocene ice dynamics and bottom-water formation associated with Cape Darnley polynya activity recorded in Burton Basin, East Antarctica. Marine Geophysical Researches 37(1), 49–70.

Boulton, G., Dongelmans, P., Punkari, M., Broadgate, M., 2001. Palaeoglaciology of an ice sheet through a glacial cycle: The European ice sheet through the Weichselian. Quaternary Science Reviews 20(4), 591–625.

Bourillet, J.-F., Reynaud, J.-Y., Baltzer, A., Zaragosi, S., 2003. The 'Fleuve Manche': the submarine sedimentary features from the outer shelf to the deep-sea fans. Journal of Quaternary Science 18(3-4), 261–282.

Boyd, R.O., Dalrymple, R.W., Zaitlin, B.A., 2006. Estuarine and Incised-Valley Facies Models. In: Posamentier, H.W., Walker, R.G. (Eds.), Facies models revisited. SEPM special publicationno. 84. Society for Sedimentary Geology, Tulsa, Okla., pp. 171–235.

Boyd, T.J., D'Asaro, E.A., 1994. Cooling of the West Spitsbergen Current: Wintertime Observations West of Svalbard. Journal of Geophysical Research 99(C11), 22597–22618.

Böse, M., 2005. The Last Glaciation and Geomorphology. In: Koster, E.A. (Ed.), The physical geography of Western Europe. The Oxford regional environments series. Oxford University Press, Oxford, pp. 61–74.

Bridgland, D.R., 2002. Fluvial deposition on periodically emergent shelves in the Quaternary: Example records from the shelf around Britain. Quaternary International 92(1), 25–34.

Brodzikowski, K., van Loon, A.J. (Eds.), 1991. Glacigenic sediments. Elsevier. Developments in Sedimentology 49, Amsterdam, New York.

Broecker, W.S., Denton, G.H., Edwards, R.L., Cheng, H., Alley, R.B., Putnam, A.E., 2010. Putting the Younger Dryas cold event into context. Quaternary Science Reviews 29(9-10), 1078–1081.

Broecker, W.S., Kennett, J.P., Flower, B.P., Teller, J.T., Trumbore, S., Bonani, G., Wolfli, W., 1989. Routing of meltwater from the Laurentide Ice Sheet during the Younger Dryas cold episode. Nature 341(6240), 318–321.

Brown, J., Hill, A.E., Fernand, L., Horsburgh, K.J., 1999. Observations of a Seasonal Jet-like Circulation at the Central North Sea Cold Pool Margin. Estuarine, Coastal and Shelf Science 48(3), 343–355.

Bungenstock, F., Schäfer, A., 2009. The Holocene relative sea-level curve for the tidal basin of the barrier island Langeoog, German Bight, Southern North Sea. Global and Planetary Change 66(1-2), 34–51.

Cage, A.G., Heinemeier, J., Austin, W.E.N., 2006. Marine Radiocarbon Reservoir Ages in Scottish Coastal and Fjordic Waters. Radiocarbon 48(01), 31–43.

Camerlenghi, A., Flores, J., Sierro, F., Colmenre, E., SVAIS scientific and technical staff, 2007. SVAIS, the Development of an Ice Stream-dominated Sedimentary System: the Southern Svalbard Continental Margin, p. 62. Cruise report University of Barcelona.

Cameron, D., van Doorn, D., Laban, C., Streif, H.J., 1993. Geology of the Southern North Sea Basin. In: Hillen, R., Verhagen, H.J. (Eds.), Coastlines of the southern North Sea. Coastlines of the world. American Society of Civil Engineers, New York, N.Y.

Carr, S.J., 2004. The North Sea basin. In: Quaternary Glaciations Extent and Chronology - Part I: Europe. Developments in quaternary sciences. Elsevier, pp. 261–270.

Carr, S.J., Holmes, R., van der Meer, J. J. M., Rose, J., 2006. The Last Glacial Maximum in the North Sea Basin: Micromorphological evidence of extensive glaciation. Journal of Quaternary Science 21(2), 131–153.

Caston, G.F., 1981. Potential gain and loss of sand by some sand banks in the Southern Bight of the North Sea. Marine Geology 41(3-4), 239–250.

Caston, V., 1972. Linear sand banks in the southern North Sea. Sedimentology 18(1-2), 63–78.

Cazenave, P., 2013. Past and present sediment transport of the north-west european continental shelf. Doctoral Thesis, University of Southampton, 336.

Charnock, H., Dyer, K.R., Huthnance, J.M., Liss, P.S., Simpson, J.H., Tett, P.B. (Eds.), 1994. Understanding the North Sea System. Springer Netherlands, Dordrecht.

Chaumillon, E., Tessier, B., Reynaud, J.Y., 2010. Stratigraphic records and variability of incised valleys and estuaries along French coasts. Bulletin de la Societe Geologique de France 181(2), 75–85.

Chiocci, F.L., Chivas, A.R., 2014. Continental shelves of the world: Their evolution during the last glacio-eustatic cycle. Geological Society, London, Memoirs 41.

Church, J.A., Aarup, T., Woodworth, P.L., Wilson, W.S., Nicholls, R.J., Rayner, R., Lambeck, K., Mitchum, G.T., Steffen, K., Cazenave, A., Blewitt, G., Mitrovica, J.X., Lowe, J.A., 2010. Sea-Level Rise and Variability: Synthesis and Outlook for the Future. In: Church, J. (Ed.), Understanding sea-level rise and variability. Blackwell Pub, Hoboken, NJ, pp. 402–419.

Clark, C.D., Hughes, A.L., Greenwood, S.L., Jordan, C., Sejrup, H.P., 2012a. Pattern and timing of retreat of the last British-Irish Ice Sheet. Quaternary Science Reviews 44, 112–146.

Clark, C.D., Sejrup, H.P., Bigg, G., Stoker, M., Lonergan, L., Raunholm, S., HAFLIDASON, H., 2004a. Did the Punctuated Demise of Glacial Ice in the North Sea Affect Thermohaline Circulation of the Ocean? Eos, Transactions American Geophysical Union 85(31), 293.

Clark, C.D., Stokes, C.R., 2003. The palaeo-Ice Stream Landsystem. In: Evans, D.J.A. (Ed.), Glacial landsystems. Arnold, London.

Clark, P.U., 1999. Northern Hemisphere Ice-Sheet Influences on Global Climate Change. Science 286(5442), 1104–1111.

Clark, P.U., Church, J.A., Gregory, J.M., Payne, A.J., 2015. Recent Progress in Understanding and Projecting Regional and Global Mean Sea Level Change. Current Climate Change Reports 1(4), 224–246.

Clark, P.U., Dyke, A.S., Shakun, J.D., Carlson, A.E., Clark, J., Wohlfarth, B., Mitrovica, J.X., Hostetler, S.W., McCabe, A.M., 2009. The Last Glacial Maximum. Science (New York, N.Y.) 325(5941), 710–714.

Clark, P.U., McCabe, A.M., Mix, A.C., Weaver, A.J., 2004b. Rapid rise of sea level 19,000 years ago and its global implications. Science (New York, N.Y.) 304(5674), 1141–1144.

Clark, P.U., Shakun, J.D., Baker, P.A., Bartlein, P.J., Brewer, S., Brook, E., Carlson, A.E., Cheng, H., Kaufman, D.S., Liu, Z., Marchitto, T.M., Mix, A.C., Morrill, C., Otto-Bliesner, B.L., Pahnke, K., Russell, J.M., Whitlock, C., Adkins, J.F., Blois, J.L., Clark, J., Colman, S.M., Curry, W.B., Flower, B.P., He, F., Johnson, T.C., Lynch-Stieglitz, J., Markgraf, V., McManus, J., Mitrovica, J.X., Moreno, P.I., Williams, J.W., 2012b. Global climate

evolution during the last deglaciation. Proceedings of the National Academy of Sciences of the United States of America 109(19), E1134-42.

Clausen, O.R., Gregersen, U., Michelsen, O., Sørensen, J.C., 1999. Factors controlling the Cenozoic sequence development in the eastern parts of the North Sea. Journal of the Geological Society 156(4), 809–816.

Cohen, K.M., Gibbard, P.L., Weerts, H., 2014. North Sea palaeogeographical reconstructions for the last 1 Ma. Netherlands Journal of Geosciences - Geologie en Mijnbouw 93(1-2), 7–29.

Coles, B.J., 2000. Doggerland: The cultural dynamics of a shifting coastline. Geological Society, London, Special Publications 175(1), 393–401.

Condron, A., Winsor, P., 2012. Meltwater routing and the Younger Dryas. Proceedings of the National Academy of Sciences of the United States of America 109(49), 19928–19933.

Conrad, C.P., 2013. The solid Earth's influence on sea level. Geological Society of America Bulletin 125(7-8), 1027–1052.

Cronin, T.M., 2012. Rapid sea-level rise. Quaternary Science Reviews 56, 11–30.

Dabrio, C.J., Zazo, C., Goy, J.L., Sierro, F.J., Borja, F., Lario, J., González, J.A., Flores, J.A., 2000. Depositional history of estuarine infill during the last postglacial transgression (Gulf of Cadiz, Southern Spain). Marine Geology 162(2–4), 381–404.

Dalrymple, R.W., Boyd, R., Zaitlin, B.A., 1994. History of Research, Types and Internal Organisation of Incised-Valley Systems. In: Dalrymple, R.W., Boyd, R., Zaitlin, B.A. (Eds.), Incised-Valley Systems. SEPM (Society for Sedimentary Geology), pp. 3–10.

Dalrymple, R.W., Leckie, D.A., Tillman, R.W., 2006. Incised valleys in time and space. SEPM special publication 85. Society for Sedimentary Geology, Tulsa, Okla.

Dalrymple, R.W., Zaitlin, B.A., Boyd, R., 1992. Estuarine facies models; conceptual basis and stratigraphic implications. Journal of Sedimentary Research 62(6), 1130–1146.

Danielssen, D.S., Edler, L., Fonselius, S., Hernroth, L., Ostrowski, M., Svendsen, E., Talpsepp, L., 1997. Oceanographic variability in the Skagerrak and Northern Kattegat, May–June, 1990. ICES Journal of Marine Science: Journal du Conseil 54(5), 753–773.

Davis, R.A., Balson, P.S., 1992. Stratigraphy of a North Sea Tidal Sand Ridge. SEPM Journal of Sedimentary Research 62(1), 116–121.

Deleu, S., van Lancker, V., van den Eynde, D., Moerkerke, G., 2004. Morphodynamic evolution of the kink of an offshore tidal sandbank: the Westhinder Bank (Southern North Sea). Continental Shelf Research 24(15), 1587–1610.

Deschamps, P., Durand, N., Bard, E., Hamelin, B., Camoin, G., Thomas, A.L., Henderson, G.M., Okuno, J., Yokoyama, Y., 2012. Ice-sheet collapse and sea-level rise at the Bolling warming 14,600 years ago. Nature 483(7391), 559–564.

Diesing, M., Schwarzer, K., 2006. Identification of submarine hard-bottom substrates in the German North Sea and Baltic Sea EEZ with high-resolution acoustic seafloor imaging. In: Nordheim, H. von, Boedeker, D., Krause, J.C. (Eds.), Progress in marine conservation in Europe: Natura 2000 sites in German offshore waters. Springer, Berlin, New York, pp. 111–125.

Dippner, J.W., 1993. A frontal-resolving model for the German Bight. Continental Shelf Research 13(1), 49–66.

Dittmers, K., Niessen, F., Stein, R., 2008. Acoustic facies on the inner Kara Sea Shelf: Implications for Late Weichselian to Holocene sediment dynamics. Marine Geology 254(3-4), 197–215.

Dixon, J.C., 2013. 13.11 Response of Periglacial Geomorphic Processes to Global Change. In: Treatise on Geomorphology. Elsevier, pp. 176–189.

Dowdeswell, J.A., Elverhøi, A., 2002. The timing of initiation of fast-flowing ice streams during a glacial cycle inferred from glacimarine sedimentation. Marine Geology 188(1-2), 3–14.

Dowdeswell, J.A., Ottesen, D., Evans, J., Cofaigh, C.Ó., Anderson, J.B., 2008. Submarine glacial landforms and rates of ice-stream collapse. Geology 36(10), 819.

Ebbesen, H., Hald, M., 2004. Unstable Younger Dryas climate in the northeast North Atlantic. Geology 32(8), 673–676.

Egbert, G.D., Ray, R.D., Bills, B.G., 2004. Numerical modeling of the global semidiurnal tide in the present day and in the last glacial maximum. Journal of Geophysical Research: Oceans 109(C3).

Ehlers, J., 2011. Das Eiszeitalter. Spektrum Akademischer Verlag, Heidelberg.

Ehlers, J., Eissmann, L., Lippstreu, L., Stephan, H.-J., Wansa, S., 2004. Pleistocene glaciations of North Germany. In: Ehlers, J., Gibbard, P.L. (Eds.), Quaternary Glaciations Extent and Chronology - Part I: Europe. Developments in quaternary sciences. Elsevier, pp. 135–146.

Ehlers, J., Gibbard, P.L., Hughes, P.D. (Eds.), 2011a. Quaternary glaciations - extent and chronology: A closer look. Elsevier. Developments in quaternary sciences v. 15, Amsterdam, Boston.

Ehlers, J., Grube, A., Stephan, H.-J., Wansa, S., 2011b. Pleistocene Glaciations of North Germany—New Results. In: Quaternary Glaciations - Extent and Chronology - A Closer Look. Developments in quaternary sciences. Elsevier, pp. 149–162.

Ehlers, J., Wingfield, R., 1991. The extension of the Late Weichselian/Late Devensian ice sheets in the North Sea Basin. Journal of Quaternary Science 6(4), 313–326.

Eisma, D., Johnston, R., Cadogan, J.I.G., 1987. The North Sea: An Overview [and Discussion]. Philosophical Transactions of the Royal Society B: Biological Sciences 316(1181), 461–485.

Eisma, D., Kalf, J., 1987. Distribution, organic content and particle size of suspended matter in the north sea. Netherlands Journal of Sea Research 21(4), 265–285.

Eynaud, F., Malaizé, B., Zaragosi, S., Vernal, A.D., Scourse, J., Pujol, C., Cortijo, E., Grousset, F.E., Penaud, A., Toucanne, S., Turon, J.-L., Auffret, G., 2012. New constraints on European glacial freshwater releases to the North Atlantic Ocean. Geophysical Research Letters 39(15).

Faugères, J.-C., Stow, D., 2008. Chapter 14 Contourite Drifts. In: Rebesco, M., Camerlenghi, A. (Eds.), Contourites. Developments in Sedimentology60. Elsevier, Amsterdam, Oxford, pp. 257–288.

Faugères, J.-C., Stow, D.A., Imbert, P., Viana, A., 1999. Seismic features diagnostic of contourite drifts. Marine Geology 162(1), 1–38.

Figge, K., 1980. Das Elbe—Urstromtal im Bereich der Deutschen Bucht (Nordsee) 30(1), 203–212 (E&G – Quaternary Science Journal).

Figge, K., 1983. Morainic deposits in the German Bight area of the North Sea. In: Ehlers, J. (Ed.), Glacial deposits in North-West Europe. Balkema, Rotterdam, pp. 299–304.

Fisher, T.G., Smith, D.G., 1994. Glacial Lake Agassiz: Its northwest maximum extent and outlet in Saskatchewan (Emerson Phase). Quaternary Science Reviews 13(9-10), 845–858.

Fitch, S., Thomson, K., Gaffney, V., 2005. Late Pleistocene and Holocene depositional systems and the palaeogeography of the Dogger Bank, North Sea. Quaternary Research 64(2), 185–196.

Fleming, K., Johnston, P., Zwartz, D., Yokoyama, Y., Lambeck, K., Chappell, J., 1998. Refining the eustatic sea-level curve since the Last Glacial Maximum using far- and intermediate-field sites. Earth and Planetary Science Letters 163(1-4), 327–342.

Flemming, N.C., Çağatay, M.N., 2014. Land beneath the waves: Submerged landscapes and sea level change; a joint geoscience-humanities strategy for European Continental Shelf Prehistoric Research, 2. ed. ed. European Marine Board Position Paper 21. European Marine Board, Ostend.

Fletcher, W.J., Sánchez Goñi, M.F., Allen, J.R., Cheddadi, R., Combourieu-Nebout, N., Huntley, B., Lawson, I., Londeix, L., Magri, D., Margari, V., Müller, U.C., Naughton, F., Novenko, E., Roucoux, K., Tzedakis, P.C., 2010. Millennial-scale variability during the last glacial in vegetation records from Europe. Quaternary Science Reviews 29(21-22), 2839–2864.

Fohrmann, H., Backhaus, J.O., Blaume, F., Haupt, B.J., Kämpf, J., Michels, K., Mienert, J., Posewang, J., Ritzrau, W., Rumohr, J., Weber, M., Woodgate, R., 2001. Modern Ocean Current-Controlled Sediment Transport in the Greenland-Iceland-Norwegian (GIN) Seas. In: Schäfer, P., Ritzrau, W., Schlüter, M., Thiede, J. (Eds.), The Northern North Atlantic: A Changing Environment. Springer Berlin Heidelberg, Berlin, Heidelberg, pp. 135–154.

Fohrmann, H., Backhaus, J.O., Blaume, F., Rumohr, J., 1998. Sediments in Bottom-Arrested Gravity Plumes: Numerical Case Studies. Journal of Physical Oceanography 28(11), 2250–2274.

Gabrielsen, R., Færseth, R., Jensen, L., Kalheim, J., Riis, F., 1990. Structural elements of the Norwegian continental shelf: Part 1, The Barents Sea Region. In: Fleet, A. J. & Boldy, S. A. R. (eds) Petroleum Geology of Northwest Europe: Proceedings of the 5th Conference, pp. 247–259.

Gaffney, V.L., Thomson, K., Fitch, S., 2007. Mapping Doggerland: The Mesolithic Landscapes of the Southern North Sea. Archaeopress, Oxford.

Ganopolski, A., Rahmstorf, S., Petoukhov, V., Claussen, M., 1998. Simulation of modern and glacial climates with a coupled global model of intermediate complexity. Nature 391, 351–356.

Garrison, J.R., van den Bergh, T., 2006. Effects of Sedimentation Rate, Rate of Relative Rise in Sea Level, and Duration of Sea-Level Cycle on the Filling of Incised Valleys: Examples of Filled and "Overfilled" Incised Valleys From the Upper Ferron Sandstone, Last Chance Delta, East-Central Utah, U.S.A. In: Dalrymple, R.W., Leckie, D.A., Tillman, R.W. (Eds.), Incised Valleys in Time and Space. SEPM (Society for Sedimentary Geology), pp. 239–279.

Gehrmann, R.A.S., Dettmer, J., Schwalenberg, K., Engels, M., Dosso, S.E., Özmaral, A., 2015. Trans-dimensional Bayesian inversion of controlled-source electromagnetic data in the German North Sea. Geophysical Prospecting 63(6), 1314–1333.

Gerdes, G., Petzelberger, B., Scholz-Böttcher, B., Streif, H., 2003. The record of climatic change in the geological archives of shallow marine, coastal, and adjacent lowland areas of Northern Germany. Quaternary Science Reviews 22(1), 101–124.

Gerritsen, H., Berentsen, C.W., 1998. A modelling study of tidally induced equilibrium sand balances in the North Sea during the Holocene. Continental Shelf Research 18(2-4), 151–200.

Gibbard, P., Lewin, J., 2002. Climate and related controls on interglacial fluvial sedimentation in lowland Britain. Sedimentary Geology 151(3-4), 187–210.

Gibbard, P.L., Rose, J., Bridgland, D.R., 1988. The History of the Great Northwest European Rivers During the Past Three Million Years [and Discussion]. Philosophical Transactions of the Royal Society of London. Series B, Biological Sciences 318(1191), 559–602.

Goñi, M.F.S., Turon, J.-L., Eynaud, F., Gendreau, S., 2000. European Climatic Response to Millennial-Scale Changes in the Atmosphere–Ocean System during the Last Glacial Period. Quaternary Research 54(3), 394–403.

Graham, A., Lonergan, L., Stoker, M., 2007. Evidence for Late Pleistocene ice stream activity in the Witch Ground Basin, central North Sea, from 3D seismic reflection data. Quaternary Science Reviews 26(5-6), 627–643.

Graham, A.G., Stoker, M.S., Lonergan, L., Bradwell, T., Stewart, M.A., 2011. The Pleistocene Glaciations of the North Sea Basin. In: Quaternary Glaciations - Extent and Chronology - A Closer Look. Developments in quaternary sciences. Elsevier, pp. 261–278.

Grave, M., 2014. Structure and Formation of Shallow Water Contourites - Geophysical and Sedimentological Analysis of the Drift inside the Kveithola trough, Western Barents Sea. Master Thesis, "Geowissenschaften" Department of Geosciences, University of Bremen, p. 58.

Greene, D.L., Rodriguez, A.B., Anderson, J.B., 2007. Seaward-Branching Coastal-Plain and Piedmont Incised-Valley Systems Through Multiple Sea-Level Cycles: Late Quaternary Examples from Mobile Bay and Mississippi Sound, U.S.A. Journal of Sedimentary Research 77(2), 139–158.

Gregoire, G., Le Roy, P., Ehrhold, A., Jouet, G., Garlan, T., 2017. Control factors of Holocene sedimentary infilling in a semi-closed tidal estuarine-like system: The bay of Brest (France). Marine Geology 385, 84–100.

Gupta, S., Collier, J.S., Palmer-Felgate, A., Potter, G., 2007. Catastrophic flooding origin of shelf valley systems in the English Channel. Nature 448(7151), 342–345.

Gyllencreutz, R., 2005. Late Glacial and Holocene paleoceanography in the Skagerrak from high-resolution grain size records. Palaeogeography, Palaeoclimatology, Palaeoecology 222(3-4), 344–369.

Gyllencreutz, R., Kissel, C., 2006. Lateglacial and Holocene sediment sources and transport patterns in the Skagerrak interpreted from high-resolution magnetic properties and grain size data. Quaternary Science Reviews 25(11-12), 1247–1263.

Haarpaintner, J., Gascard, J.-C., Haugan, P.M., 2001. Ice production and brine formation in Storfjorden, Svalbard. Journal of Geophysical Research: Oceans 106(C7), 14001–14013.

Hagedorn, J., 1989. Glacial and periglacial morphology of the Lüneburg Heath. In: Ahnert, F. (Ed.), Landforms and Landform Evolution in West Germany. Schweizerbart Science Publishers, Stuttgart, Germany.

Hald, M., Andersson, C., Ebbesen, H., Jansen, E., Klitgaard-Kristensen, D., Risebrobakken, B., Salomonsen, G.R., Sarnthein, M., Sejrup, H.P., Telford, R.J., 2007. Variations in temperature and extent of Atlantic Water in the northern North Atlantic during the Holocene. Quaternary Science Reviews 26(25-28), 3423–3440.

Hald, M., Hagen, S., 1998. Early Preboreal cooling in the Nordic seas region triggered by meltwater. Geology 26(7), 615–618.

Hall, I.R., Moran, S.B., Zahn, R., Knutz, P.C., Shen, C.-C., Edwards, R.L., 2006. Accelerated drawdown of meridional overturning in the late-glacial Atlantic triggered by transient pre-H event freshwater perturbation. Geophysical Research Letters 33(16).

Hall, P., Davies, A.M., 2004. Modelling tidally induced sediment-transport paths over the northwest European shelf: The influence of sea-level reduction. Ocean Dynamics 54(2), 126–141.

Hammer, Ø., Planke, S., Hafeez, A., Hjelstuen, B.O., Faleide, J.I., Kvalø, F., 2016. Agderia – a postglacial lost land in the southern Norwegian North Sea. Norwegian Journal of Geology 96, 43–60.

Hanebuth, T., 2000. Rapid Flooding of the Sunda Shelf: A Late-Glacial Sea-Level Record. Science 288(5468), 1033–1035.

Hanebuth, T.J., Voris, H.K., Yokoyama, Y., Saito, Y., Okuno, J., 2011. Formation and fate of sedimentary depocentres on Southeast Asia's Sunda Shelf over the past sea-level cycle and biogeographic implications. Earth-Science Reviews 104(1-3), 92–110.

Hanebuth, T.J., Zhang, W., Hofmann, A.L., Löwemark, L.A., Schwenk, T., 2015. Oceanic density fronts steering bottom-current induced sedimentation deduced from a 50 ka contourite-drift record and numerical modeling (off NW Spain). Quaternary Science Reviews 112, 207–225.

Hanebuth, T.J.J., Lantzsch, H., Bergenthal, M., Caburlotto, A., Dippold, S., Düßmann, R., Freudenthal, T., Hörner, T., Kaszemeik, K., Klar, S., Llopart, J., Lucchi, R.G., Nicolaisen, L.S., Noorlander, K., Osti, G., Özmaral, A., Rebesco, M., Rosiak, U., Sabbatini, A., Schmidt, W., Stachowski, A., Urgeles, R., 2013. CORIBAR Ice dynamics and meltwater deposits: coring in the Kveithola Trough, NW Barents Sea - Cruise MSM30 - July 16 - August 15, 2013 - Tromsø (Norway) - Tromsø (Norway) (41 pages / MARIA S. MERIAN-Berichte; MSM30; 1-41; ISSN 2195-8483).

Hanebuth, T.J.J., Rebesco, M., Urgeles, R., Lucchi, R.G., Freudenthal, T., 2014. Drilling Glacial Deposits in Offshore Polar Regions. Eos, Transactions American Geophysical Union 95(31), 277–278.

Harris, P.T., 1989. Sandwave movement under tidal and wind-driven currents in a shallow marine environment: Adolphus Channel, northeastern Australia. Continental Shelf Research 9(11), 981–1002.

Harris, P.T., Brancolini, G., Armand, L., Busetti, M., Beaman, R.J., Giorgetti, G., Presti, M., Trincardi, F., 2001. Continental shelf drift deposit indicates non-steady state Antarctic bottom water production in the Holocene. Marine Geology 179(1–2), 1–8.

Hays, J.D., Imbrie, J., Shackleton, N.J., 1976. Variations in the Earth's Orbit: Pacemaker of the Ice Ages. Science (New York, N.Y.) 194(4270), 1121–1132.

Hemming, S.R., 2004. Heinrich events: Massive late Pleistocene detritus layers of the North Atlantic and their global climate imprint. Reviews of Geophysics 42(1).

Hepp, D.A., Warnke, U., Hebbeln, D., Mörz, T., 2017. Tributaries of the Elbe-Palaeovalley: features of a hidden palaeolandscape in the German Bight, North Sea. In: Bailey, G.N. (Ed.), Under the Sea: Archaeology and palaeolandscapes. Springer International Publishing, [S.l.].

Hijma, M.P., Cohen, K.M., Roebroeks, W., Westerhoff, W.E., Busschers, F.S., 2012. Pleistocene Rhine-Thames landscapes: geological background for hominin occupation of the southern North Sea region. Journal of Quaternary Science 27(1), 17–39.

Hill, A.E., Brown, J., Fernand, L., Holt, J., Horsburgh, K.J., Proctor, R., Raine, R., Turrell, W.R., 2008. Thermohaline circulation of shallow tidal seas. Geophysical Research Letters 35(11).

Houbolt, J., 1968. Recent sediments in the southern bight of the North Sea. Geologie en mijnbouw 47(4), 245–273.

Houmark-Nielsen, M., Kjaer, K.H., 2003. Southwest Scandinavia, 40-15 kyr BP: Palaeogeography and environmental change. Journal of Quaternary Science 18(8), 769–786.

Houmark-Nielsen, M., Linge, H., Fabel, D., Schnabel, C., Xu, S., Wilcken, K.M., Binnie, S., 2012. Cosmogenic surface exposure dating the last deglaciation in Denmark: Discrepancies with independent age constraints suggest delayed periglacial landform stabilisation. Quaternary Geochronology 13, 1–17.

Howarth, M.J., Dyer, K.R., Joint, I.R., Hydes, D.J., Purdie, D.A., Edmunds, H., Jones, J.E., Lowry, R.K., Moffat, T.J., Pomroy, A.J., Proctor, R., 1994. Seasonal cycles and their spatial variability. In: Charnock, H., Dyer, K.R., Huthnance, J.M., Liss, P.S., Simpson, J.H., Tett, P.B. (Eds.), Understanding the North Sea System. Springer Netherlands, Dordrecht, pp. 5–25.

Hughes, A.L.C., Gyllencreutz, R., Lohne, Ø.S., Mangerud, J., Svendsen, J.I., 2016. The last Eurasian ice sheets - a chronological database and time-slice reconstruction, DATED-1. Boreas 45(1), 1–45.

Huisink, M., 2000. Changing river styles in response to Weichselian climate changes in the Vecht valley, eastern Netherlands. Sedimentary Geology 133(1-2), 115–134.

Huuse, M., Lykke-Andersen, H., 2000. Overdeepened Quaternary valleys in the eastern Danish North Sea: Morphology and origin. Quaternary Science Reviews 19(12), 1233–1253.

Huuse, M., Lykke-Andersen, H., Michelsen, O., 2001. Cenozoic evolution of the eastern Danish North Sea. Marine Geology 177(3-4), 243–269.

Imbrie, J., Boyle, E.A., Clemens, S.C., Duffy, A., Howard, W.R., Kukla, G., Kutzbach, J., Martinson, D.G., McIntyre, A., Mix, A.C., Molfino, B., Morley, J.J., Peterson, L.C., Pisias, N.G., Prell, W.L., Raymo, M.E., Shackleton, N.J., Toggweiler, J.R., 1992. On the Structure and Origin of Major Glaciation Cycles 1. Linear Responses to Milankovitch Forcing. Paleoceanography 7(6), 701–738.

Jakobsson, M., Björck, S., Alm, G., Andrén, T., Lindeberg, G., Svensson, N.-O., 2007. Reconstructing the Younger Dryas ice dammed lake in the Baltic Basin: Bathymetry, area and volume. Global and Planetary Change 57(3-4), 355–370.

Jakobsson, M., Mayer, L., Coakley, B., Dowdeswell, J.A., Forbes, S., Fridman, B., Hodnesdal, H., Noormets, R., Pedersen, R., Rebesco, M., Schenke, H.W., Zarayskaya, Y., Accettella, D., Armstrong, A., Anderson, R.M., Bienhoff, P., Camerlenghi, A., Church, I., Edwards, M., Gardner, J.V., Hall, J.K., Hell, B., Hestvik, O., Kristoffersen, Y., Marcussen, C., Mohammad, R., Mosher, D., Nghiem, S.V., Pedrosa, M.T., Travaglini, P.G., Weatherall, P., 2012. The International Bathymetric Chart of the Arctic Ocean (IBCAO) Version 3.0. Geophysical Research Letters 39(12), 1–6.

Jansen, J., 1976. Late pleistocene and hologene history of the northern North Sea, based on acoustic reflection records. Netherlands Journal of Sea Research 10(1), 1–43.

Janszen, A., 2012. Tunnel valleys. Ph.D. thesis, TU Delft, Delft University of Technology.

Jelgersma, S., 1979. Sea-level changes in the North Sea basin. In: Oele, E., Schüttenhelm, R., Wiggers, A.J. (Eds.), The quaternary history of the North Sea. Acta Universitatis Upsaliensis2. Almqvist & Wiksell, Stockholm, pp. 233–248.

Jensen, J.B., Leth, J.O. Borre, S., Nørgaard-Pedersen, N., 2010. Model for potentielle sand- og grusforekomster for de danske farvande. Jyske Rev – Lille Fisker Banke området, 54. GEUS Rapport.

Jessen, S.P., Rasmussen, T.L., Nielsen, T., Solheim, A., 2010. A new Late Weichselian and Holocene marine chronology for the western Svalbard slope 30,000–0 cal years BP. Quaternary Science Reviews 29(9-10), 1301–1312.

Jungclaus, J.H., Backhaus, J.O., Fohrmann, H., 1995. Outflow of dense water from the Storfjord in Svalbard: A numerical model study. Journal of Geophysical Research 100(C12), 24719–24728.

Kaiser, K., Lorenz, S., Germer, S., Juschus, O., Küster, M., Libra, J., Bens, O., Hüttl, R., 2012. Late Quaternary evolution of rivers, lakes and peatlands in northeast Germany reflecting past climatic and human impact – an overview. E&G – Quaternary Science Journal 61, 103–132.

Kappenberg, J., Grabemann, I., 2001. Variability of the Mixing Zones and Estuarine Turbidity Maxima in the Elbe and Weser Estuaries. Estuaries 24(5), 699–706.

Kehew, A.E., Lord, M.L., Kozlowski, A.L., Fisher, T.G., 2009. Proglacial megaflooding along the margins of the Laurentide Ice Sheet. In: Burr, D., Baker, V.R., Carling, P. (Eds.), Megaflooding on Earth and Mars. Cambridge University Press, Cambridge, pp. 104–127.

Kenyon, N.H., Cooper, W.S., 2005. Sand Banks, Sand Transport and Offshore Wind Farms, UK Government. Department of Energy & Climate Change, London.

Kiden, P., Denys, L., Johnston, P., 2002. Late Quaternary sea-level change and isostatic and tectonic land movements along the Belgian-Dutch North Sea coast: Geological data and model results. Journal of Quaternary Science 17(5-6), 535–546.

King, E.L., Bøe, R., Bellec, V.K., Rise, L., Skarðhamar, J., Ferré, B., Dolan, M.F., 2014. Contour current driven continental slope-situated sandwaves with effects from secondary current processes on the Barents Sea margin offshore Norway. Marine Geology 353, 108–127.

Kleman, J., Stroeven, A.P., Lundqvist, J., 2008. Patterns of Quaternary ice sheet erosion and deposition in Fennoscandia and a theoretical framework for explanation. Geomorphology 97(1-2), 73–90.

Knutz, P.C., Zahn, R., Hall, I.R., 2007. Centennial-scale variability of the British Ice Sheet: Implications for climate forcing and Atlantic meridional overturning circulation during the last deglaciation. Paleoceanography 22(1), n/a-n/a.

Kolstrup, E., 2005. Periglacial geomorphology. In: Koster, E.A. (Ed.), The physical geography of Western Europe. The Oxford regional environments series. Oxford University Press, Oxford.

Konradi, P.B., 2000. Biostratigraphy and environment of the Holocene marine transgression in the Heligoland Channel, North Sea. Bulletin of the Geological Society of Denmark 47, 71–79.

Koster, E.A. (Ed.), 2005. The physical geography of Western Europe. Oxford University Press. The Oxford regional environments series, Oxford.

Köhn, W., 1991. Die nacheiszeitliche Entwicklung der südlichen Nordsee: Paläographische Karten für die südliche Nordseeküste. Hannoversche geographische Arbeiten Band 45. Höller und Zwick, Hannover.

Kristensen, T.B., Huuse, M., Piotrowski, J.A., Clausen, O.R., 2007. A morphometric analysis of tunnel valleys in the eastern North Sea based on 3D seismic data. Journal of Quaternary Science 22(8), 801–815.

Kwoll, E., Becker, M., Winter, C., 2014. With or against the tide: The influence of bed form asymmetry on the formation of macroturbulence and suspended sediment patterns. Water Resources Research 50(10), 7800–7815.

Laban, C., 1995. The Pleistocene glaciations in the Dutch sector of the North Sea. Proefschrift (PhD) thesis, University of Amsterdam, Amsterdam, 195.

Laberg, J.S., Andreassen, K., Vorren, T.O., 2012. Late Cenozoic erosion of the high-latitude southwestern Barents Sea shelf revisited. Geological Society of America Bulletin 124(1-2), 77–88.

Laberg, J.S., Vorren, T.O., 1996. The Middle and Late Pleistocence evolution and the Bear Island Trough Mouth Fan. Global and Planetary Change 12(1-4), 309–330.

Lambeck, K., 1995. Late Devensian and Holocene shorelines of the British Isles and North Sea from models of glacio-hydro-isostatic rebound. Journal of the Geological Society 152(3), 437–448.

Lambeck, K., Chappell, J., 2001. Sea level change through the last glacial cycle. Science (New York, N.Y.) 292(5517), 679–686.

Lambeck, K., Esat, T.M., Potter, E.-K., 2002a. Links between climate and sea levels for the past three million years. Nature 419(6903), 199–206.

Lambeck, K., Purcell, Anthony, P., Zhao, J., Svensson, N.-O., 2010. The Scandinavian Ice Sheet: From MIS 4 to the end of the Last Glacial Maximum. Boreas 39(2), 410–435.

Lambeck, K., Rouby, H., Purcell, A., Sun, Y., Sambridge, M., 2014. Sea level and global ice volumes from the Last Glacial Maximum to the Holocene. Proceedings of the National Academy of Sciences of the United States of America 111(43), 15296–15303.

Lambeck, K., Smither, C., Johnston, P., 1998. Sea-level change, glacial rebound and mantle viscosity fornorthern Europe. Geophysical Journal International 134(1), 102–144.

Lambeck, K., Yokoyama, Y., Purcell, T., 2002b. Into and out of the Last Glacial Maximum: Sea-level change during Oxygen Isotope Stages 3 and 2. Quaternary Science Reviews 21(1-3), 343–360.

Larsen, N.K., Knudsen, K.L., Krohn, C.F., Kronborg, C., Murray, A.S., Nielsen, O.B., 2009. Late Quaternary ice sheet, lake and sea history of southwest Scandinavia – a synthesis. Boreas 38(4), 732–761.

Lebesbye, E., Vorren, T.O., 1996. Submerged terraces in the southwestern Barents Sea: Origin and implications for the late Cenozoic geological history. Marine Geology 130(3-4), 265–280.

Lekens, W., Sejrup, H.P., Haflidason, H., Petersen, G., Hjelstuen, B., Knorr, G., 2005. Laminated sediments preceding Heinrich event 1 in the Northern North Sea and Southern Norwegian Sea: Origin, processes and regional linkage. Marine Geology 216(1-2), 27–50.

Lekens, W.A.H., Sejrup, H.P., Haflidason, H., Knies, J., Richter, T., 2006. Meltwater and ice rafting in the southern Norwegian Sea between 20 and 40 calendar kyr B.P: Implications for Fennoscandian Heinrich events. Paleoceanography 21(3), n/a-n/a.

Lericolais, G., Auffret, J.-P., Bourillet, J.-F., 2003. The Quaternary Channel River: Seismic stratigraphy of its palaeo-valleys and deeps. Journal of Quaternary Science 18(3-4), 245–260.

Lericolais, G., Berné, S., Féniès, H., 2001. Seaward pinching out and internal stratigraphy of the Gironde incised valley on the shelf (Bay of Biscay). Marine Geology 175(1-4), 183–197.

Li, C., Wang, P., Fan, D., Yang, S., 2006. Characteristics and Formation of Late Quaternary Incised-Valley-Fill Sequences in Sediment-Rich Deltas and Estuaries: Case Studies from China. In: Dalrymple, R.W., Leckie, D.A., Tillman, R.W. (Eds.), Incised Valleys in Time and Space. SEPM (Society for Sedimentary Geology), pp. 141–160.

Litt, T., Behre, K.-E., Meyer, K.-D., Stephan, H.-J., Wansa, S., 2007. Stratigraphische Begriffe für das Quartär des norddeutschen Vereisungsgebietes (E&G – Quaternary Science Journal; Vol. 56 No 1-2; 7-65; ISSN 0424-7116).

Liu, Z., Berné, S., Saito, Y., Yu, H., Trentesaux, A., Uehara, K., Yin, P., Paul Liu, J., Li, C., Hu, G., Wang, X., 2007. Internal architecture and mobility of tidal sand ridges in the East China Sea. Continental Shelf Research 27(13), 1820–1834.

Llopart, J., Urgeles, R., Camerlenghi, A., Lucchi, R.G., Rebesco, M., Mol, B. de, 2015. Late Quaternary development of the Storfjorden and Kveithola Trough Mouth Fans, northwestern Barents Sea. Quaternary Science Reviews 129, 68–84.

Long, D., Laban, C., Streif, H., Cameron, T., Schuttenhelm, R.T.E., Paepe, R., 1988. The Sedimentary Record of Climatic Variation in the Southern North Sea [and Discussion]. Philosophical Transactions of the Royal Society B: Biological Sciences 318(1191), 523–537.

Long, D., Stoker, M.S., 1986. Channels in the North Sea: the Nature of a Hazard. In: Oceanology. Advances in Underwater Technology, Ocean Science and Offshore Engineering. Springer Netherlands, Dordrecht, pp. 339–351.

Lucchi, R.G., Camerlenghi, A., Rebesco, M., Colmenero-Hidalgo, E., Sierro, F.J., Sagnotti, L., Urgeles, R., Melis, R., Morigi, C., Bárcena, M.-A., Giorgetti, G., Villa, G., Persico, D., Flores, J.-A., Rigual-Hernández, A.S., Pedrosa, M.T., Macri, P., Caburlotto, A., 2013. Postglacial sedimentary processes on the Storfjorden and Kveithola trough mouth fans: Significance of extreme glacimarine sedimentation. Global and Planetary Change 111, 309–326.

Lucchi, R.G., Sagnotti, L., Camerlenghi, A., Macrì, P., Rebesco, M., Pedrosa, M.T., Giorgetti, G., 2015. Marine sedimentary record of Meltwater Pulse 1a along the NW Barents Sea continental margin. Arktos.

Ludwig, G., Müller, H., Streif, H., 1981. New Dates on Holocene Sea-Level Changes in the German Bight. In: Nio, S.-D., Shuettenhelm, R.T.E., van Weering, T.C.E. (Eds.), Holocene marine sedimentation in the North

Sea basin: (Texel meeting; Texel, September, 1979). Special publication of the International Association of Sedimentologistsno. 5. Blackwell Scientific Publications, Oxford, pp. 211–219.

Lutz, R., Kalka, S., Gaedicke, C., Reinhardt, L., Winsemann, J., 2009. Pleistocene tunnel valleys in the German North Sea: Spatial distribution and morphology
[Pleistozäne Rinnen in der deutschen Nordsee: Verbreitung und Morphologie]. Zeitschrift der Deutschen Gesellschaft für Geowissenschaften 160(3), 225–235.

Lüthgens, C., Böse, M., 2011. Chronology of Weichselian main ice marginal positions in north-eastern Germany. E&G – Quaternary Science Journal 60(2-3), 236–247.

Lüthgens, C., Böse, M., 2012. From morphostratigraphy to geochronology – on the dating of ice marginal positions. Quaternary Science Reviews 44, 26–36.

Manabe, S., Broccoli, A.J., 1985. The influence of continental ice sheets on the climate of an ice age. Journal of Geophysical Research 90(D1), 2167–2190.

Mangerud, J., 2004. Ice-dammed lakes and rerouting of the drainage of northern Eurasia during the Last Glaciation. Quaternary Science Reviews 23(11-13), 1313–1332.

Mangerud, J., Gulliksen, S., 1975. Apparent radiocarbon ages of recent marine shells from Norway, Spitsbergen, and Arctic Canada. Quaternary Research 5(2), 263–273.

Marcott, S.A., Shakun, J.D., Clark, P.U., Mix, A.C., 2013. A reconstruction of regional and global temperature for the past 11,300 years. Science (New York, N.Y.) 339(6124), 1198–1201.

Marotta, A.M., Bayer, U., Thybo, H., 2000. The legacy of the NE German Basin - reactivation by compressional buckling. Terra Nova 12(3), 132–140.

Maselli, V., Trincardi, F., 2013. Large-scale single incised valley from a small catchment basin on the western Adriatic margin (central Mediterranean Sea). Global and Planetary Change 100, 245–262.

Masselink, G., Russell, P., 2013. Impacts of climate change on coastal erosion, 71-86. MCCIP Science Review.

Mattheus, C.R., Rodriguez, A.B., 2011. Controls on late Quaternary incised-valley dimension along passive margins evaluated using empirical data. Sedimentology 58(5), 1113–1137.

McCave, I.N., Langhorne, D.N., 1982. Sand waves and sediment transport around the end of a tidal sand bank. Sedimentology 29(1), 95–110.

Meijer, X.D., 2002. Modelling the drainage evolution of a river-shelf system forced by Quaternary glacio-eustasy. Basin Research 14(3), 361–377.

Mellett, C.L., Hodgson, D.M., Plater, A.J., Mauz, B., Selby, I., Lang, A., 2013. Denudation of the continental shelf between Britain and France at the glacial–interglacial timescale. Geomorphology 203, 79–96.

Ménot, G., Bard, E., Rostek, F., Weijers, J.W.H., Hopmans, E.C., Schouten, S., Damste, J.S.S., 2006. Early Reactivation of European Rivers During the Last Deglaciation. Science 313(5793), 1623–1625.

Midttun, L., 1990. Surface temperatures of the Barents Sea. Polar Research 8(1), 11–16.

Missiaen, T., Slob, E., Donselaar, M.E., 2008. Comparing different shallow geophysical methods in a tidal estuary, Verdronken Land van Saeftinge, Western Scheldt, the Netherlands. Netherlands Journal of Geosciences 87(02), 151–164.

Mitchum, R.M., Vail, P.R., Thompson III, S., 1977. Seismic stratigraphy and global changes of sea level: Part 2. The depositional sequence as a basic unit for stratigraphic analysis: Section 2. Application of seismic reflection configuration to stratigraphic interpretation, 53–62.

Mitrovica, J.X., Milne, G.A., 2002. On the origin of late Holocene sea-level highstands within equatorial ocean basins. Quaternary Science Reviews 21(20-22), 2179–2190.

Mittelstaedt, E., Soetje, K., 1982. Die Zirkulation in der Deutschen Bucht im August und September 1979. Deutsche Hydrographische Zeitschrift 35(2), 59–72.

Mol, J., 1997. Fluvial response to Weichselian climate changes in the Niederlausitz (Germany). Journal of Quaternary Science 12(1), 43–60.

Mol, J., Vandenberghe, J., Kasse, C., 2000. River response to variations of periglacial climate in mid-latitude Europe. Geomorphology 33(3-4), 131–148.

Moossen, H., Bendle, J., Seki, O., Quillmann, U., Kawamura, K., 2015. North Atlantic Holocene climate evolution recorded by high-resolution terrestrial and marine biomarker records. Quaternary Science Reviews 129, 111–127.

Mörner, N.A., 1979. The Fennoscandian uplift and late cenozoic geodynamics: Geological evidence. GeoJournal 3(3), 287–318.

Murton, D.K., Murton, J.B., 2012. Middle and Late Pleistocene glacial lakes of lowland Britain and the southern North Sea Basin. Quaternary International 260, 115–142.

Murton, J.B., Bateman, M.D., Dallimore, S.R., Teller, J.T., Yang, Z., 2010. Identification of Younger Dryas outburst flood path from Lake Agassiz to the Arctic Ocean. Nature 464(7289), 740–743.

Müller-Michaelis, A., Uenzelmann-Neben, G., 2015. Using seismic reflection data to reveal high-resolution structure and pathway of the upper Western Boundary Undercurrent core at Eirik Drift. Marine Geophysical Researches 36(4), 343–353.

Müther, D., Back, S., Reuning, L., Kukla, P., Lehmkuhl, F., 2012. Middle Pleistocene landforms in the Danish Sector of the southern North Sea imaged on 3D seismic data. Geological Society, London, Special Publications 368(1), 111–127.

Nauw, J., Haas, H. de, Rehder, G., 2015. A review of oceanographic and meteorological controls on the North Sea circulation and hydrodynamics with a view to the fate of North Sea methane from well site 22/4b and other seabed sources. Marine and Petroleum Geology 68, 861–882.

Neill, S.P., Scourse, J.D., Bigg, G.R., Uehara, K., 2009. Changes in wave climate over the northwest European shelf seas during the last 12,000 years. Journal of Geophysical Research 114(C6).

Neill, S.P., Scourse, J.D., Uehara, K., 2010. Evolution of bed shear stress distribution over the northwest European shelf seas during the last 12,000 years. Ocean Dynamics 60(5), 1139–1156.

Nittrouer, C.A., Austin, J.A., Field, M.E., Kravitz, J.H., Syvitski, J.P.M., Wiberg, P.L., 2007. Writing a Rosetta Stone: Insights into Continental-Margin Sedimentary Processes and Strata. In: Nittrouer, C.A., Austin, J.A., Field, M.E., Kravitz, J.H., Syvitski, J.P.M., Wiberg, P.L. (Eds.), Continental Margin Sedimentation. Blackwell Publishing Ltd, Oxford, UK, pp. 1–48.

Nordfjord, S., Goff, J.A., Austin, J.A., Gulick, S., 2006. Seismic Facies of Incised-Valley Fills, New Jersey Continental Shelf: Implications for Erosion and Preservation Processes Acting During Latest Pleistocene-Holocene Transgression. Journal of Sedimentary Research 76(12), 1284–1303.

Nordfjord, S., Goff, J.A., Austin, J.A., Sommerfield, C.K., 2005. Seismic geomorphology of buried channel systems on the New Jersey outer shelf: Assessing past environmental conditions. Marine Geology 214(4), 339–364.

Ospar Commision, 2000. Quality status report 2000: Region II: Greater North Sea. OSPAR Commission, London.

Ottesen, D., Dowdeswell, J.A., Rise, L., 2005. Submarine landforms and the reconstruction of fast-flowing ice streams within a large Quaternary ice sheet: The 2500-km-long Norwegian-Svalbard margin (57°–80°N). Geological Society of America Bulletin 117(7), 1033.

Ottesen, D., Stokes, C.R., Bøe, R., Rise, L., Longva, O., Thorsnes, T., Olesen, O., Bugge, T., Lepland, A., Hestvik, O.B., 2016. Landform assemblages and sedimentary processes along the Norwegian Channel Ice Stream. Sedimentary Geology.

Otto, L., Zimmerman, J., Furnes, G.K., Mork, M., Saetre, R., Becker, G., 1990. Review of the physical oceanography of the North Sea. Netherlands Journal of Sea Research 26(2-4), 161–238.

Passeri, D.L., Hagen, S.C., Medeiros, S.C., Bilskie, M.V., Alizad, K., Wang, D., 2015. The dynamic effects of sea level rise on low-gradient coastal landscapes: A review. Earth's Future 3(6), 159–181.

Patton, H., Hubbard, A., Andreassen, K., Winsborrow, M., Stroeven, A.P., 2016. The build-up, configuration, and dynamical sensitivity of the Eurasian ice-sheet complex to Late Weichselian climatic and oceanic forcing. Quaternary Science Reviews 153, 97–121.

Payenberg, T.H.D., Boyd, R., Beaudoin, J., Ruming, K., Davies, S., Roberts, J., Lang, S.C., 2006. The Filling of an Incised Valley by Shelf Dunes—an example from Hervey Bay, East Coast OF Australia. In: Dalrymple,

R.W., Leckie, D.A., Tillman, R.W. (Eds.), Incised Valleys in Time and Space. SEPM (Society for Sedimentary Geology), pp. 87–98.

Peck, V.L., Hall, I.R., Zahn, R., Elderfield, H., Grousset, F., Hemming, S.R., Scourse, J.D., 2006. High resolution evidence for linkages between NW European ice sheet instability and Atlantic Meridional Overturning Circulation. Earth and Planetary Science Letters 243(3-4), 476–488.

Peck, V.L., Hall, I.R., Zahn, R., Scourse, J.D., 2007. Progressive reduction in NE Atlantic intermediate water ventilation prior to Heinrich events: Response to NW European ice sheet instabilities? Geochemistry, Geophysics, Geosystems 8(1), n/a-n/a.

Pedrosa, M.T., Camerlenghi, A., Mol, B. de, Urgeles, R., Rebesco, M., Lucchi, R.G., 2011. Seabed morphology and shallow sedimentary structure of the Storfjorden and Kveithola trough-mouth fans (North West Barents Sea). Marine Geology 286(1-4), 65–81.

Pelling, H.E., Uehara, K., Green, J.A.M., 2013. The impact of rapid coastline changes and sea level rise on the tides in the Bohai Sea, China. Journal of Geophysical Research: Oceans 118(7), 3462–3472.

Peltier, W.R., Fairbanks, R.G., 2006. Global glacial ice volume and Last Glacial Maximum duration from an extended Barbados sea level record. Quaternary Science Reviews 25(23-24), 3322–3337.

Pickering, M.D., Wells, N.C., Horsburgh, K.J., Green, J., 2012. The impact of future sea-level rise on the European Shelf tides. Continental Shelf Research 35, 1–15.

Pisarska-Jamroży, M., 2015. Factors controlling sedimentation in the Toruń-Eberswalde ice-marginal valley during the Pomeranian phase of the Weichselian glaciation: An overview. Geologos 21(1), 1–29.

Plaza-Morlote, M., Rey, D., Santos, J.F., Ribeiro, S., Heslop, D., Bernabeu, A., Mohamed, K.J., Rubio, B., Martíns, V., 2017. Southernmost evidence of large European Ice Sheet-derived freshwater discharges during the Heinrich Stadials of the Last Glacial Period (Galician Interior Basin, Northwest Iberian Continental Margin). Earth and Planetary Science Letters 457, 213–226.

Polyak, B., Lehman, S.J., Gataullin, V., Timothy Jull, A.J., 1995. Two-step deglaciation of the southeastern Barents Sea. Geology 23(6), 567.

Polyak, L., Forman, S.L., Herlihy, F.A., Ivanov, G., Krinitsky, P., 1997. Late Weichselian deglacial history of the Svyataya (Saint) Anna Trough, northern Kara Sea, Arctic Russia. Marine Geology 143(1-4), 169–188.

Poulain, P.-M., Warn-Varnas, A., Niiler, P.P., 1996. Near-surface circulation of the Nordic seas as measured by Lagrangian drifters. Journal of Geophysical Research 101(C8), 18237–18258.

Presti, M., Santis, L. de, Busetti, M., Harris, P.T., 2003. Late Pleistocene and Holocene sedimentation on the George V Continental Shelf, East Antarctica. Recent investigations of the Mertz Polynya and George Vth Land continental margin, East Antarctica 50(8–9), 1441–1461.

Quadfasel, D., Rudels, B., Kurz, K., 1988. Outflow of dense water from a Svalbard fjord into the Fram Strait. Deep Sea Research Part A. Oceanographic Research Papers 35(7), 1143–1150.

Rasmussen, E., 2004. The interplay between true eustatic sea-level changes, tectonics, and climatic changes: What is the dominating factor in sequence formation of the Upper Oligocene–Miocene succession in the eastern North Sea Basin, Denmark? Global and Planetary Change 41(1), 15–30.

Rasmussen, S.O., Andersen, K.K., Svensson, A.M., Steffensen, J.P., Vinther, B.M., Clausen, H.B., Siggaard-Andersen, M.-L., Johnsen, S.J., Larsen, L.B., Dahl-Jensen, D., Bigler, M., Röthlisberger, R., Fischer, H., Goto-Azuma, K., Hansson, M.E., Ruth, U., 2006. A new Greenland ice core chronology for the last glacial termination. Journal of Geophysical Research 111(D6), 527.

Rasmussen, T.L., Thomsen, E., 2014. Brine formation in relation to climate changes and ice retreat during the last 15,000 years in Storfjorden, Svalbard, 76-78°N. Paleoceanography 29(10), 911–929.

Rasmussen, T.L., Thomsen, E., 2015. Palaeoceanographic development in Storfjorden, Svalbard, during the deglaciation and Holocene: Evidence from benthic foraminiferal records. Boreas 44(1), 24–44.

Rasmussen, T.L., Thomsen, E., Ślubowska, M.A., Jessen, S., Solheim, A., Koç, N., 2007. Paleoceanographic evolution of the SW Svalbard margin (76°N) since 20,000 14C yr BP. Quaternary Research 67(1), 100–114.

Rebesco, M., 2005. Sedimentary Environments | Contourites. In: Encyclopedia of Geology. Elsevier, pp. 513–527.

Rebesco, M., Camerlenghi, A. (Eds.), 2008a. Contourites. Elsevier. Developments in Sedimentology 60, Amsterdam, Oxford.

Rebesco, M., Camerlenghi, A., 2008b. Preface. In: Rebesco, M., Camerlenghi, A. (Eds.), Contourites. Developments in Sedimentology60. Elsevier, Amsterdam, Oxford, pp. xvii–xviii.

Rebesco, M., Hernández-Molina, F.J., van Rooij, D., Wåhlin, A., 2014a. Contourites and associated sediments controlled by deep-water circulation processes: State-of-the-art and future considerations. Marine Geology 352, 111–154.

Rebesco, M., Laberg, J.S., Pedrosa, M.T., Camerlenghi, A., Lucchi, R.G., Zgur, F., Wardell, N., 2014b. Onset and growth of Trough-Mouth Fans on the North-Western Barents Sea margin – implications for the evolution of the Barents Sea/Svalbard Ice Sheet. Quaternary Science Reviews 92, 227–234.

Rebesco, M., Liu, Y., Camerlenghi, A., Winsborrow, M., Laberg, J.S., Caburlotto, A., Diviacco, P., Accettella, D., Sauli, C., Wardell, N., Tomini, I., 2011. Deglaciation of the western margin of the Barents Sea Ice Sheet — A swath bathymetric and sub-bottom seismic study from the Kveithola Trough. Marine Geology 279(1-4), 141–147.

Rebesco, M., Özmaral, A., Urgeles, R., Accettella, D., Lucchi, R.G., Rüther, D., Winsborrow, M., Llopart, J., Caburlotto, A., Lantzsch, H., Hanebuth, T.J., 2016a. Evolution of a high-latitude sediment drift inside a glacially-carved trough based on high-resolution seismic stratigraphy (Kveithola, NW Barents Sea). Quaternary Science Reviews 147, 178–193.

Rebesco, M., Stow, D., 2001. Seismic expression of contourites and related deposits: a preface. Marine Geophysical Researches 22(5/6), 303–308.

Rebesco, M., Urgeles, R., Özmaral, A., 2016b. Grounding-zone wedges and mega-scale glacial lineations in Kveithola Trough, Barents Sea. In: Dowdeswell, J.A., Canals, M., Jakobsson, M., Todd, B.J., Dowdeswell, E.K., Hogan, K.A. (Eds.), Atlas of Submarine Glacial Landforms: Modern, Quaternary and Ancient. Geological Society of London Memoirs Series46. Geological Society, London, pp. 231–232.

Rebesco, M., Wåhlin, A., Laberg, J.S., Schauer, U., Beszczynska-Möller, A., Lucchi, R.G., Noormets, R., Accettella, D., Zarayskaya, Y., Diviacco, P., 2013. Quaternary contourite drifts of the Western Spitsbergen margin. Deep Sea Research Part I: Oceanographic Research Papers 79, 156–168.

Reicherter, K., Kaiser, A., Stackebrandt, W., 2005. The post-glacial landscape evolution of the North German Basin: Morphology, neotectonics and crustal deformation. International Journal of Earth Sciences 94(5-6), 1083–1093.

Reijenstein, H.M., Posamentier, H.W., Bhattacharya, J.P., 2011. Seismic geomorphology and high-resolution seismic stratigraphy of inner-shelf fluvial, estuarine, deltaic, and marine sequences, Gulf of Thailand. AAPG Bulletin 95(11), 1959–1990.

Reimer, P.J., Bard, E., Bayliss, A., Beck, J.W., Blackwell, P.G., Bronk Ramsey, C., Buck, C.E., Cheng, H., Edwards, R.L., Friedrich, M., Grootes, P.M., Guilderson, T.P., HAFLIDASON, H., Hajdas, I., Hatté, C., Heaton, T.J., Hoffmann, D.L., Hogg, A.G., Hughen, K.A., Kaiser, K.F., Kromer, B., Manning, S.W., Niu, M., Reimer, R.W., Richards, D.A., Scott, E.M., Southon, J.R., Staff, R.A., Turney, C.S.M., van der Plicht, J., 2013. IntCal13 and Marine13 Radiocarbon Age Calibration Curves 0–50,000 Years cal BP. Radiocarbon 55(4), 1869–1887.

Reynaud, J.-Y., Dalrymple, R.W., 2012. Shallow-Marine Tidal Deposits. In: Davis, R.A., Dalrymple, R.W. (Eds.), Principles of Tidal Sedimentology. Springer Netherlands, Dordrecht, pp. 335–369.

Reynaud, J.-Y., Tessier, B., Berné, S., Chamley, H., Debatist, M., 1999. Tide and wave dynamics on a sand bank from the deep shelf of the Western Channel approaches. Marine Geology 161(2-4), 339–359.

Rinterknecht, V.R., Clark, P.U., Raisbeck, G.M., Yiou, F., Bitinas, A., Brook, E.J., Marks, L., Zelcs, V., Lunkka, J.-P., Pavlovskaya, I.E., Piotrowski, J.A., Raukas, A., 2006. The last deglaciation of the southeastern sector of the Scandinavian ice sheet. Science (New York, N.Y.) 311(5766), 1449–1452.

Rippeth, T.P., Scourse, J.D., Uehara, K., McKeown, S., 2008. Impact of sea-level rise over the last deglacial transition on the strength of the continental shelf CO_2 pump. Geophysical Research Letters 35(24).

Rise, L., Bøe, R., Ottesen, D., Longva, O., Olsen, H.A., 2008. Postglacial depositional environments and sedimentation rates in the Norwegian Channel off southern Norway. Marine Geology 251(1-2), 124–138.

Risebrobakken, B., Moros, M., Ivanova, E.V., Chistyakova, N., Rosenberg, R., 2010. Climate and oceanographic variability in the SW Barents Sea during the Holocene. The Holocene 20(4), 609–621.

Roche, D.M., Wiersma, A.P., Renssen, H., 2010. A systematic study of the impact of freshwater pulses with respect to different geographical locations. Climate Dynamics 34(7-8), 997–1013.

Rodriguez, A.B., Greene, D.L., Anderson, J.B., Simms, A.R., 2008. Response of Mobile Bay and eastern Mississippi Sound, Alabama, to changes in sediment accommodation and accumulation. In: Anderson, J.B., Rodriguez, A.B. (Eds.), Response of upper Gulf Coast estuaries to Holocene climate change and sea-level rise. Special paper443. Geological Society of America, Boulder, Colo., pp. 13–29.

Roebroeks, W., 2014. Terra incognita: The Palaeolithic record of northwest Europe and the information potential of the southern North Sea. Netherlands Journal of Geosciences - Geologie en Mijnbouw 93(1-2), 43–53.

Rosgen, D.L., 1994. A classification of natural rivers. CATENA 22(3), 169–199.

Rudels, B., Quadfasel, D., 1991. Convection and deep water formation in the Arctic Ocean-Greenland Sea System. Journal of Marine Systems 2(3-4), 435–450.

Rüther, D.C., 2012. Palaeoenvironment of the Barents Sea during the last deglaciation and Holocene processes and timing. PhD Thesis, University of Tromsø.

Rüther, D.C., Bjarnadóttir, L.R., Junttila, J., Husum, K., Rasmussen, T.L., Lucchi, R.G., Andreassen, K., 2012. Pattern and timing of the northwestern Barents Sea Ice Sheet deglaciation and indications of episodic Holocene deposition. Boreas 41(3), 494–512.

Sarnthein, M, Kreveld, S., Erlenkeuser, H, Grootes, M, P., Kucera, Pflaumann, U, Schulz, 2003a. Centennial-to-millennial-scale periodicities of Holocene climate and sediment injections off the western Barents shelf, 75°N. Boreas 32(3), 447–461.

Sarnthein, M., Pflaumann, U., Weinelt, M., 2003b. Past extent of sea ice in the northern North Atlantic inferred from foraminiferal paleotemperature estimates. Paleoceanography 18(2).

Schauer, U., 1995. The release of brine-enriched shelf water from Storfjord into the Norwegian Sea. Journal of Geophysical Research 100(C8), 16015–16028.

Schieber, J., 2016a. Mud re-distribution in epicontinental basins – Exploring likely processes. Marine and Petroleum Geology 71, 119–133.

Schieber, J., 2016b. Mud re-distribution in epicontinental basins – Exploring likely processes. Marine and Petroleum Geology 71, 119–133.

Schrottke, K., Becker, M., Bartholomä, A., Flemming, B.W., Hebbeln, D., 2006. Fluid mud dynamics in the Weser estuary turbidity zone tracked by high-resolution side-scan sonar and parametric sub-bottom profiler. Geo-Marine Letters 26(3), 185–198.

Schwarz, C., 1996. Neue Befunde zur Verbreitung und Dimension pleistozäner Rinnensysteme auf dem deutschen Nordseeschelf. Geologisches Jahrbuch(A 146), 233–244.

Scourse, J.D., Haapaniemi, A.I., Colmenero-Hidalgo, E., Peck, V.L., Hall, I.R., Austin, W.E., Knutz, P.C., Zahn, R., 2009. Growth, dynamics and deglaciation of the last British–Irish ice sheet: The deep-sea ice-rafted detritus record. Quaternary Science Reviews 28(27-28), 3066–3084.

Sejrup, H.P., Clark, C.D., Hjelstuen, B.O., 2016. Rapid ice sheet retreat triggered by ice stream debuttressing: Evidence from the North Sea. Geology 44(5), 355–358.

Sejrup, H.P., Hjelstuen, B.O., Torbjørn Dahlgren, K.I., HAFLIDASON, H., Kuijpers, A., Nygård, A., Praeg, D., Stoker, M.S., Vorren, T.O., 2005. Pleistocene glacial history of the NW European continental margin. Marine and Petroleum Geology 22(9-10), 1111–1129.

Sejrup, H.P., Landvik, J.Y., Larsen, E., Janocko, J., Eiriksson, J., King, E., 1998. The jæren area, a border zone of the norwegian channel ice stream. Quaternary Science Reviews 17(9-10), 801–812.

Sejrup, H.P., Larsen, E., Landvik, J., King, E.L., Haflidason, H., Nesje, A., 2000. Quaternary glaciations in southern Fennoscandia: Evidence from southwestern Norway and the northern North Sea region. Quaternary Science Reviews 19(7), 667–685.

Sejrup, H.P., Nygård, A., Hall, A.M., Haflidason, H., 2009. Middle and Late Weichselian (Devensian) glaciation history of south-western Norway, North Sea and eastern UK. Quaternary Science Reviews 28(3-4), 370–380.

Shapiro, G.I., Huthnance, J.M., Ivanov, V.V., 2003. Dense water cascading off the continental shelf. Journal of Geophysical Research 108(C12).

Shennan, I., Lambeck, K., Flather, R., Horton, B., McArthur, J., Innes, J., Lloyd, J., Rutherford, M., Wingfield, R., 2000. Modelling western North Sea palaeogeographies and tidal changes during the Holocene. Geological Society, London, Special Publications 166(1), 299–319.

Siddall, M., Abe-Ouchi, A., Andersen, M., Antonioli, F., Bamber, J., Bard, E., Clark, J., Clark, P., Deschamps, P., Dutton, A., Elliot, M., Gallup, C., Gomez, N., Gregory, J., Huybers, P., Kawarnura, K., Kelly, M., Lambeck, K., Lowell, T., Milrovica, J., Otto-Bliesner, B., Richards, D., Stanford, J., Stirling, C., Stocker, T., Thomas, A., Thompson, B., Toernqvist, T., Riveiros, N.V., Waelbroeck, C., Yokoyama, Y., Yu, S., Grp, P.L.W., 2010. The sea-level conundrum: case studies from palaeo-archives. Journal of Quaternary Science 25(1), 19–25.

Siddall, M., Chappell, J., Potter, E.-K., 2007. 7. Eustatic sea level during past interglacials. In: Sirocko, F. (Ed.), The climate of past interglacials. Developments in Quaternary science7. Elsevier, Amsterdam, Oxford, pp. 75–92.

Siegert, M.J., Dowdeswell, J.A., Hald, M., Svendsen, J.-I., 2001. Modelling the Eurasian Ice Sheet through a full (Weichselian) glacial cycle. Global and Planetary Change 31(1-4), 367–385.

Simms, A.R., Aryal, N., Miller, L., Yokoyama, Y., 2010. The incised valley of Baffin Bay, Texas: A tale of two climates. Sedimentology 57(2), 642–669.

Simms, R, A., Anderson, B, J., Taha, P, Z., Rodriguez, B, A., 2006. Overfilled versus underfilled incised valleys: examples from the Quaternary Gulf of Mexico. In: Dalrymple, R.W. (Ed.), Incised valleys in time and space. SEPM special publication85. Society for Sedimentary Geology, Tulsa, Okla.

Skogseth, R., 2004. Ice and brine production in Storfjorden from four winters of satellite and in situ observations and modeling. Journal of Geophysical Research 109(C10).

Skogseth, R., Smedsrud, L.H., Nilsen, F., Fer, I., 2008. Observations of hydrography and downflow of brine-enriched shelf water in the Storfjorden polynya, Svalbard. Journal of Geophysical Research 113(C8), 1–13.

Ślubowska, M.A., Koç, N., Rasmussen, T.L., Klitgaard-Kristensen, D., 2005. Changes in the flow of Atlantic water into the Arctic Ocean since the last deglaciation: Evidence from the northern Svalbard continental margin, 80°N. Paleoceanography 20(4), 1–15.

Ślubowska-Woldengen, M., Rasmussen, T.L., Koç, N., Klitgaard-Kristensen, D., Nilsen, F., Solheim, A., 2007. Advection of Atlantic Water to the western and northern Svalbard shelf since 17,500calyr BP. Quaternary Science Reviews 26(3-4), 463–478.

Smith, A.J., 1985. A catastrophic origin for the palaeovalley system of the eastern English Channel. Marine Geology 64(1-2), 65–75.

Smith, D.E., Harrison, S., Firth, C.R., Jordan, J.T., 2011. The early Holocene sea level rise. Quaternary Science Reviews 30(15-16), 1846–1860.

Sørensen, J.C., Michelsen, O., 1995. Upper Cenozoic sequences in the southeastern North sea basin. Bulletin of the Geological Society of Denmark 42(1), 74–95.

Steffen, H., Wu, P., 2011. Glacial isostatic adjustment in Fennoscandia: A review of data and modeling. Journal of Geodynamics 52, 169–204.

Stewart, M.A., Lonergan, L., 2011. Seven glacial cycles in the middle-late Pleistocene of northwest Europe: Geomorphic evidence from buried tunnel valleys. Geology 39(3), 283–286.

Stiansen, J., Filin, A., 2008. Joint PINRO/IMR Report on the State of the Barents Sea Ecosystem in 2007, with Expected Situation and Considerations for Management., p. 185. IMR-PINRO Joint Report Series 2008(1), Institute of Marine Research, Bergen, Norway.

Stoker, S, M., Balson, S, P., Long, D, Tappin, R, D., 2011. An overview of the lithostratigraphical framework for the Quaternary deposits on the United Kingdom continental shelf, 49, British Geological Survey, Nottingham, UK.

Stow, D.A., Faugères, J.-C., 2008. Contourite facies and the facies model. Developments in Sedimentology 60, 223–256.

Stow, D.A.V., Faugeres, J.-C., Howe, J.A., Pudsey, C.J., Viana, A.R., 2002. Bottom currents, contourites and deep-sea sediment drifts: Current state-of-the-art. Geological Society, London, Memoirs 22(1), 7–20.

Streif, H., 2004. Sedimentary record of Pleistocene and Holocene marine inundations along the North Sea coast of Lower Saxony, Germany. Quaternary International 112(1), 3–28.

Stride, A.H., 1982. Offshore tidal sands: Processes and deposits / edited by A.H. Stride. Chapman and Hall, London.

Stroeven, A.P., Hättestrand, C., Kleman, J., Heyman, J., Fabel, D., Fredin, O., Goodfellow, B.W., Harbor, J.M., Jansen, J.D., Olsen, L., Caffee, M.W., Fink, D., Lundqvist, J., Rosqvist, G.C., Strömberg, B., Jansson, K.N., 2016. Deglaciation of Fennoscandia. Quaternary Science Reviews 147, 91–121.

Strong, N., Paola, C., 2008. Valleys That Never Were: Time Surfaces Versus Stratigraphic Surfaces. Journal of Sedimentary Research 78(8), 579–593.

Stuiver, M., Reimer, P.J., 1993. Extended 14C Data Base and Revised CALIB 3.0 14C Age Calibration Program. Radiocarbon 35(01), 215–230.

Svendsen, J.I., Alexanderson, H., Astakhov, V.I., Demidov, I., Dowdeswell, J.A., Funder, S., Gataullin, V., Henriksen, M., Hjort, C., Houmark-Nielsen, M., Hubberten, H.W., Ingólfsson, Ó., Jakobsson, M., Kjær, K.H., Larsen, E., Lokrantz, H., Lunkka, J.P., Lyså, A., Mangerud, J., Matiouchkov, A., Murray, A., Möller, P., Niessen, F., Nikolskaya, O., Polyak, L., Saarnisto, M., Siegert, C., Siegert, M.J., Spielhagen, R.F., Stein, R., 2004. Late Quaternary ice sheet history of northern Eurasia. Quaternary Science Reviews 23(11–13), 1229–1271.

Swift, D.J., 1970. Quaternary shelves and the return to grade. Marine Geology 8(1), 5–30.

Talley, L.D., Pickard, G.L., Emery, W.J., Swift, J.H., 2011. Gravity Waves, Tides, and Coastal Oceanography. In: Talley, L.D. (Ed.), Descriptive physical oceanography: An introduction / Lynne D. Talley [and others]. Elsevier, pp. 1–31.

Tamura, T., Ohshima, K.I., Nihashi, S., 2008. Mapping of sea ice production for Antarctic coastal polynyas. Geophysical Research Letters 35(7), n/a-n/a.

Telford, R.J., Heegaard, E., Birks, H., 2004. The intercept is a poor estimate of a calibrated radiocarbon age. The Holocene 14(2), 296–298.

Teller, J.T., 1990. Meltwater and precipitation runoff to the North Atlantic, Arctic, and Gulf of Mexico from the Laurentide Ice Sheet and adjacent regions during the Younger Dryas. Paleoceanography 5(6), 897–905.

Thieler, E.R., Butman, B., Schwab, W.C., Allison, M.A., Driscoll, N.W., Donnelly, J.P., Uchupi, E., 2007. A catastrophic meltwater flood event and the formation of the Hudson Shelf Valley. Palaeogeography, Palaeoclimatology, Palaeoecology 246(1), 120–136.

Thomas, D.N., Dieckmann, G., 2010. Sea ice, 2nd ed. ed. Wiley-Blackwell, Oxford.

Thomas, M., Sündermann, J., 1999. Tides and tidal torques of the world ocean since the last glacial maximum. Journal of Geophysical Research: Oceans 104(C2), 3159–3183.

Thomas, M.A., Anderson, J.B., 1994. Sea-Level Controls on the Facies Architecture of the Trinity/Sabine Incised-Valley System, Texas Continental Shelf. In: Dalrymple, R.W., Boyd, R., Zaitlin, B.A. (Eds.), Incised-Valley Systems. SEPM (Society for Sedimentary Geology), pp. 63–82.

Thomsen, C., Blaume, F., Fohrmann, H., Peeken, I., Zeller, U., 2001. Particle transport processes at slope environments — event driven flux across the Barents Sea continental margin. Marine Geology 175(1-4), 237–250.

Toucanne, S., Soulet, G., Freslon, N., Silva Jacinto, R., Dennielou, B., Zaragosi, S., Eynaud, F., Bourillet, J.-F., Bayon, G., 2015. Millennial-scale fluctuations of the European Ice Sheet at the end of the last glacial, and their potential impact on global climate. Quaternary Science Reviews 123, 113–133.

Toucanne, S., Zaragosi, S., Bourillet, J.F., Cremer, M., Eynaud, F., van Vliet-Lanoë, B., Penaud, A., Fontanier, C., Turon, J.L., Cortijo, E., 2009a. Timing of massive 'Fleuve Manche' discharges over the last 350kyr: İnsights into the European ice-sheet oscillations and the European drainage network from MIS 10 to 2. Quaternary Science Reviews 28(13-14), 1238–1256.

Toucanne, S., Zaragosi, S., Bourillet, J.F., Gibbard, P.L., Eynaud, F., Giraudeau, J., Turon, J.L., Cremer, M., Cortijo, E., Martinez, P., Rossignol, L., 2009b. A 1.2Ma record of glaciation and fluvial discharge from the West European Atlantic margin. Quaternary Science Reviews 28(25-26), 2974–2981.

Toucanne, S., Zaragosi, S., Bourillet, J.-F., Marieu, V., Cremer, M., Kageyama, M., van Vliet-Lanoë, B., Eynaud, F., Turon, J.-L., Gibbard, P.L., 2010. The first estimation of Fleuve Manche palaeoriver discharge during the last deglaciation: Evidence for Fennoscandian ice sheet meltwater flow in the English Channel ca 20–18ka ago. Earth and Planetary Science Letters 290(3-4), 459–473.

Törnqvist, T.E., Hijma, M.P., 2012. Links between early Holocene ice-sheet decay, sea-level rise and abrupt climate change. Nature Geoscience 5(9), 601–606.

Trentesaux, A., Stolk, A., Berné, S., 1999. Sedimentology and stratigraphy of a tidal sand bank in the southern North Sea. Marine Geology 159(1-4), 253–272.

Turner, F., Tolksdorf, J.F., Viehberg, F., Schwalb, A., Kaiser, K., Bittmann, F., Bramann, U. von, Pott, R., Staesche, U., Breest, K., Veil, S., 2013. Lateglacial/early Holocene fluvial reactions of the Jeetzel river (Elbe valley, northern Germany) to abrupt climatic and environmental changes. Quaternary Science Reviews 60, 91–109.

Uehara, K., Scourse, J.D., Horsburgh, K.J., Lambeck, K., Purcell, A.P., 2006. Tidal evolution of the northwest European shelf seas from the Last Glacial Maximum to the present. Journal of Geophysical Research 111(C9).

Valentin, H., 1957a. Die grenze der letzten Vereisung im Nordseeraum. Verhandlungen des Deutschen Geographentages 30, 359–366.

Valentin, H., 1957b. Glazialmorphologische Untersuchungen in Ostengland: ein Beitrag zum Problem der letzten Vereisung im Nordseeraum. Habilitationsschrift Freie Universität Berlin, Berlin.

van der Molen, J., 2002. The influence of tides, wind and waves on the net sand transport in the North Sea. Continental Shelf Research 22(18-19), 2739–2762.

van der Molen, J., Swart, H.E. de, 2001a. Holocene tidal conditions and tide-induced sand transport in the southern North Sea. Journal of Geophysical Research: Oceans 106(C5), 9339–9362.

van der Molen, J., Swart, H.E. de, 2001b. Holocene wave conditions and wave-induced sand transport in the southern North Sea. Continental Shelf Research 21(16-17), 1723–1749.

van der Plicht, J., Amkreutz, L., Niekus, M., Peeters, J., Smit, B.I., 2016. Surf'n Turf in Doggerland: Dating, stable isotopes and diet of Mesolithic human remains from the southern North Sea. Journal of Archaeological Science: Reports 10, 110–118.

van Heteren, S., Meekes, J., Bakker, M., Gaffney, V., Fitch, S., Gearey, B.R., Paap, B.F., 2014. Reconstructing North Sea palaeolandscapes from 3D and high-density 2D seismic data: An overview. Netherlands Journal of Geosciences - Geologie en Mijnbouw 93(1-2), 31–42.

van Wagoner, C, J., Posamentier, W, H., Mitchum, M, R., Vail, R, P., Sarg, F, J., Loutit, S, T., Hardenbol, J, 1998. An overview of sequence stratigraphy and key definitions. In: Wilgus, C.K., Hastings, B.S., Posamentier, H., van Wagoner, J., Ross, C.A., Christopher G. St. C. Kendall (Eds.), Sea-level changes: An integrated approach: An integrated approach. Special publication / Society of Economic Paleontologists and Mineralogists42. Society of Economic Paleontologists and Mineralogists, Tulsa, Okla., pp. 39–45.

van Weering, T., Stoker, M., Rebesco, M., 2008. High-Latitude Contourites. In: Rebesco, M., Camerlenghi, A. (Eds.), Contourites. Developments in Sedimentology60. Elsevier, Amsterdam, Oxford, pp. 457–489.

Vandenberghe, J., 1995. Timescales, climate and river development. Quaternary Science Reviews 14(6), 631–638.

Vandenberghe, J., 2008. The fluvial cycle at cold–warm–cold transitions in lowland regions: A refinement of theory. Geomorphology 98(3-4), 275–284.

Vandenberghe, J., Woo, M.-K., 2002. Modern and ancient periglacial river types. Progress in Physical Geography 26(4), 479–506.

Veenstra, H.J., 1965. Geology of the Dogger Bank area, North Sea. Marine Geology 3(4), 245–262.

Vink, A., Steffen, H., Reinhardt, L., Kaufmann, G., 2007. Holocene relative sea-level change, isostatic subsidence and the radial viscosity structure of the mantle of northwest Europe (Belgium, the Netherlands, Germany, southern North Sea). Quaternary Science Reviews 26(25-28), 3249–3275.

Voelker, A.H., Lebreiro, S.M., Schönfeld, J., Cacho, I., Erlenkeuser, H., Abrantes, F., 2006. Mediterranean outflow strengthening during northern hemisphere coolings: A salt source for the glacial Atlantic? Earth and Planetary Science Letters 245(1–2), 39–55.

Voigt, I., Henrich, R., Preu, B.M., Piola, A.R., Hanebuth, T.J., Schwenk, T., Chiessi, C.M., 2013. A submarine canyon as a climate archive — Interaction of the Antarctic Intermediate Water with the Mar del Plata Canyon (Southwest Atlantic). Marine Geology 341, 46–57.

Voronina, E., Polyak, L., Vernal, A.D., Peyron, O., 2001. Holocene variations of sea-surface conditions in the southeastern Barents Sea, reconstructed from dinoflagellate cyst assemblages. Journal of Quaternary Science 16(7), 717–726.

Vorren, T., Laberg, J., 1996. Late glacial air temperature, oceanographic and ice sheet interactions in the southern Barents Sea region. In: Andrews, J., Austin, W., Bergsten, H., Jennings, A. (Eds.), Late Quaternary Palaeoceanography of the North Atlantic Margins interactions in the southern Barents Sea region. 111. Geological Society, London, pp. 303–321.

Vorren, T., Laberg, J., Blaume, F., Dowdeswell, J., Kenyon, N.H., Mienert, J., Rumohr, J., Werner, F., 1998. The Norwegian–Greenland Sea continental margins: morphology and late Quaternary sedimentary processes and environment. Quaternary Science Reviews 17(1-3), 273–302.

Walcott, R.I., 1972. Past Sea Levels, Eustasy and Deformation of the Earth. Quaternary Research 2(1), 1–14.

Ward, I., Larcombe, P., 2013. Determining the preservation rating of submerged archaeology in the post-glacial southern North Sea: A first-order geomorphological approach. Environmental Archaeology 13(1), 59–83.

Ward, I., Larcombe, P., Lillie, M., 2006. The dating of Doggerland – post-glacial geochronology of the southern North Sea. Environmental Archaeology 11(2), 207–218.

Ward, S.L., Green, J.A.M., Pelling, H.E., 2012. Tides, sea-level rise and tidal power extraction on the European shelf. Ocean Dynamics 62(8), 1153–1167.

Ward, S.L., Neill, S.P., Scourse, J.D., Bradley, S.L., Uehara, K., 2016. Sensitivity of palaeotidal models of the northwest European shelf seas to glacial isostatic adjustment since the Last Glacial Maximum. Quaternary Science Reviews 151, 198–211.

Ward, S.L., Neill, S.P., van Landeghem, K.J., Scourse, J.D., 2015. Classifying seabed sediment type using simulated tidal-induced bed shear stress. Marine Geology 367, 94–104.

Weaver, A.J., Saenko, O.A., Clark, P.U., Mitrovica, J.X., 2003. Meltwater pulse 1A from Antarctica as a trigger of the Bolling-Allerod warm interval. Science (New York, N.Y.) 299(5613), 1709–1713.

Weber, M.E., Niessen, F., Kuhn, G., Wiedicke, M., 1997. Calibration and application of marine sedimentary physical properties using a multi-sensor core logger. Marine Geology 136(3-4), 151–172.

Wellner, R.W., Bartek, L.R., 2003. The Effect of Sea Level, Climate, and Shelf Physiography on the Development of Incised-Valley Complexes: A Modern Example from the East China Sea. Journal of Sedimentary Research 73(6), 926–940.

Weninger, B., Schulting, R., Bradtmöller, M., Clare, L., Collard, M., Edinborough, K., Hilpert, J., 2008. The catastrophic final flooding of Doggerland by the Storegga Slide tsunami. Documenta Praehistorica 35(0), 1–24.

Westaway, R., Bridgland, D.R., 2010. Causes, consequences and chronology of large-magnitude palaeoflows in Middle and Late Pleistocene river systems of northwest Europe. Earth Surface Processes and Landforms 35(9), 1071–1094.

Winsborrow, M.C., Andreassen, K., Corner, G.D., Laberg, J.S., 2010. Deglaciation of a marine-based ice sheet: Late Weichselian palaeo-ice dynamics and retreat in the southern Barents Sea reconstructed from onshore and offshore glacial geomorphology. Quaternary Science Reviews 29(3-4), 424–442.

Winther, N.G., Johannessen, J.A., 2006. North Sea circulation: Atlantic inflow and its destination. Journal of Geophysical Research 111(C12).

Wobus, F., Shapiro, G.I., Huthnance, J.M., Maqueda, M.A., 2013. The piercing of the Atlantic Layer by an Arctic shelf water cascade in an idealised study inspired by the Storfjorden overflow in Svalbard. Ocean Modelling 71, 54–65.

Woldstedt, P., 1950. Norddeutschland und angrenzende Gebiete im Eiszeitalter. K. F. Koehler, Stuttgart.

Wolters, S., Zeiler, M., Bungenstock, F., 2010. Early Holocene environmental history of sunken landscapes: Pollen, plant macrofossil and geochemical analyses from the Borkum Riffgrund, southern North Sea. International Journal of Earth Sciences 99(8), 1707–1719.

Woodroffe, C.D., Murray-Wallace, C.V., 2012. Sea-level rise and coastal change: The past as a guide to the future. Quaternary Science Reviews 54, 4–11.

Wright, L.D., 1995. Morphodynamics of inner continental shelves. Marine science series. CRC Press, Boca Raton, London.

Wunderlich, J., Wendt, G., Müller, S., 2005. High-resolution Echo-sounding and Detection of Embedded Archaeological Objects with Nonlinear Sub-bottom Profilers. Marine Geophysical Researches 26(2-4), 123–133.

Yilmaz, Ö., 2001. Seismic Data Analysis. Society of Exploration Geophysicists.

Yokoyama, Y., Esat, T., 2011. Global Climate and Sea Level: Enduring Variability and Rapid Fluctuations Over the Past 150,000 Years. Oceanography 24(2), 54–69.

Zaitlin, B.A., Dalrymple, R.W., Boyd, R., 1994. The stratigraphic organization of incised-valley systems associated with relative sea-level change. In: Dalrymple, R.W., Boyd, R., Zaitlin, B.A. (Eds.), Incised-Valley Systems. SEPM (Society for Sedimentary Geology), pp. 45–60.

Zecchin, M., Catuneanu, O., Rebesco, M., 2015. High-resolution sequence stratigraphy of clastic shelves IV: High-latitude settings. Marine and Petroleum Geology 68, 427–437.

Zeiler, M., Schulz-Ohlberg, J., Figge, K., 2000. Mobile sand deposits and shoreface sediment dynamics in the inner German Bight (North Sea). Marine Geology 170(3-4), 363–380.

Zgur, F., Caburlotto, A., Deponte, D., De Vittor, C., Facchin, L., Pelos, C., Tomini, I., Rebesco, M., 2008. EGLACOM, Evolution of a GLacial Arctic COntinental Margin: the Southern Svalbard Ice Stream - Dominated Sedimentary System, p. 88. OGS Cruise Report 111.

Ziegler, P.A. (Ed.), 1988. Evolution of the Arctic-North Atlantic and the Western Tethys. American Association of Petroleum Geologists.

Ziegler, P.A., 1992. North Sea rift system. Tectonophysics 208(1-3), 55–75.

Appendix

Appendix A: Trans-dimensional Bayesian inversion of controlled-source electromagnetic data in the German North Sea

Romina A. S. Gehrmann[1,2], Jan Dettmer[1,3], Katrin Schwalenberg[2], Martin Engels[2], Stan E. Dosso[1] and Aslı Özmaral[4]

[1]*School of Earth and Ocean Sciences, University of Victoria, Victoria, BC, Canada*

[2]*BGR - Federal Institute for Geosciences and Natural Resources, Hanover, Germany*

[3]*College of Physical & Mathematical Sciences, Australian National University, Canberra, Australia*

[4]*Faculty of Geosciences, University of Bremen, Germany*

Geophysical Prospecting

Trans-dimensional Bayesian inversion of controlled-source electromagnetic data in the German North Sea

Romina A. S. Gehrmann[1,2]*, Jan Dettmer[1,3], Katrin Schwalenberg[2],
Martin Engels[2], Stan E. Dosso[1] and Asli Özmaral[4]

[1]*School of Earth and Ocean Sciences, University of Victoria, Victoria, BC, Canada,* [2]*BGR - Federal Institute for Geosciences and Natural Resources, Hanover, Germany,* [3]*College of Physical & Mathematical Sciences, Australian National University, Canberra, Australia, and* [4]*Faculty of Geosciences, University of Bremen, Germany*

ABSTRACT

This paper presents the first controlled-source electromagnetic survey carried out in the German North Sea with a recently developed seafloor-towed electrical dipole–dipole system, i.e., HYDRA II. Controlled-source electromagnetic data are measured, processed, and inverted in the time domain to estimate an electrical resistivity model of the sub-seafloor. The controlled-source electromagnetic survey targeted a shallow, phase-reversed, seismic reflector, which potentially indicates free gas. To compare the resistivity model to reflection seismic data and draw a combined interpretation, we apply a trans-dimensional Bayesian inversion that estimates model parameters and uncertainties, and samples probabilistically over the number of layers of the resistivity model. The controlled-source electromagnetic data errors show time-varying correlations, and we therefore apply a non-Toeplitz data covariance matrix in the inversion that is estimated from residual analysis. The geological interpretation drawn from controlled-source electromagnetic inversion results and borehole and reflection seismic data yield resistivities of ∼1 Ωm at the seafloor, which are typical for fine-grained marine deposits, whereas resistivities below ∼20 mbsf increase to 2–4 Ωm and can be related to a transition from fine-grained (Holocene age) to unsorted, coarse-grained, and compacted glacial sediments (Pleistocene age). Interface depths from controlled-source electromagnetic inversion generally match the seismic reflector related to the contrast between the different depositional environments. Resistivities decrease again at greater depths to ∼1 Ωm with a minimum resistivity at ∼300 mbsf where a seismic reflector (that marks a major flooding surface of late Miocene age) correlates with an increased gamma-ray count, indicating an increased amount of fine-grained sediments. We suggest that the grain size may have a major impact on the electrical resistivity of the sediment with lower resistivities for fine-grained sediments. Concerning the phase-reversed seismic reflector that was targeted by the survey, controlled-source electromagnetic inversion results yield no indication for free gas below it as resistivities are generally elevated above the reflector. We suggest that the elevated resistivities are caused by an overall decrease in porosity in the glacial sediments and that the seismic reflector could be caused by an impedance contrast at a thin low-velocity layer. Controlled-source electromagnetic interface depths near the reflector are quite uncertain and variable. We conclude

*E-mail: Romina.Gehrmann@bgr.de

that the seismic interface cannot be resolved with the controlled-source electromagnetic data, but the thickness of the corresponding resistive layer follows the trend of the reflector that is inclined towards the west.

INTRODUCTION

The marine controlled-source electromagnetic (CSEM) method has become a popular tool to detect electrical resistivity contrasts in the seabed that may relate to potential hydrocarbon reservoirs (e.g., Constable and Srnka 2007). The bulk resistivity of marine sediments is mainly controlled by conductive pore water, and resistivity contrasts relate to changes in porosity, permeability, and hydrocarbon content among other factors. The CSEM method is a diffusion method, i.e., sensitive to volume resistivity changes, and the solution to the sub-seafloor resistivity structure is generally non-unique (Edwards 2005; Constable 2010). To evaluate the 1-D structural resolution of the CSEM data, we apply a trans-dimensional Bayesian inversion approach that samples probabilistically over the number of sub-seafloor resistivity layers. Instead of treating the number of unknowns as constant, which is often done in geophysical inverse problems, trans-dimensional inversion uses the data to constrain the resolvable subsurface structure (e.g., Green 1995; Sambridge *et al.* 2006). Furthermore, Bayesian approaches treat the parameters as random variables that are sampled probabilistically and result in an ensemble of models rather than a single optimal model. Trans-dimensional Bayesian inversion provides layering-structure estimates (including uncertainties) that are consistent with the local resolving power of the data (i.e., adapts model complexity locally as required by the data). Probabilistic sampling approaches, unlike linearized inversions, can provide rigorous estimates of model parameter uncertainties (e.g., Malinverno 2002). Trans-dimensional Bayesian inversion has recently been applied to invert various geophysical data sets (e.g., Bodin and Sambridge 2009; Dettmer, Dosso and Holland 2010; Ray *et al.* 2013a; Dosso *et al.* 2014).

The CSEM instrument used in this study is a seafloor-towed array consisting of a horizontal source dipole and four electrical receiver dipoles developed recently at the German Federal Institute for Geosciences and Natural Resources (BGR). This instrument targets shallow resistivity structure (to a few hundred metres depth) and is sensitive to horizontal and vertical resistivity changes (Schwalenberg and Engels 2012a, 2012b).

While many multi-channel seismic (MCS) profiles have been collected in the North Sea, only a small number of CSEM surveys have been conducted, mostly targeting deep natural gas reservoirs in the British and Norwegian sectors (e.g., MacGregor *et al.* 2006; Ziolkowski *et al.* 2010). A special challenge for marine CSEM methods in the North Sea is the relatively shallow water (compared with the maximum offset of the array) and the resulting sensitivity of the instrument response to the strong resistivity contrast between the conductive seawater and the insulating air above. The electromagnetic field is "guided" along this resistivity contrast producing an "airwave", which decreases the overall sensitivity to the subsurface structure due to complicated coupling between signals interacting with the subsurface, seawater, and air (Weiss 2007; Weidelt 2007; Andréis and MacGregor 2008). While data analysis in the time or frequency domains theoretically yields the same information, practical differences exist due to the amount of data selected for processing, the use of different sources, and differing noise levels. For example, frequency-domain data are often displayed in terms of real and quadrature components of the recorded electric and magnetic fields as a function of transmitter–receiver offsets for a limited number of frequencies, whereas time-domain data are given by the step-on response of the electric field as a function of logarithmic time for each offset (e.g., Cheesman, Edwards, and Chave 1987). Time-domain data are preferred in shallow water as a broader frequency range is available, and the static limit (DC part) is included, which contains most of the seabed response, similar to terrestrial CSEM (Weiss 2007; Weidelt 2007).

The time-domain CSEM data presented here were acquired in September 2012 about 30 km NWW from Heligoland in the North Sea on the rim of the Elbe Palaeo-valley (see Fig. 1). The CSEM survey targeted a shallow, phase-reversed reflector observed on MCS line Aur03-23a acquired by the BGR in 2003 (Kudraß *et al.* 2003). This reflector was chosen as it could potentially indicate shallow gas occurrences or significant lithological changes. The CSEM experiment was part of a joint project to study the geological evolution, stratigraphy, and potential for energy resources (hydrocarbon reservoirs, and locations for wind and water power plants) of the German North Sea (Schwalenberg *et al.* 2012; Arfai *et al.* 2011).
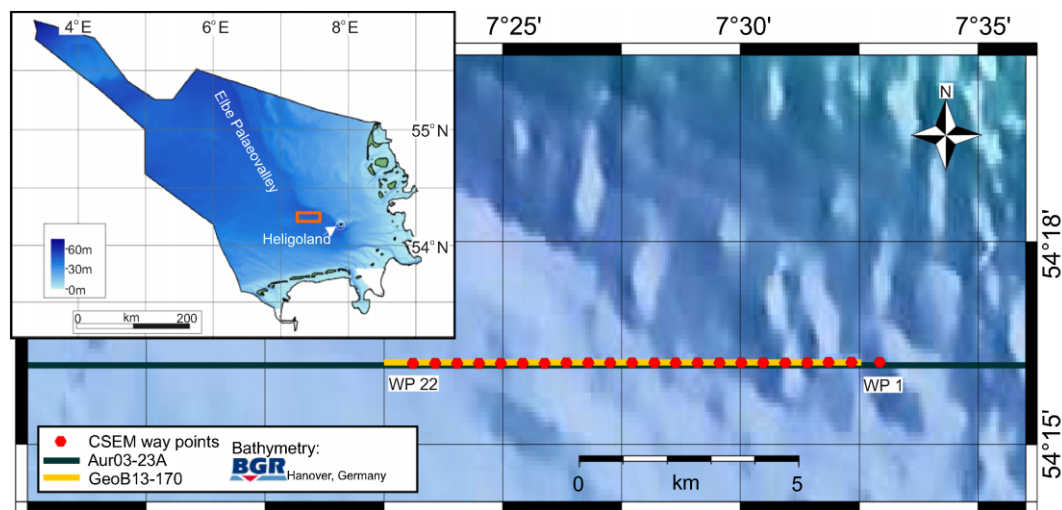
Figure 1 Bathymetry of the study area with CSEM way points (red dots) and MCS lines Aur03-23A and GeoB13-170. Inlay: German sector of the North Sea with study area (orange rectangle) located northwest of Heligoland in the Elbe Palaeovalley.

The geological history of the North Sea goes back to the Permian when two large basin systems opened up. A number of phases of stretching, subsidence, and uplift have caused several kilometres of sediment deposition (and erosion) since then. Several layers of salt deposits within the sediments uplifted and deformed the upper sediment layers, causing widely abundant diapir formations during the late Permian (Arfai *et al.* 2011). Northern Germany was below sea level until the late Tertiary, when the sea retreated westward. While sedimentation during the Paleogene was dominated by marine clays, a great influx of sediments during the Miocene was dominated by river deposits and was followed by large sea-level changes during the Pleistocene. Several protruding glaciers deformed the landscape and deposited glacial tills, and meltwater cut into older sediments to form tunnel valleys (e.g., Hepp *et al.* 2012). After the last ice age, sea levels rose again and supported moor and swamp development, and thin layers of peat can be found within marine Holocene sediments (Vink *et al.* 2007, Kirsch *et al.* 2012). The present geographic shape of the German sector of the North Sea resembles a duck's bill that extends towards Great Britain and is relatively shallow with a maximum depth of ~65 m (see Fig. 1).

CONTROLLED SOURCE ELECTROMAGNETIC METHOD

The marine controlled-source electromagnetic (CSEM) method typically uses a range of frequencies $< 10^3$ Hz to allow penetration through seawater and marine sediments and keep spatial decay small. Therefore, the CSEM method is based on electromagnetic diffusion as conductivities of common earth materials are larger than the product of electric permittivity and frequency. The electromagnetic wave equation is then dominated by the wave attenuation term (conduction currents are larger than displacement currents; Ward and Hohmann 1988), which explains the limitation in penetration depth and structural resolution compared with seismic reflection methods. Further, seismic and electromagnetic methods are sensitive to different physical parameters and can complement each other in interpretations of the sub-seafloor geology. The active seismic method, for example, is sensitive to impedance contrasts and therefore resolves structural changes, but it is poor at detecting gradual changes within the sediment volume. Furthermore, strong seismic impedance contrasts transmit relatively little seismic energy to greater depths. Gas concentrations in the sediment volume are difficult to estimate seismically as small amounts of free gas cause a strong impedance contrast reflecting most of the energy. The CSEM method, in comparison, is more sensitive to bulk volume changes in resistivity, and different levels of pore space occupation with resistive material (e.g., free gas) are differentiable (Constable 2010). In this paper, we compare active seismic reflection data with trans-dimensional Bayesian inversion results of CSEM data to draw a combined geological interpretation of the sub-seafloor. The CSEM data in this study were acquired with the horizontal inline electric dipole–dipole technique, which is generally preferred compared with broadside source configurations in marine CSEM for its better vertical resolution and sensitivity to resistive layers (Cox 1980; Edwards 2005; Key 2009). The electromagnetic field injected at the
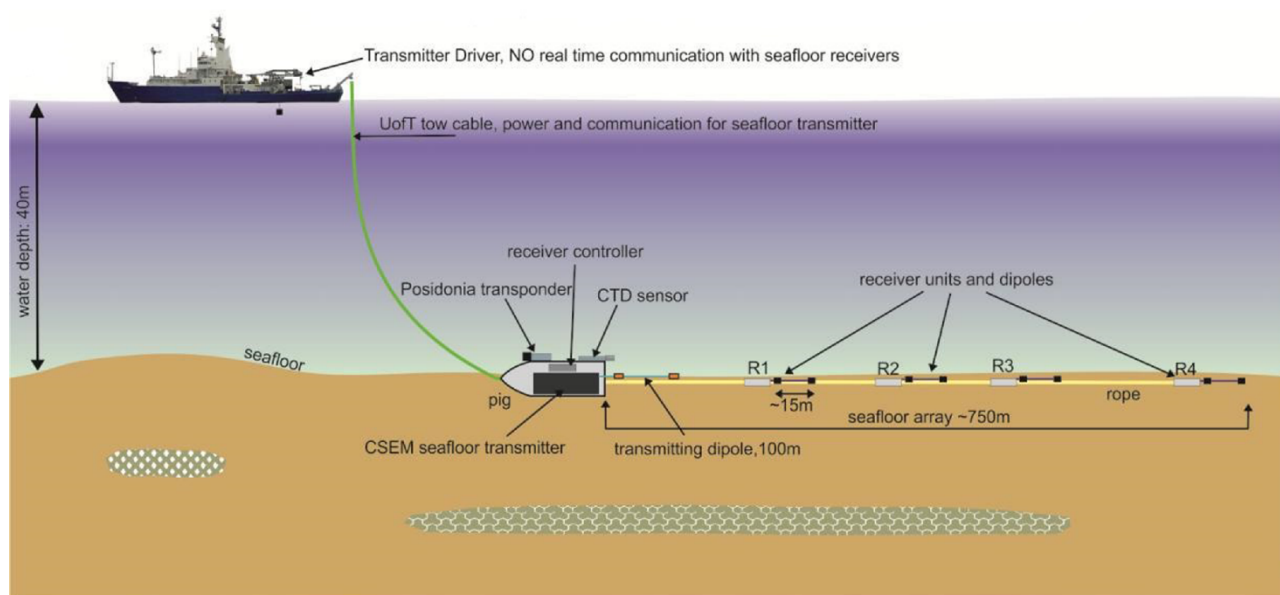
Figure 2 CSEM array configuration during data acquisition. The array is held on the ground by a heavy weight (pig) that contains the transmitter and receiver controllers and the Posidonia transponder and a CTD sensor. The transmitter unit (including current generator) and the cable (green line) were developed at the University of Toronto. The transmitter dipole with copper electrodes (red rectangles) and four receivers were developed at the BGR as part of the bottom-towed electric multi-receiver system HYDRA II (Schwalenberg *et al.* 2012).

transmitter source dipole diffuses outward and propagates faster in resistive material and along boundaries with resistive material. The step-on response measured at the receivers is always an expression of the whole volume between the transmitter and the receiver, as illustrated in modelling studies by, for example, Swidinsky and Edwards (2010) and others.

Instrumentation and data processing

The CSEM array used here (see Fig. 2) is a seafloor-towed system with a horizontal electric transmitter dipole ($\sim$100 m) and four electric receiver dipoles (Rx) at offsets of 150 m, 252 m, 453 m, and 754 m developed at the BGR (Schwalenberg and Engels 2012a). The current generator and the tow and communication cable used in this survey were provided by the University of Toronto. The array provides data with a high signal-to-noise ratio due to minimal electronic noise (signal resolution below 10 nV), as well as a high sampling rate (10 kHz) and precise timing. It also includes a conductivity, temperature, and depth (CTD) probe to measure seawater resistivities and water depth, and an ultrasound positioning system (Posidonia transponder). In operation, the CSEM array is held stationary for $\sim$5 min at each measurement site (waypoint, WP). A square-wave signal with a maximum amplitude of $\pm$50 A and a period of 6 s is injected at the transmitter dipole (Tx). During the measurement, the horizontal electric

field is recorded at the four $\sim$15 m-long receiver dipoles. Data processing includes the identification of stationary half periods (each 3 s long), timing correction, DC offset and gain correction, electrode drift correction for each half period, and an iterative scheme for the selection of accepted half periods for stacking. Figure 3 shows half periods for Rx_1–Rx_4 at one measurement site. About 64 half periods (green) are accepted for stacking; other half periods with erratic noise are discarded. The mean step-on response and the standard deviation of the mean are derived from stacking of the accepted preprocessed data. The stacked data show only a small amount of high-frequency electronic noise. Systematic data errors (e.g., from electronics, electrodes, timing errors, geometry errors, and uncertainty in water depth) are believed to be larger for the present data set than stacking errors and have been addressed in preliminary analyses by introducing error scaling factors and a minimum error floor (Schwalenberg *et al.* 2012).

Inversion

CSEM data contain information about bulk resistivities in the subsurface volume. Typical for diffusion methods, data interpretation for a heterogeneous subsurface resistivity model is non-unique (several sub-seafloor resistivity models may result in a similar data response). Interpretation requires

Figure 3 Half periods for Rx$_1$–Rx$_4$. About 64 half periods (green) are selected for stacking (stacked half periods in red), whereas others are rejected due to erratic noise (black).
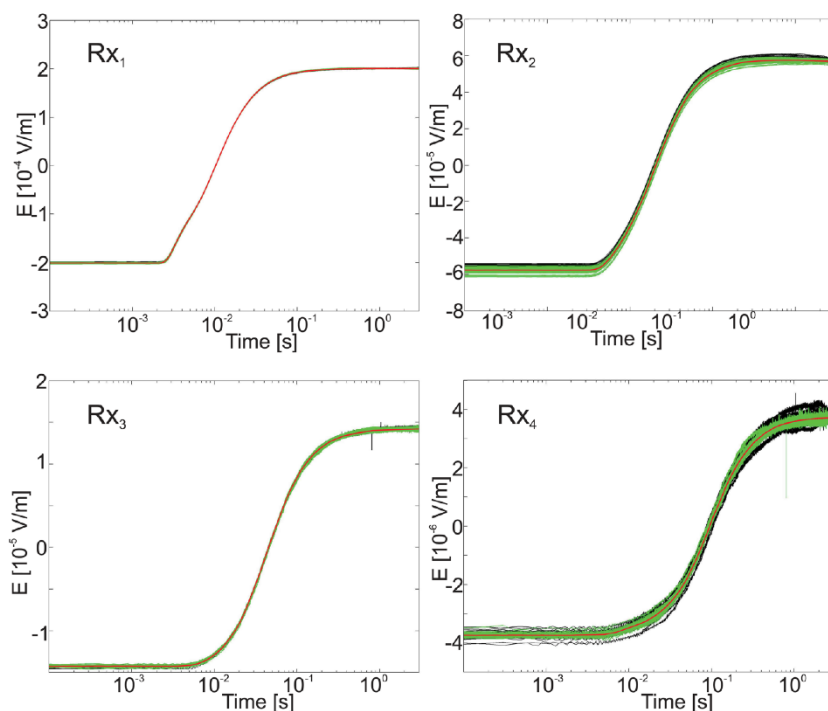
sophisticated inversion techniques or additional structural constraints to estimate model parameters. Model parameters are often dependent on each other and might only be resolved in combination (e.g., the product of resistivity and layer thickness; Edwards 1997). Linearized 1-D inversions for both time- and frequency-domain data have been carried out extensively and successfully in the past (e.g., Schwalenberg *et al.* 2010; Scholl 2010; Key 2009). A widely applied technique is Occam's inversion (Constable *et al.* 1987), which parametrises the model using a large number of interfaces at fixed depths such that layer thicknesses are below the resolution of the data, and introduces a regularization term minimizing the second depth derivative of resistivity to constrain the result to a minimum-structure model. Occam's inversion addresses EM diffusion data by smoothest-model regularization (usually represented by an L$_2$ norm which discriminates strongly against abrupt changes) and avoids over-fitting the data. However, abrupt changes in the resistivity model may be desirable in some cases. In addition, regularization is typically global (i.e., cannot automatically adapt locally to the structure supported by the data), which can result in over- and/or under-smoothing of various depth regions of the resistivity profile. Finally, linearized uncertainty estimates from Occam's inversion are limited by both the linear approximation and the smoothing regularization. In general, regularization alters the inverse problem, and

objective estimation of the trade-off parameter (between regularization and data fit) can be challenging. Alternatively, this paper implements a trans-dimensional Bayesian inversion to infer parameter and uncertainty estimates in the presence of unknown layering (Green 1995). The approach does not require linearization or regularization, but it samples probabilistically over the number of subsurface layers and layer parameters based on the information content of the data. The trans-dimensional inversion implemented here is based on the natural parsimony of Bayes' rule to appropriately limit structure without additional regularization. However, all results need to be interpreted considering the choice of prior information (as discussed, e.g., in Sambridge *et al.* 2013); in our case, we used uniform probability density functions over the model parameters. Bayesian inversion and regularization have been combined in past work by defining the prior accordingly and carefully adjusting the acceptance criteria. For example, smoothness regularization has been included by Minsley (2011), and the regularization weight has been sampled rather than specified by Rosas-Carbajal *et al.* (2013) and Guo *et al.* (2011). Other implementations of Bayesian algorithms for marine CSEM in fixed dimensions either constrain the subsurface resistivity layering using depths inferred from seismic data such as hydrocarbon reservoir depth (Chen *et al.* 2007), severely constrain the prior parameter widths (Buland and Kolbjørnsen 2012), or use the Bayesian information criterion

to estimate the most probable number of sub-seafloor layers, which is held fixed in the inversion (Gehrmann *et al.* 2015).

Trans-dimensional inversion represents a powerful and general approach that has been applied for several geophysical problems (e.g., Malinverno 2002; Sambridge *et al.* 2006; Bodin and Sambridge 2009; Dettmer *et al.* 2010; Bodin *et al.* 2012; Dosso *et al.* 2014). Ray and Key (2012) implemented a trans-dimensional inversion for frequency-domain CSEM data to estimate the resolution of different field components of the electromagnetic response, and they illustrated the challenges of CSEM inversion when targeting deep-situated, thin hydrocarbon reservoirs in anisotropic environments. Our approach implements an algorithm similar to that described in Dettmer *et al.* (2010) and addresses the unknown layering of the earth model by introducing a hyper-parameter, which indexes models with various numbers of interfaces. Transitions (jumps) between models with differing numbers of layers are implemented by creating a new interface (referred to as a birth step) or deleting an existing interface (death step). Jumps are accepted probabilistically according to the Metropolis–Hastings–Green criterion. Additionally, parallel tempering (Dosso, Holland, and Sambridge 2012; Dettmer and Dosso 2012) is applied to improve the acceptance rate of dimension jumps and the efficiency of parameter-space exploration for multi-modal solutions. Ray *et al.* (2013a) have shown that parallel tempering can significantly speed up convergence to the posterior model distribution when inverting CSEM data with the trans-dimensional inversion scheme. While Ray and Key (2012) and Ray *et al.* (2013a) assumed independent data errors and worked with diagonal data covariance matrices, Ray, Key, and Bodin (2013b) have shown how spurious structure is introduced when ignoring correlated data errors, and used non-diagonal covariance matrices instead. We account for correlated errors with a non-Toeplitz data covariance matrix estimated from residual errors (difference of observed and predicted data) and verify data assumptions by applying posterior statistical tests for Gaussianity and randomness to standardized residual errors.

TRANS-DIMENSIONAL BAYESIAN INVERSION

Bayes' theorem

In geophysical problems, Bayesian inversion, based on the assumption that the model parameters are random variables, can provide quantitative parameter and uncertainty estimates and rigorous error treatment. Bayesian inversion quantifies

the posterior probability density (PPD), $P(\mathbf{m}|\mathbf{d}, H)$, which represents the probability of the model parameters $\mathbf{m}$ given the observed data $\mathbf{d}$, the prior information, and the model choice H. The model choice is here defined by a 1-D parametrization with the number of subsurface interfaces k, the model parameters (resistivity and thickness) for each layer, and the data error model. The PPD is described with Bayes' rule:

$$P(\mathbf{m}|\mathbf{d}, H) = \frac{P(\mathbf{d}|\mathbf{m}, H)P(\mathbf{m}|H)}{P(\mathbf{d}|H)}. \tag{1}$$

In equation (1), $P(\mathbf{d}|\mathbf{m}, H)$ is the conditional probability of the data $\mathbf{d}$ (given $\mathbf{m}$ and H), which quantifies the residual-error statistics. For fixed observed data, $P(\mathbf{d}|\mathbf{m}, H)$ can be interpreted as a function of $\mathbf{m}$ rather than $\mathbf{d}$, and is referred to as the likelihood function $L(\mathbf{m}, H)$. The prior density $P(\mathbf{m}|H)$ represents any probabilistic information about the model parameters independent of the observed data. The conditional probability for the observed data $P(\mathbf{d}|H)$ is called the Bayesian evidence. Evidence is independent of the model parameters and is treated as a normalization term in this study. In the following, we first treat the fixed-dimensional case (no variation in k which causes no variation in H) and then generalize it to the trans-dimensional case.

Likelihood

This study uses a likelihood function $L(\mathbf{m})$ for Gaussian-distributed errors:

$$L(\mathbf{m}, \mathbf{C}_d, a) = \prod_{i=1}^{N_{\mathrm{Rx}}} \left\{ \frac{1}{(2\pi)^{N_i/2} \left| \mathbf{C}_{d_i} \right|^{1/2}} \right.$$

$$\left. \times \exp\left[-\frac{1}{2}(\mathbf{d}_i - a_i\mathbf{f}_i(\mathbf{m}))^T \mathbf{C}_{d_i}^{-1}(\mathbf{d}_i - a_i\mathbf{f}_i(\mathbf{m})) \right] \right\}, \tag{2}$$

where N_{Rx} is the number of receivers (here, four), and $\mathbf{f}_i(\mathbf{m})$, N_i, $\mathbf{C}_{d_i}$, and a_i are the predicted data, the number of data, the data covariance matrix, and an unknown calibration factor for the i-th receiver, respectively.

The data covariance matrices are generally not known independently and must be estimated from the data. One approach is to use a diagonal covariance matrix with the variance of the mean obtained from data stacking. Such estimates are often used in linearized inversion algorithms to evaluate regularization and convergence criteria. However, this approach does not account for systematic, correlated errors, which can be due to deviations from the assumed geometry

of the controlled-source electromagnetic array, the choice of a 1-D model in a potentially 2-D or 3-D environment, and approximations in numerically implementing the physical theory of the forward problem. To address correlated errors, we apply a non-diagonal, non-stationary (non-Toeplitz) data covariance matrix estimated from the auto-correlation of the residual errors (Dosso and Dettmer 2011):

$$\mathbf{r}_i = \mathbf{d}_i - a_i \mathbf{f}_i(\hat{\mathbf{m}}) \tag{3}$$

for a model estimate $\hat{\mathbf{m}}$ estimated from a preliminary inversion assuming uncorrelated errors. Residuals are first standardized by their estimated standard deviation to $\tilde{r}_i = r_i / \hat{\sigma}_i$ with (i is dropped for readability)

$$\hat{\sigma}_j^2 = \frac{1}{n} \sum_{l=j-n/2}^{j+n/2} r_l^2 \tag{4}$$

for a window of data samples of width n centred at the current data point j to accommodate standard deviations that vary slowly across the data set (e.g., standard deviations from stacking have been shown to be higher when the electric field response is close to zero). The non-Toeplitz data covariance matrix is estimated by computing the auto-correlation of the residuals for each receiver, analogously to Dosso *et al.* (2006), with (i is dropped for readability)

$$C_d^{jl} = \frac{\hat{\sigma}_j \hat{\sigma}_l}{N} \sum_{k=1}^{N-|j-l|} (\tilde{r}_k - \bar{r})(\tilde{r}_{k+|j-l|} - \bar{r}) \cos^p \frac{\pi |j-l|}{2(N-1)}, \tag{5}$$

where $j = 1, N$; $l = 1, N$, and the cosine term represents a damping that drops off more strongly with increasing $p > 1$ (here, $p = 16$). Damping is applied to suppress correlation values for widely spaced data samples as these covariances are expected to be small and the available number of samples $(N - |j - l|)$ may be insufficient to meaningfully estimate the covariance values. Residual errors are standardized with the Cholesky decomposition of the non-Toeplitz covariance matrix with $\tilde{\mathbf{r}} = \mathbf{C}_d^{-1/2}(\mathbf{d} - a\mathbf{f}(\mathbf{m}))$.

Metropolis–Hastings sampling

To estimate model parameters and uncertainties, Metropolis-Hastings sampling (MHS) can be applied (Geyer *et al.* 2011). In MHS, a Markov chain samples from the posterior by perturbing a set of model parameters $\mathbf{m}$ to obtain $\mathbf{m}'$ using a proposal density $Q(\mathbf{m}'|\mathbf{m})$ and accepting that perturbation with probability α:

$$\alpha = \min \left[1, \frac{P(\mathbf{m}')}{P(\mathbf{m})} \left(\frac{L(\mathbf{m}')}{L(\mathbf{m})} \right)^{1/T} \frac{Q(\mathbf{m}|\mathbf{m}')}{Q(\mathbf{m}'|\mathbf{m})} \right], \tag{6}$$

where T is the sampling temperature, a relaxation factor for the likelihood function, which can be taken to be unity here (non-unity values are considered in the following section). Equation (6) can be applied by drawing a uniform random number ξ on [0, 1] and accepting the perturbation if $\xi < \alpha$. If the perturbation is not accepted, another copy of the current model is included as the next step in the Markov chain. In fixed-dimensional inversion with a uniform bounded prior and a symmetric proposal density, $Q(\mathbf{m}'|\mathbf{m}) = Q(\mathbf{m}|\mathbf{m}')$, equation (6) simplifies to the likelihood ratio. Here, the symmetric proposal density is taken to be a Cauchy distribution centred at the current parameter value that allows occasional large steps (Dosso and Wilmut 2008).

Reversible-jump Markov-chain Monte Carlo

Reversible-jump Markov-chain Monte Carlo (rjMCMC) sampling enables transitions between models that change dimensions (e.g., number of sub-seafloor layer interfaces), and it ensures reversibility for each transition (Green 1995, 2003). The methodology is based on partition modelling (Denison *et al.* 2002, pp. 177) and trans-dimensional jumps of the birth–death form (Geyer and Møller 1994; Malinverno 2002; Dettmer *et al.* 2010). The acceptance criterion in equation (6) is extended to the Metropolis–Hastings–Green criterion

$$\alpha = \min \left[1, \frac{P(k')P(\mathbf{m}'_{k'}|k')}{P(k)P(\mathbf{m}_k|k)} \left(\frac{L(k', \mathbf{m}'_{k'})}{L(k, \mathbf{m}_k)} \right)^{1/T} \right.$$
$$\left. \times \frac{Q(k, \mathbf{m}_k|k', \mathbf{m}'_{k'})}{Q(k'\mathbf{m}'_{k'}|k, \mathbf{m}_k)} |\mathbf{J}| \right], \tag{7}$$

where k is a hyper-parameter that indexes the model choice (number of interfaces), and $|\mathbf{J}|$ is the determinant of the Jacobian for the transition function (Green 2003). If changes in k are limited to ± 1 for each dimension transition and parameter values within a new layer depend only on the values of the originating layer, $|\mathbf{J}|$ is unity (e.g., Agostinetti and Malinverno 2010). The first term in equation (7) is the ratio of the prior probability densities for interface k' (new model) and k (old model). The prior probability density is defined as the product of the interface probability $P(k)$ and the parameter probability $P(\mathbf{m}_k|k)$, which consists of the prior density for depth partition $\mathbf{z}$, i.e., $P(\mathbf{z}|k)$, and the prior density for layer resistivities ρ, i.e., $P(\rho|k)$. The prior density for depth partition $P(\mathbf{z}|k)$ is defined for a fictitious grid that cancels out in the final acceptance proposal ratio (Denison *et al.* 2002; Dettmer *et al.* 2010). The resistivities are sampled in the logarithmic domain

from uniform priors constrained by minimum and maximum resistivity values [ρ_{min}, ρ_{max}].

In rjMCMC, a birth move introduces a new interface at a random depth drawn from a uniform prior. The parameters of the old layer are transcribed into the two new layers. One layer is randomly chosen and its parameters perturbed with a Gaussian proposal distribution. A death move reduces the model by one randomly chosen interface. The parameters of the new layer are randomly selected from one of the two original values. The acceptance probabilities for birth and death moves become (simplified from Dettmer *et al.* (2010) as every layer has only one physical parameter here, resistivity ρ)

$$\alpha_{birth} = \min\left[1, \frac{1}{\rho_{max} - \rho_{min}}\right.$$
$$\left. \times \sqrt{2\pi\sigma_\rho^2} \exp\left(\frac{1}{2}(\rho' - \rho)^2/\sigma_\rho^2\right) \frac{L(k', \mathbf{m}'_{k'})}{L(k, \mathbf{m}_k)}\right]$$
$$(8)$$

$$\alpha_{death} = \min\left[1, (\rho_{max} - \rho_{min}) \frac{\exp\left(-\frac{1}{2}(\rho' - \rho)^2/\sigma_\rho^2\right)}{\sqrt{2\pi\sigma_\rho^2}}\right.$$
$$\left. \times \frac{L(k', \mathbf{m}'_{k'})}{L(k, \mathbf{m}_k)}\right],$$
$$(9)$$

where σ_ρ^2 is the fixed variance of the Gaussian proposal, and k' is the proposed number of interfaces ($k' = k + 1$ for birth and $k' = k - 1$ for death of an interface).

In addition, parallel tempering (Geyer 1991; Dettmer and Dosso 2012) is applied to improve the sampling efficiency. The sampling is augmented by running a sequence of increasingly tempered ($T > 1$ in equation (7)) Markov chains in parallel. High-temperature chains deemphasize the effect of the likelihood function and sample the parameter space more widely, and, in particular, significantly improve the acceptance rate of birth and death steps (which can be the limiting factor in trans-D inversion). However, Markov chains at $T > 1$ provide biased sampling of the PPD. To obtain a robust ensemble model, samples are probabilistically exchanged between the chains according to the MHS criterion

$$\alpha = \min\left[1, \left(\frac{L(k', \mathbf{m}')}{L(k, \mathbf{m})}\right)^{1/T - 1/T'}\right]$$
$$(10)$$

for chains at temperatures T and T', and only models collected by the $T = 1$ chain(s) are retained as the PPD sample (Dosso *et al.* 2012).

Inversion sequence and error analysis

Inversions are carried out in a two-stage process. A preliminary inversion with diagonal data covariance matrices based on the estimated variance from data stacking is carried out to obtain a preliminary PPD and median model estimate. Data residuals are computed for the preliminary median model and used to estimate a non-Toeplitz data covariance matrix, which accounts for correlated errors and is then applied in a second inversion to infer the PPD used for interpretation. We infer individual parameters from the PPD by marginalization (integrating over all parameters but the parameter(s) of interest). The seabed depth profile is partitioned for plotting purposes, and marginal probability densities are evaluated at each depth interval. The highest probability density credibility intervals displayed throughout this work represent the narrowest interval that contains 95% of the model samples. The new median model estimate is examined with statistical tests as the formulation of the likelihood in equation (2) is based on the assumption of Gaussian-distributed residual errors with zero mean and data covariance $\mathbf{C}_d$. If assumptions are reasonably met, the standardized residuals should be random (uncorrelated) and Gaussian distributed with unit standard deviation. These assumptions are tested with the Kolmogorov–Smirnov (KS) test for Gaussianity (Massey 1951), which is based on the maximum difference between the cumulative marginal distributions of the residual errors and the standard Gaussian, and the run test (median-delta test) that tests if the residual errors are random or serially correlated by counting the number of runs of the residual errors on either side of the median value (Dosso *et al.* 2006).

Calibration factor

The CSEM data at the first receiver for all waypoints (WPs) generally exhibit a high signal-to-noise ratio (see Fig. 3). The standard deviation of the mean from stacking seems to be dominated by a slight bias of the individual pre-stack data possibly due to an electrode drift. Preliminary inversions with standard deviation from stacking have shown that the amplitudes of the first receiver cannot be matched by a 1-D subsurface model within the derived error bounds. Amplitudes of the predicted data are a few percentage smaller than the observed. Deviations in amplitudes can be accounted for with a multiplicative calibration factor (CF; Scholl 2005). The CF was originally named after the calibration of each electrode pair before deployment. However, receiver electronics (offset and scale factor) were calibrated precisely during the cruise,

and the CF in this inversion was implemented to account for unknown effects such as a conductive target close to the source, 3-D structure, unknown clock drifts between the data recording units, geometry variations, or topography changes. Preliminary inversions have shown that the CF at all WPs is generally close to 1 with a higher value for the first receiver and higher uncertainties for the other receivers (probably due to the larger distance and therefore smaller signal-to-noise ratio). Possible causes were analyzed, and the following conclusions were drawn.

- Highly conductive bodies close to the transmitter (e.g., metallic ship wrecks) would have been observed on images from the echo sounder EM710 and PARASOUND P70 system on board and can be excluded.

- Two-and-a-half-dimensional multi-channel seismic data indicate only very small changes in the layered structure perpendicular to the CSEM profile (Damm *et al.* 2012), and we believe that 2-D and/or 3-D structure likely does not affect our data.

- A time shift between the transmitter and the receiver clocks was observed in the data and corrected for in the laboratory. The transmitter recording unit uses a microprocessor-compensated crystal oscillator, whereas all receivers have chip-sized highly precise atomic clocks installed. We inverted for a single time shift that applies to all four receivers but were not able to improve the overall data fit. We conclude that a time shift can be at most a small part of the problem.

- A slight error in the system geometry (e.g., electrode dipole lengths) is possible. A deviation of only 30 cm from the assumed receiver dipole length leads to 2% deviations of step-on response amplitudes. This might explain different calibrations factors for each receiver. Values also differ slightly from WP to WP.

- Water depth uncertainties could be another factor. The water depth is just $\sim$40 m, and the data are strongly affected by the airwave. Water depths in the region were found to range from $\sim$39 m to 42 m along the whole profile. The instrument array is $\sim$750 m long, and small changes in topography may cause varying CFs. Additionally, the observed water depth suffers from variable ship draft and might deviate up to a metre from the derived value.

Initial inversions indicated that marginal densities for CF for Rx_2–Rx_4 are wider than for Rx_1 and usually overlap with a value of 1. Hence, we conclude that including an unknown CF for Rx_2–Rx_4 is not necessary to fit the data. Preliminary inversions also indicate additional (unnecessary) parameters in the inversion have a detrimental effect on the recovery of subsurface parameters: the problem becomes highly under-

Table 1 Synthetic model with four layers similar to the median model estimate from inversion results for WP 19. Seawater resistivity is 0.232 Ωm, and water depth is 41.1 m.

Layer	Resistivity [Ωm]	Depth [mbsf]
1	0.8	20
2	3	60
3	1	600
Halfspace	4	–

determined, and unreasonable subsurface structure can be introduced. Therefore, the inversion results shown in this paper are based on inverting for CF at Rx_1 only.

Simulation study

This section applies the Bayesian inversion to simulated data for a subsurface model similar to the model estimate for WP 19 (see next section). The median model consists of four layers including a half-space (see Table 1). We chose this model to examine if a thin resistive layer at a shallow depth and a very deep resistivity contrast (relative to the maximum offset at Rx_4 of 750 m) can be resolved with the data. We added random correlated errors generated from the data covariance matrix derived while inverting WP 19. Standard deviations are on average $\sim$2% of the predicted data. Figure 4 shows Bayesian inversion results for the synthetic data in terms of interface-depth probabilities and the marginal probability density profile of the resistivity. Marginal probability densities are normalized to unit area for plotting purposes. Interface probabilities as a function of depth indicate two distinct interfaces at 20 m and 60 m below seafloor (mbsf). Both interfaces are well estimated with low uncertainty (a few metres) and are in excellent agreement with the true model. The third interface is highly uncertain with probability extending from $\sim$450 mbsf to 800 mbsf. The 95% credibility intervals (CIs) exhibit characteristics typical of the resolution of electromagnetic diffusion methods and demonstrate decreasing sensitivity of the data with depth: CI at shallow depth (up to 400 mbsf) are narrow (< 1 Ωm in width) and widen to a maximum of 0.4–14 m at about 700 mbsf. However, the trend of the resistivity distribution follows the true model by indicating another contrast to a half-space with larger resistivities below 600 mbsf. Figure 4 also shows marginal probability density for CF a_1, which is well determined near 1 (true value), and the marginal probability distribution for the number of interfaces k has a peak at 3 interfaces (true value) although the distribution extends to the upper bound of 10.
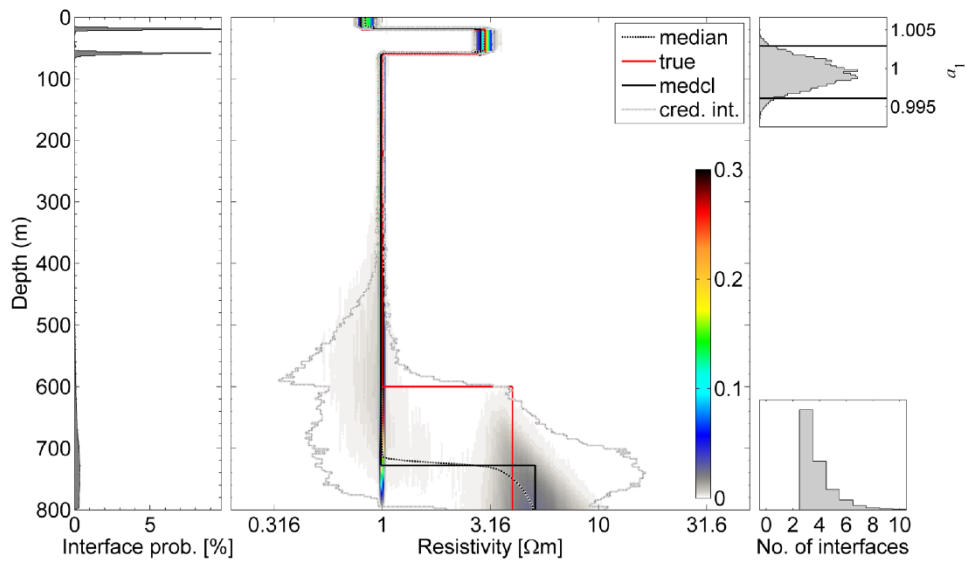
Figure 4 Left: Interface probability as a function of depth. Middle: Resistivity marginal probability profile. Colour indicates probability density for 10^5 samples from the inversion of synthetic data (model in Table 1) with correlated errors. A model with four layers closest to the posterior median model profile is chosen to evaluated residual error statistics and is referred to as "medcl". Credibility intervals contain 95% of the model samples evaluated at each depth interval. Right: Marginal probability density for calibration factor a_1 (top) and for number of interfaces (bottom). Three interfaces (four layers) are most probable.
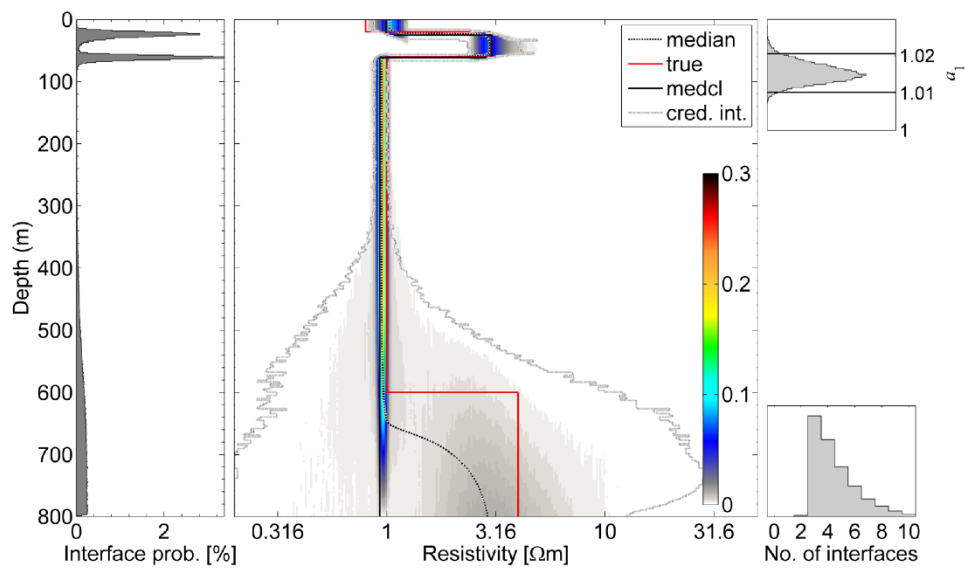

Figure 5 Interface probability and marginal probability depth profile for synthetic data (model in Table 1), which is modelled with different water depth for different receivers and with correlated errors, and inverted with one calibration factor a_1, one fixed water depth for the array and with a non-Toeplitz data covariance matrix from residual error analysis.

To examine the impact of additional unknowns, two further simulations are carried out. First, data were generated for different water depths for different receivers: the water depths for Rx_1, $Rx_{2,3}$, and Rx_4 are 40, 42, and 41.1 m respec-

tively. However, the assumed water depth in the inversion is taken to be 41.1 m for all receivers, and an unknown CF a_1 is included. Inversion results in Fig. 5 show wider credibility intervals at depths >350 mbsf. The third interface of the true
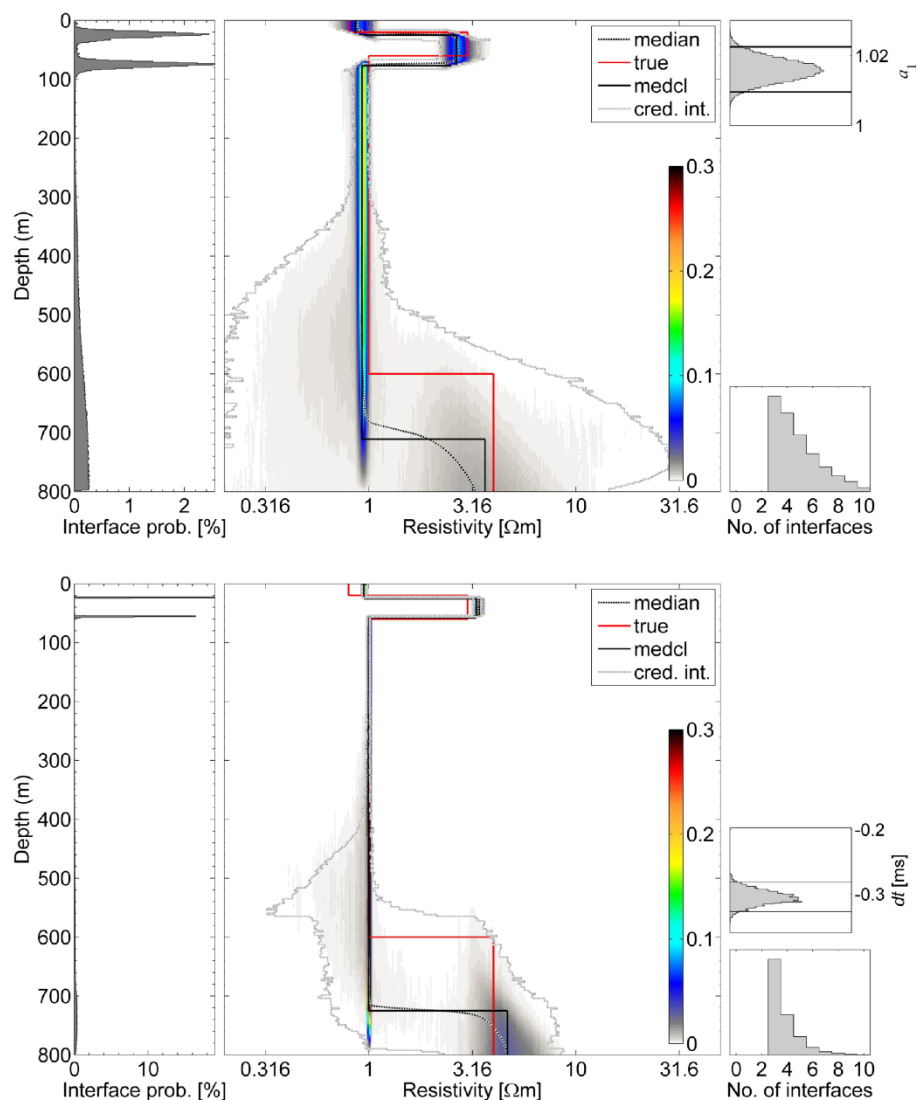
Figure 6 Interface probabilities and marginal probability depth profile for synthetic data (model in Table 1) that were modelled with 0.3-ms time shift between Tx and Rx and correlated errors. Inversion for unknown calibration factor a_1 (top), and dt (bottom).

model is hardly resolved. The resistivity of the overburden is estimated higher than the true model, and a_1 is slightly above 1 to compensate for the depth discrepancy.

   The second test addresses a possible time shift between transmitter and receiver clocks. The time of the receivers was shifted by 0.3 ms, and the inversion was run twice, once with an unknown a_1 and once with an unknown time delay dt. Inversion results are shown in Fig. 6. The inversion scheme resolves the structure of the true model when inverting for a_1 with a_1 slightly above 1 or dt where dt is well determined with −0.3 ms.

   The synthetic modelling suggests that the inversion algorithm with a_1 for the first receiver efficiently resolves the model

even in cases of deviating water depth or time shift. However, model uncertainties increase with additional systematic uncertainties and CIs below ∼400 mbsf become increasingly wider with depth, although a qualitative resistivity contrast similar to the true model is preserved.

GERMAN NORTH SEA INVERSION RESULTS

We have chosen WP 19 to demonstrate in detail the trans-dimensional Bayesian algorithm and results for measured CSEM data. Way point 19 lies in the centre west of the profile (see Fig. 1) and is generally representative
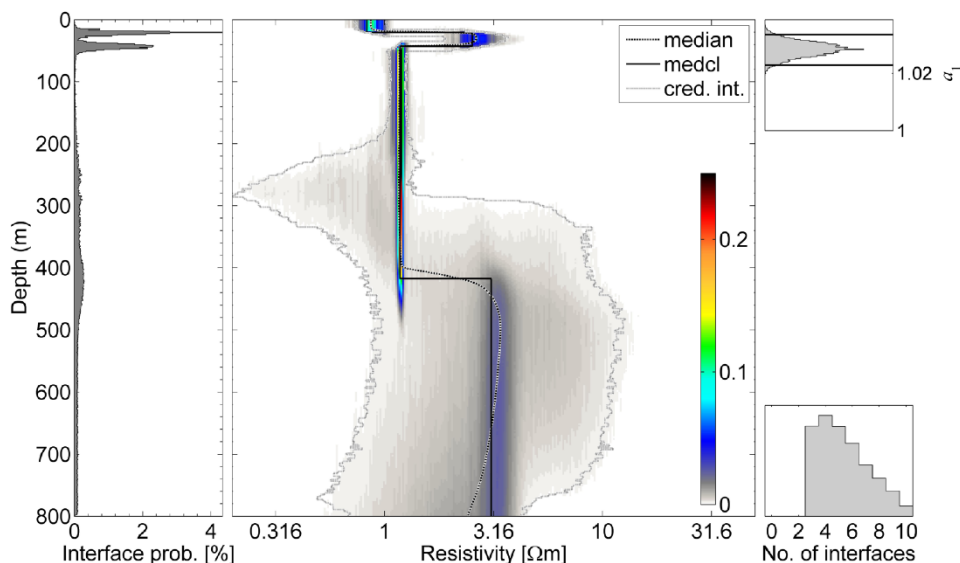
Figure 7 Interface probability (left) and marginal probability density (middle) as a function of depth for WP 19, where "median" refers to the posterior median profile, and "medcl" to the median model estimate, and credibility intervals contain 95% of all model samples evaluated at each depth interval; (right) marginal probability densities for calibration factor a_1 and number of interfaces k.

of other way points. Interface probabilities and marginal probability densities from inversion are shown in Fig. 7. The first two interfaces are well defined at ∼20 mbsf and 50 mbsf. The interface probability also increases between 180 mbsf and 520 mbsf indicating one or more interfaces with large depth uncertainty. The marginal probability profile exhibits narrow credibility intervals of width <1 Ωm down to ∼200 m depth, whereas below this depth, widths increase to ∼10 Ωm. The number of interfaces with the highest probability is four, whereas the median model estimate suggests three interfaces. The CF for the first receiver is well determined and slightly over 1, which may be related to unknown parameters such as water depth and time shift as discussed in the sections above.

Figure 8 shows observed CSEM data and the predicted data for the median model estimate, as well as standardized residuals for WP 19. The runs test and KS test are applied to the standardized residuals (Dosso *et al.* 2006) of the median model estimate. Standardized residuals pass tests if p-values for a two-sided test are larger than a significance level of 0.025, and test results are shown in the bottom row of Fig. 8. The p-values for runs and KS test are shown in the title, and standard deviation and mean value of the standardized residuals are shown above the histogramms. Statistical tests result in general acceptance of the assumption of Gaussian distributed errors and the process of addressing correlated errors.

The posterior median model profiles for all 22 WPs are shown in Fig. 9 as coloured bars above the MCS line AUR03-23a. The width of the bars corresponds to the spacing between Tx and Rx_4, and the location of the WPs are matched with the MCS line. The coloured bars are overlain with the resistivity standard deviation profile (black line), which is normalized so that 750 m (the maximum offset of the array) equate ∼$\log_{10}$(6 Ωm). We have chosen to show median models because they generally represent the model space with the maximum probability density given that the marginal probability profiles are not multi-modal in our work. However, the reader is referred to Fig. 7 where the uncertainty information is displayed in terms of a marginal probability profile. More detailed display options have been used to image the PPD for 2-D profiles, for example, by Ray *et al.* (2014).

Inversion results for all WPs agree on a ∼5 m to 20 m thick surface layer with resistivities of ∼0.7 to 1 Ωm. Below the surface layer is a second layer with increased resistivity of ∼1.8 Ωm to 3.5 Ωm. The maximum thickness of the second layer is ∼200 m at WP 1–9, and this layer thins to the west where neighbouring resistivities become more heterogeneous. Inversions of WP 9, 11, 16, 18 and 20 include a thin conductive layer that is geologically unlikely, but improves the fit to the observed data. Ways to overcome these artefacts for greater smoothness between neighbouring WPs could be to use a sequential trans-dimensional inversion (Dettmer *et al.*
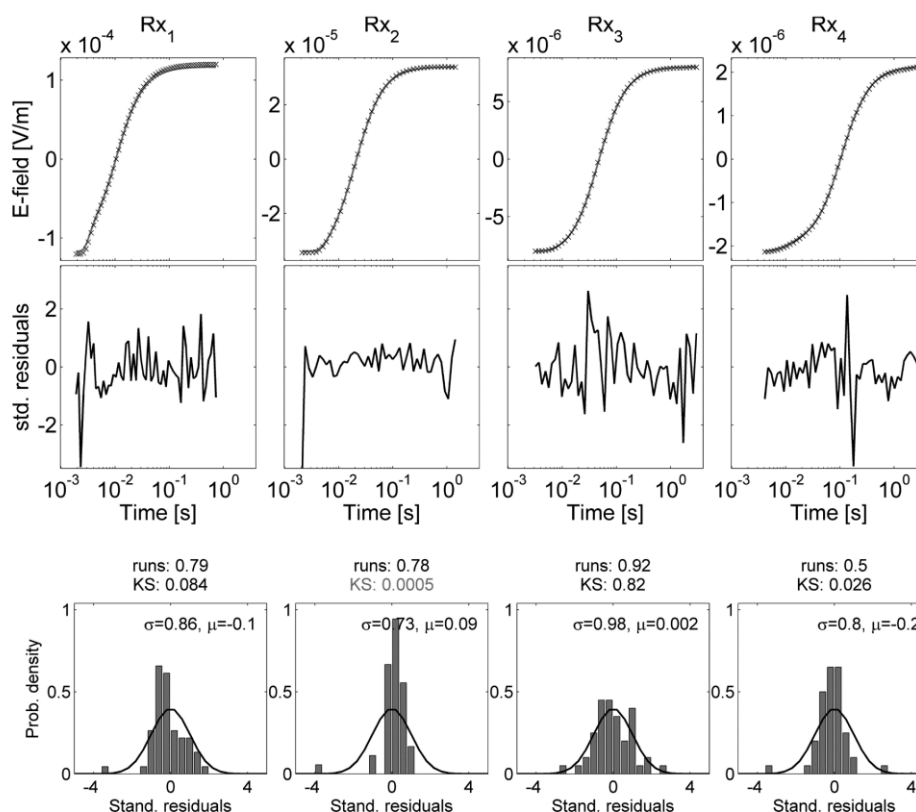
Figure 8 Top row: Predicted (black line) and observed data (crosses) for WP 19. Middle row: Standardized residuals. Bottom row: Histograms of standardized residuals for Rx_1 to Rx_4 with p-values for runs and KS test and standard deviation σ and mean μ for standardized residual errors compared with a standard Gaussian distribution.

2011) or parametrise the subsurface with a 2-D grid such as Voronoi cells (Ray *et al.* 2014). Moghadas *et al.* (2015, same special issue) inverted the same data set presented here with a 1D linearized approach as well as a global optimization with lateral constraints, and present 1-D models with greater lateral smoothness. The model interpretations given in this paper ignore small-scale artefacts that correspond to high uncertainties in the 1-D inversions (black lines in top panel of Figure 9). Resistivities below ∼200 metres below sea level (mbsl) decrease to ∼1 Ωm, with increased uncertainties due to the limited penetration depth of the array. The inversion results suggest an increase in resistivity for the deepest layer (approximately >400 mbsl) of ∼3 Ωm, but the width of the CIs for the resistivity (∼0.5–10 Ωm) are relatively large.

The bottom panel in Fig. 9 shows multi-channel seismic (MCS) line AUR03-23a (Kudraß *et al.* 2003), which was acquired along the same line as the CSEM data. The location of the WPs in respect to the common midpoint (CMP) of the MCS line may deviate by a few metres. Three major reflectors can be traced on the seismic profile: The red reflec-

tor at 0.6-s two-way travel time (TWT) is related to the mid Miocene unconformity (MMU). The MMU is interpreted as the base of the downlap sequence, a result of the Eridanos Delta (Baltic river system). It has a distinct wavy structure related to rapid dewatering of clayey sediments and is highly recognizable in gamma-ray (GR) logs due to a high content of organic material in the clay (Arfai *et al.* 2011). The blue reflector at 0.3 s TWT is defined to be of late Tortonian age. Horizontally layered sediments above the blue reflector are also defined as late Miocene origin. The GR log of borehole R-1 (see Fig. 5 in Thöle *et al.* 2014) shows a GR count maximum at the blue reflector indicating an increased content of fine-grained sediments and marking it as a maximum flooding surface. The GR count decreases above and below the blue reflector. Other strong reflectors correlate with sharp GR-count increases over thin depth intervals. The horizontally layered sediments in the late Miocene are alternating layers of sand, silt, and clay due to worldwide sea-level changes, high basin subsidence rates, uplift and erosion of Paleogene clays, sandy river deposits, and massive flooding events (Rasmussen 2004;
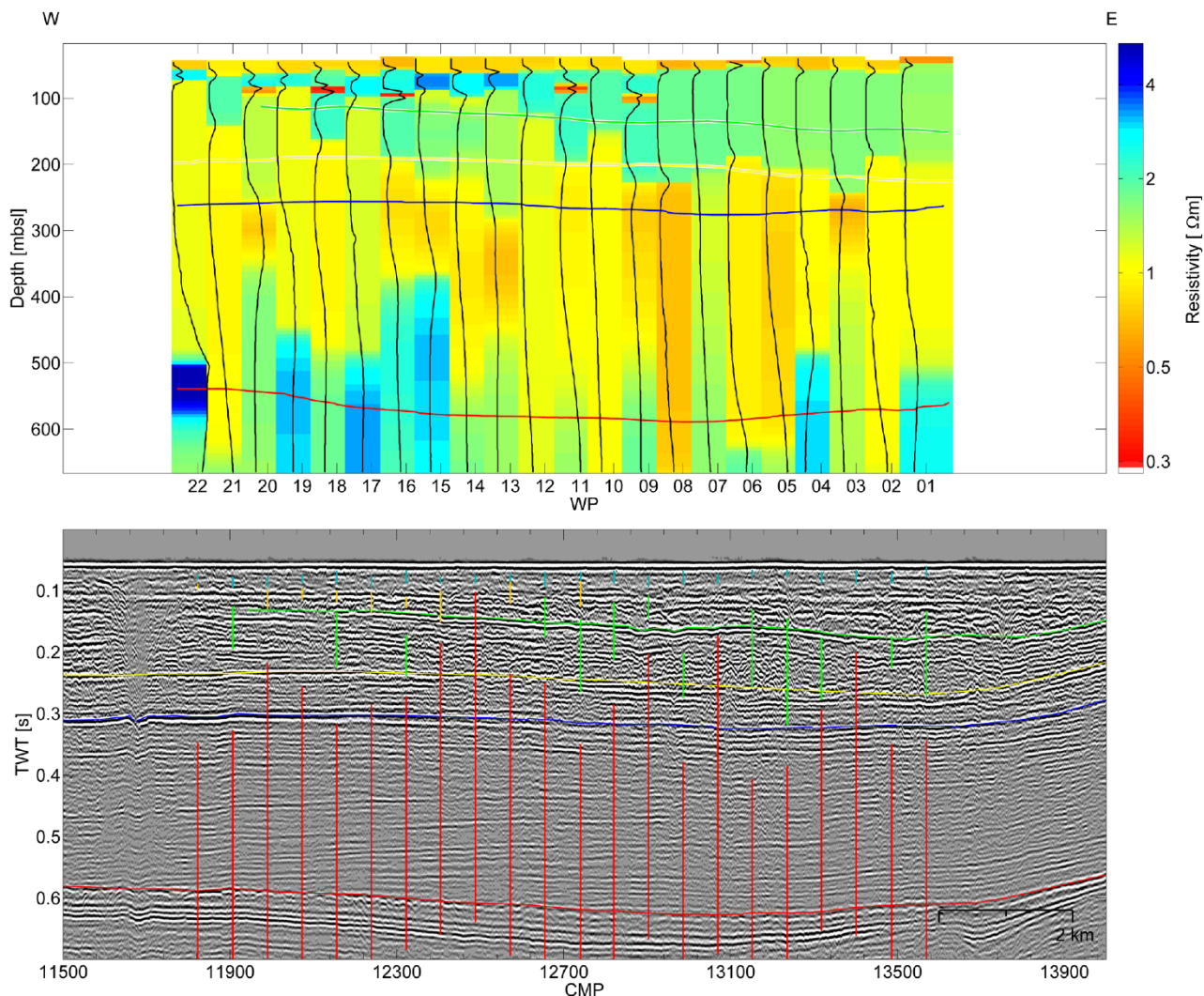
Figure 9 Top: Posterior median profiles from CSEM inversion shown as coloured bars that represent the $Tx-Rx_4$ offset and whose location corresponds to the location of the CMP of the MCS line below. Black lines: Standard deviations of the marginal probability density profile for resistivity over depth which are normalised so that 750 m equate $\sim\log_{10}(6 \ \Omega m)$. Coloured horizontal lines: Seismic horizons converted from TWT to depth; green - Pleistocene basin, blue/yellow - late Tortonian sediments, red - MMU. Bottom: MCS line AUR03-23a with seismic horizons. Coloured vertical lines: Credibility interval widths for interface depths from CSEM inversion (colour coding is subjectively chosen to match with seismic horizons).

Sørensen *et al.* 1997). The green reflector is a phase-reversed dipping reflector between TWT of 0.1 s and 0.2 s from Pleistocene origin that was targeted by the survey because of enhanced, phase-reversed amplitudes between CMP 12500 and 13500 which are caused by a negative impedance contrast possibly related to shallow gas or a boundary from course- to fine-grained sediments. The reflectors were converted to depth with a velocity model from AUR03-23a and superimposed onto the resistivity posterior median profiles. While the seismic method is highly sensitive to small-scale impedance

changes, the CSEM method has a depth-averaging character. Hence, we do not expect the seismic reflectors to match with the median profiles perfectly. However, large-scale changes in sediment properties which affect both seismic impedance and resistivity should be observed on both seismic and CSEM results.

Figure 10 is analogous to Fig. 9 but focuses on the first 300 mbsf and shows MCS line GeoB13-170, which was acquired by the University of Bremen with a high-frequency seismic system (Keil and Hepp 2013). Credibility intervals for
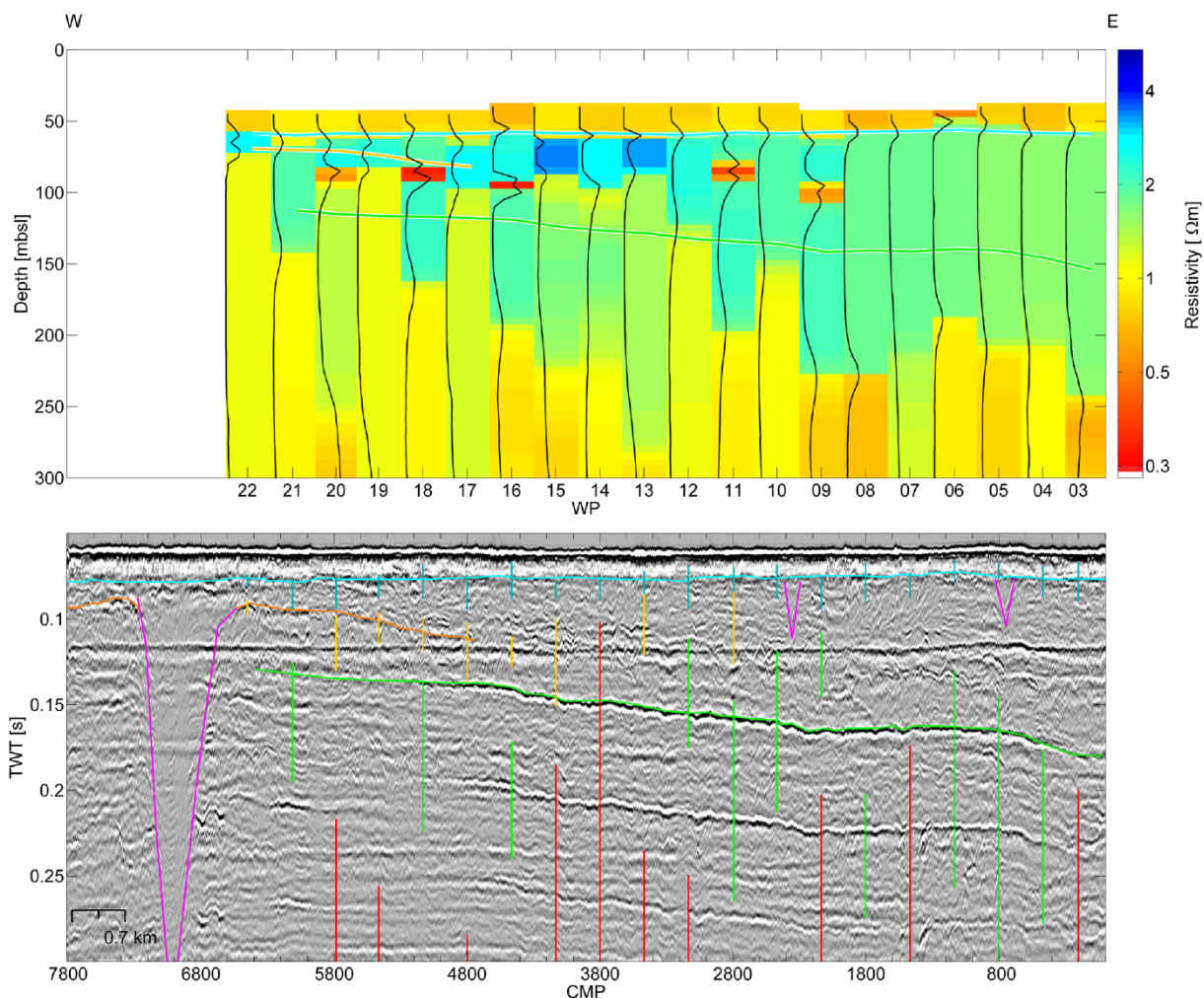
Figure 10 Posterior median profiles from CSEM inversion overlying MCS line GeoB13-170. Black lines on the median models represent resistivity standard deviations normalised so that 750 m equate ~$\log_{10}$(6 Ωm). Horizontal coloured lines are seismic horizons and vertical coloured lines on the seismic profile represent credibility interval widths for interface depths from CSEM inversion (colour coding is subjectively chosen to match with seismic horizons).

interface depths from the CSEM inversions were converted to TWT and plotted on the seismic section with a colour coding chosen to correspond to the interpreted relationship between the interfaces at adjacent WPs and the seismic reflectors. For example, the first interface is cyan for all WPs because it is interpreted to match with the cyan seismic reflector on Fig. 10. However, interface probabilities from CSEM inversion are more difficult to match with seismic reflectors at greater depth, and the colour choice becomes subjective. The main seismic reflectors above the green reflector (target of the CSEM survey) are the base of the fine-grained Holocene and Pleistocene sediments (cyan), two small and one large tunnel valleys (pink), and a reflector within the Pleistocene sediments (orange).

INTERPRETATION AND DISCUSSION

This section presents a geologic interpretation of the sub-seafloor resistivity model from controlled-source electro-magnetic (CSEM) inversion together with the multi-channel seismic (MCS) reflection data and logs from two boreholes (J-14-1/2/3, 130 m deep with grain size information on the CSEM profile, and R-1, 3062 m deep with GR information approximately 100 km to the northwest of the CSEM profile). The first 5 m of sediments below the seafloor are fine-grained Holocene deposits observed in borehole J-14-1/2/3 (close to WP 20). The Holocene deposits in this borehole are followed by 5 m of fine-grained Pleistocene deposits and 120 m of middle to coarse-grained Pleistocene sediments. The CSEM
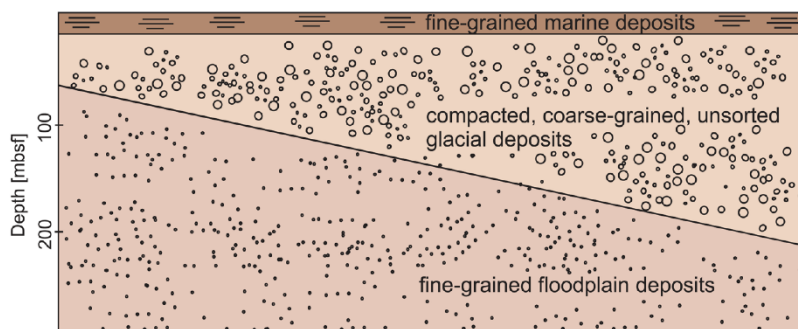
Figure 11 Sketch of the geological interpretation of CSEM inversion results to approximately 300 mbsf. Depth scale is only approximate. Boundary between fine-grained marine deposits and coarse-grained, compacted glacial deposits may be related to the cyan reflector in Fig. 10. The boundary between glacial deposits and fine-grained floodplain deposits may be approximately between the green and yellow reflector in Fig. 9.

inversion results support ~10 m–20 m of fine-grained, highly porous sediments with typically low resistivities for marine sediments around 0.8 Ωm–1 Ωm. The credibility intervals for interface depths overlain on the MCS line in Fig. 10 match the cyan seismic reflector that represents the transition from fine-grained overburden sediments to course-grained Pleistocene sediments.

The second interface from CSEM inversion is more difficult to match with a single seismic reflector. Between WP 16 and 22, the interface correlates with the orange reflector in Fig. 10, and between WPs 13 and 15, it correlates with irregular seismic reflections at the same depth for the orange reflector. Uncertainties in matching CSEM and seismic features increase with depth due to the uncertainties of the seismic velocities (only a few metres) and due to the lower resolution of CSEM parameters with depth.

The traceable phase-reversed (green) reflector in Fig. 9 only partially matches probability distributions for interface depths from CSEM inversion, and the inferred resistivities are generally elevated above the reflector that does not support the free gas hypothesis (which would require elevated resistivities underneath the reflector). The green reflector might instead be caused by a lithological change within the Pleistocene sediments, and the phase reversal might be due to a transition from sands to a layer rich in clayey sediment, as large amounts of clay typically result in lower velocities. A similar phase-reversed reflections can be observed in the depth of the MMU (red reflector), which is caused by a transition of sandy river deposits to marine clays (Arfai *et al.* 2011).

The reason for the observed elevated resistivities (2 Ωm–4 Ωm) below the marine Holocene surface layer (below ~20 mbsf) from CSEM inversion may instead be a general porosity reduction (see, e.g., Hamilton 1970, 1972) in the coarse-grained Pleistocene sediments. Glacial tills typically consist of a coarse-grained granular skeleton and binding agents such

as clay minerals and finely distributed calcite. The porosity of glacial tills decreases with increasing age due to the filling of pore space with the binding agents (see e.g., Baermann and Wüstenhagen 1985). Another reason might be more resistive pore water due to an amount of fresh water in the glacial sediments. Unfortunately *in-situ* porosity or resistivity values are not available in the target area.

The boundary between Pleistocene glacial sediments and Pliocene river deposits (kaolinitic sands) is difficult to distinguish with seismic or CSEM data, which might be due to the similar physical characteristics of the two sediment types. The sediment units between the yellow and red reflectors in Fig. 9 are dated to be of Messinian to late Tortonian age by Thöle *et al.* (2014). The GR count in borehole R-1 (see Fig. 5 in Thöle *et al.* 2014), drilled in the same geological units ~100 km northwest of this site increases with depth from the yellow to the blue reflector and then decreases toward the MMU. A high GR count can be related to an increase in fine-grained silts and clays. Clay minerals in seawater form thin double layers and deposit in a high-porous flocculated (edge to face) manner. The flocculant structure collapses under pressure to a denser dispersed structure (see, e.g., Erchul 1972). The resisitivities of sediments are often reduced with increasing amounts of clay (see, e.g., Jones 1999). At ~300 mbsl (the depth of the blue reflector shown in Fig. 9), the lower resistivities of around 1 Ωm could be caused by the increased clay content. Further measurements are necessary, preferably logging-while-drilling, to investigate the effect of clay content and composition, porosity, permeability, and resistivity of the pore water on the bulk resistivity at this location. The overall interpretation of the grain size distribution up to 300 mbsf from borehole, seismic and CSEM inversion results is summarized in Fig. 11.

Posterior median model resistivities tend to increase below the blue reflector towards the red reflector (MMU), but interface probabilities are wide (>400 m), which makes it

difficult to relate the seismic reflector with CSEM interface depths. Resistivities from CSEM inversion beneath the blue reflector exhibit high uncertainties, and synthetic studies (earlier in this paper) also showed that interfaces below 500 m depth may not be resolved. However, deep marine Paleogene clays are known to have resistivities of 1 Ωm–5 Ωm (Jørgensen *et al.* 2003), and the Oligocene sediments are dominated by silts and clays (Arfai *et al.* 2011), so that one explanation for elevated resistivities in greater depth might be sediment compaction.

CONCLUSION

This paper examined the information content of marine controlled-source electromagnetic (CSEM) data with transdimensional Bayesian inversion where the number of subseafloor layers resolved by the data is treated as an unknown in the inverse problem. Time-domain CSEM data were acquired in the German North Sea with a seafloor-towed electric dipole–dipole array with four receivers and a maximum offset of 750 m. The survey was carried out to study the subseafloor resistivity structure and to analyse if a shallow, phasereversed reflector observed on multi-channel seismic data was caused by the abundance of free gas in the sediments.

Simulation studies with realistic correlated errors were carried out to investigate the ability of trans-dimensional Bayesian inversion to estimate model parameters and uncertainties. Inversion results of simulated data show that slight biases in water depth or time synchronization increase uncertainties and decrease the resolution of resistivity structure with depth. Including additional unknowns such as water depth and clock drift tends to over-parametrize the inverse problems, and unreasonable structure can be introduced into the subsurface model. For observed CSEM data in the German North Sea we, therefore, limit the number of additional parameters to the calibration factor for the first receiver. We estimate a non-Toeplitz (non-stationary) data covariance matrix from residual errors to account for correlated errors and varying variance with time. Standardized residual errors generally pass posterior statistical test for Gaussianity and randomness. Interface probabilities from trans-dimensional inversion demonstrate the decreasing resolution of the CSEM data with depth, which are well defined within the first 200 mbsl and a few hundred metres wide below ∼400 mbsl (see bottom panel of Figure 9). As is true for any inversion algorithm, the Bayesian approach can only provide information on model structure that can be resolved by the data, which may

result in a simplified representation of the actual subsurface resistivity structure. For example, thin resistive layers below the data resolution may go undetected or be averaged over in the inversion results, and uncertainties may be increased due to the ambiguity in resolving a layer's thickness and resistivity independently. Data sensitivity to subsurface structure is also reduced in shallow waters due to the signal interaction with the air. However, an average of four layers with different resistivities to a depth of 800 m can be identified, although the last layer has high uncertainties for depth position and resistivity, and is probably below the penetration depth of the CSEM array.

The following geological interpretation was drawn from the CSEM inversion results together with borehole and reflection seismic data. A thin (∼20 m) overburden layer of fine-grained Holocene (to late Pleistocene) sediments is well encased by relatively low resistivities (0.8–1 Ωm) as delineated by high interface probabilities in the Bayesian inversion results. Pleistocene sediments underneath show elevated resistivities (2 Ωm–4 Ωm) that may be related to a coarse-grained, unsorted, and compacted glacial till. Higher amounts of finegrained materials in Miocene sediments, again, correlate with lower resistivities (∼1 Ωm). The geological interpretation excludes the possibility of free gas and relates the targeted seismic reflector to a thin layer of fine-grained sediments, which was likely deposited upon an erosional unconformity.

Trans-dimensional Bayesian inversion not only provides parameter estimates but also parameter uncertainties, including estimates of the number of interfaces (along with uncertainties) and the resolution of interface depths. Interface probabilities with depth can be compared with seismic reflection data. It can be observed that the resolution of CSEM data decreases faster with depth compared with the seismic reflection data, and that strong seismic reflectors do not necessarily correlate with changes in resistivity. We have considered CSEM inversion based on fixing the number of interfaces and their depths from seismic interpretation with results (not shown) that involve more complex resistivity structures and poorer data fit than trans-dimensional inversion. This work demonstrates how marine CSEM data complements ambiguous seismic imaging when investigating the existence of free gas in marine sediments, which is especially important when considering drilling production wells. In the future 2-D inversion analysis (especially important for longer CSEM arrays targeting 2-D structure) will become more practical with faster computational resources including graphics processing units (GPUs) and parallel computer clusters.

ACKNOWLEDGMENTS

REFERENCES

Agostinetti N.P. and Malinverno A. 2010. Receiver function inversion by trans-dimensional Monte Carlo sampling. *Geophysical Journal Internal* **181**, 858–872.

Andréis D. and MacGregor L. 2008. Controlled-source electromagnetic sounding in shallow water: Principles and applications. *Geophysics* **73**(1), F21–F32.

Arfai J., Jaehne F., Lutz R., Reinhardt L., Thöle H. and Wirth H. 2011. Datengrundlage, Arbeitskonzepte und Erste Vorlaeufige Ergebnisse zum Projekt Geopotenzial Deutsche Nordsee (2009-2010).

Baermann D.M.A. and Wüstenhagen K. 1985. Ingenieurgeologische Untersuchungen an Geschiebemergeln im Hamburger Raum. In: *Ingenieurgeologische Probleme im Grenzbereich zwischen Locker- und Festgesteinen*, pp. 434–448. Springer.

Bodin T. and Sambridge M. 2009. Seismic tomography with the reversible jump algorithm. *Geophysical Journal International* **178**, 1411–1436.

Bodin T., Sambridge M., Tkalcic H., Arroucau P., Gallagher K. and Rawlinson N. 2012. Transdimensional inversion of receiver functions and surface wave dispersion. *Journal of Geophysical Research* **117**, 24.

Buland A. and Kolbjørnsen O. 2012. Bayesian inversion of CSEM and magnetotelluric data. *Geophysics* **77**(1), E33–E42.

Cheesman S.J., Edwards R.N. and Chave A.D. 1987. On the theory of sea floor conductivity mapping using transient electromagnetic systems. *Geophysics* **52**, 204–217.

Chen J., Hoversten G.M., Vasco D., Rubin Y. and Hou Z. 2007. A Bayesian model for gas saturation estimation using marine seismic AVA and CSEM data. *Geophysics* **72**(2), WA85–WA95.

Constable S. and Srnka L.J. 2007. An introduction to marine controlled-source electromagnetic methods for hydrocarbon exploration. *Geophysics* **72**(2), WA3–WA12.

Constable S.C. 2010. Ten years of marine CSEM for hydrocarbon exploration. *Geophysics* **75**(5), 75A67–75A81.

Constable S.C., Parker R.L. and Constable C.G. 1987. Occam's inversion: a practical algorithm for generating smooth models from electromagnetic sounding data. *Geophysics* **52**, 289–300.

Constable S.C. and Weiss C.J. 2006. Mapping thin resistors and hydrocarbons with marine EM methods: Insights from 1D modeling. *Geophysics* **71**(2), G43–G51.

Cox C. 1980. Electromagnetic induction in the oceans and inferences on the constitution of the earth. *Geophysical Surveys* **4**, 137–156.

Damm V., Adam J., Bargeloh O., Behrens T., Block M., Demir U. *et al.* 2012. 3D-Test North Sea, Geopotenzial Deutsche Nordsee (GPDN) - CSEM, Cruise No. 88, Leg 1, Aug. 10 - Sept. 6, Bremerhaven - Bremerhaven. Meteor-Berichte, Leitstelle Deutsche Forschungsschiffe, Institut fuer Meereskunde der Universitaet Hamburg.

Denison D.G.T., Holmes C.C., Mallick B.K. and Smith A.F.M. 2002. *Bayesian Methods for Nonlinear Classification and Regression 1st edn.* Wiley.

Dettmer J. and Dosso S.E. 2012. Trans-dimensional matched-field geoacoustic inversion with hierarchical error models and interacting Markov chains. *Journal of the Acoustical Society of America* **132**(4).

Dettmer J., Dosso S.E. and Holland C.W. 2010. Trans-dimensional geoacoustic inversion. *Journal of the Acoustical Society of America* **128**(6), 3393–3405.

Dettmer J., Dosso S.E. and Holland C.W. 2011. Sequential trans-dimensional Monte Carlo for range-dependent geoacoustic inversion. *Journal of the Acoustical Society of America* **129**(4), 1794–1806.

Dettmer J., Holland C.W. and Dosso S.E. 2013. Transdimensional uncertainty estimation for dispersive seabed sediments. *Geophysics* **78**(3), WB63–WB76.

Dosso S.E. and Dettmer J. 2011. Bayesian matched-field geoacoustic inversion. *Inverse Problems* **27**, 23.

Dosso S.E., Dettmer J., Steininger G. and Holland C.W. 2014. Efficient trans-dimensional Bayesian inversion for geoacoustic profile estimation. *Inverse Problems* **30**, 30.

Dosso S.E., Holland C.W. and Sambridge M. 2012. Parallel tempering for strongly nonlinear geoacoustic inversion. *Journal of the Acoustical Society of America* **132**(5), 3030–3040.

Dosso S.E., Nielsen P.L. and Wilmut M.J. 2006. Data error covariance in matched-field geoacoustic inversion. *Journal of the Acoustical Society of America* **119**(1).

Dosso S.E. and Wilmut M.J. 2008. Uncertainty estimation in simultaneous Bayesian tracking and environmental inversion. *Journal of the Acoustical Society of America* **124**(1), 82–97.

Edwards R.N. 1997. On the resource evaluation of marine gas hydrate deposits using sea-floor transient electric dipole-dipole methods. *Geophysics* **62**(1), 63–74.

Edwards R.N. 2005. Marine controlled source electromagnetics: principles, methodologies, future commercial applications. In: *Surveys in Geophysics, vol. 26*, pp. 675–700. Springer, Berlin, Heidelberg, New York.

Erchul R.A. 1972. The use of electrical resistivity to determine porosity of marine sediments, University of Rhode Island, USA.

Gehrmann R.A.S., Schwalenberg K., Riedel M., Dosso S.E. and Spence G.D. 2015. Bayesian inversion of controlled source electromagnetic data at the upper slope offshore Vancouver Island. *in preparation.*

Geyer C.J. 1991. Markov chain Monte Carlo maximum likelihood. In: *Computing Science and Statistics: Proceedings of the 23rd Symposium on the Interface*, pp. 156–163.

Geyer C.J. and Møller J. 1994. Simulation procedures and likelihood inference for spatial point processes. *Scandinavian Journal of Statistics* **21**(4), 359–373.

Geyer C.J., Robert C., Casella G., Fan Y., Sisson S.A., Rosenthal J. *et al.* 2011. *Handbook of Markov Chain Monte Carlo.* Chapman and Hall/CRC.

Green P.J. 1995. Reversible jump Markov chain Monte Carlo computation and Bayesian model determination. *Biometrika* 82(4), 711–732.

Green P.J. 2003. Trans-dimensional Markov chain Monte Carlo. In: *Highly Structured Stochastic Systems, Oxford Statistical Science Series* (eds. P.J. Green, N.L. Hjort and S. Richardson), pp. 179–198. Oxford University Press, Oxford.

Guo R., Dosso S.E., Liu J., Dettmer J. and Tong X. 2011. Nonlinearity in Bayesian 1-D magnetotelluric inversion. *Geophysical Journal International* 185(2), 663–675.

Hamilton E.L. 1970. Sound velocity and related properties of marine sediments, North Pacific. *Journal of Geophysical Research* 75(23), 4423–4446.

Hamilton E.L. 1972. Compressional-wave attenuation in marine sediments. *Geophysics* 37(4), 620–646.

Hepp D.A., Hebbeln D., Kreiter S., Keil H., Bathmann C. and T. Mörz J.E. 2012. An east-west-trending Quaternary tunnel valley in the south-eastern North Sea and its seismic-sedimentological interpretation. *Journal of Quaternary Sciences* 27, 844–853.

Jones E.J.W. 1999. *Marine Geophysics.* John Wiley and Sons, Ltd.

Jørgensen F., Sandersen P., Auken E., Lykke-Andersen H. and Sørensen K.I. 2003. Contributions to the geological mapping of Mors, Denmark: A study based on a large-scale TEM survey. *Bulleting of the Geological Society of Denmark* 57, 167–178.

Keil H. and Hepp D.A. 2013. Tracing the Holocene transgression of the North Sea in the German Bight. RV Heincke HE-405, Bremerhaven-Bremerhaven, June 27–July 13 2013. Marum - Centre for Marine Environmental Sciences.

Key K. 2009. 1D inversion of multicomponent, multifrequency marine CSEM data: methodology and synthetic studies for resolving thin resistive layers. *Geophysics* 74(2), F9–F20.

Kirsch R., Burschil T., Roeloffs R., Ketelsen H., Scheer W., Steinmann F. *et al.* 2012. Der Untergrund von Föhr: Geologie, Grundwasser und Erdwaerme. Ergebnisse des INTERREG-Projektes CLI-WAT. Tech. rep., Leibniz Institute for Applied Geophysics and State Agency for Agriculture, Environment and Rural Areas, Germany.

Kudraß H.R., Bönnemann C., Gaedicke C., Ladage S., Neben S., Reinhardt L. *et al.* 2003. Cruise report, BGR03-AUR Nordsee, MV-Aurelia, September 16–October 9, 2003. Federal Institute for Geoscience and Natural Resources.

MacGregor L.M., Andreis D., Tomilinson J. and Barker N. 2006. Controlled-source electromagnetic imaging on the Nuggets-1 reservoir. *The Leading Edge* 25.

Malinverno A. 2002. Parsimonious Bayesian Markov chain Monte Carlo inversion in a non linear geophysical problem. *Geophysical Journal International* 151, 675–688.

Massey F.J. 1951. The Kolmogorov-Smirnov test for goodness of fit. *Journal of American Statistical Association* 46, 68–78.

Minsley B.J. 2011. A trans-dimensional Bayesian Markov chain Monte Carlo algorithm for model assessment using frequency-domain electromagnetic data. *Geophysical Journal International* 187(1), 252–272.

Moghadas D., Engels M. and Schwalenberg K. 2015. 1D joint multi-offset inversion of time-domain marine controlled source electromagnetic data. *Geophysical Prospecting* 63(6), 1440–1460.

Rasmussen E.S. 2004. Stratigraphy and depositional evolution of the uppermost Oligocene - Miocene succession in western Denmark. *Bulletin of the Geological Society of Denmark* 51, 89–109.

Ray A., Alumbaugh D.L., Hoversten G.M. and Key K. 2013a. Robust and accelerated Bayesian inversion of marine controlled-source electromagnetic data using parallel tempering. *Geophysics* 78(6), E271–E280.

Ray A. and Key K. 2012. Bayesian inversion of marine CSEM data with a trans-dimensional self parametrizing algorithm. *Geophysical Journal International* 191, 1135–1151.

Ray A., Key K., Bodin T., Myer D. and Constable S. 2014. Bayesian inversion of marine CSEM data from the Scarborough gas field using a transdimensional 2-D parametrization. *Geophysical Journal International* 199(3), 1847–1860.

Ray A., Key K. and Bodin T. 2013b. Hierarchical Bayesian inversion of marine CSEM data over the Scarborough gas field-a lesson in correlated noise. SEG Annual Meeting, Houston, USA. Society of Exploration Geophysicists.

Rosas-Carbajal M., Linde N., Kalscheuer T. and Vrugt J.A. 2013. Two-dimensional probabilistic inversion of plane-wave electromagnetic data: methodology, model constraints and joint inversion with electrical resistivity data. *Geophysical Journal International,* ggt482.

Sambridge M., Bodin T., Gallagher K. and Tkalcic H. 2013. Transdimensional inference in the geosciences. *Philosophical Transactions of the Royal Society A: Mathematical, Physical and Engineering Sciences* 371(1984), 20110547.

Sambridge M., Gallagher K., Jackson A. and Rickwood P. 2006. Trans-dimensional inverse problems, model comparison and the evidence. *Geophysical Journal International* 167, 528–542.

Scholl C. 2005. The influence of multidimensional structures on the interpretation of LOTEM data with one-dimensional models and the application to data from Israel. Ph.D. thesis, University of Cologne, Germany.

Scholl C. 2010. Resolving an onshore gas-hydrate layer with long-offset transient electromagnetics (LOTEM). In: *Geophysical Characterization of Gas Hydrates* (eds. M. Riedel, E.C. Willoughby and S. Chopra), pp. 149–162. Society of Exploration Geophysicists.

Schwalenberg K. and Engels M. 2012a. Marine controlled source electromagnetic methods for gas hydrate assessment: Latest results from the Black Sea and the Hikurangi Margin, NZ. 21st Workshop on Electromagnetic Induction in the Earth, Darwin, Australia, July 25-31, 2012, Extended Abstracts.

Schwalenberg K. and Engels M. 2012b. Marine controlled source electromagnetic methods for gas hydrate assessment: New instrumentation and first results from the Black Sea test cruise. In: *Protokoll über das 24. Schmucker-Weidelt-Kolloquium für Elektromagnetische Tiefenforschung,* Neustadt Weinstraße, Germany, September 19–23, 2011, pp. 239–249.

Schwalenberg K., Engels M., Mir R.A. and of M88/2" S.P. 2012. Geopotenzial Deutsche Nordsee (GPDN) - CSEM, Cruise No. 88, Leg 2, Sept. 08-22, Bremerhaven - Bremerhaven. Meteor-Berichte,

Leitstelle Deutsche Forschungsschiffe, Institut für Meereskunde der Universität Hamburg.

Schwalenberg K., Haeckel M., Poort J. and Jegen M. 2010. Evaluation of gas hydrate deposits in an active seep area using marine controlled source electromagnetics: Results from Opouawe Bank, Hikurangi Margin, New Zealand. *Marine Geology* **272**(1–4), 89–98. doi:10.1016/j.margeo.2009.07.006.

Sørensen J.C., Gregersen U., Breiner M. and Michelsen O. 1997. High-frequency sequence stratigraphy of Upper Cenozoic deposits in the central and southeastern North Sea areas. *Marine and Petroleum Geology* **14**(2), 99–123.

Swidinsky A. and Edwards R.N. 2010. The transient electromagnetic response of a resistive sheet: extension to three dimensions. *Geophysical Journal International* **182**, 663–674.

Vink A., Steffen H., Reinhardt L. and Kaufmann G. 2007. Holocene relative sea-level change, isostatic subsidence and the radial viscosity structure of the mantle of northwest Europe (Belgium, the Netherlands, Germany, southern North Sea). *Quaternary Science Reviews* **26**(25–28), 3249–3275. dx.doi.org/10.1016/j.quascirev.2007.07.014.

Ward S.H. and Hohmann G.W. 1988. Electromagnetic theory for geophysical applications. In: *Electromagnetic Methods in Applied Geophysics, Vol. 1* (ed. M.N. Nabighian), pp. 131–313. Society of Exploration Geophysicists.

Weidelt P. 2007. Guided waves in marine CSEM. *Geophysical Journal International* **171**, 153–176.

Weiss C.J. 2007. The fallacy of the "shallow-water problem" in marine CSEM exploration. *Geophysics* **72**(6), A93–A97.

Ziolkowski A., Parr R., Wright D., Nockles V., Limond C., Morris E. *et al.*, 2010. Multi-transient electromagnetic repeatability experiment over the North Sea Harding field. *Geophysical Prospecting* **58**, 1159–1176.

Appendix B: Grounding zone wedges and mega-scale glacial lineations in Kveithola Trough, Barents Sea

M. Rebesco[1]*, R. Urgeles[2], A. Özmaral[3] & CORIBAR scientific party[4]

[1]*Istituto Nazionale di Oceanografia e di Geofisica Sperimentale (OGS), 34010 Sgonico (TS), Italy*
[2]*Institut de Ciències del Mar (CSIC), 08003 Barcelona, Spain*
[3]*MARUM—Center for Marine Environmental Sciences, University of Bremen, 28359 Bremen, Germany*
[4]*T.J.J. Hanebuth, H. Lantzsch, A. Caburlotto, T. Hörner, J. Llopart, R.G. Lucchi, L.S. Nicolaisen, G. Osti & A. Sabbatini*

*Corresponding author (e-mail: <u>mrebesco@ogs.trieste.it</u>)

Multibeam-bathymetric data from Kveithola Trough show a seafloor characterized by east–west trending mega-scale glacial lineations (MSGLs) overprinted by transverse grounding-zone wedges (GZWs). GZWs are thought to form by deposition of subglacial till at temporarily stable ice-sheet marine termini between successive episodic retreats (Batchelor & Dowdeswell 2015). Subbottom profiles show that the present-day morphology of Kveithola Trough is largely inherited from the palaeo-seafloor topography of the GZWs, which is now draped by deglacial to early Holocene glacimarine sediment about 15 m thick. The ice stream that produced such subglacial morphology was flowing from east to west towards the shelf edge in Kveithola Trough during the Last Glacial Maximum (LGM). Its rapid retreat was probably associated with progressive lift-off and successive rapid melting of grounded ice induced by eustatic sea-level rise.

Description

The east–west-trending Kveithola Trough in the Barents Sea (Fig. C.1) shows well-preserved subglacial landform morphologies (Rebesco et al. 2011; Bjarnadóttir et al. 2012; Fig. C.1) including GZWs and MSGLs. Iceberg ploughmarks overprint these landforms.

The GZWs are up to 70 m high and spaced about 15 km apart, which gives the axial profile of the trough the appearance of a succession of stairs. The GZWs extend transversely across the entire width of the trough, except for the outermost wedge at the shelf edge which is fan-shaped. They have asymmetric axial profiles with steeper, markedly lobate, west-facing outer slopes and more gentle eastward-dipping inner sides. The seafloor of the eastern (inner) side of each GZW is marked by MSGLs that are sub-parallel to the flanks of the trough and divergent in the region of the trough mouth. The MSGLs comprise ridges and depressions 100–600 m wide, < 15 m high and about 8 km long. They have length to width ratios of > 10:1.

The upper surface of the GZWs and the flanks of the trough have been impacted by the grounding of iceberg keels producing a vertical roughness of about 1 m (Fig. C.1a). The iceberg ploughmarks are sinuous to linear in planform but also include sharp corners or kinks along their paths. In general, the ploughmarks have trough-parallel orientations on the northern flank of the trough and along-slope orientations beyond the shelf edge.

Sub-bottom profiler data (Fig. C.1b) show that the transparent facies in which the GZWs and MSGLs have formed is capped by a stratified sedimentary drape. Although this drape attains a thickness of 20 ms two-way travel time (about 15 m when converted using a sound velocity of 1500 m s^{-1}), it does not obscure the morphologies inherited from the palaeo-subglacial landforms beneath it.

Interpretation

The GZWs and MSGLs in the Kveithola Trough are similar to submarine glacial landforms identified elsewhere on the Norwegian–Svalbard margin (e.g. Ottesen et al. 2005). MSGLs are thought to be produced by deformation of a subglacial till layer of low shear strength under rapid ice-flow velocities beneath ice streams (e.g. Clark 1993; Dowdeswell et al. 2004). The ice stream that produced the subglacial morphologies in Kveithola Trough was flowing from east to west in the trough during the LGM (Rebesco et al. 2011). The morphological and acoustic character of the GZWs suggests that these features formed by deposition of unconsolidated, water-saturated subglacial till during temporary stillstands in the grounding-zone position of the ice-stream (Batchelor & Dowdeswell 2015). The wedges are clearly superimposed on the MSGL, implying that these landforms were produced mostly, but not exclusively (Bjarnadóttir et al. 2012), through a recessional trend during the deglaciation phase. Streamlining of the eastwards (upstream) sides of the GZWs demonstrates that the ice stream remained grounded and active throughout its overall retreat, and that individual phases of sudden retreat were rapid enough to prevent the obliteration of the MSGLs. We speculate that the rapid retreat phases were associated with lift-off of grounded ice induced by rapid global sea-level rise, as suggested by Lucchi et al. (2013).
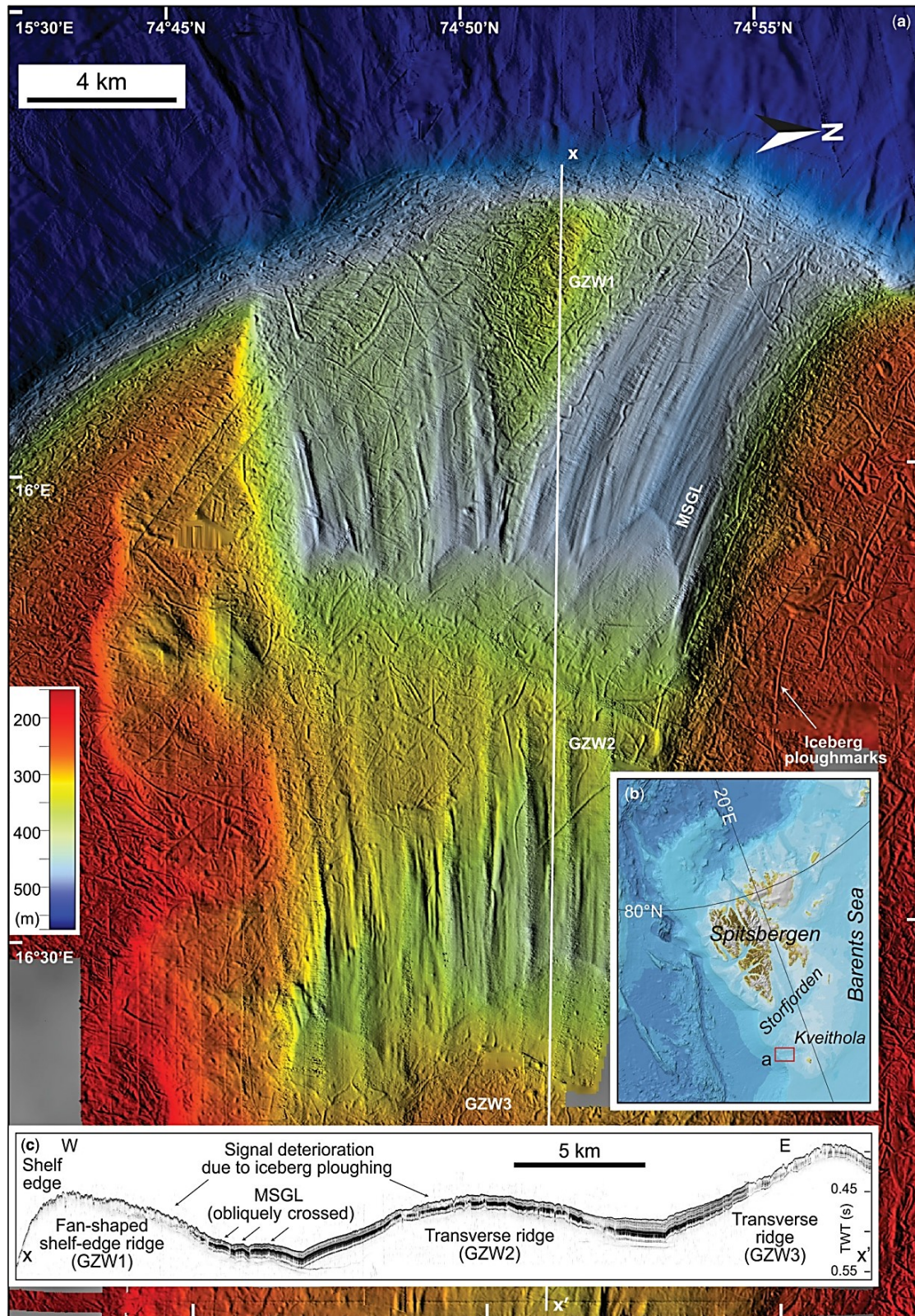
Figure B.1 (a) Sun-illuminated multibeam bathymetric image (10 m grid cell), showing outer part of the Trough, obtained by merging Reson Seabat 8111 and Kongsberg EM1002 data from EGLACOM (Rebesco et al. 2011) and CORIBAR (Hanebuth et al. 2014) cruises, respectively. (b) Location of study area (red box; map from IBCAO v. 3.0). (c) Parasound profile showing the sub-bottom characteristics of Kveithola Trough landforms. The sedimentary drape overlies a transparent unit, interpreted as a GZW. VE x 40.

References

Batchelor, C.L. & Dowdeswell, J.A. 2015. Ice-sheet grounding-zone wedges (GZWs) on high-latitude continental margins. Marine Geology, 363, 65 – 92.

Bjarnadóttir, L.R., Rüther, D.C., Winsborrow, M.C.M. & Andreassen, K. 2012. Grounding-line dynamics during the last deglaciation of Kveithola, W Barents Sea, as revealed by seabed geomorphology and shallow seismic stratigraphy. Boreas, 42, 84 – 107.

Clark, C.D. 1993. Mega-scale glacial lineations and cross-cutting ice-flow landforms. Earth Surface Processes and Landforms, 18, 1 – 29.

Dowdeswell, J.A., O´ Cofaigh, C. & Pudsey, C.J. 2004. Thickness and extent of the subglacial till layer beneath an Antarctic paleoice stream. Geology, 32, 13 – 16.

Hanebuth, T.J.J., Rebesco, et al. 2014. Drilling glacial deposits in offshore polar regions. Eos, 95, 277-278.

Lucchi, R.G., Camerlenghi, A. et al. 2013. Postglacial sedimentary processes on the Storfjorden and Kveithola trough mouth fans: significance of extreme glacimarine sedimentation. Global and Planetary Change, 111, 309 – 326.

Ottesen, D., Dowdeswell, J.A. & Rise, L. 2005. Submarine landforms and the reconstruction of fast-flowing ice streams within a large Quaternary ice sheet: the 2500-km-long Norwegian-Svalbard margin (57 – 80°N). Geological Society of America Bulletin, 117, 1033 – 1050.

Rebesco, M., Liu, Y. et al. 2011. Deglaciation of the western margin of the Barents Sea Ice Sheet – a swath bathymetric and sub-bottom seismic study from the Kveithola Trough. Marine Geology, 279, 141 – 147.

Versicherung an Eides Statt

gem. § 5 Abs. 5 der Promotionsordnung vom 15.07.2015

Ich, Asli Özmaral, H.-H.-Meier-Allee 51, 28213 Bremen, Mat.-Nr. 2949400), versichere an Eides Statt durch meine Unterschrift, dass ich die vorstehende Arbeit selbständig und ohne fremde Hilfe angefertigt und alle Stellen, die ich wörtlich dem Sinne nach aus Veröffentlichungen entnommen habe, als solche kenntlich gemacht habe, mich auch keiner anderen als der angegeben Literatur oder sonstiger Hilfsmittel bedient habe.

Ich versichere an Eides Statt, dass ich die vorgenannten Angaben nach bestem Wissen und Gewissen gemacht habe und dass die Angaben der Wahrheit entsprechen und ich nichts verschwiegen habe.

Die Strafbarkeit einer falschen eidesstattlichen Versicherung ist mir bekannt, namentlich die Strafandrohung gemäß § 156 StGB bis zu drei Jahren Freiheitsstrafe oder Geldstrafe bei vorsätzlicher Begehung der Tat bzw. gemäß § 161 Abs. 1 StGB bis zu einem Jahr Freiheitsstrafe oder Geldstrafe bei fahrlässiger Begehung.

Bremen, 10.04.2017   Aslı Özmaral

_____   _____

Ort, Datum   Unterschrift